Modifications to M_2M' Heterometallic Chain Compounds and their Spectroscopic, Magnetic, and Electronic Consequences

By
Jill Ann Chipman

A dissertation submitted in partial fulfillment of
the requirements for the degree of

Doctor of Philosophy
(Chemistry)

at the
UNIVERSITY OF WISCONSIN – MADISON
2019

Date of final oral examination: 7/24/2019

This dissertation is approved by the following members of the Final Oral Committee:

John F. Berry, Professor, Chemistry

Thomas C. Brunold, Professor, Chemistry

Daniel C. Fredrickson, Professor, Chemistry

Jennifer M. Schomaker, Professor, Chemistry

József S. Pap, Laboratory Head, Hungarian Academy of Sciences

Modifications to M_2M' Heterometallic Chain Compounds and their Spectroscopic, Magnetic, and Electronic Consequences

Jill Ann Chipman

Under the supervision of Professor John F. Berry
University of Wisconsin – Madison

Abstract

Asymmetric $M_AM_AM_B$ Hetererometallic Extended Metal Atom Chain (HEMAC) compounds supported by the 2,2' – dipyridylamine (dpa) ligand present a wide range of structural, spectroscopic, and magnetic phenomena. An introduction for a general audience as part of the Wisconsin Initiative for Science Literacy is presented in Chapter 1. An overview of the synthetic, electronic structure, and magnetic properties of symmetric and asymmetric trimetallic HEMACs is part of the work in Chapter 2. This chapter more broadly covers paramagnetic heterometallic metal-metal bonded compounds including heterobimetallic compounds and heterometallic compounds of higher nuclearity. Chapters 3 and 4 deal with the Mo_2Ni supported HEMACs. Chapter 3 discusses the results of one-electron oxidation on the $Mo_2Ni(dpa)_4Cl_2$ compound, which results in a species with extraordinarily large ferromagnetic coupling. A synthetic breakthrough for facile axial ligand substitution on a Mo_2Ni chain is presented in Chapter 4. This chapter includes a thorough investigation of the structural, magnetic, and spectroscopic consequences of different axial ligands on a Mo_2Ni chain. The next two chapters further investigate axial ligand effects with Chapter 5 exploring the effects of three axial halides with a $Cr_2Fe(dpa)_4X_2$ (X = Cl, Br, and I) compound via Mössbauer spectroscopy while Chapter 6 investigates the unusual spin state of $Mo_2Co(dpa)_4Br_2$ in comparison to $Mo_2Co(dpa)_4Cl_2$ via SQUID magnetometry, magnetic circular dichroism spectroscopy (MCD), and density functional theory (DFT) computations. Chapter 7 concludes the thesis with ongoing work regarding the ability of $Mo_2Ni(dpa)_4X_2$ compounds to behave as molecular wires in addition to the effects on electron transport of different axial ligands on the homometallic $Ni_3(dpa)_4X_2$ chain compound.

DEDICATION

This work is dedicated to my parents, Jay and Debbie Chipman who have supported me unconditionally on this path to a Ph.D. I also dedicate this to my Gammy and Gampy for always being there for me, Ja cię kocham. To Grandpa and Grandma Chipman, I haven't stopped laughing.

ACKNOWLEDGEMENTS

I would like to first thank my advisor, Professor John F. Berry for taking me into his group after declaring to him that I had never taken a formal inorganic chemistry class, mentoring me, and helping me find my own self in the world of chemistry. I have been fortunate enough to explore projects that fascinate me that have led to both expected results and serendipitous discoveries.

Equally as supportive is Bassam Shakhashiri for initially letting me into the Science is Fun group as a TA for his class to providing me with endless support. He is one of the most insightful, caring, and brilliant minds I have met here. I would not be here today without him. He has kept me on the path to defending my thesis through all the challenges that come with being a grad student. I cannot thank him enough for all he has done. The Science is Fun crew have all been amazing to work with too!

I would like to thank the members of the Berry group. They have helped me grow as a person as and as a scientist through their support and encouragement. Specifically I would like to thank Dr. Brian Dolinar for teaching me the art of air-free chemistry as well as continuing to answer my questions even though he has moved on to bigger and better things. I thank Dan, Amelia, and Trey for being fantastic office mates and friends. I also thank Dr. Caleb Harris, Dr. Christian Wallen, Sungho Park, Michael Roy, Mike "Tren" Trenerry, and Mike Aristov for being such supportive colleagues. I thank the former Berry Lab members who helped me during my early years in this group: Dr. Amanda Corcos, Dr. Wes Brogden, and Dr. Nick Yang. I have been fortunate enough to have three wonderful undergrads; Josh Powell, Josie Lange, and David "Davie!!" Beshensky. I will miss you all.

My committee has been more than supportive; Danny and Thomas have been apart of my committee since the beginning. Thomas especially has provided me with more support and guidance than I realized was possible. For my final committee, Prof. Jen Schomaker and Dr. Jozsef Pap were kind enough to serve on my dissertation committee.

I would not be able to have completed the research I did without the help of the instrument staff. To that end, thank you Desiree Bates for computational support, Ilia Guzei for crystallographic insights, Heike, Charlie, and Lingchao for NMR/EPR/SQUID assistance, and Martha Vestling for help with mass spectrometry. I'm also grateful for Tracy Drier in the glass shop for teaching me the art of glassblowing and fixing the multiple pieces of glassware I broke over the past five years and the kaliaparat my cat broke…

I definitely would not be here without my high school chemistry teacher, Christine Wilckens. She was the first teacher to *really* spark my passion for something. I wouldn't have started this twelve year journey without her "unconventional" wisdom and support.

My family has been extremely supportive. From the moments when I declared I wanted to quit grad school, to changing my mind, and then repeating this about 50 times; they've been here. My mom and dad, Gampy, and Uncle Chip have always been there and provided me with the love and care I needed to get this far. However, I've lost two pillars of support along the way. Grandpa Chipman, who died during my second year, taught me something valuable as I left for grad school "Grandpa Chipman always says that if you can't left, you're in *deep* shit" I would have gone insane without the laughter my friends in Madison have given me. Gammy, who died before my fourth year, was the biggest rock someone could ever ask for. I knew I could call her at midnight if I needed to, even if it was just to say "I love you." I wear her necklace every day so she can never really leave me. Ja cię kocham.

As my friend Dan proudly declared in the office "Life is a giant column, some people stick to the silica, others just pass through" when describing friendships. He could not be more accurate.. Those people, whether they're in Madison or elsewhere in the world, are my friends. Amanda, Anastasiya, Desiree, "The Golden Girls", Katheen, Laur, Manar, Ming, Moira, Sara, and Sarah are all wonderful human beings that I'm lucky to call my friends. I'd especially like to acknowledge Max, whom I met in college. He has helped me stay focused and motivated as I wrote this thesis. He has also been an incredibly supportive and wonderful human being. I'd also like to acknowledge my best friend since high school, Anna. Thank you.

As per tradition, I must end every acknowledgement section with my pets. Moe the hamster, George and Kramer the guinea pigs, Elaine the cat, and the Berry Lab goldfish Cosmo have been just the things I've needed to come home to… even if one of them wakes me up at 3 am for food, shreds my resume, and pees on the guinea pig, she will remain nameless.

Everyone I've mentioned here deserves their name on this degree with me (maybe not the cat.) Thank you all.

TABLE OF CONTENTS

LIST OF CHARTS

LIST OF FIGURES

LIST OF SCHEMES

LIST OF TABLES

Chapter One

Dr. Chipman or: How I Learned to Stop Worrying and Love Transition Metals

Wisconsin Initiative for Science Literacy: Introduction for a General Audience

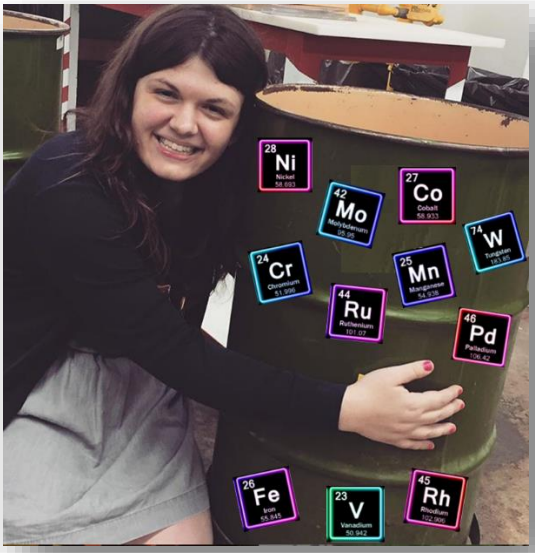

This chapter begins with a reflection on my education in Inorganic Chemistry followed by a description of the field and what I've accomplished in my doctoral research.

As any student is told in their high school chemistry course, inorganic chemistry involves the science of "that short stubby rectangle" in the middle of the periodic table. I was no different. Figure 1.1 shows the same periodic table that I learned from when I took my first chemistry course in 2007. While a large portion of inorganic chemistry is centered on that rectangle, inorganic chemistry encompasses so much more! Nonetheless, I was told I would learn more about that magical rectangle in college.

I entered college in August of 2010 and sat through General Chemistry, Organic Chemistry, and then Biochemistry before I was finally able to take a course on "that short stubby rectangle." To my dismay, I was placed in "Advanced Inorganic Materials" because the introductory course didn't fit my schedule. This meant two things: 1) I waited until my junior year of *college* (Fall 2012) before I could learn anything substantive about inorganic chemistry, and 2) I would graduate college in 2014, seven years after I started taking chemistry courses, without taking a fundamental inorganic chemistry basics course. Logically, this meant I enrolled at UW–Madison in Fall 2014 for grad school and joined John Berry's *inorganic* chemistry

research group. I nervously informed John that "I have never taken a formal inorganic chemistry course." This turned out to be ok in his eyes and five years later in 2019, I'm defending the research I did in inorganic chemistry to become Dr. Jill Ann Chipman.

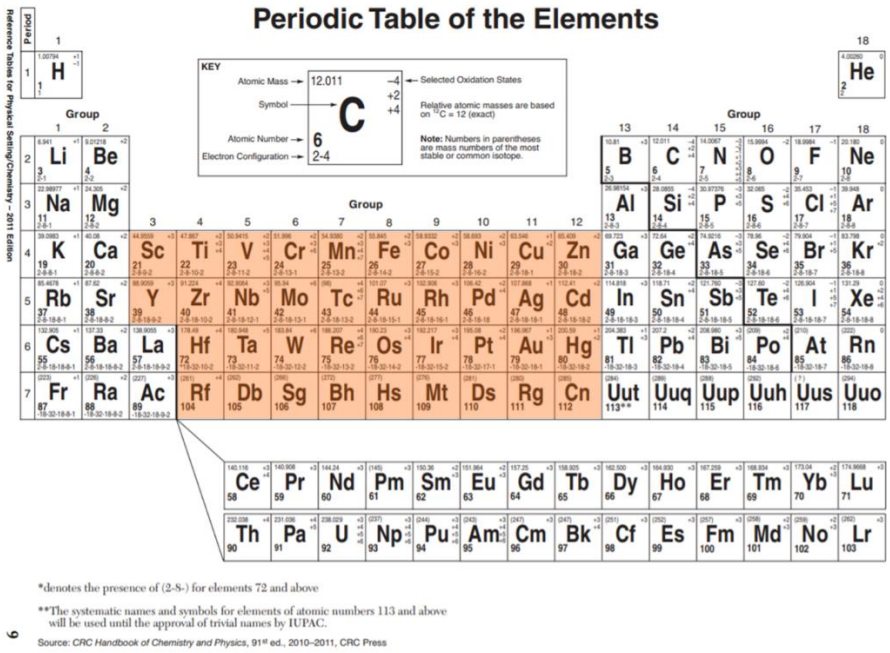

Figure 1.1 The New York State Reference Tables Periodic Table of the Elements. This is the periodic table I used while learning chemistry in high school. "That short stubby rectangle" is highlighted in orange.[1]

I've really found my space in the field of inorganic chemistry, but it took twelve years to get here! It took about half that time to even begin to understand inorganic chemistry. For a field that supports life as we know it, inorganic chemistry shouldn't be a mysterious black box to society. It needs a better introduction than "the short stubby rectangle" or "*not* organic." I've therefore written this introductory chapter as means to answer two questions:

1.) What *is* Inorganic Chemistry?

2.) How did my research *contribute* to Inorganic Chemistry?

1.1 What *is* Inorganic Chemistry?

The American Chemical Society defines inorganic chemistry by stating "Inorganic chemistry is concerned with the properties and behavior of inorganic compounds, which include metals, minerals, and

organometallic (defined below) compounds."[2] Whereas organic compounds *must* contain a carbon–hydrogen bond, inorganic compounds are largely centered on compounds that do not contain carbon. Organometallics are a special mix of organic and inorganic chemistry and they contain a metal bonded to a carbon. Generally speaking, many inorganic compounds include a metal; more specifically, a transition metal. As mentioned above, the transition metals are "that short stubby block" in the middle of the periodic table. That block makes up about 1/3 of the periodic table.

In contrast to the other 2/3 of the elements, the transition metals contain two key properties. Many non-transition metals have one of these two properties, but *not* both! Transition metals are conductive, lustrous, malleable, and ductile, just like the other elements of the periodic table classified as metals. Conductive means that the material can allow electricity (aka a current) to flow through. For example, the electrical wires in many homes are made of copper, a transition metal. Transition metals are also lustrous, meaning they're shiny. The remaining two properties, malleability and ductility are very similar. We can think about them by thinking of a large block of any transition metal. We may want a sheet of our metal; transition metals are malleable and are easily flattened into sheets. Maybe we don't want a sheet, we instead want to make our block a wire; transition metals are ductile and can be drawn into thin wires. These are all properties of transition metals that we can see with our naked eyes. The property that interests me about transition metals, however, is one we *can't* see with the naked eye.

The other distinctive property of transition metals is that they can house different numbers of electrons and still be stable. Most elements can exist in two states; neutral (atom) or charged (ion). Transition metals are no different in this way, but they are different in that they can exist in multiple charged states. That is, they can hold different numbers of electrons and still be stable. In comparison to the other elements of the periodic table, this is a relatively unique property. For example, the element fluorine (F) which is not a transition metal, can exist in a neutral form, or as an ion, with a –1 charge, by housing an additional electron. Meanwhile, the element iron (Fe), which is a transition metal, can exist in a neutral form, but it can also exist with +2 *or* +3 charge, by losing two or three of its electrons, respectively. Figure 1.2 illustrates these differences. Not very many other elements outside the transition metals are capable of doing this. It is only the transition metals that have both of these properties.

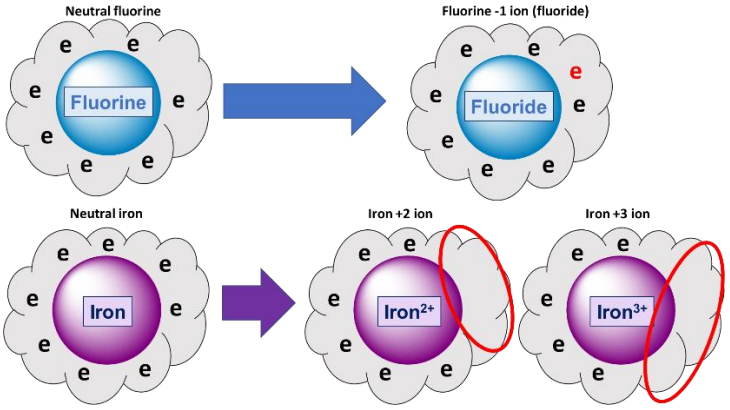

Figure 1.2 Fluorine can house one additional electron when it is an ion (top); Iron can lose either two or three electrons when it is an ion (bottom). Electrons are denoted by the letter "e"

Given these two properties, chemists can tailor the environment around a transition metal in order to give it desired behaviors. As chemists, we must carefully design our compounds to have them behave in ways that we would like. However, nature has been able to harness the power of transition metals too. They are found in minerals, plants, and animals. For example, many of the precious gemstones we value come from some of the most common minerals in the world. However, with a small amount of a transition metal "impurity" these common minerals skyrocket in value. For example, the ruby is formed when a chromium impurity is present in the mineral corundum.[3] Figure 1.3 below shows the mineral corundum in comparison to both a rough and a cut ruby.

Figure 1.3 The mineral corundum is composed of aluminum and oxygen. Upon introduction of a chromium impurity, a ruby can be formed. Both a rough ruby and cut ruby are shown for contrast. [4]

Our bodies are full of red blood cells, which get their distinctive red color from the iron center in a complex called heme, which lives in a protein called hemoglobin (Figure 1.4 top). Heme has more responsibilities than just binding oxygen and making our blood red. It helps promote a variety of chemical reactions in our bodies that allow us to live.[5] Our bodies do not just contain iron however and many of the medications that help humans to overcome health complications contain a transition metal. One of the most well-known cancer drugs, cisplatin, was initially discovered in 1845 (Figure 1.4 bottom). It remains in use today and contains platinum.[6] Moving outside of our bodies, we can also find platinum in the catalytic converter of the cars that we drive. We might also find rhodium, cobalt, zinc, and copper, which are all transition metals.[7] Moving to smaller items, metals including copper, nickel, silver, gold, and lead, are also found in our cell phones, computers, and tablets. It would be negligent to disregard the point that many of these metals do come from non–renewable sources.[8] This means we are responsible for recycling our used electronics and car parts in a way that allow us to sustain our way our life without damaging the world around us!

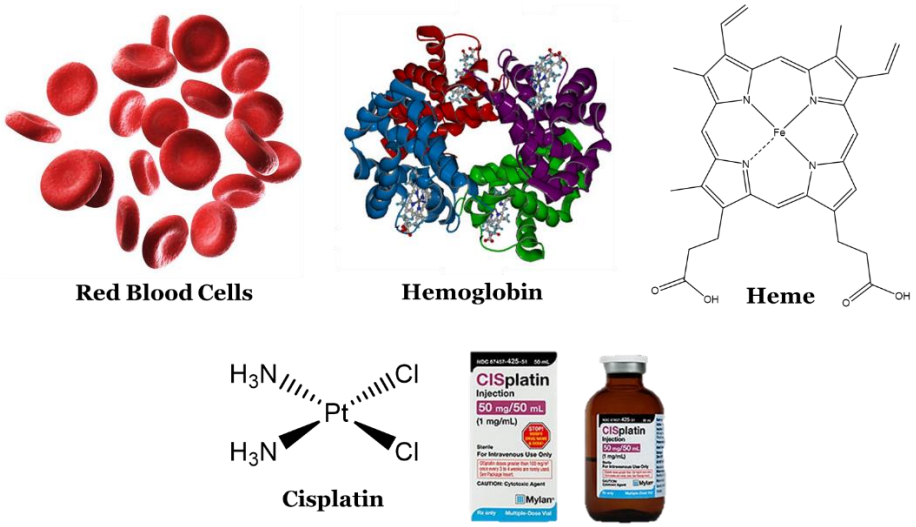

Figure 1.4 (Top) the iron center in heme gives red blood cells their distinctive red color. Heme is a part of the protein known as hemoglobin. (Bottom) cisplatin is one of the most well-known and used cancer drugs.[9]

For inorganic chemists, nature provides an amazing inspiration source. A great deal of inorganic research is focused on understanding how metals in living things do what they do. Other chemists marry the field of inorganic chemistry with organic chemistry (the chemistry of the element carbon) to form a hybrid field called organometallic chemistry. Organometallic complexes contain at least one metal–carbon bond. While both of these topics are studied in the Chemistry department at UW–Madison, neither one

represents my research. My research remains in understanding some of the most fundamental aspects of inorganic chemistry and finding applications for some of the complexes that I make.

1.2 How did my research contribute to Inorganic Chemistry?

One of the characteristics of a transition metal is the ability to conduct electricity. The big picture goal of my research is take that ability, fine tune it, and make small–scale single molecule electronic pieces. In order to make smaller electronics that have the same (or more) strength as their larger versions, we need smaller building blocks. The smallest possible building block? A molecule! My research has involved making **H**eterometallic **E**xtended **M**etal **A**tom **C**hains, or HEMACs, for short. The chains I work with are three metal atoms long, with two different metals arranged asymmetrically. The metal chain is surrounded by four paddlewheel supports, called ligands. A ligand is most generally defined as something that is bound to a metal. A ligand can be as simple as one atom or it can be part of group of atoms. The ligand used in this work is dpa (or 2, 2' dipyridylamine). There are an additional two capping ligands on either end of the chain. Our group has a well-established method for building these chains, and much of my work has focused on the effects of changing the capping ligands on the ends of the chains.[10-16]

Scheme 1.1 shows the general HEMAC structure as well as the places I have made modifications as part of my research. If we look at a HEMAC and compare it to a normal electronic wire, there's a similarity! A wire contains a core that carries current and it is surrounded by an insulating blanket. A HEMAC contains a three-metal atom long chain (the core) and surrounds it with insulating ligand! Of course, my research goes a little bit further than just a visual similarity, shown in Figure 1.5. I've chosen to focus this section on the two contributions I've made that are closest to molecular electronics.

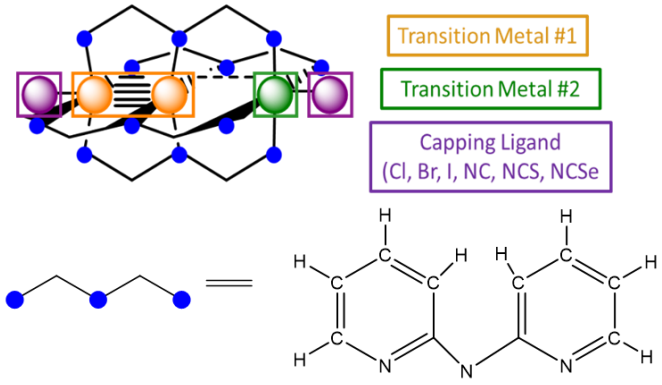

Scheme 1.1 The general structure of one of my HEMAC compounds supported by the dpa ligand. Different spheres represent different portions of the HEMAC that I have modified.

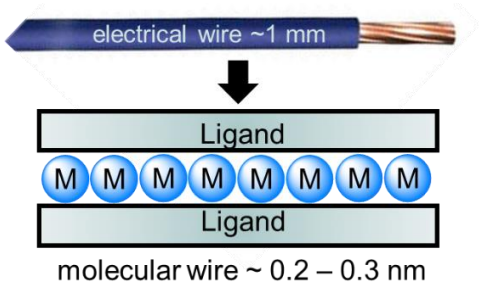

Figure 1.5 The visual comparison between an electric wire and a molecular wire. The molecular wire is much smaller than a normal electric wire but shares the same design.

My first major success in research used molybdenum (Mo) and nickel (Ni) to form a Mo–Mo–Ni chain that didn't behave like any other previously made chain.[17] The compound I started with was $Mo_2Ni(dpa)_4Cl_2$. Our group had not yet made this compound, so this in itself is a new advancement. A structure of this chain is shown below (Figure 1.6).

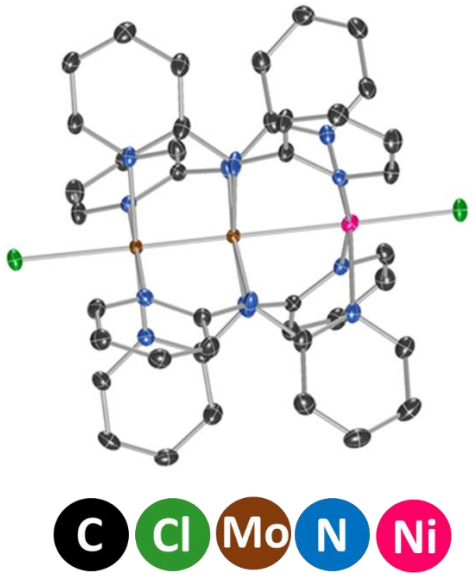

Figure 1.6 A structural representation of $Mo_2Ni(dpa)_4Cl_2$. Different color spheres represent different atoms. Hydrogen atoms have been removed for clarity.

This chain consists of a Mo_2 species that is bound together and contains no unpaired electrons in addition to a Ni^{2+} ion that contains two unpaired electrons. When I remove an electron from the overall chain, it can come from either Ni^{2+} or Mo_2, for this chain, it came from Mo_2. This means that in total I have three electrons each with a preferred spin (think clockwise or counterclockwise). Two spins can pair (couple) together with the same spin (ferromagnetically) or with opposing spins (antiferromagnetically). This is illustrated in Figure 1.7.

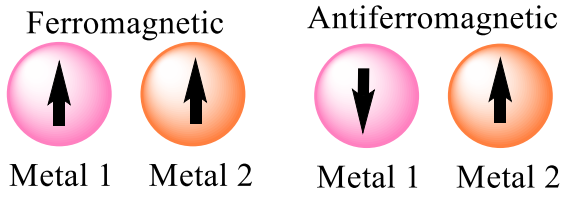

Figure 1.7 Electrons in different metals can pair together with spins that are in the same direction (ferromagnetic: left) or opposite (antiferromagnetic: right).

In order to figure out which situation was occurring, I turned to a new instrument in our department called a SQUID magnetometer (Figure 1.8). A magnetometer is a great instrument in that it allows the user to determine what the electrons in their compound are doing. It can also be used to

determine if the compound of study is behaving like a single molecule magnet. When I conducted SQUID measurements on my $MoNi(dpa)_4Cl_2$ chain, I determined the electrons are coupled in the same direction, meaning they are coupled ferromagnetically. This was a surprising result as all the other chains prior to this one have electrons that couple in the opposite direction; meaning they couple antiferromagnetically.[18-22] Using other methods, including computations, I was able to learn why this occurred and make a generalized statement for future work. As I leave this project to our younger students, they can apply the same methods to our other chains as I did to my $Mo_2Ni(dpa)_4Cl_2$ HEMAC. We would like to see one of the HEMACs behave like a small magnet, called a single molecule magnet. These are especially valuable in computers and other electronics, which continue to be made smaller and smaller (meaning they need smaller and smaller parts).

Figure 1.8 The SQUID magnetometer at UW–Madison.[23]

Most of our chains are made with chlorine (Cl) capping ligands bound to the terminal ends. However, one of the long-term goals of this project is to bind our chains to gold surfaces and determine if our HEMACs can act like tiny wires. Past work from other labs have determined that homometallic extended metal atoms can act like small wires.[24] Computational chemists have suggested that HEMACs would do the same.[25-26] This testing occurs by using an instrument called a scanning tunneling microscope (STM) to measure the current response across one molecule (Figure 1.9).[27] The molecules of interest are bound to a gold surface and separated by other molecules that do not have a response. This is where the

challenge lies for HEMACs. All of the HEMACs up until 2018 were made using chlorine capping ligands and chlorine does not bind to gold. The ligand of choice for chain compounds is the thiocyanate ligand. This ligand is made of a nitrogen (N), a carbon (C), and a sulfur (S) atom all in a line; N–C–S. The important part of this ligand is a sulfur atom, which can bind very strongly to gold, although there are other options.

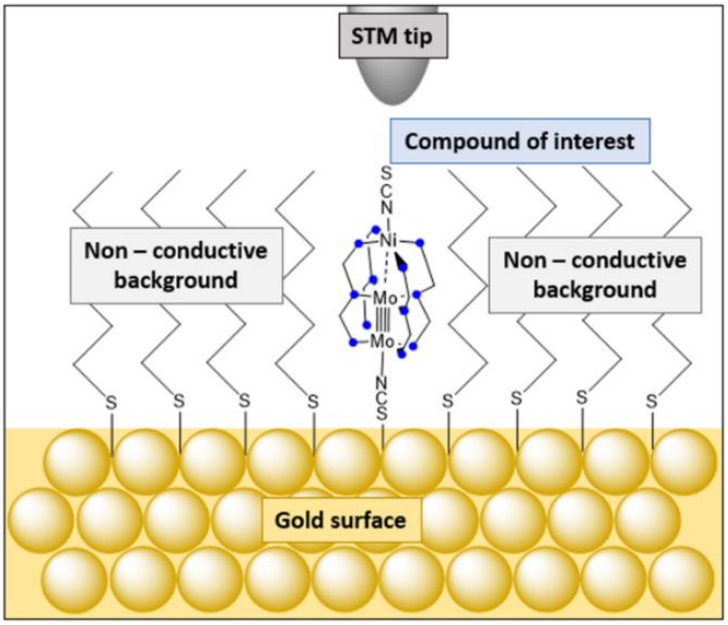

Figure 1.9 An STM is used to measure the current properties of HEMACs. HEMACs are bound to a gold surface and may be isolated from one another by other species that do not have a current response.

Our group has tried in the past to switch the chlorine out for one of these ligands, but it has been quite challenging..[28-29] My second major project made this transformation simpler. I've developed a way to swap the capping ligands on the ends of the HEMACs out for whatever capping ligand we would like.[30] I've made a small library of HEMACs based on the same Mo_2Ni chain in my first project with different capping ligands, some of which contain sulfur. They are currently being tested as wires by another research group. These different capping ligands will likely affect how well each HEMAC behaves as a wire. We're especially excited about this work because we're using two different metals instead of one. This means we might have current flow in one direction over another. This is called a diode. Just as with a single molecule magnet, these potential single molecule wires or diodes would be valuable in electronic devices as we continue to make smaller and smaller electronics!

These two pieces of my research don't cover all of the work that I've done over the past five years. Instead, they're the two pieces that are closest to molecular wires *and* have solidified my understanding of

inorganic chemistry the most. Further, even though my work represents only a small section of the field, I hope that you, the reader have a better understanding of the field of inorganic chemistry as a whole and if someone asks you what inorganic chemistry is you don't need to say "that small stubby rectangle" or "*not* organic."

Thank you for reading. I hope you enjoy the rest of this dissertation.

References

1. Periodic table was taken from http://www.p12.nysed.gov/assessment/reftable/

2. https://www.acs.org/content/acs/en/careers/college-to-career/areas-of-chemistry/inorganic-chemistry.html

3. https://www.fourmine.com/education/gemstone-education/ruby/formation

4. Corrdunum image taken from https://uwaterloo.ca/earth-sciences-museum/resources/detailed-rocks-and-minerals-articles/corundum. Rough ruby image taken from http://www.geologyin.com/2017/01/the-largest-rough-ruby-crystal-in-world.html. Cut ruby taken from https://www.africagems.com/ruby-pear-0-92-2018473.html

5. Mense, S. M.; Zhang, L., Heme: a versatile signaling molecule controlling the activities of diverse regulators ranging from transcription factors to MAP kinases. *Cell Research* **2006,** *16*, 681 - 692.

6. Platinum Anticancer Drugs. In *Metals in Medicine*.

7. Bardi, U.; Caporali, S., Precious Metals in Automotive Technology: An Unsolvable Depletion Problem? *Minerals* **2014,** *4*, 388 - 398.

8. Steinbach, V.; Wellmer, F.W., Consumption and Use of Non-Renewable Mineral and Energy Raw Materials from an Economic Geology Point of View. *Sustainability* **2010**, 2, 1408 - 1430.

9. Red blood cell image taken fromhttps://www.verywellhealth.com/erythrocytosis-401324. Hemoglobin image taken from http://www.chemistry.wustl.edu/~edudev/LabTutorials/CourseTutorials/Tutorials/Hemoglobin/Hemoglobin.htm. Cisplatin vial image taken from https://www.webmd.com/drugs/2/drug-8756/cisplatin-intravenous/details

10. Nippe, M.; Berry, J. F., Introducing a Metal–Metal Multiply Bonded Group as an "Axial Ligand" to Iron: Synthetic Design of a Linear Cr–Cr···Fe Framework. *J. Am. Chem. Soc.* **2007,** *129*, 12684-12685.

11. Nippe, M.; Victor, E.; Berry, J. F., Do Metal–Metal Multiply-Bonded "Ligands" Have a trans Influence? Structural and Magnetic Comparisons of Heterometallic Cr≣Cr···Co and Mo≣Mo···Co Interactions. *Eur. J. Inorg. Chem.* **2008**, 5569-5572.

12. Nippe, M.; Wang, J.; Bill, E.; Hope, H.; Dalal, N. S.; Berry, J. F., Crystals in Which Some Metal Atoms are More Equal Than Others: Inequalities From Crystal Packing and Their Spectroscopic/Magnetic Consequences. *J. Am. Chem. Soc.* **2010,** *132*, 14261-14272.

13. Nippe, M.; Bill, E.; Berry, J. F., Group 6 Complexes with Iron and Zinc Heterometals: Understanding the Structural, Spectroscopic, and Electrochemical Properties of a Complete Series of MM···M′ Compounds. *Inorg. Chem.* **2011,** *50*, 7650-7661.

14. Brogden, D. W.; Berry, J. F., Heterometallic Multiple Bonding: Delocalized Three-Center σ and π Bonding in Chains of 4d and 5d Transition Metals. *Inorg. Chem* **2014,** *53*, 11354-11356.

15. Brogden, D. W.; Berry, J. F., Heterometallic Second-Row Transition Metal Chain Compounds in Two Charge States: Syntheses, Properties, and Electronic Structures of $[Mo–Mo–Ru]^{6+/7+}$ Chains. *Inorg. Chem.* **2015,** *54*, 7660-7665.

16. Brogden, D. W.; Christian, J. H.; Dalal, N. S.; Berry, J. F., Completing the series of Group VI heterotrimetallic $M_2Cr(dpa)_4Cl_2$ (M_2 = Cr_2, Mo_2, MoW and W_2) compounds and investigating their metal–metal interactions using density functional theory. *Inorg. Chim. Acta* **2015,** *424*, 241-247.

17. Chipman, J. A.; Berry, J. F., Extraordinarily Large Ferromagnetic Coupling ($J \geq 150$ cm^{-1}) by Electron Delocalization in a Heterometallic Mo≡Mo–Ni Chain Complex. *Chem. Eur. J* **2018,** *24*, 1494-1499.

18. Liu, I. P.C.; Lee, G.H.; Peng, S.M.; Bénard, M.; Rohmer, M.M., Cu–Pd–Cu and Cu–Pt–Cu Linear Frameworks: Synthesis, Magnetic Properties, and Theoretical Analysis of Two Mixed-Metal Complexes of Dipyridylamide (dpa), Isostructural, and Isoelectronic with $[Cu_3(dpa)_4Cl_2]^+$. *Inorg. Chem.* **2007,** *46*, 9602-9608.

19. Rohmer, M.M.; Liu, I. P.C.; Lin, J.C.; Chiu, M.J.; Lee, C.H.; Lee, G.H.; Bénard, M.; López, X.; Peng, S.-M., Structural, Magnetic, and Theoretical Characterization of a Heterometallic Polypyridylamide Complex. *Angew. Chem. Int. Ed.* **2007,** *46*, 3533-3536.

20. Huang, G.C.; Bénard, M.; Rohmer, M.-M.; Li, L.A.; Chiu, M.J.; Yeh, C.Y.; Lee, G.H.; Peng, S.M., $Ru_2M(dpa)_4Cl_2$ (M = Cu, Ni): Synthesis, Characterization, and Theoretical Analysis of Asymmetric Heterometal String Complexes of the Dipyridylamide Family. *Eur. J. Inorg. Chem.* **2008**, 1767-1777.

21. Yu, L. C.; Lee, G. H.; Sigrist, M.; Lin, T. S.; Peng, S. M., Structure and Antiferromagnetism of Trinuclear Heterometallic Strings Containing $Mn^{II}M^{II}Mn^{II}$ Frameworks (M = Ni, Pd, Pt. *Eur. J. Inorg. Chem.* **2016**, 4250-4256.

22. Liu, Y.C.; Hua, S.A.; Cheng, M.C.; Yu, L.C.; Demeshko, S.; Dechert, S.; Meyer, F.; Lee, G.H.; Chiang, M.H.; Peng, S.M., Electron Delocalization of Mixed-Valence Diiron Sites Mediated by Group 10 Metal Ions in Heterotrimetallic Fe-M-Fe (M=Ni, Pd, and Pt) Chain Complexes. *Chem. Eur. J.* **2018,** *24* , 11649-11666.

23. SQUID magnetometer image taken from https://squid.chem.wisc.edu/

24. Tsai, T.W.; Huang, Q.R.; Peng, S.M.; Jin, B.Y., Smallest Electrical Wire Based on Extended Metal-Atom Chains. *J. Phys. Chem. C.* **2010,** *114*, 3641-3644.

25. DeBrincat, D.; Keers, O.; McGrady, J. E., Can heterometallic 1-dimensional chains support current rectification? *Chem. Commun.* **2013,** *49*, 9116-9118.

26. Weng, T.; DeBrincat, D.; Arcisauskaite, V.; McGrady, J. E., In search of structure-function relationships in transition-metal based rectifiers. *Inorg. Chem. Front.* **2014,** *1*, 468-477.

27. Berry, J. F., Metal–Metal Bonds in Chains of Three or More Metal Atoms: From Homometallic to Heterometallic Chains. In *Metal-Metal Bonding*, Parkin, G., Ed. Springer Berlin Heidelberg: Berlin, Heidelberg, 2010; pp 1-28.

28. Nippe, M.; Turov, Y.; Berry, J. F., Remote Effects of Axial Ligand Substitution in Heterometallic Cr≡Cr···M Chains. *Inorg. Chem.* **2011,** *50*, 10592-10599.

29. Turov, Y.; Berry, J. F., Synthesis, characterization and thermal properties of trimetallic N_3-Cr≣Cr··· M-N_3 azide complexes with M = Cr, Mn, Fe, and Co. *Dalton Trans.* **2012,** *41*, 8153-8161.

30. Chipman, J. A.; Berry, J. F., Facile Axial Ligand Substitution in Linear Mo≣Mo–Ni Complexes. *Inorg. Chem.* **2018,** *57*, 9354-9363.

Chapter 2

Paramagnetic Metal–Metal Bonded Heterometallic Complexes

Jill A. Chipman and John F. Berry

This chapter is in preparation for submission to Chemical Reviews

Contents

1. Introduction and Overview

Metal-metal bonded coordination compounds represent and important extension of the classical chemistry exemplified by Werner's coordination theory.[1-3] The first molecular compound containing a metallic metal-metal bond was reported by Wilkinson and coworkers in 1960.[4] The complex was an otherwise symmetric dimer, $CpMo(CO)_3–CpW(CO)_3$, that is diamagnetic.[4] Guidelines for the preparation of such closed shell heterometallic metal-metal bonded compounds were put forth by Coffey, Lewis, and Nyholm[5] and are still generally applicable today.

It was not until 1969-1970 that it was recognized that metal-metal bonded complexes could also be paramagnetic.[6-7] The early examples made use of one-electron or three-electron bonds, which had been described earlier by Pauling.[8] More important in fields beyond chemistry is the "double exchange" mechanism of spin coupling that requires delocalization of one or more unpaired electrons. This mechanism is invoked to described ferromagnetic coupling in adjacent spin centers in magnetic solid materials,[9] in proteins containing Fe–S clusters,[10] and in small coordination compounds.[11] The electron delocalization in these systems often is best described by metal-metal bonding.

There were relatively few paramagnetic complexes with heterometallic metal-metal bonds reported before 2007 – we note in particular some example of earlier compounds below. In 2007, a concerted effort began to prepare new examples of paramagnetic heterometallic metal-metal bonded complexes, and the results of these studies will be the major topic of this review. In this section, we describe some cross-cutting concepts and themes before describing in detail heterobimetallic compounds, heterotrimetallic compounds, and compounds of higher nuclearity.

2.1.1 Development of Metal-Metal Bonding: From Homometallic to Heterometallic

A question of fundamental significance is how a heterometallic metal-metal bond differs from a homometallic one. To explore this question, we start with the first metal-metal multiple bond to be

described; the Re≣Re quadruple bond in the $[Re_2Cl_8]^{2-}$ ion, shown in Figure 2.1A.[12] Ligand field analysis indicates the availability of d_{z^2}, d_{xy}, d_{xz}, and d_{yz} Re valence orbitals to engage in metal-metal bonds of σ, 2 x π, and δ symmetry, respectively. In the D_{4h} symmetry of the $[Re_2Cl_8]^{2-}$ ion, the two Re d_{z^2} orbitals overlap strongly to yield σ type bonding (a_{1g}) and antibonding (a_{2u}^*) combinations. The overlap of π-symmetry orbitals in less, and δ bonds are weaker still. Nevertheless, the $\sigma^2 \pi^4 \delta^2$ quadruple bond is the most useful and accurate description of the ground state of the $[Re_2Cl_8]^{2-}$ ion. [13-14]

Next, let's consider a hypothetical heterometallic complex that is isoelectronic to the $[Re_2Cl_8]^{2-}$ ion: $[WOsCl_8]^{2-}$. The polar heterometallic bond lowers the molecular symmetry to C_{4v}. The same four valence orbitals that were available in the Re_2 system are still available for the WOs compound: d_{z^2}, d_{xz}, d_{xz}, d_{yz}. However, as emphasized in the Figure 2.1B, the difference in effective nuclear charge between W and Os will result in the W 5d orbitals lying uniformly higher in energy than the Os 5*d* orbitals. Overlap of the W and Os d_{z^2} orbitals will result in a σ bonding (a_1) and antibonding (a_1^*) combination, but the interaction is not as covalent as in the Re_2 case. The a_1 orbital will by polarized toward Os with a_1^* polarized toward W. Similar effects, with even stronger polarization, will happen in the π an δ symmetry orbitals such that the b_2^* orbitals may have close to 100% W character and be considered non–bonding. While the polarization of these bonds is still a consequence of their heterometallic nature, it should be emphasized that these effects can be further exacerbated (or even mitigated) by an appropriate choice of W or Os supporting ligands.

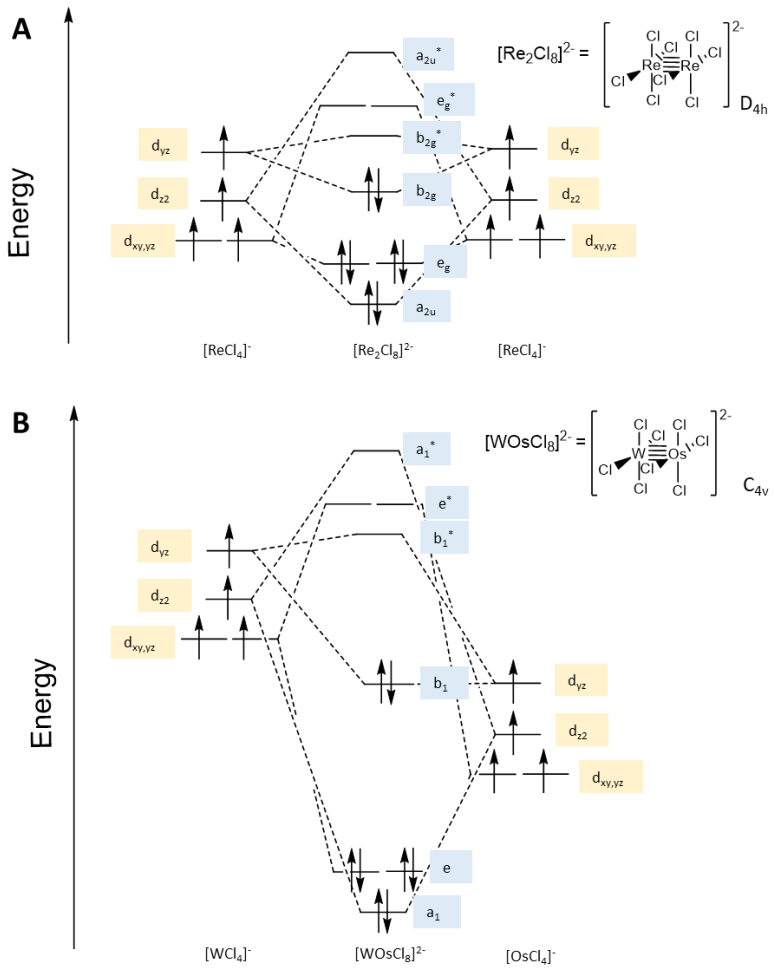

Figure 2.1 Qualitative molecular orbital (MO) diagram for (A) $[Re_2Cl_8]^{2-}$ and (B) $[WOsCl_8]^{2-}$

Another issue highlighted in Figure 2.1 deals with the bookkeeping of electrons. For the $[Re_2Cl_8]^{2-}$ ion, most chemists (although not all) are comfortable assigning an Re^{3+} oxidation state to the two Re ions. This is emphasized in Figure 2.1A where we have split the $[Re_2Cl_8]^{2-}$ ion into hypothetical $[ReCl_4]^-$ fragments each with a d^4 valence electron configuration. A similar deconstruction of the $[WOsCl_8]^{2-}$ ion yields d^3 $[WCl_4]^-$ and d^5 $[OsCl_4]^-$ fragments. Does the uneven electron distribution make sense? Should we consider d^4 $[WCl_4]^{2-}$ and d^4 $OsCl_4$ fragments with an uneven distribution of charge? Moreover, the fact that all of the valence electrons in the $[WOsCl_8]^{2-}$ ion occupy bonding orbitals that are (perhaps heavily) polarized towards Os suggest significant electron transfer from W to Os towards a limit of W^{6+}/Os^0 (i.e., d^0/d^8). Attempts to assign specific oxidation states to the metal atoms in these compounds are fraught with difficulty and only sow discord and confusion. Thomas and coworkers have promoted a useful shorthand, inspired by Enemark-Feltham notation for metal nitrosyls, that obviates these bookkeeping difficulties.[15] Here, the

$[WOsCl_8]^{2-}$ compound is described as having a $\{WOs\}^8$ configuration: eight electrons occupy the valence orbitals, and W–Os bond covalency prevents us from making any more specific an assignment.

While the examples given in Figure 2.1 are diamagnetic compounds, this review focuses on compounds that are paramagnetic, which raises an important point about metal-metal bond polarization. We have a very specific and useful reason for this. Consider the hypothetical open-shell $[WOsCl_8]^-$ ion, formally having one electron removed from the $[WOsCl_8]^{2-}$ ion. Based on Figure 2.1B, we may suggest a $\sigma^2 \pi^4 \delta^1$ electron configuration for this species. The δ-symmetry unpaired electron provides the opportunity to probe the composition of the b_2 orbital. Since both W and Os have naturally occurring isotopes with nuclear spins, the W and Os hyperfine interactions with the unpaired electron, easily measured by EPR spectroscopy, allow the polarization of the valence orbital to be measured directly. We include these data in this review where they are available.

We also include a significant amount of crystallographic data, including metal-metal bond distances. These distances must be considered carefully. For example, the Re-Re distance in the $[Re_2Cl_8]^{2-}$ ion may not be directly comparable to the W–Os distance in $[WOsCl_8]^{2-}$ because the atoms involved are all different sizes. The situation is worse if we are comparing first–row transition metals to those in the second or third row. In order to deal with this issue, where possible, we include a normalization of the metal-metal distances using Cotton's formal shortness ratio (FSR), defined as FSR = $\frac{d}{R_{1,A} + R_{1,B}}$.[1] Here, d is the observed metal-metal distance, and the R_1 values are metallic radii given by Pauling.[16] In essence, the FSR described how much shorter (or longer) a distance would be than that of a metallic sample of the element(s) involved. Also germane to this discussion are bond radii for the elements. Alvarez and coworkers have used crystallographic data to compile a list of covalent radii (R_c) for the elements.[17] Distances within the sum of covalent radii indicate that bonding between the two atoms may be considered (Note: an analysis of the electronic structure must support the claim of a bond, not just distances!) With regard to multiple bonding, we also point out the sets of single,[18] double,[19] and triple bond[20] covalent radii determined by analysis of experimental and theoretical data from Pyykkö and coworkers. These data are used in Table 2.1, to compare the $Re_2Cl_8^{2-}$ and $WOsCl_8^{2-}$ ions.

Table 2.1. Comparative bond length/radius data for $Re_2Cl_8^{2-}$ and $WOsCl_8^{2-}$. Values in parentheses are FSR values.

	Exp.	Sum of covalent radii	Sum of single bond radii	Sum of double bond radii	Sum of triple bond radii
$Re_2Cl_8^{2-}$	2.22 Å	3.02 Å	2.62 Å	2.38 Å	2.20 Å
	(0.87)	(1.18)	(1.02)	(0.93)	(0.86)
$WOsCl_8^{2-}$	N/A	3.06 Å	2.66 Å	2.36 Å	2.24 Å
		(1.19)	(1.04)	(0.92)	(0.87)

The Re–Re bond distances in the $Re_2Cl_8^{2-}$ ion is known from crystallographic data, 2.22Å.[21] This distance is clearly shorter than the sum of the covalent, single, or double-bond radii for Re. Its agreement with the sum of the Re–Re triple bond radii provides strong support for a Re–Re bond with a bond order of at least three. Though experimental data for the $WOsCl_8^{2-}$ ion are lacking, we can see good agreement between the sums of radii comparing to the Re_2 case, and in the case that the $\{WOs\}^8$ unit possesses a full $\sigma^2\pi^4\delta^2$ quadruple bond like the $Re_2Cl_8^{2-}$ ion, we may anticipate a similar metal-metal distance.

FSR data are also given in Table 2.1 and allow us to make more specific recommendations about how FSR data may be interpreted generally. For any given metal, we may calculate the expected FSR value at the covalent limit as R_c/R_1 with R_c = the Alvarez covalent radius, and R_1 the Pauling metallic radius. FSR values expected for single, double, or triple bonds may likewise be calculated from the Pyykkö datasets. Averaging over all transition metals gives the results shown in Table 2.2 and summarized in Figure 2.2. We thus see that covalent metal-metal bonding may be considered for compounds ≤ 1.22, with single bonds having FSR ~ 1.01, double bonds ~ 0.92, and higher bond orders having FSR ≤ 0.92. We note that these rough guidelines should not be used prescriptively, but instead should be used to support other experimental or theoretical evidence for metal-metal bonding.

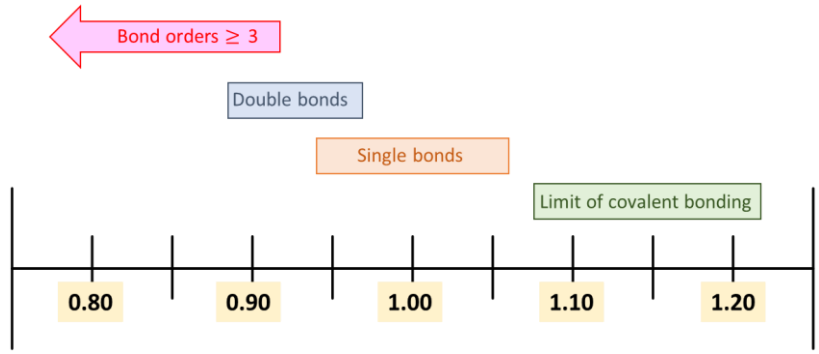

Figure 2.2. FSR ranges for multiple bonds, single bonds, and the covalent bonding limit for transition metal-metal bonding. Error bars are drawn to one standard deviation.

Table 2.2. FSR values expected for covalent, single, double, or triple bonds.

	Covalent FSR	Single–Bond	Double–Bond	Triple–Bond
Dataset 1[a]				
Average	1.15	1.01	0.92	0.89
Standard Deviation	0.07	0.05	0.04	0.05
Dataset 2[b]				
Average	1.17	1.02	0.88	0.86
Standard Deviation	0.06	0.05	0.06	0.06

[a] Dataset 1 contains the elements from Group 4 to Group 9
[b] Dataset 2 contains the elements from Group 3 to Group 9, including the lanthanides

1.2 Guiding Principles in Controlling Spin States

1.2.1 Localized vs. Delocalized Unpaired Electrons

One of the greatest challenges and goals in molecular magnetism is the ability to control spins at the single electron level.[22-25] This can be accomplished in heterometallic compounds largely by tuning the nature of localized delocalized orbitals that house unpaired electrons. Localized orbitals tend to be of either π or δ symmetry with respect to the metal-metal bond whereas delocalized orbitals tend to be of σ symmetry. The double exchange mechanism (described in Section 1.2.3) best illustrates the significance of delocalization in molecular magnetism. Electrons present in mixed-valent systems will couple with one another via the double exchange mechanism to give rise to an overall high-spin system.[26-28] Additionally, electrons that are present in overlapping orbitals will couple antiferromagnetically via the superexchange mechanism (described in Section 1.2.2), whereas they will couple ferromagnetically if the orbitals are orthogonal.[29] In examining the magnetic properties and electron transport abilities of the heterometallic

compounds presented in this review, we note that the delocalized σ pathway is a guiding principle that supports the majority of these interactions.

2.1.2.2 Superexchange

The superexchange mechanism is used to understand the interaction of two paramagnetic ions via a bridging diamagnetic ion with guiding principles outlined in the Goodenough-Kanamori rules (Scheme 2.1).[26, 30-32] Here, we apply these rules to heterometallic metal-metal bonded compounds. The main idea behind superexchange is that unpaired electrons on two metal centers may interact with filled orbitals from a third central metal atom or from bridging ligands. As emphasized in Scheme 2.1A and 2.1B, these situations both tend to be antiferromagnetic interactions. Ferromagnetic interactions may result from the example situation in Scheme 2.1C in which the magnetic orbitals are rigorously orthogonal.

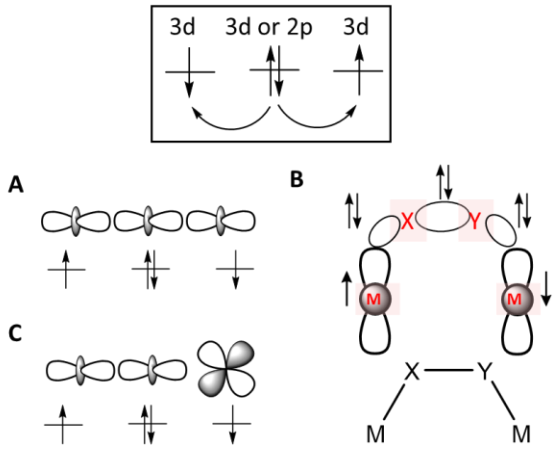

Scheme 2.1 General mechanism for superexchange (top). Orbital interactions that give rise to different magnetic coupling (bottom). Interactions **A** and **B** results in antiferromagnetic interactions while **C** results in a ferromagnetic coupling.

2.1.2.3 Double Exchange

The double exchange mechanism occurs most often in systems containing two magnetic centers that contain a different number of valence electrons from one another. The magnetic centers themselves may be different from one another. The key feature is the presence of one or more "extra" electrons that are delocalized across two metal atoms. If the other spins on the two magnetic centers all align in a parallel (i.e. ferromagnetic) arrangement, the "extra" electrons do not need to flip spins as it resonates between the two metal centers.

[33-36] An antiferromagnetic state requires the "extra" electron to undergo a spin flip to form a Pauli-allowed state, which is not favorable. This effect is exemplified in $[Fe_2(\mu\text{-}OH)_3\text{-}(tmtacn)_2]^{2+}$ (tmtacn = 1,4,7-trimethyl-1,4,7- triazacyclononane) where a mixed valent Fe(II/III) system presents an overall S = 9/2 ground state as a result of the double exchange mechanism (Scheme 2.2).[33]

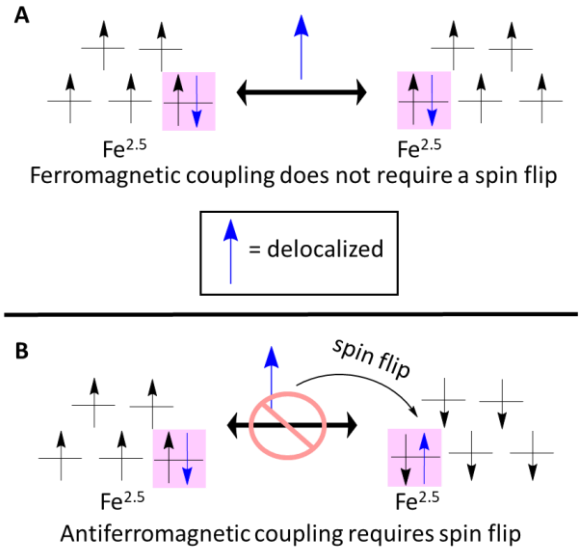

Scheme 2.2 Mechanism by which double exchange occurs using a bimetallic mixed valent $Fe^{II/III}$ species. Ferromagnetic alignment is energetically favorable.

The electron delocalization in $[Fe_2(\mu\text{-}OH)_3\text{-}(tmtacn)_2]^{2+}$ occurs via direct Fe–Fe bonding. As in the other edge sharing biooctahedral structures, the most important metal-metal interaction takes place via overlap of two d_{z^2} orbitals, which form a bonding and antibonding combination as shown in Figure 2.3. The "extra" itinerant electron described above is the spin-down electron occupying the σ bonding combination of d_{z^2} orbitals. Thus, the double-exchange coupling mechanism is intimately tied to metal-metal bonding.

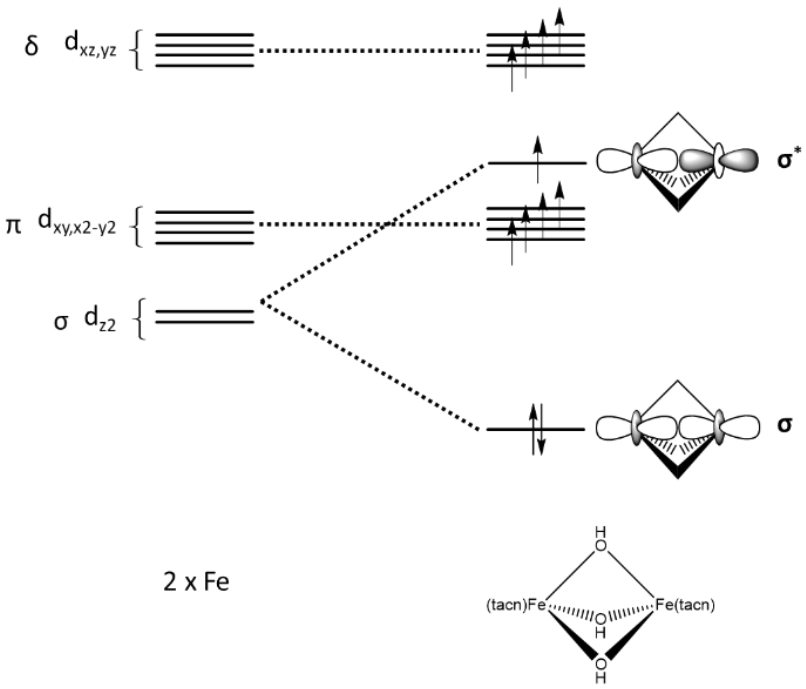

Figure 2.3 MO diagram for $[Fe_2(\mu\text{-}OH)_3\text{-}(tmtacn)_2]^{2+}$ emphasizing the σ bonding interaction via overlap of the Fe d_{z^2} orbitals. The $\sigma^2\sigma^{*1}$ electron configuration constitutes a 2-center, 3-electron bond, and the lone β spin electron represents the "extra" double–exchange mechanism.

Notably, in the $[Fe_2(\mu\text{-}OH)_3\text{-}(tmtacn)_2]^{2+}$ system, and other systems showing double exchange, the delocalized itinerant electron, is a β-spin, or minority spin electron. Recently, Berry and coworkers have described a heterometallic complex in which delocalized, itinerant electron is a majority spin electron. As outlined in Scheme 2.3, this delocalized electron may align ferromagnetically with electrons delocalized in orbitals that are orthogonal to the one carrying the delocalized electron. While clearly related to the concept of double exchange, this mechanism differs in that the "extra" electron belongs to the majority spin. This interaction has been dubbed "double orthogonality" by Berry.[37]

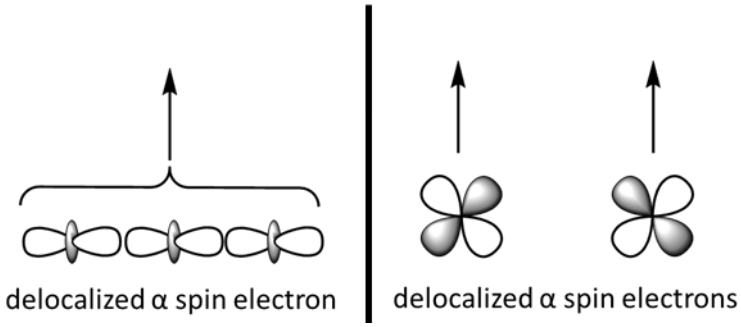

Scheme 2.3 Ferromagnetic spin coupling via double orthogonality: a delocalized α-spin electron is orthogonal to other, localized unpaired electrons. The orbital orthogonality leads to a ferromagnetic alignment of spins.

1.3 Early Examples of Paramagnetic Heterometallic Metal-Metal Bonded Compounds and Previous Reviews

Before 2007 few examples of paramagnetic heterometallic metal-metal bonded compounds were reported. Lippert and coworkers introduced paramagnetic heterometallic metal-metal bonded chains in 1981.[38] Their synthetic strategy was to use Pt^{II}–nucleobase complexes as metalloligands, producing a wide variety of Pt–M–Pt heterotrimetallic compounds having paramagnetic central M atoms.[39-45] For example, the methylthymine complex with a central Pd^{II} ion is shown in Figure 2.4. Analysis of the electronic transitions and EPR spectra of these compounds led to the conclusion that the filled Pt d_{z^2} orbitals act as ligands to the central metal atom.[46] This conclusion continues to support many of the higher nuclearity chains discussed in Section 4 of this review. Another related trimetallic species with a Cu_2Pt core was supported by the 1-methylcytosinate ligand. The diamagnetism of the compound stems from strong antiferromagnetic coupling between the two Cu^{II} mediated by the central Pt^{II} d_{z^2} orbital.[45]

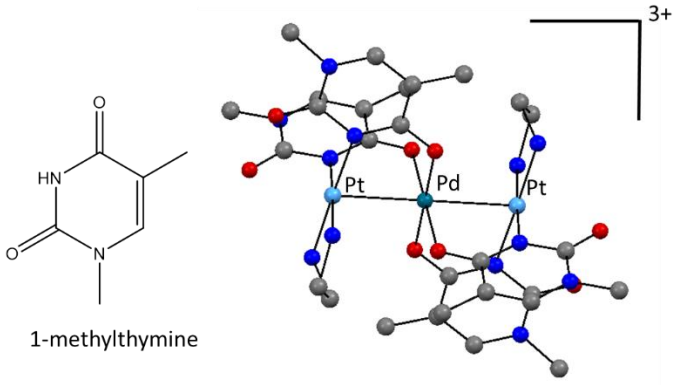

Figure 2.4 Heterotrimetallic PtPdPt complex synthesized in the Lippert lab.[41]

In 2005, Matsumoto and coworkers reported a quasi 1D system of paramagnetic Pt–Rh octomers bridged by Cl ions (Figure 2.5).[47] Each chain contains a [–Pt–Rh–Pt–Pt–Pt–Pt–Rh–Pt–Cl–] unit built of $[Pt_2]^{4+}$ and $[PtRh]^{5+}$ building blocks with one unpaired electron per octomer unit. In this case, the unpaired electron does not occupy the d_{z^2} orbitals of Pt; rather it occupies the d_{xy} orbital of Rh and "hops" from one Rh to another. This class of systems has been subsequently developed further by the Uemura and Ebihara groups and will be discussed in detail in Section 4.

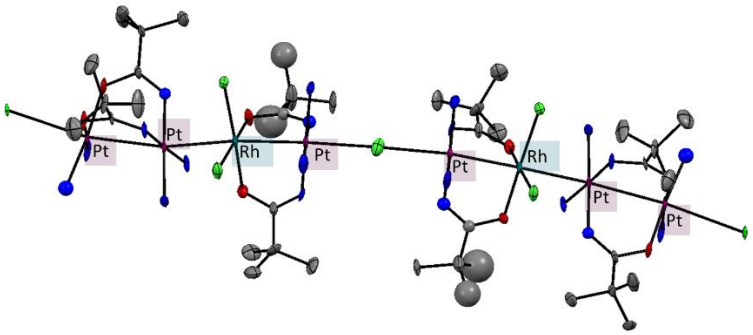

Figure 2.5 Quasi 1D chain complex containing Pt and Rh synthesized by Matsumoto and coworkers.[47]

Zhou and coworkers reported a pair of Pt–Cr heterobimetallics supported by either the ε-thiocaprolactam or 2-mercaptopyridine ligand to support their complexes (Figure 2.6).[48] These early structures were made using the metalloligand approach (discussed in Sections 2.1.2 and 3.1.1.3). Furthermore, the 2-mercaptopyridine is the same ligand used to support compound **B29**.

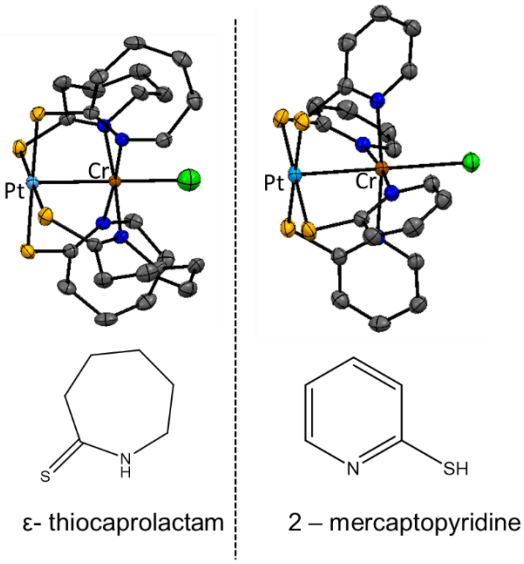

Figure 2.6 Pt–Cr heterobimetallics from H.C Zhou and coworkers.[48]

Several reviews and book chapters have been compiled that cover individual aspects of this review. The book chapter "Metal–Metal Bonds in Chains of Three or Metal Atoms: From Homometallic to Heterometallic Chains" in *Metal–Metal Bonding* provides a good introduction to trimetallic and polymetallic chains as well as their applications in molecular electronics.[49] Similarly, in 2015 Peng and coworkers published a mini review highlighting the advances of homometallic and heterometallic chain compounds in molecular electronics.[50] The groups of Thomas and Lu have compiled several reviews and book chapters that highlight the work done on C_3 symmetric bimetallic compounds including both structure and bonding as well as their reactivity.[51-52] The book *Molecular Metal–Metal Bonds: Compounds, Synthesis, Properties* contains examples of paramagnetic heterometallic metal-metal bonded compounds although it does not contain a specific chapter covering heterometallic compounds. [2] Our goal in this review is to provide a holistic and comprehensive view of the field of metal bonded compounds from bimetallic species to infinite chains.

2.1.4 Organization of this Review

We categorize paramagnetic heterometallic metal–metal bonded compounds into three classes based on the number of metal atoms present; heterobimetallic, heterotrimetallic, and heteropolymetallic. Each section further describes synthesis, magnetic properties and electronic structure of all of the

compounds. Since there are limited examples of heterometallic metal-metal bonded species before 2007, this review will primarily cover material from 2007 onward. We have chosen to focus this review on transition metal heterometallics only, excluding lanthanides, actinides, and main group metals. Additionally, we focus on coordination compounds: low-spin organometallic species and low spin cluster compounds will not be included.

2.2. Paramagnetic Heterobimetallic Complexes

Heterobimetallics represent the simplest way to observe the impact of two different metals on one another. To this extent the groups of Lu and Thomas have utilized three-fold symmetric ligand scaffolds to support a variety of unique heterobimetallic species.[53-84] Some of these species have found success in catalytic transformations and small molecule activation,[51, 57, 64-65, 85-86] cross-coupling reactions,[51, 69, 87-88] and C–H activation.[64, 89] Detailed reviews of their reactivity is described elsewhere.[51, 85, 90] In addition to these three-fold symmetric species, the groups of Doerrer, Zamora, and Berry have synthesized heterobimetallic compounds supported by four ligands in a paddlewheel arrangement, affording structures with C_4 symmetry.[91-99] Remarkably, the compounds comprising this section display a wide range of magnetic behavior, which is sometimes counterintuitive and surprising.

In 2009, the Thomas group reported a trio of paramagnetic heterobimetallic Zr–Co complexes each supported by a different ligand and yielding a final compound with C_3 symmetric structure.[63] Since 2009, her group has studied many early-late heterobimetallic complexes in the context of reactivity[64-65, 67-70, 80, 82-83, 87-88, 90, 100-102]. These compounds have also been explored magnetically. Thomas and coworkers have also studied other transition metal pairings outside of early-late heterobimetallics in order to explore their bonding and magnetic properties.[71-72, 75, 78-79, 81]. In addition to these C_3 symmetric complexes, the group of Connie Lu reported a heterobimetallic Cr–Fe species in 2013.[53] Since this time, her group has explored heterobimetallic complexes spanning a wide range of bond orders and spin states enabling her group to make predictions regarding magnetism and electronic structure. [53-62, 103] Turning to C_4 symmetric species, the group of Linda Doerrer reported a trio of Pt–M (M = Fe, Co, Ni) supported by thiocarboxylate ligands in 2012.[95] The Co and Ni heterobimetallic proved interesting in that their magnetic behavior in the solid state and solution is quite different. Since 2012, her group has continued to explore the effect of different

thiocarboxylates as well as axial ligands on the magnetic properties of numerous heterobimetallic species.[95-99, 104]

The heterobimetallic compounds discussed in this section all contain a M-M bond and either three or four bridging ligands that buttress the M-M bonded unit. The exception to this are the compounds made by the Lu group. These compounds are supported by tripodal chelating ligands that contain an apical N atom, which constrains substrate binding to the remaining open site metal site only; these ligands (L_1-L_3) are shown in Figure 2.7. The Thomas group has used phosphinoamide based ligands that were first explored in the context of early-late heterobimetallic catalyzed reactions by Nagashima and coworkers.[105-107] The phosphinoamide ligands with altered substituents on the N or P atoms (Ligands T_1-T_3 in Figure 2.7). Both Doerrer and Berry labs have taken advantage of hard-soft acid base theory to form C_4 symmetric compounds using the ligands shown in Figure 2.8. The Doerrer and Zamora groups have utilized a thiocarboxylate backbone while the Berry group has used a thiopyridone.[95-96, 98-99, 104, 108-109]

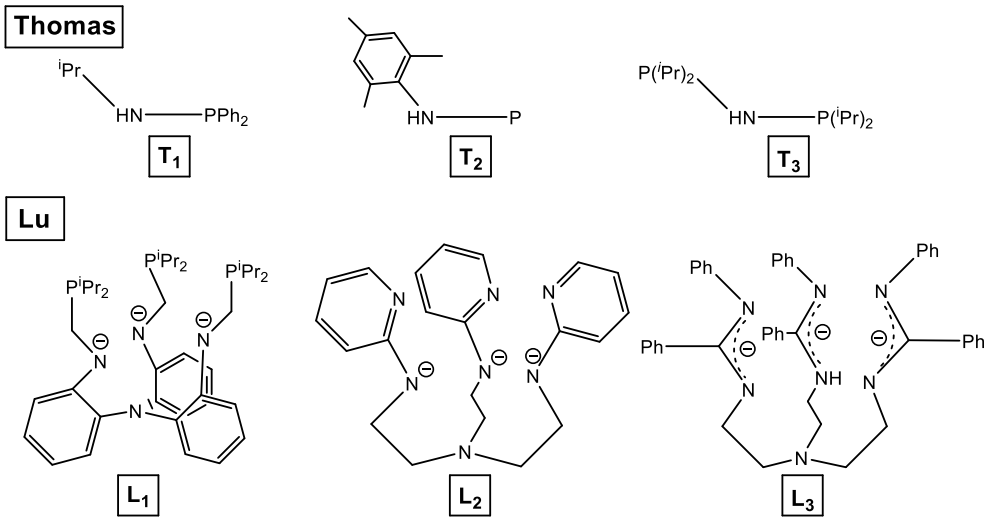

Figure 2.7 Ligands used to support C_3 symmetric bimetallic complexes synthesized by the Thomas and Lu groups.[58,63]

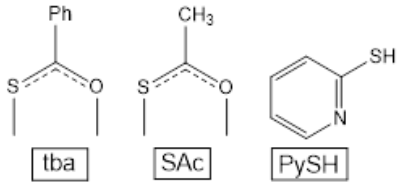

Figure 2.8 Ligands used to support C_4 symmetric bimetallic complexes by Doerrer, Zamora, and Berry. [97, 108]

2.2.1 Synthetic Methods Used to Form Heterobimetallic Compounds

2.2.1.1 Self-Assembly

Simple addition of K_2PtCl_4, $MCl_2 \cdot xH_2O$, and the sodium salts of tba or Sac in aqueous solution affords selectively the Pt-M heterobimetallic compounds **B1-B5** (see Tables 2.3-2.6 for compound labels). For example, the preparation of **B15** from the aquo **B3** is shown in Scheme 2.4. The selectively of thee reactions stems from the concept of hard/soft acid/base theory (HSAB), where the soft Lewis acid Pt^{II} preferentially binds to the softer S-donor atom of the ligand.

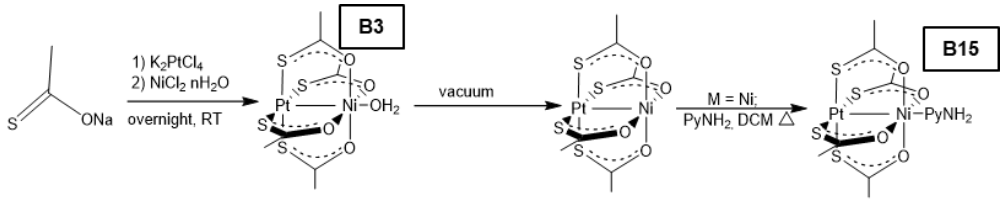

Scheme 2.4 Self–Assembly method used to form thiocarboxylate heterobimetallics.[95-96]

2.2.1.2 Metalloligand Approach

The metalloligand approach is another successful synthetic strategy in forming heterobimetallics. In the metalloligand approach, a monometallic precursor is made first. This species is then added as a "ligand" to the second metal. In some cases, an external reductant such as Zn, or KC_8 is used to reduce the bimetallic species and form a metal-metal multiple bond. Several examples are shown in Scheme 2.5.

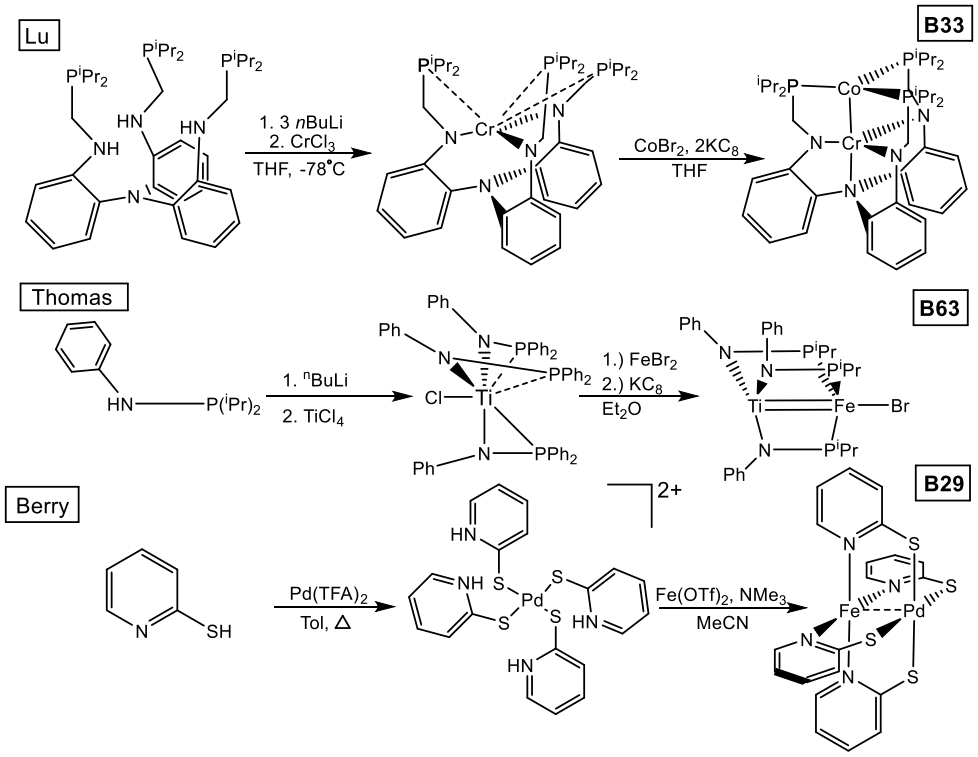

Scheme 2.5 Metalloligand approach used in the synthesis of heterobimetallic compounds.[78, 103, 108]

2.2 Structural Information

2.1.1 Bond Distances and Formal Shortness Ratios for M-M distances

The most valuable metric for structural comparison for any bimetallic species is the metal-metal distance. To make reasonable comparisons among 26 unique metal pairings, we use the FSR with bond cutoffs described in Section 1.1. We note that in compounds where the author does not consider a bond to be present, we do not include here. The FSR values for the compounds synthesized by the Thomas and Lu groups range from dative interactions to triple bonds (0.79 to 1.09).

When considering four-fold symmetric compounds, an additional parameter arises that will in turn influence the magnetic behavior of the compound. In the crystallization process, many of the compounds for the Doerrer lab crystallize as dimers of two bimetallic units. Over the course of developing their library, Doerrer and coworkers noticed that their compounds crystallized into one of four general classes. The four categories are known as staggered, eclipsed, partially eclipsed, and square geometries as shown in Figure 2.9. Note, only the two M ions are paramagnetic however, the Pt–Pt interaction provides the intramolecular

pathway for spin coupling. The FSR values for these species (FSR = 1.02 to 1.11) suggest a weak single bonding or covalent interaction between the Pt and 3d metal.

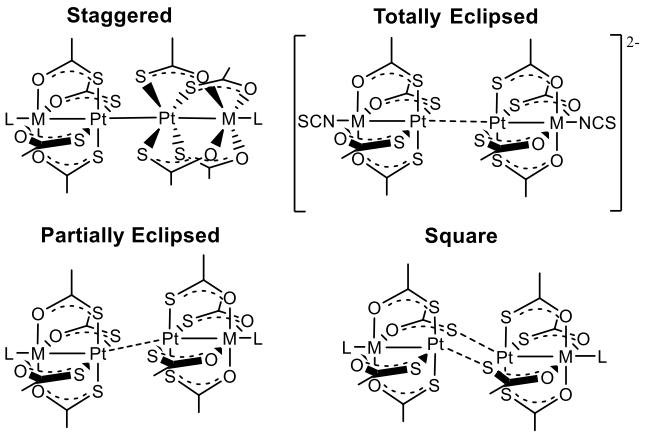

Figure 2.9 The four crystallization geometries observed in C_4 symmetric structures.[97]

2.2.2 Correlation of Metal-Metal Distance with Valence Electron Count

Valence electron counts, *n* in $\{MM'\}^n$ are also given in Tables 2.3-2.6. In investigating the valence electron counts of each heterobimetallic along with its corresponding FSR value, we sought to understand the relationship between these two parameters. To investigate these two properties, scatterplots correlating *d*-electron count against FSR for C_3 symmetric compounds was generated (Figure 2.10). There is a clear decrease in the FSR lower bound as the number of *d* electrons increases, to a point. At 10 *d*-electrons, there exists only one C_3-symmetric compound: **B93** $(T_3)Zr(\mu^2\text{-}\eta^1\ \eta^3\text{-}^t BuN_3)(T_3)_2Co$. The general "10 electron vacancy" may be attributed to the tendency for C_3 symmetric compounds with 10 *d*-electrons to be diamagnetic with a quintuply bonded configuration. 10 *d*-electrons are capable of populating all of the bonding orbitals and thus, once the number of *d*-electrons exceeds 10, the antibonding orbitals can be populated. This effect can be seen by a general increase in FSR lower limits. Despite the clear trend in the FSR lower limits there is a distinct spread in FSR values at each valence electron count. This spread is strong structural evidence for a continuum of bonding, from strong multiple bonds to weak interactions, that can occur at any valence electron count due to mismatches in orbital overlap for two differing metal atoms. A comparison between **B35** and **B80** provides a good illustration of this effect. Both compounds have a $\{MM'\}^9$ configuration but the FSR for **B35** is 0.79 while that for **B80** is 1.05. Three main effects can help us to rationalize this disparity. First, is the effect of orbital mismatch described above. Compound **B35**

contains a $\{VFe\}^9$ core whereas **B8o** is $\{ZrCo\}^9$. The metal atoms are only four columns away from each other in the former complex to six in the latter. Thus, there will be a greater disparity of *d* orbital energies in **B8o** due to the large differences in effective nuclear charge. Compound **B8o** also contains two other features that serve to lengthen the metal-metal bond. The Zr atom has an increased coordination number with a bidentate ligand bound to the axial site. Furthermore, the Co atom has a strong π-acceptor ligand, N_2, trans to the metal-metal interaction. The Co–N_2 π backbonding will render the Co π-symmetry orbitals less available to interact with Zr.

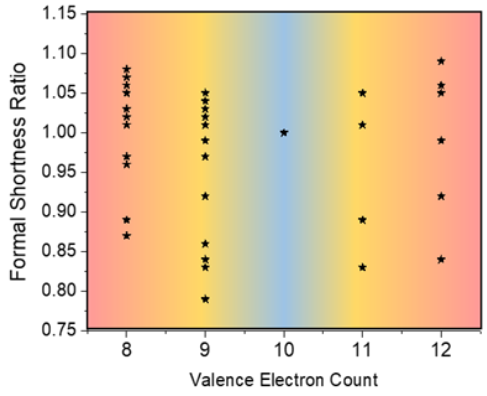

Figure 2.10 Scatterplot correlating valence electron count and FSR values for C_3 symmetric heterobimetallics.

Table 2.3 Magnetic data and bond metrics for compounds synthesized in the Doerrer lab. All bond distances are reported in Å. All magnetic data was obtained via SQUID magnetometry or via Evans method and is reported at room temperature in cm^3 K mol^{-1}.

	Code	Geometry	χT	$\{M_2\}^n$	Spin State	Pt–M	FSR	Pt–S	M–O	Pt–Ax	M–Ax	Ref
$PtFe(tba)_4OH_2$	B1	Square	3.24 (Evans) 3.24 (SQUID)	14	2	2.6320(6)	1.07	2.3289[9]	2.097[2]	N/A	2.025(2)	95
$PtCo(tba)_4OH_2$	B2	Staggered	3.15 (Evans) 2.85 (SQUID)	15	3/2	2.5674[6] 2.5521(6)	1.05 1.05	2.323[2] 2.339[4]	2.070[4] 2.077[3]	N/A N/A	2.052(3) 2.035(3)	95
$PtNi(tba)_4OH_2$	B3	Staggered	1.21 (Evans) 1.81 (SQUID)	16	1	2.570(1)	1.06	2.314[2]	2.025[8]	N/A	2.0454(4)	95
$PtCo(SAc)_4OH_2$	B4	Staggered	3.04 (Evans) 5.71 (SQUID)	15	3/2	2.6243(5) 2.6343(5)	1.08 1.08	2.3283[9] 2.3267[9]	2.065[2] 2.052[2]	N/A N/A	2.069(3) 2.082(3)	98
$PtNi(SAc)_4OH_2$	B5	Staggered	1.01 (Evans) 1.68 (SQUID)	16	1	2.585(2) 2.571(2)	1.06 1.06	2.319[4] 2.323[4]	2.01[1] 2.02[1]	N/A N/A	2.050(9) 2.07(1)	98
$PtCo(SAc)_4pyNO_2$	B6	Partially eclipsed	3.20 (Evans) 5.74 (SQUID)	15	3/2	2.6347(4)	1.08	2.321[1]	2.052[3]	N/A	2.114(3)	98
$PtNi(SAc)_4pyNO_2$	B7	Staggered	1.16 (Evans) 2.04 (SQUID)	16	1	2.5682(9) 2.5625(9)	1.06 1.06	2.329[1] 2.329[2]	2.035[5] 2.019[5]	N/A N/A	1.996(7) 2.065(7)	98
$PtCo(SAc)_4(py)_2$	B78	[a]	3.35 (Evans) 3.18 (SQUID)	15	3/2	2.5817(6)	1.06	2.3252[7]	2.098[2]	2.568(4)	2.105(4)	96
$PtNi(SAc)_4(py)_2$	B9	[a]	1.24 (Evans) 1.40 (SQUID)	16	1	2.5506(4)	1.05	2.3234[5]	2.062[1]	2.533(2)	2.067(2)	96
$PtCo(SAc)_4py$	B10	Square	2.66 (Evans) 3.09 (SQUID)	15	3/2	2.6298(5)	1.07	2.318[1]	2.081[3]	N/A	2.101(3)	96
$PtNi(SAc)_4py$	B11	Square	1.19 (Evans) 1.41 (SQUID)	16	1	2.5831(6)	1.06	2.3194[9]	2.051[2]	N/A	2.059(3)	96
$PtMn(SAc)_4pyNH_2$	B12	Square	4.4 (Evans)	13	5/2	2.7296(6)	1.11	2.316[1]	2.158[3]	N/A	2.164(4)	104
$PtFe(SAc)_4pyNH_2$	B13	Square	2.42 (Evans)	14	2	2.6785(5)	1.09	2.3263[7]	2.112[2]	N/A	2.106(2)	104
$PtCo(SAc)_4pyNH_2$	B14	Square	2.96 (Evans) 3.18 (SQUID)	15	3/2	2.6405(4)	1.08	2.3264[7]	2.080[2]	N/A	2.072(2)	96

$PtNi(SAc)_4pyNH_2$	B15	Square	1.10 (Evans)A1.19 (SQUID)	16	1	2.5952(3)	1.06	2.3239[7]	2.050[2]	N/A	2.043(2)	[96]
$PtMn(SAc)_4pySMe$	B16	Square	4.2 (Evans)	13	5/2	2.7064(4)	1.10	2.3273[7]	2.156[2]	N/A	2.185(2)	[104]
$PtFe(SAc)_4pySMe$	B17	Staggered	3.8 (Evans)	14	2	2.6728(6) 2.6759(6) 2.6851(6) 2.6629(6)	1.09 1.09 1.09 1.08	2.322[1] 2.329[1] 2.329[1] 2.324[1]	2.080[4] 2.094[3] 2.085[3] 2.100[4]	N/A N/A N/A N/A	2.127(4) 2.136(4) 2.131(4) 2.118(4)	[104]
$PtCo(SAc)_4pySMe$	B18	Staggered	3.4 (Evans)	15	3/2	2.648(1) 2.643(1) 2.657(1) 2.634(1)	1.08 1.08 1.08 1.08	2.327[3] 2.321[3] 2.328[4] 2.321[3]	2.070[7] 2.056[8] 2.054[8] 2.066[8]	N/A N/A N/A N/A	2..084(8) 2.089(8) 2.100(8) 2.089(8)	[104]
$PtNi(SAc)_4pySMe$	B19	Staggered	1.8 (Evans)	16	1	2.5918(4) 2.6047(4) 2.6166(4) 2.5945(4)	1.06 1.06 1.07 1.06	2.3225[9] 2.3288[9] 2.3266[9] 2.3245[9]	2.039[3] 2.035[3] 2.019[3] 2,034[3]	N/A N/A N/A N/A	2.040(3) 2.038(3) 2.049(3) 2.042(3)	[104]
$[PtCr(tba)_4(NCS)_2]_n$	B20	[a]	2.33		3/2	2.5252(9)	1.03	2.339[1]	1.972[3]	N/A	2.034(3)	[99]
$[ClPtNi(tba)_4]^-$	B21	Partially Eclipsed	1.00	16	1	2.5940(7)	1.07	2.323[2]	2.059[4]	N/A	2.325(2)	[109]
$[ClPtNi(tba)_4OH_2]^+$	B22	[a]	0.48	17	1/2	2.488(3)	1.02	2.359[6]	2.03[2]	2.430(5)	2.00(2)	[109]
$PtCo(SAc)_4(DMSO)$	B23	Square	3.14 (Evans) 3.35 (SQUID)	15	3/2	2.6223(9)	1.07	2.323[2]	2.081[5]	N/A	2.033(4)	[96]
$PtNi(SAc)_4(DMF)$	B24	Square	1.15 (Evans) 1.06 (SQUID)	16	1	2.5571(6)	1.05	2.323[1]	2.045[3]	N/A	2.032(3)	[96]
$[Na(12C4)_2][PtCo(SAc)_4(NCS)]$	B25	Totally Eclipsed	3.18 (Evans)	15	3/2	2.669(1) 2.669(1) 2.6691(9)	1.09 1.09 1.09	2.330[3] 2.328[2] 2.334[6]	2.078[6] 2.077[6] 2.076[7]	N/A N/A N/A	2.022(7) 2.035(7) 2.027(5)	[99]
$[Na(12C4)_2][PtNi(SAc)_4(NCS)]$	B26	Totally Eclipsed	1.30 (Evans)	16	1	2.616(4) 2.613(4) 2.606(5)	1.08 1.08 1.07	2.315[6] 2.345[8] 2.327[1]	2.03[2] 2.08[2] 2.06[2]	N/A N/A N/A	2.00(2) 2.00(2) 2.02(2)	[99]
$[Na(15C5)_2][PtCo(SAc)_4(NCS)]$	B27	Partially Eclipsed	3.13 (Evans)	15	3/2	2.6550(6) 2.6638(6)	1.09 1.09	2.3258[9] 2.3266[9]	2.085[2] 2.080[2]	N/A N/A	2.043(3) 2.047(3)	[99]
$[Na(15C5)_2][PtNi(SAc)_4(NCS)]$	B28	Partially Eclipsed	1.16 (Evans)	16	1	2.6015(6)	1.07	2.326[1]	2.050[3]	N/A	2.012(4)	[99]

$PtFe(PyS)_4(MeCN)$	B29	N/A	4.50	14	2	2.5954(9)	1.06	2.3224[9]	2.1943[2]	N/A	2.180(2)	[108]

[a] *by nature of having ligands on both sides of the paddlewheel or by being infinite chains* ***B8***, ***B9***, ***B20***, ***B22*** *cannot adopt a dimer crystallization motif.*

Table 2.4. Magnetic data and bond metrics for compounds synthesized in the Lu lab. The metal listed first is the metal at the bottom of the ligand scaffold (M_B), bound to both three equatorial nitrogen atoms (N_E) and one apical nitrogen atom (N_A). All bond distances are reported in Å. All magnetic data was obtained via SQUID magnetometry or via the Evans method at 300K unless otherwise noted and are reported in $cm^3\ K\ mol^{-1}$.

	Code	$\{M_2\}^n$	χT	Spin State	M_B–M_T	FSR	M_B – N_A	M_T – P/N[a]	M_B – N_E	M_T – Ax	Ref
$FeCrL_1$	B30	11	[b]	1/2	1.943(1) 1.944(1)	0.83 0.83	2.2758(3) 2.275(3)	2.262[1] 2.267[2]	1.960(3) 1.960(3)	N/A	[53]
$K[FeCrL_1]$ (crypt-222)	B31	12	0.87	1	1.974(1)	0.84	2.3484(4)	2.2444[8]	2.027(2)	N/A	[53]
$CrNiL_1$	B32	13	1.81	3/2	2.4105(7)	1.04	2.086(3)	2.225[8]	1.956(9)	N/A	[55]
$CrCoL_1$	B33	12	0.95	1	2.135(1) 2.145(1)	0.92 0.92	2.216(4) 2.226(4)	2.214[2] 2.216[2]	1.925(4) 1.920(4)	N/A	[55]
$CrCoL_1N_2$	B34	13	1.60	3/2	2.582(1) 2.588(1)	1.10 1.10	2.202(2) 2.183(4)	2.193[4] 2.208[1]	1.969(4) 1.96(4)	N_2:1.792(5) N_2:1.813(5)	[57]
$[VFeL_1]BPh_4$	B35	9	0.32	1/2	1.9791(6)	0.83	2.2954(8)	2.149[5]	1.934(2)	N/A	[60]
$VNiL_1$	B36	12	0.71	1	2.487(1)	1.05	2.149(5)	2.205[1]	1.957(3)	N/A	[60]
$VCoL_1$	B37	11	0.41	1/2	2.1234(4)	0.89	2.227(2)	2.2355[6]	1.956[2]	N/A	[60]
K $[N_2CoVL_1]$ (crypt-222)	B38	12	0.90	1	2.6466(7) 2.6661(7)	1.11 1.12	2.212(2) 2.222(3)	2.206[1] 2.197[3]	1.955[3] 1.951[3]	N_2:1.796(3) N_2:1.788(3)	[53]
$FeCoL_1$	B39	14	5.45	3	2.2597(9)	0.97	2.245[4]	2.303[2]	1.976(5)	N/A	[61]
$ClCoFeL_1$	B40	13	8.02	7/2	2.5899(4)	1.12	2.300(2)	2.381[8]	1.965[2]	Cl: 2.2476(7)	[61]
$TiFeL_1$	B41	9	[b]	1/2	2.0635(6) 2.0458(8)	0.83 0.82	2.340(2) 2.328(2)	2.287(1) 2.286(2)	2.016(3) 2.019(5)	N/A N/A	[62]
$[TiFeL_1]BAr^F_4$	B42	8	1.12	1	2.161(1)	0.87	2.297(4)	2.361(1)	1.998(3)	N/A	[62]
$TiFeL_1Br$	B43	8	1.10	1	2.3853(4)	0.96	2.354(2)	2.389(1)	1.996(3)	Br:	[62]
$CoMnL_2Cl$	B44	12	0.85	1	2.5312(4)	1.09	2.018[2]	2.1691[8]	1.9051(8)	Cl: 2.361(1)	[56]

$CoFeL_2Cl$	B45	13	0.36	1/2	2.4913(3)	1.07	2.010[1]	2.1073[8]	1.9011(7)	Cl: 2.3455(4)	56
$CoCuL_2Cl$	B46	16	1.10	1	2.3963(3)	1.02	1.946[1]	2.075[1]	1.884[1]	Cl: 2.3548(4)	59
$CoCuL_2$ (MeCN)	B47	17	[b]	3/2	2.4707(4)	1.06	2.067[2]	2.118[2]	1.918(2)	MeCN: 2.120(2)	59
$FeMnL_2Cl$	B48	13	0.45	1/2	2.5283(3)	1.08	2.053[1]	2.1768[8]	1.9416(8)	Cl: 2.3559(5)	56
$CoFeL_3$	B49	14	5.68	3	2.1846(4)	0.94	2.115[2]	2.0528[9]	1.927(1)	N/A	54

[a] Only ligand L_1 contains a P in the top metal site, ligands L_2 and L_3 contain N atoms
[b] These spin values were determined via EPR spectroscopy and no SQUID magnetometry data are provided.

Table 2.5 Magnetic data and bond metrics for compounds synthesized in the Thomas lab. M_N and M_P denote metals bonded to nitrogen an phosphorus, respectively. All bond distances are reported in Å. All magnetic data was obtained via SQUID or via the Evans method at 300 K unles otherwise notesd and is reported in cm^3 K mol^{-1}.

	Code	$\{M_2\}^n$	χT	Spin State	M_N–M_P	FSR	M_N–N	M_P–P	M_N–Ax	M_P - Ax	Ref
$ICo(T_1)_3ZrCl$	B50	8	1.07	1	2.7315(5)	1.05	2.103[2]	2.3004[7]	2.4226(7)	2.5434(4)	63
$ICo(T_1)_3HfCl$	B51	8	1.13	1	2.7548(5)	1.06	2.085(2)	2.2886(6)	2.351(1)	2.5541(6)	66
$V(T_1)_3FeI$	B52	9	0.45	1/2	2.067(5) 2.0745(5)	0.86	1.924[2] 1.921[2]	2.2919[3] 2.2987[7]	N/A N/A	2.6336(4) 2.6658(4)	71
$FV(T_1)_3FeI$	B53	8	0.98	1	2.4377(5) 2.4571(5)	1.02	1.932[2] 1.930[2]	2.3172[7] 2.3133[7]	1.873(1) 1.8765(4)	2.5725(4) 2.5579(4)	71
$Cl–Nb(T_1)_3Fe–Br$	B54	8	1.15	1/2	2.4269(4)	0.97	2.049[2]	2.2936[8]	2.4511(7)	2.3963(5)	79
$Cl–Nb(T_1)_3Cu–Br$	B55	11	0.25	1/2	2.6572(4)	1.05	2.042[2]	2.3151[8]	2.3505(8)	2.3685(4)	81
$Cr(T_1)_3Fe–I$	B56	10	2.92	1/2	2.369(1)	1.00	1.875(2)	2.2720(8)	N/A	2.5563(8)	72
$Cr(T_1)_3Fe–PMe_3$	B57	11	1.73	1/2	2.3835(5)	1.01	1.892(1)	2.2500(4)	N/A	2.2626(8)	72
$Cr(T1)_3Co–PMe_3$	B58	12	1.01	1	2.3316(5)	0.99	1.866(1)	2.1753(4)	N/A	2.1878(7)	72
$ICo(T_2)_3ZrCl$	B59	8	1.03	1	2.6280(5)	1.01	2.131[2]	2.3688[9]	2.4450(7)	2.5837(4)	63
$ICo(T_2)_3HfCl$	B60	8	1.36	1	2.6839(5)	1.03	2.107[2]	2.3526(5)	2.3972(5)	2.5989(5)	66
$N_2Co(T_2)_3HfX$ (X = N_2, I)	B61	9	0.66	1/2	2.5624(4)	0.99	2.120[2]	2.278[1]	2.4252(8)	N_2–1.856(4) I – 2.40(2)	66
$V(T_2)_3FeI$	B62	9	0.41	1/2	2.0186(7) 2.0195(7)	0.84 0.85	1.931[3] 1.924[3]	2.3464[9] 2.349[1]	N/A N/A	2.6758(5) 2.6738(5)	78
$Ti(T_2)_3FeBr$	B63	8	1.16	1	2.2212(7)	0.89	1.975[3]	2.367[1]	N/A	2.4352(6)	78

$(OC)Co(T_2)_3Zr(O)Na(THF)_3$	B64	9	0.50	1/2	2.5333(5) 2.5332(5)	0.97 0.97	2.153[3] 2.151[3]	2.192[1] 2.191[1]	2.071(2) 2.076(2)	1.742(3) 1.739(2)	65
$((p\text{-}OMeC_6H_4)_2CO)$ $Zr(T_2)_3Co(N_2)$	B65	9	0.38	1/2	2.4039(4)	0.92	2.148[2]	2.218[7]	2.313(2)	1.840(2)	80
$(C_{13}H_8\cdot)$-O-$Zr(T_2)_3Co$-N_2	B66	9	0.76	1	2.6324(3)	1.01	2.151[1]	2.2751[5]	2.071(1)	N_2–1.816(2) I – 2.552(1)	82
$(C_{13}H_9)$-O-$Zr(T_2)_3Co$-N_2	B67	9	0.51	1/2	2.6958(5)	1.03	2.152[2]	2.2643[9]	1.945(2)	1.851(3)	82
$(Ph_2CN{=}NH)Co(T_2)_3ZrOSiPh_3$	B68	8	0.41	1	2.8250(6)	1.08	2.139[3]	2.313[1]	1.978(2)	1.918(3)	76
$(OC(H)O)Co(T_2)_3ZrOSiPh_3$	B69	8	1.32	1	2.8141(5)	1.08	2.141(1)	2.3230(5)	1.964(2)	1.986(3)	76
$(PhHC{=}N)Co(T_2)_3ZrOSiPh_3$	B70	8	1.09	1	2.7914(3)	1.07	2.140[2]	2.3025[5]	1.981(1)	1.872(2)	76
$(PhO)Zr(T_2)_3CoN_2$	B71	9	0.42	1/2	2.6723(4)	1.02	2.133[2]	2.2745[7]	1.975(2)	N_2–1.867(3) I – 2.78(1)	67
$(HO)Zr(T_2)_3CoN_2$	B72	9	0.58	1/2	2.7166(9)	1.04	2.137[4]	2.272[2]	1.953(3)	N_2–1.821(5) I – 2.550(1)	67
					2.7121(9)	1.04	2.135[4]	2.274[1]	1.954(3)	N_2–1.817(5) I – 2.550(1)	
$(HO)Zr(T_2)_3Co(CO)$	B73	9	0.56	1/2	2.7486(6)	1.05	2.139[3]	2.266[1]	1.909(2)	1.758(4)	68
$(MeO)Zr(T_2)_3Co(CO)$	B74	9	0.48	1/2	2.750(1)	1.05	2.133[6]	2.268[2]	1.912(5)	1.81(1)	68
$(Me_3SiO)Zr(T_2)_3Co(CO)$	B75	8	0.70	1	2.7616(6)	1.06	2.133(2)	2.2762(6)	1.955(3)	CO1.792(7) I – 2.45(1)	68
$(\kappa^2\text{-}AcO)Zr(T_2)_3Co(CO)$	B76	9	0.42	1/2	2.7110(5)	1.04	2.161[3]	2.254[1]	2.253(2) 2.244(2)	1.774(3)	68
$[(18\text{-}Crown\text{-}6)]K(\kappa^2\ CO_3)$ $Zr(T_2)_3Co(CO)$	B77	9	0.38	1/2	2.8468(5)	1.04	2.179[2]	2.2558[9]	2.136(2) 2.130(2)	CO 1.750(4) I – 2.709(5)	68
$ClZr(T_2)_3Co(CO)$	B78	9	0.41	1/2	2.5965(4)	0.99	2.134[1]	2.2743[7]	2.4460(6)	1.780(3)	68
$(\eta^2\text{-}NPhNH_2)$ $Zr(T_2)_3Co(NHPh)$	B79	8	0.97	1	2.6981(4)	1.03	2.170[2]	2.2518[8]	2.137(2), 2.265(2)	1.852(2)	70
					2.7155(4)	1.04	2.168[2]	2.2473[8]	2.135(2), 2.269(2)	1.841(1)	
$(\eta^2\text{-}NPhNH_2)$ $Zr(T_2)_3CoN_2$	B80	9	0.50	1/2	2.7350(2)	1.05	2.150[1]	2.266[4]	2.040(1), 2.333(1)	1.830(1)	70
$ICo(T_3)_3ZrCl$	B81	8	1.20	1	2.6309(5)	1.01	2.115(7)	2.338(9)	2.451(1)	2.5497(4)	63
$ICo(T_3)_3HfCl$	B82	8	1.13	1	2.6370(7)	1.01	2.086[4]	2.337[2]	2.427(2)	2.5570(8)	66

Table 2.6 Magnetic data and bond metrics for compounds synthesized in the Thomas lab that have a κ^2 bound ligand. M_N and M_P denote metals bonded to nitrogen and phosphorus, respectively. All bond distances are reported in Å. All magnetic data was obtained via SQUID or via the Evans method at room temperature unless otherwise noted and is reported in $cm^3\ K\ mol^{-1}$.

Compound	Code	$\{M_2\}^n$	χT	Spin State	M_N - M_P	FSR	M_N – N	M_P – P	M_P – Ax	M_N– Ax_P	Ref.
$BrCo(T_2)_2$ (μ-Br)$Zr(T_2)$	B83	8	1.09	1	2.7602(3)	1.05	2.098(2)	2.2839(6)	2.3603(3)	N – 2.137(2) P – 2.6716(5)	74
$(T_2)Zr(\mu\text{-}I)(T_2)_2CoI$	B84	8	1.13	1	2.7811(3)	1.06	2.130[2]	2.2848[5]	2.5640(3)	N - 2.142(2) P - 2.6585(5)	64
$(^t$BuNC)$Co(T_2)_2(\mu\text{-}NAd)Zr(T_2)$	B85	8	1.01	1	2.7338(3)	1.04	2.204[2]	2.2775[6]	1.882(2)	N – 2.170(2) P – 2.7487(6)	77
$(\eta^3\text{-}P^iPr_2N\{C_6(CH_3)_2H_2(CH_2)\}e)$ $Zr(T_2)_2CoI$	B86	8	1.33	1	2.5562(4)	0.98	2.136(2)	2.3133(8)	2.5647(4)	N – 2.099(2) P – 2.6897(7)	64
$(\eta^3\text{-}P^iPr_2N\{C_6(CH_3)_2H_2(CH_2)\})$ $Zr(T_2)_2CoCl$	B87	8	1.54[a]	1	2.6036(6)	0.99	2.142(3)	2.284(1)	Cl 2.262(3) I 2.534(5)	N – 2.106(3) P – 6935(9)	64
$Ph_2(^iPr_2P)COZr(\mu\text{-}NMes)(T_2)_2Co$	B88	8	0.97	1	2.6749(6)	1.02	2.150[3]	2.259[1]	O 1.976(2)	N/A	83
(Pyridine)$Co(^i T_2)_2(\mu\text{-}O)Zr(T_2)$	B89	8	1.16	1	2.7086(3)	1.03	2.204[1]	2.2681[5]	2.042(1)	N 2.212(1) P 2.6810(4)	76
$(T_2)Ti(T_2)_2CoI$	B90	9	1.28	1	2.2735(8)	0.92	1.984(3)	2.251(1)	2.5227(5)	N – 1.991(3) P – 2.609(1)	84
					2.2734(8)		1.982(3)	2.250(1)	2.5227(5)	N – 1.986(3) P – 2.612(1)	
$(T_2)Ti(T_2)_2(\mu\text{-}Cl)CoI$	B91	8	0.49	1/2	2.6530(4)	1.07	1.982(1)	2.2743(4)	2.5513(3)	N – 1.963(1) P – 2.5215(5)	84
$[(T_3)Zr(\mu\text{-}SPh)(T_3)_2CoSPh]$	B92	8	1.12	1	2.7381(3)	1.04	2.123[1]	2.2898[4]	2.2543(4)	N 2.146(1) P 2.6829(4)	67
$(T_3)Zr(\mu^2\text{-}\eta^1\ \eta^3\text{-}^tBuN_3)(T_3)_2Co$	B93	10	1.00	1	2.7835(3)	1.06	2.154[2]	2.2445[5]	N/A	N – 2.165(2) P – 2.7164(5)	73
$ClCr(T_3)_2Ir(T_2)$	B94	11	1.83	3/2	2.6064(4)	1.07	1.883(2)	2.2773(7)	2.2769(8)	N – 2.087(2) P – 2.3060(7)	75

$ClCr(T_2)_2Rh(T_2)$	B95	11	1.82	3/2	2.6095(3)	1.08	1.875(2)	2.2838(5)	2.660(6)	N – 2.093(2) P– 2.22897(5)	75

[a] This value is considered artificially high as a result of poor solubility

2.2.3 Electronic Structure of Heterobimetallic Compounds

The electronic structure of each complex featured in this section can be derived from either an idealized C_3-symmetric or C_4-symmetric structure. Those derived from the idealized C_3-symmetry structure can be further classified into one of two generalized structures. These general possible structures are shown in Figure 2.11.

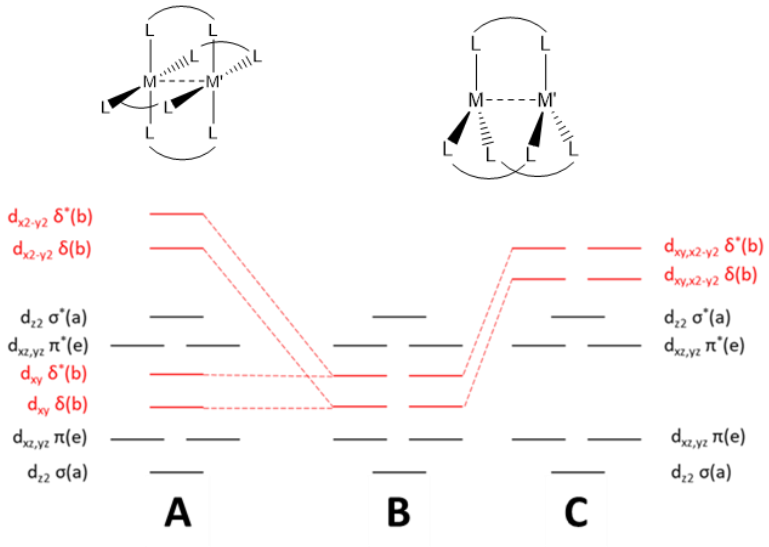

Figure 2.11 Qualitative MO diagrams for C_4 (left) and C_3 symmetric (middle and right) structures. For C_3 structures, the electronic structure is highly dependent on metal and ligand identities.[52]

2.3.1 Electronic Structure of C_4 Symmetric Heterobimetallics

In a C_4 structure the five metal *d* orbitals transform into 2 π, 1 σ, and 2 δ symmetry orbitals representing the d_{xz}, d_{yz}, d_{z^2}, d_{xy}, and $d_{x^2-y^2}$ orbitals, respectively (2.11A). The δ symmetry $d_{x^2-y^2}$ orbital is predominantly involved in metal-ligand bonding and is typically not occupied unless the metal ions are high-spin.[1] This stituation is similar to that posed in the hypothetical $[WOsCl_8]^{2-}$ species presented in Figure 2.1B. In the compounds listed in Table 2.3 we have a low spin $\{PtS_4\}$ and a high spin $\{MO_4L\}$ (M = Mn, Fe, Co, Ni); both in a square planar environment. These centers can than interact with d_{z^2} overlapping to form σ symmetry orbitals, d_{xz} d_{yz} forming those of π symmetry, and d_{xy} forming δ symmetry orbitals. Again, the $d_{x^2-y^2}$ orbitals are primarily involved with metal-ligand bonding and not metal-metal bonding. A

qualitative MO diagram for **B3** is shown in Figure 2.12. Here the 16 electrons of the {PtNi}^{16} unit fill up to the σ* and Ni $d_{x^2-y^2}$ levels, resulting in an S = 1 ground state (reflecting the interaction of a d^8 Pt^{II} center with a high spin Ni^{II} ion).

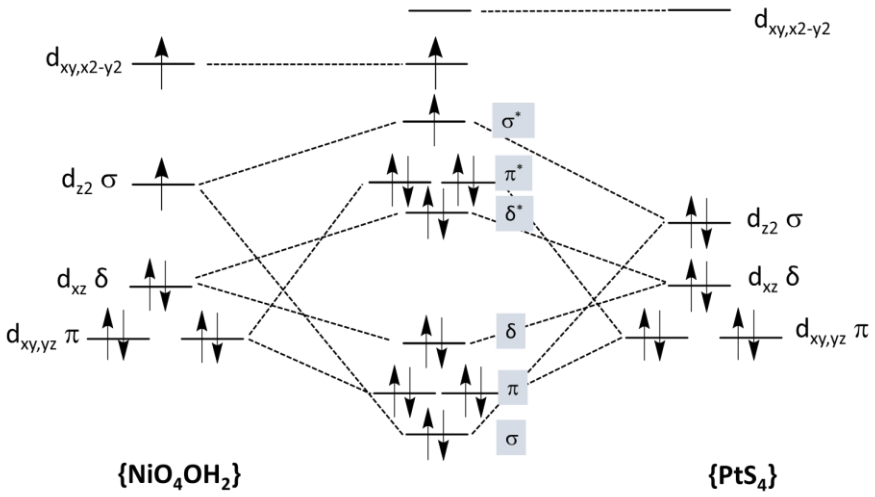

Figure 2.12 Qualitative MO diagram for PtNi(tba)$_4$OH$_2$.[95]

2.2.3.2 Electronic Structure of C_3 Symmetric Heterobimetallics

In comparison to the tetragonal ligand field imposed by C_4 symmetric species, the trigonal ligand field found the within C_3-symmetric structures. This in consequence, allows all five metal d orbitals to pariticpate in metal-metal bonding. In a C_3 structure, the d_{xy} and $d_{x^2-y^2}$ orbitals become degenerate orbitals of δ symmetry (2.11B). In some metal-ligand pairings with strong π-donor ligands however, these orbitals are the highest in energy but are still low enough to partipate in metal-metal bonding (2.11C).

Looking at three-fold symmetric structures subtle changes in bonding can be correlated the the difference between the group numbers of the two metals, ΔN, as shown in Figure 2.13.[58] At the left end, in which ΔN is either zero or one, all valence orbitals have sufficient overlap to form a quintuple bond. The Lu group has isolated two compounds with quintuple bonds, the heterobimetallic MnCrL$_1$ complex has a quintuple bond and is diamagnetic and a homometallic CrCrL$_1$.[58] The middle compound (**B31**) has a ΔN of two, and contains a triple bond. In this bonding schematic, the δ symmetry orbitals have been localized to one metal center or the other and are therfore nonbonding. All of the other orbitals remain delocalized. Moving to the right end is a case in which the ΔN value is five (such as in **B36**). In this case, all of the orbitals

localize to one metal center or the other. This trend is due to the energy mismatch of the participating orbitals stemming from differences in the effective nuclear charge. Large differences in energy prevent delocalized bonds from forming as in the case of **B36** with only a dative interaction. A notable feature of this dataset is that is shows clearly that the symmetry of the *d* orbitals strongly affects the degree of energy mismatch. Thus, δ-symmetry orbitals, which have relatively poor overlap to begin with, are the first orbitals to "localize" when ΔN increases. Thus, **B31** can be described as having only a $\sigma^2\pi^4$ configuration contributing to its metal-metal bonding describe being a $\{MM'\}^{12}$ complex.

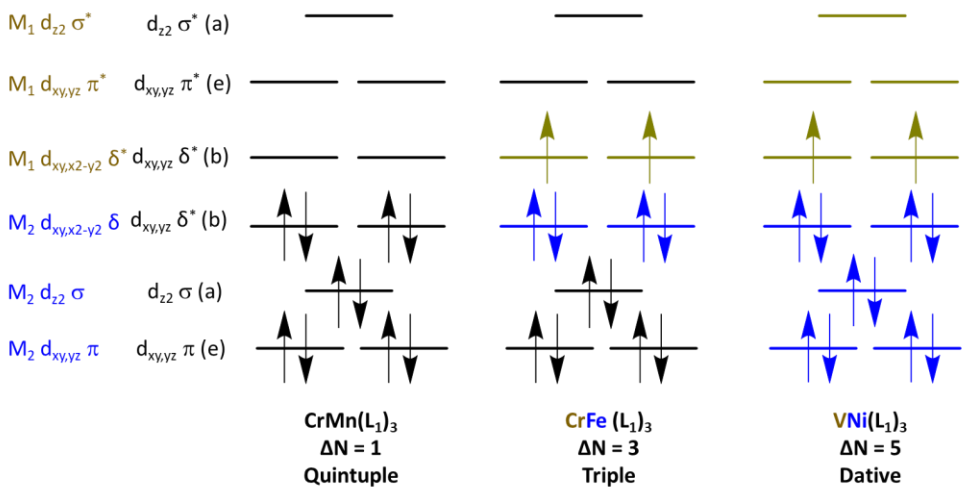

Figure 2.13 Qualitative MO diagrams for three heterobimetallic species synthesized by Lu and coworkers. These compounds range from having a quintuple bond (left) to a dative interaction (right). orbitals depicted in black represent highly delocalized orbitals across the chain. As the difference in group number increases, the orbitals become localized onto one metal center. These localized orbitals are denoted in either blue or gold and correlate to the metal of that color.[58]

As in the case of **B30** and **B31**, the dominant electronic structures of Lu's complexes are similar to that shown in Figure 2.11B.[53] Compounds **B30** and **B31** both contain Fe and Cr (ΔN = 2) and are nearly identital structurally. However, **B30** $\{M_2\}^n$ =11 is the neutral form of **B31** $\{M_2\}^n$ =12. In the eletronic structure of both **B30** and **B31** ΔN = 2 leads to the δ and δ* orbitals being replaced with localized d orbitals for Fe and Cr, respectively with no δ bonding. In the case of **B30**, there is one unoccupied δ* orbital on the chromium center. This vacancy leads to a break in denegeracy of d orbitals and is instead found highest in energy.

It is important to note that computational treatment of heterometallic metal-metal bonded species is challenging as many of the compounds are multiconfigurational. While some compounds such as **B41**-**B43** *can* be treated with DFT methods.[62] The majority of the compounds listed in Table 2.4(**B30**-**B40**, **B46**, **B48**) are multiconfigurational and have been treated with ab initio CASSCF/CASPT2 multireference methods. The dominant component represents between 40% and 90% of the total electronic wavefunction.[53-55, 57, 59-61] However, there are also examples, such as **B44**, **45**, and **B47** in which the dominant component represents as little as 7% of the overal electronic wavefunction.[56]

Many examples of complexes synthesized in the Thomas lab contain the early-late pairing of Zr and Co. The mismatch in orbital energy, $\Delta N = 5$, is significant in these complexes. This leads to highly polarized Co–Zr bonds that ultimately promote reactivity toward substrates with polar bonds. Furthermore, these bonds are often quite weak and can be best described as dative π bonds and/or σ single bonds.[52] Despite having similarities in both metal identities and ligand sets, many subtle differences are present in the electronic structures of the Lu and Thomas' compounds. Notably, the C_3 symmetric compounds synthesized in the Lu lab contain a three atom long bridge in the ligand between the two metal centers. For the Thomas compounds, this bridge is only two atoms in length. This two atom long bridge enforces a pseudotetrahedral geometry at the metal bound to the phosphorus centers. In contrast, the three atom long linkage allows a more flexible geometry enabling the metal center to interact with the lone pairs of the phosphorus atoms (Scheme 2.6). In contrast to the compounds from Lu and workers that feature traditionally low overall spin states and large metal-metal bond orders, those from the Thomas lab present smaller metal-metal bond orders with overall higher spin states. [52, 72]

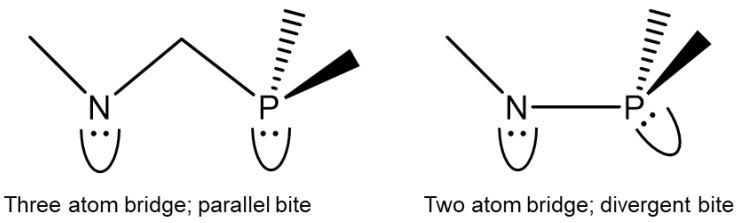

Scheme 2.6 Effect of bridge length between N and P atoms on lone pair orientation.

While the majority of the complexes from the Thomas lab contain metals of two diferent rows, they have also synthesized pairings of exclusively 3d transition metals. Specifically, **B52**-**B53** and **B62**, which contain a V and Fe pairing as well as **B56**-**B58** which contain Cr paired with either Fe or Co. In the VFe heterobimetallics, the resultant electronic structures are analogus to the CrFe heterobimetallic **B30** prepared by Lu and coworkers. Both feature a σ bond and two π bonds, resulting in extremely short bonds with FSR values much less than one. Turning to the Cr based heterometallics **B56**-**B58**, In contrast to the VFe species and despite the more favorable ΔN of two, the Cr and Fe containing **B56** and **B57** contain longer metal-metal distances, as evidenced by FSR values near one. Furthermore **B56** contains an $S = 2$ ground spin state. These observations are justified by examining the π^* orbital energy of **B56** being lower in energy than the localized nonbonding Fe *d* orbitals. As a result, electrons are able to populate both the nonbonding and antibonding orbitals, thus leading to longer metal-metal distances with higher spin states (Figure 2.14).

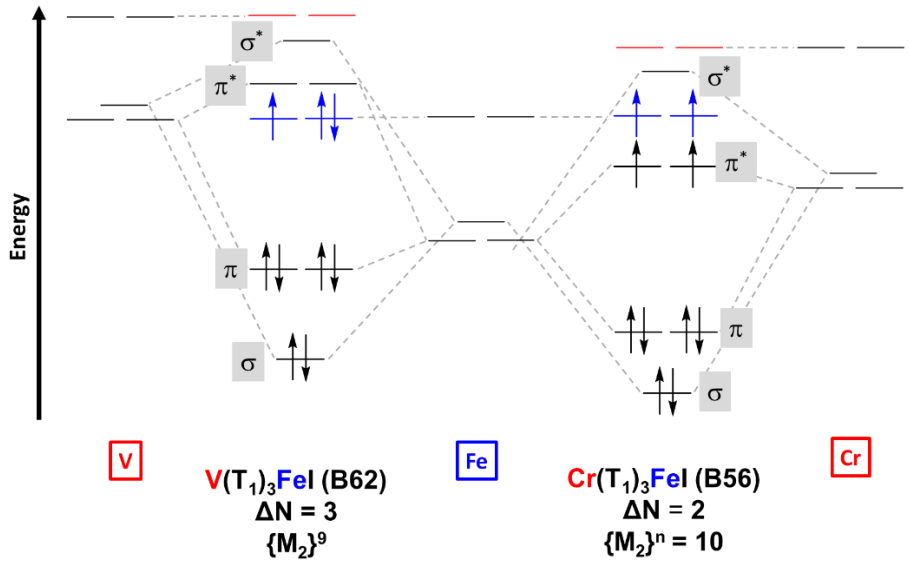

Figure 2.14 Qualitative MO diagrams for the bonding manifolds in the compounds made in the Thomas lab that give rise to both multiple bonds and dative interactions. Orbitals that are in red or blue are localized to the corresponding color metal. The π^* orbitals have been emphasized with a box.

2.2.4 Magnetic Properties

Despite containing only two metals, the range of magnetic interactions presented is wide-ranging. Depending on the location of the unpaired electrons and the energies of the *d* orbitals they reside in,

unpaired electrons may be localized to one metal center or be delocalized over both centers and coupling can be ferro– or antiferromagnetic. Many of the complexes syntheisized by Lu and Thomas are made of exclusively first-row metals that can exist in multiple spin states. Furthermore, the magnetic characterization done on many of the species synthesized in the Thomas lab have allowed her group to elucidate mechanistic details of several organic transformations including N–N bond cleavage, [84] hydrosilyation of ketones, [69] and N–H bond activation. [70]

2.2.4.1 Isolated Magnetic Ions

Despite strong metal-metal bonding, it is possible for unpaired electrons in a heterobimeatallic complexes to remain localized on one metal center or the other. For example, all the heterobimetallics in the Lu group contain metals that couple with one another. For example, the series of L_1 supported **B35**, **B36**, and **B37**, all contain V–M bonding interactions butspins that are isolated on eiether V or M.[60, 78] Compounds **B35** and **B37** both have $S = 1/2$ ground states as initially determined via the Evans method. However, the unpaired electron for **B35** is localized on Fe whereas the spin in **B37** is V-centered. Compound **B37** was also examined via the Evans method and found to have an $S = 1$ ground state. The low effective magnetic moment of 0.71 cm^3 K cm^{-1} was attributed to the presence of a localized V^{III} d^2 ion with $g < 2$. The half integer spin systems of **B35** and **B37** were also investigated via EPR spectroscopy. The EPR spectrum for **B35** has a nearly axial signal, with g values of 2.04, 2.08, and 2.23. The spectrum lacks large hyperfine splitting and, paired with g values larger than two, Lu and coworkers determined the spin was localized to the iron center. The opposite is true for **B37**, which presented a rhombic signal with g values of 2.00, 1.92, and 1.80. Additionally hyperfine coupling (70.4, 22.8, 74.7) x 10^{-4} cm^{-1} is observed which could come from either ^{59}Co (I=7/2) or ^{51}V (I=7/2). However, the g values less than two suggest that the spin is housed on the V center.[60] The electronic strutures of all three species were examined computationally and the computational results supported localized spin centers as described above with localization attributable to large ΔN.

Consistent with Lu's observation of isolated metal centers on compounds with large disparities in group numbers, Thomas and coworkers have seen similar behavior in most of their 3d transition metal supported complexes. In two of the limited number of their heterobimetallics containing a 4d or 5d transition metals such as **B94** and **B95** both illustrate (FSR 1.07 and 1.06, respectively) metal-metal

interactions. These interactions involve a Cr(III) and either a Rh(I) or Ir(I) species. Both **B94** and **B95** have spin states of S = 3/2. This is attributable to a diamagnetic Rh or Ir species and Cr(III) ion housing localized *d* electrons.

As mentioned in Section 2.2.1, the geometry of the crystallized dimer of heterobimetallic units in compounds **B1** to **B28**, dictates their magnetic behavior. For compounds that exist in the square geometry, the magnetic data suggest that each bimetallic paddlwheel units behaves independently with one high-spin metal (II) ion. This is also the case for **B8** and **B9** which are axially ligated on both sides and cannot dimerize. The rationale for the isolated behavior lies in the communication via Pt d_{z^2} orbitals. When these species dimerize they do so with Pt atoms facing each other. When the Pt atoms are in close enough proximity (as with every geometry except square), unpaired electrons on the terminal 3d metals can communicate via this pathway and couple. The square geometry does not have this magnetic pathway available. This behavior is only possibly in the solid state when the compound is in a crystallized form. We may consider compounds **B2**-**B7**, which exist in either the staggered or partially ecliped geometries. The solution state (Evans method) magnetic moment for **B2**-**B7** are all consistent with an isolated spin center. Their solid state behavior will be discussed in Section 4.

2.2.4.2 Spin Coupled Magnetic Centers

The Lu group has prepared a systematic series of compounds that enable them to enumerate trends in magnetic properties and make synthetic choices to tune these properties. For example, they have used the L_2 ligand to form a series of isostructural $MM'L_2Cl$ (M = Co, Fe; M' = Fe, Mn, Cu) complexes. Compounds **B44** (CoMn) , **B45** (CoFe), and **B48** (FeMn) were examined via SQUID magnetometry. In **B44**, **B45**, and **B48**, antiferromagnetic coupling was observed, the magnitude of the coupling decreases going from **B45** > **B48** > **B44**. These data are summarized in Table 2.7. For this series, the spin state can best be described as $S_{total} = |S_M - S_{M'}|$.

Table 2.7. Coupling and *g* values for **B44**,**B45**,**B48**. For **B44**, **B45**, and **B48**, these data were obtained from SQUID magnetometry measurements at room temperature. For **B44** *g* values were determined from EPR spectroscopy.

Compound	M_1	M_2	$\{M_2\}^n$	S_1	S_2	S_{total}	g_1	g_2	g_3	J (cm^{-1})	Ref
B44	Co	Mn	12	3/2	5/2	1	2.00	2.09	N/A	-120	[56]

B45	Co	Fe	13	3/2	2	1/2	2.16	2.16	N/A	-184	[56]
B48	Fe	Mn	11	2	5/2	1/2	2.00	2.06	N/A	-145	[56]

There are two possible mechanisms for exchange coupling to consider. In a direct exchange mechanism, coupling would occur through *d* orbital overlap on adjacent metal centers. This mechanism was ruled out by considering the strength of the coupling constant (*J*) against a homobimetallic Fe_2L_2Cl complex, which has the greatest *d* orbital overlap. Therefore it should present the largest antiferromagnetic coupling value. However, the opposite is observed and Fe_2L_2Cl instead presents a weak ferromagnetic interaction between the metal centers. Thus, the dominant magnetic pathway was determined to be through superexchange via the bridging ligands. Based on the Goodenough-Kanamori rules, the unpaired d electrons present on the metal backbone of δ symmetry are capable of interacting with each other via the conjugated π system of the ligand backbone. However, compounds **B44**, **B45**, and **B48** also contain unpaired *d* electrons of π symmetry. These are not capable of interacting via the bridging ligand. Thus, a degree of direct exchange is believed to occur in these systems.[56]

2.2.5 Reactivity and Catalytic Applications of Heterobimetallic Compounds

2.2.5.1 Reactivity of Heterobimetallic Compounds

Thomas and coworkers have extensively examined the ability of early-late heterobimetallic complexes to react with small organic or inorganic substrates. These reactivity studies may generally be summarized in Scheme 2.7, which specifically highlights the compound (thf)Zr(MesNP(^{i}Pr)$_2$)$_3$Co(N_2), which has been the most widely studied complex. Other compounds whose reactivity have been studied include: (1) anionic compounds with a halogen ligand at Zr in place of the thf ligand,[66] (2) compounds with Ti[84] or Hf[66] in place of Zr, (3) alternative bridging N–P ligands ^{i}PrNP(^{i}Pr)$_2$,[67] XylNP(^{i}Pr)$_2$,[74,84], or ^{i}PrNP(Ph)$_2$, (4) terminal ligands other than N_2 on Co (CO,[68] or isonitriles[77, 101] have been utilized).

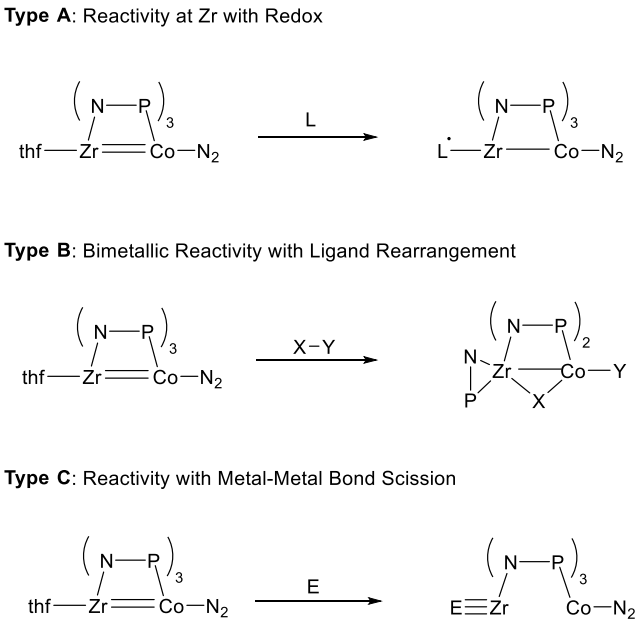

Scheme 2.7 The three types of reactivity patterns observed for early-late heterobimetallics.

There are three general reaction types that have been observed for these early-late heterobimetallics. In the first (Type A Scheme 2.7), ligand substitution occurs at the early metal site and is accompanied by one electron reduction of the incoming substrate. Examples include reactions with diaryl ketones, which give either stable or unstable ketyl radical complexes,[69, 80, 82-83] hydrazine and hydrazine derivatives,[70, 84] alcohols, and water,[68 67] which eliminate H_2 to yield alkoxide and hydroxide complexes, respectively, and also alkyl peroxides. [67] In the Hf–Co complex, methyl iodide also shows Type A reactivity, liberating ethane.[66] Ethyl diazoacetate undergoes similar reactivity, being reduced by two electrons between a pair of Zr–Co complexes.[77] Even these reactions occur at Zr(IV), the low-valent Co is the source of the electron reducing the substrate.

Type B reactivity involves addition of X–Y molecules across the Zr–Co bond yielding products in which X bridges between the two metals, and Y adds as a terminal ligand to Co. In the process, one of the bridging N–P ligands shifts to a terminal chelating mode opening up the bridging site for the X group. The result is a net two-electron oxidative addition, and a broad range of X–Y molecules may be activated through this process. These include: I_2,[64] methyl iodide (yielding a bridging methyl ligand),[64 66] CO_2, yielding a bridging oxo/terminal CO product,[65]ketones, which form bridging oxo/terminal carbene

products,[80, 83]ketimines, which add the N–H bond to yield terminal hydride species,[82] disulfides giving bridging and terminal thiolates. [67] Adamantyl azide reacts somewhat similarly, yielding the bridging-to-chelating N–P ligand switch, and a bridging imido group from loss of N_2; the Co terminal ligand remains unchanged.[77] In addition to the Type B product, oxidative addition of I_2 also yields $ZrCo(N–P)_3I_2$ in which the overall C_3 symmetry is retained (no ligand switch), having the two I atoms in the terminal positions, one at each metal site.[64] Generally, these are reactions that leave a soft donor ligand that preferentially bonds to the low-valent Co atom.

Pyridine N-oxide also undergoes Type B reactivity forming a complex with a bridging O atom and a Co-bound pyridine ligand.[76] The bridging O atom can be further functionalized by reaction with triphenylsilane to yield a Zr-terminal siloxide product bound to a Co-terminal hydride. The hydride complex shows hydridic reactivity upon reaction with formic acid, and adds across the multiple bonds of other substrates (CO_2, diphenyldiazomethane, benzonitrile, and phenylacetylene).[76]

The third reactivity pattern, Type C, involves cleavage of the metal-metal bond, and generally occurs when the incoming substrate can form more than one bond to Zr, or can lead to a Zr≡E multiple bond. For example, O_2 adds oxidatively to form an end-on peroxo ligand at Zr.[101] A similar oxidation by pyridine N-oxide yields the terminal Zr≡O species.[101] Both have Zr–Co distances outside the bonding range.[101] Other substrates that react in this way include diphenyldiazomethane and mesityl azide.[77]

In addition to the three reactivity patterns outlined above, there are also reactions that involve activation of a N–P ligand C–H bond,[64] destruction of the N–P ligand by scission of the N–P bond,[**N**] or oxidation of the P end of the N–P ligand. [84] Reaction of $(thf)Zr(MesNP(^iPr)_2)_3Co(N_2)$ with H_2 was found to selectively cleave one N–P bond;[64] Thomas and coworkers sought to counteract this irreversible reaction by employing a new generation of Zr–Co complexes bearing only two N–P ligands, which react cleanly with H_2 via a Type B reaction as shown in Scheme 2.8.[102] This non-destructive reactivity has allowed the bis-N–P-ligated complexes to be used as catalysts for hydrogenation (vide infra). [102]

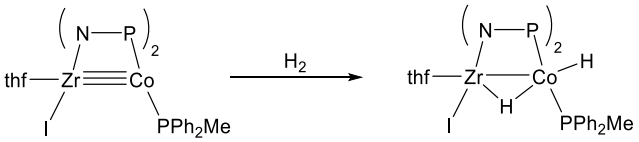

Scheme 2.8. Oxidative addition of H_2 to Zr–Co complex supported by only two N–P ligands.

2.5.2.2 Catalytic Applications of Heterobimetallic Compounds

The Zr–Co complex (thf)Zr(MesNP(^{i}Pr)$_2$)$_3$Co(N_2) has been utilized as a catalyst for two types of reactions: silylation of ketones and Kumada cross coupling. The ketone silylation is based on the Type A reactivity of the Zr–Co complex with ketones, expanded to 13 substrates including aryl/alkyl and alkyl/alkyl ketones. PhSiH3 is used as the silylating reagent and the silyl ethers are not isolated but converted in situ to the alcohols via acidic workup.[69] The Kumada coupling reaction involves metathesis of *n*-octylmagnesium bromide with a wide variety of alkyl halides.[74, 87] Generally, primary alkyl halides gave higher yields than secondary, and aryl halides were activated, but not well. The reactivity of the halides, I > Br > Cl, is as expected. The reaction mechanism was studied by Ess and coworkers,[88] and the Zr–Co structure was found to facilitate both the oxidative addition and reductive elimination steps in comparison to a model mononuclear Co complex.

The analogous Ti–Co complex was found to catalyze the disproportionation of hydrazine to ammonia and nitrogen. This catalytic reaction was developed from the stoichiometric Type A reactivity observed with hydrazine. At 2 mol %, the Ti–Co complex was capable of 18 turnovers for hydrazine disproportionation.[84]

As mentioned above, the Zr–Co complexes supported by only two N–P ligands are active catalysts for hydrogenation. Hydrogenation of diphenylacetylene was studied, and nearly quantitative conversion was achieved with 10 mol % Zr–Co complex. The reaction is selective for semihydrogenation forming up to 98 % of a mixture of stilbenes (57:43 *Z*:*E*).[102]

3. Paramagnetic Heterotrimetallic Compounds

Unlike heterobimetallic compounds that can exist in only one topology, heterotrimetallic compounds can exist in one of three forms: symmetric chain, asymmetric chain, or cluster. The chain forms

have been studied by the groups of Peng, Nuss, and Berry.[37, 110-134] In addition, triangle-shaped high-spin trimetallic species have been explored by Betley and coworkers.[135-136]

3.1 Synthetic Methods and Structural Data for Heterotrimetallic Compounds

3.1.1 Heterotrimetallic Chain Compounds

The majority of the chain compounds presented in this section are supported by the dpa (2,2' dipyridylamine) ligand[137] although complexes employing both the npo (1,8 naphthyridin-2(1*H*)-one)[118] and npa (2-naphthyridylphenylamine)[114] ligands have also been reported as shown in Figure 2.15.

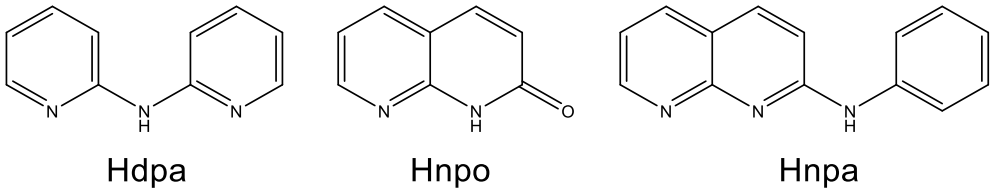

Figure 2.15. The three ligands (in their protonated forms) used to support heterometallic extended metal atom chains (HEMACs).[114, 118, 123]

In 2007, the Berry group[123] and the group of Peng[112] separately reported the first examples of heterometallic extended metal atom chain compounds (HEMACs). We reported the asymmetric $Cr_2Fe(dpa)_4Cl_2$ chain,[123] while Peng and coworkers reported the symmetric $CoPdCo(dpa)_4Cl_2$ complex.[112] This follows extensive work on the homometallic EMACs of Cr_3,[23, 138-146] Co_3,[139, 147-155], Cu_3, [146, 156-157] Ni_3,[154, 158-163] Ru_3, [142, 164-166] and Rh_3,[167] all with unique magnetic behavior. Our lab has primarily focused on asymmetric chains of the form $M_AM_AM_B$,[37, 123-124, 126-128, 130-132, 134] in which the $M_A{\equiv}M_A$ core is a quadruply bonded diamagnetic unit while the Peng lab has worked with both symmetric chains of the form $M_AM_BM_A$ [111-112, 117, 119] and asymmetric $M_AM_AM_B$ chains (which do not necessarily contain a quadruple bond).[113-114, 118, 120] Both our lab and the Peng lab have also constructed $M_AM_BM_C$ chains.[116, 125] To construct these chains, three general methodologies have been established. These are described below. The bond metrics for symmetric $M_AM_BM_A$ HEMACs are shown in Table 2.8 the bond metrics for asymmetric $M_AM_AM_B$ HEMACs are shown in Table 2.9 while the $M_AM_BM_C$ data are shown in Table 2.10.

3.1.1.1 Self-Assembly

The self-assembly method has proven to be an effective method in the generation of both symmetric and asymmetric HEMACs. For symmetric HEMACs, the central metal (M_B) is limited to a Group 10 metal, although the terminal metals (M_A) span the entirety of the 3d transition metals.[111-112, 117, 119] These HEMACs are made by adding M_ACl_2 (note: when M_A = Ni, $Ni(OAc)_2{\cdot}4H_2O$ is used), either $K_2M_BCl_4$ or $M_BCl_2(MeCN)_2$, Hdpa, and *t*BuOK to napthalene and the reagents are allowed to react at elevated temperatures (Scheme 2.9A).[117] This chain may be the desired final product however this step may be followed by a metal-atom substitution step to replace M_A (Section 3.2.1.2). Using slightly different starting materials, asymmetric HEMACs may also be synthesized using this method.[114, 118] For $M_AM_AM_B$ HEMACs (**R33**,**R38-44**) containing a, the M_A source is either a $M_2(OAc)_4$ or $M_2(OAc)_4Cl$ precursor while the M_B source is an M_BCl_2. Reaction of these metal starting materials, the desired ligand, and in some reactions *t*BuOK are allowed to react in molten naphthalene (Scheme 2.9B).[118] During this time, excess NaNCS may be added to alter the axial ligand identity from Cl to NCS (ligand substitution discussed in Section 3.1.1.4).

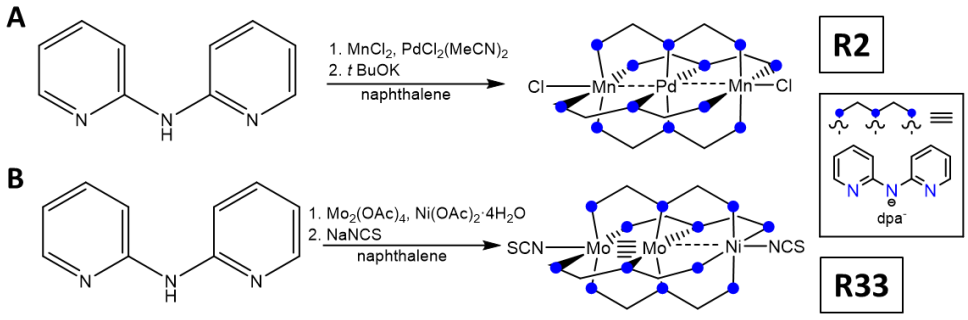

Scheme 2.9. Self-assembly method used to make heterometallic chain compounds.[117-118]

3.1.1.2 Metal-Atom Substitution

Heterotrimetallic chain compounds are amendable to metal-atom exchange reactions at the outer positions. To accomplish such a reactivity, the initial HEMAC is treated with a slight excess of incoming M_ACl_2 in molten naphthalene, substituting out the initial M_A. This scenario is exemplified in the synthesis of the $FeM_BFe(dpa)_4Cl_2$ series with M_B = Ni, Pd, or Pt (compounds **R4**-**R6**). Self-assembly from $FeCl_2$ and M_BCl_2 was successful in the synthesis of $FeNiFe(dpa)_4Cl_2$ and $FePdFe(dpa)_4Cl_2$ (Scheme 2.10A);the same is not true for $FePtFe(dpa)_4Cl_2$. Extended reaction times led to product decomposition and/or oxidation of

the Fe^{II} centers. To combat this, a CdPtCd intermediate species is first synthesized and then treated with $FeCl_2$ in a metal-atom substitution step to afford the desired product (Scheme 2.10B).[119]

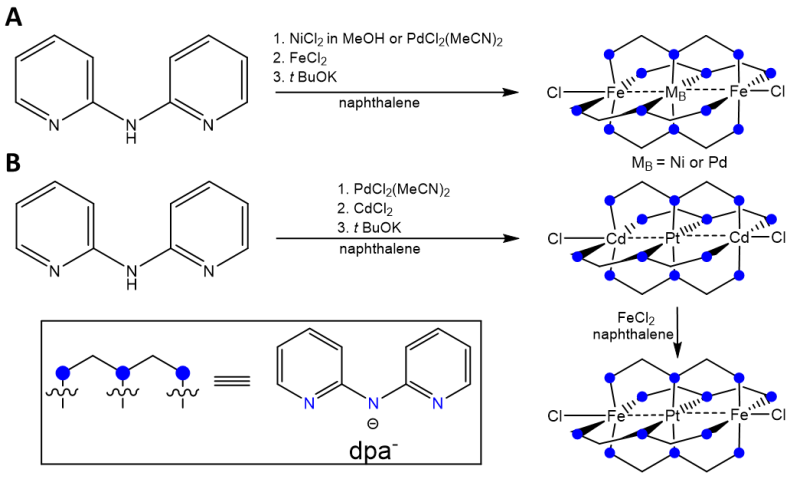

Scheme 2.10 Synthetic methods for compounds **R4**-**R6**. Compound **R6** requires metal atom substitution.[119]

3.1.1.3 Metalloligand Approach

The metalloligand approach is not unlike the methods discussed in Section 2.1.1. A bimetallic quadruply bonded Group VI $M_2(dpa)_4$ core with $M_2 = Cr_2$, Mo_2, W_2 or MoW are synthetically accessible. For $Cr_2(dpa)_4$, this is accomplished through addition of a large excess of NaCN to the homotrimetallic $Cr_3(dpa)_4Cl_2$. In this reaction, a Cr is abstracted to presumably form the $Cr(CN)_6^{2-}$ ion (Scheme 2.11 A). In contrast, $Mo_2(dpa)_4$ and $MoW(dpa)_4$ are made in a similar way to one another. Either $Mo_2(OAc)_4$ or $MoW(piv)_4$ is treated with four equivalents of Lidpa to afford the desired dpa supported core (Scheme 2.11 B,C). The $W_2(dpa)_4$ core is made by the treatment of two equivalents $W(CO)_6$ with four equivalents of Hdpa in molten naphthalene (Scheme 2.11 D).

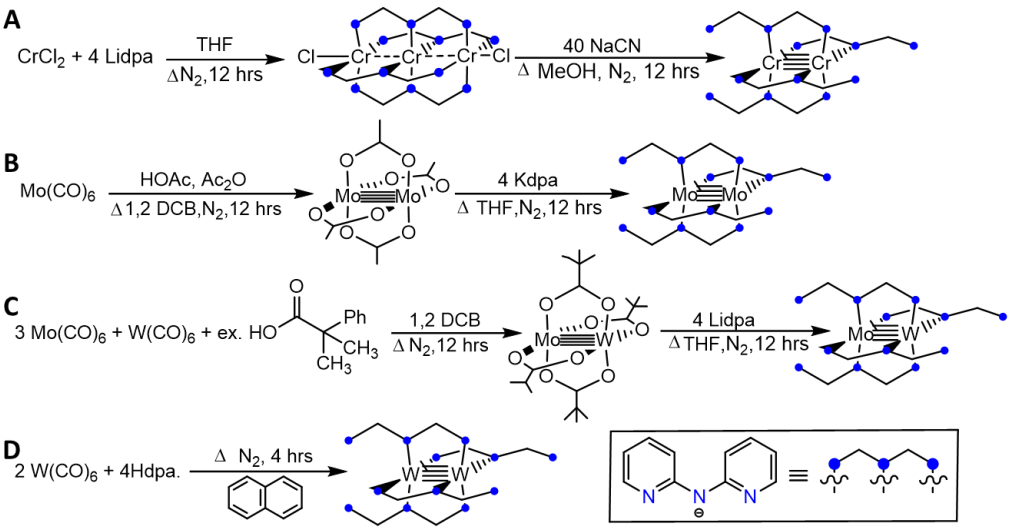

Scheme 2.11 M_2 core formation for $M_AM_AM_B$ HEMACs.

To this initial core, a heterometal can be introduced (typically) in the form of a M(II) halide.[37, 123-127, 132] High temperatures are required to rearrange the dpa ligands on the M_2 core from their initial trans-2,2 orientation to the 4,0 geometry required for the HEMAC structures. For Cr_2-supported HEMACs, refluxing THF is sufficient (Scheme 2.12A).[121, 123-124, 126-127] For Mo_2, W_2, and MoW, molten naphthalene is needed to achieve this transformation (Scheme 2.12B).[37, 124-127, 130-132]

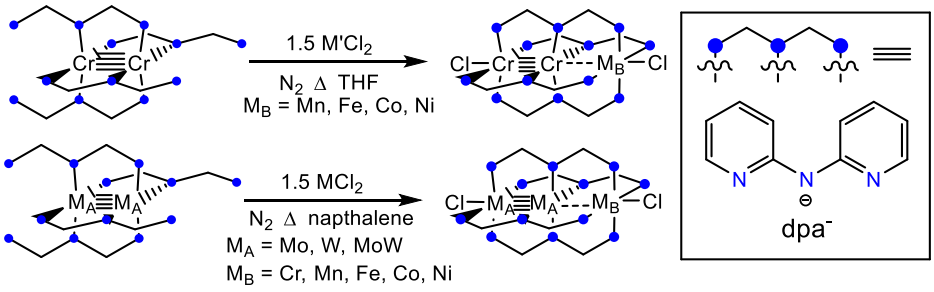

Scheme 2.12. Metalloligand approach for $M_A{\equiv}M_A{\cdots}M_B$ HEMACs.

Initial synthetic efforts in this area began with Cr_2-supported HEMACs while varying M_B (**R13-R16**).[123-124, 126] Berry and coworkers subsequently developed a method for Mo_2 supported HEMACs (**R25-R29**),[37, 124, 126-127, 130, 132] followed shortly thereafter by W_2 (**R36-R37**)[127, 132] and MoW (**R49**)[125] compounds.

These chains utilize a 3d transition metal in the M_B position. In 2014 the first example of a $M_A \equiv M_A \cdots M_B$ chain in which M_B is not a first row transition metal was reported with the synthesis of $Mo_2Ru(dpa)_4Cl_2$, $W_2Ru(dpa)_4Cl_2$, and the one electron oxidized $[Mo_2Ru(dpa)_4Cl_2][OTf]$ (**R35**) although only the latter is paramagnetic.[130-131] For these reactions, a simple halide salt was unavailable and instead half an equivalent of $[Ru(CO)_3Cl_2]_2$ was used in reaction with the $M_2(dpa)_4$ starting materials to prepare the HEMAC chains.

Compound **R45** and **R46** are also made via a metalloligand approach using a $Ru_2(dpa)_4Cl$ "ligand".[120] The $Ru_2(dpa)_4Cl$ "ligand" can then be treated with either $[Rh(COD)_2]BF_4$/LiCl (**R45**) or $[Ir(COD)Cl]_2$ (**R46**). This is followed by addition of KPF_6 and allowed to stir with the reaction mixture in air affording **R45** and **R46** in 68% and 52% yield, respectively. [120]

3.1.1.4 Axial Ligand Substitution

Early efforts toward axial ligand substitution were attempted by Berry and coworkers on Cr_2-supported HEMACs. These efforts were met with poor yields, loss of M_B, and inconsistent yields across a period. These axial ligand substitution reactions required large excesses of the incoming ligand, which was hypothesized to cause loss of M_B.[128] Berry attempted to counter this problem through the use of labile axial ligands and stoichiometric amounts of incoming ligand. [128-129] While this was somewhat successful, yields remained inconsistent. Furthermore, in axial ligand substitution of $Cr \equiv Cr–Fe$ compounds, small amounts of $Cr \equiv Cr–Cr$ were detected as an impurity suggestive of metal-atom scrambling.[129] It was hypothesized that a strong three-center three-electron bond across the Mo_2-supported HEMACs would be more amenable to axial ligand substitution. Indeed, successful axial ligand substitution was achieved by Berry with a series of Mo_2Ni HEMACs. It is possible to utilize $M(OTf)_2$ salts instead of MCl_2 salts when introducing the heterometal to the M_2 core. The use of a more labile triflate ligand in the axial position has enabled Berry and coworkers to successfully substitute the axial triflates for -NCS and -NCSe ligands in a Mo_2Ni complex in good yield (Scheme 2.13).[134]

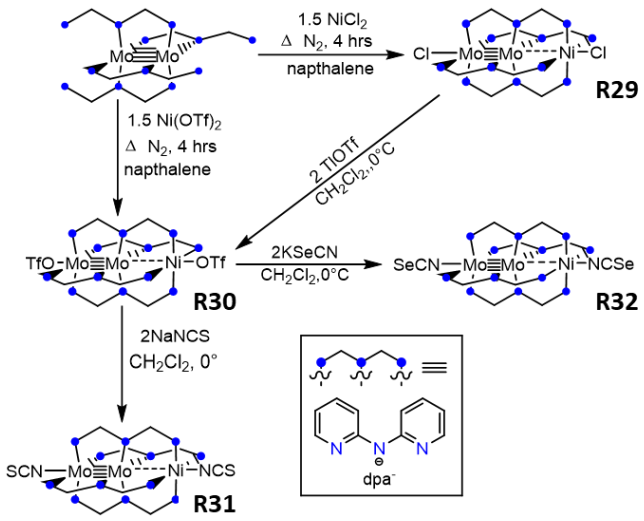

Scheme 2.13 Synthesis of $Mo_2Ni(dpa)_4Cl_2$ HEMAC followed by facile axial ligand substitution.[134]

Table 2.8. Symmetric $M_AM_BM_A$ HEMAC bond metrics and magnetic data. M_A represents the terminal metal, M_B represents the central metal, N_I represents the inner nitrogen, N_O represents the outer nitrogen atoms. All bond distances are reported in Å. The χT values are reported at room temperature in units of $cm^3\ K\ mol^{-1}$.

Compound	Code	χT	Cl – M_A	M_A – M_B	M_B – M_A	M_A – Cl	M_A – N_O	M_A – N_O	M_B – N_I	Ref
$MnNiMn(dpa)_4Cl_2$*	R1	7.08	2.359(1)	2.6296(9)	2.619(1)	2.3752(8)	2.252[2[	2.254[2]	1.898(4)	[117]
$MnPdMn(dpa)_4Cl_2$	R2	5.73	2.3538(8)	2.6347(4)	2.6425(4)	2.3752(8)	2.247[2]	2.262[2]	2.036(2)	[117]
$MnPtMn(dpa)_4Cl_2$	R3	3.69	2.365(1)	2.6289(7)	2.6358(6)	2.365(1)	2.249[4]	2.259[3]	2.035(3)	[117]
$FeNiFe(dpa)_4Cl_2$	R4	4.57	2.318(1)	2.575(1)	2.587(1)	2.322(1)	2.177[3]	2.74[3]	1.901[3]	[119]
$FePdFe(dpa)_4Cl_2$	R5	4.30	2.310(1)	2.582(1)	2.586(1)	2.329(1)	2.202[3]	2.216[3]	2.012[3]	[119]
$FePtFe(dpa)_4Cl_2$	R6	1.87	2.336(1)	2.571(1)	2.570(1)	2.315(1)	2.208[2]	2.198[2]	2.026[2]	[119]
$[FeNiFe(dpa)_4Cl_2][PF_6]$	R7	5.55	2.264(1)	2.534(1)	2.550(1)	2.277(1)	2.137[2]	2.144[2]	1.890[2]	[119]
$[FePtFe(dpa)_4Cl_2][PF_6]$	R8	3.70	2.268(1)	2.519(1)	2.549(1)	2.300(1)	2.162[3]	2.182[3]	2.010[3]	[119]
$[FeNiFe(dpa)_4Cl_2][PF_6]$	R9	6.20	2.201(3)	2.532(2)	2.518(2)	2.204(3)	2.13[1]	2.12[1]	1.87[2]	[119]
$CoPdCo(dpa)_4Cl_2$	R10	3.09	2.3256(6)	2.5156(4)	2.5156(4)	2.3474(8)	2.151[2]	2.159[2]	2.014[2]	[112]
$CuPdCu(dpa)_4Cl_2$	R11	0.50	2.4387(7)	2.4971(3)	2.5022(3)	2.4752(7)	2.091[1]	2.100[2]	2.010(2)	[111]
$CuPtCu(dpa)_4Cl_2$	R12	0.50	2.412(2)	2.5016(8)	2.5053(8)	2.451(2)	2.098[5]	2.111[5]	2.006(5)	[111]

* The $MnNiMn(dpa)_4Cl_2$ complex has not been reported in the CCSD. The M_A–N_O bond distance is reported from the paper as the average for all M_A–N_O and were not separated by outer metal.

Table 2.9 Asymmetric $M_AM_AM_B$ HEMAC bond metrics and magnetic data. M_A represents the majority metal, M_B represents the heterometal, N_I represents the inner nitrogen, N_O represents the outer nitrogen atoms. All bond distances are reported in Å. The χT values are reported at room temperature, with the corresponding spin value at this temperature in the adjacent column.

	Code	χT	Spin	M_A–Ax	M_A–M_A	M_A–M_B	M_B–Ax	M_A–No	M_A–N_I	M_B–No	Ref
$Cr_2Mn(dpa)_4Cl_2$	R13	3.90	5/2	2.7264(2)	2.04(1)	2.78(2)	2.259(2)	2.132[5]	2.03[2]	2.190[5]	[126]
$Cr_2Fe(dpa)_4Cl_2$	R14	3.90	5/2	2.673(2)	2.025(2)	2.715(2)	2.328(1)	2.196[2]	2.124[2]	2.204[3]	[127]
$Cr_2Co(dpa)_4Cl_2$ (100K)	R15A	3.00	$3/2^A$	2.370(1)	2.067(5)	2.491(1)	2.567(5)	2.102[3]	2.022[7]	2.125[3]	[124]
$Cr_2Co(dpa)_4Cl_2$ (12K)	R15B	N/A	$½^A$	2.5671(5)	2.036(5)	2.4965(7)	2.5671(5)	2.054[2]	2.013[2]	2.054[2]	[124]
$Cr_2Ni(dpa)_4Cl_2$	R16	1.49	1	2.580(2)	2.034(2)	2.582(2)	2.339(2)	2.101[3]	2.026[2]	2.105[3]	[121]
$Cr_2Mn(dpa)_4(OTf)_2$	R17	[A]	5/2	2.386(5)	1.955(4)	2.726(4)	1.972(6)	2.129[6]	2.134[7]	2.165[6]	[129]
$Cr_2Fe(dpa)_4(OTf)_2$	R18	2.86	2	2.369(3)	1.868(8)	2.728(6)	2.020(5)	2.114[5]	2.02[1]	2.136[5]	[128]
$Cr_2Fe(dpa)_4(N_3)_2$	R19	3.38	2	2.285(2)	2.102(3)	2.560(3)	2.016(3)	2.117[3]	2.034[5]	2.128[4]	[129]
$Cr_2Mn(dpa)_4(N_3)_2$	R20	[A]	5/2	2.348(8)	2.082(8)	2.706(8)	2.021(8)	2.12[1]	2.032[4]	2.16[1]	[129]
$Cr_2Co(dpa)_4(N_3)_2$	R21	1.37	$1/2^B$	2.175(2)	2.050(2)	2.534(1)	2.026(2)	2.060[2]	2.016[5]	2.026[2]	[128]
$[Cr_2Co(dpa)_4(MeCN)_2][PF_6]_2$	R22	0.32	$1/2^B$	2.249(2)	2.050(2)	2.4665(8)	2.026(2)	2.037[6]	2.016[5]	2.037[2]	[129]
$OTfCr_2Fe(dpa)_4Cl$	R23	2.39	2	2.345(2)	1.9641(7)	2.7317(7)	2.3966(9)	2.077[5]	2.029[5]	2.190[3]	[128]
$OTfCr_2Co(dpa)_4Cl$	R24	[A]	$3/2^B$	2.370(9)	1.939(3)	2.715(2)	2.359(2)	2.268[5]	2.044[3]	2.029[6]	[128]
$Mo_2Cr(dpa)_4Cl_2$	R25	2.86	2	2.7891(8)	2.098(4)	2.6885(6)	2.525(1)	2.217[2]	2.127[2]	2.127[2]	[132]
$Mo_2Mn(dpa)_4Cl_2$	R26	[A]	5/2	2.768(1)	2.094(2)	2.797(5)	2.327(2)	2.209[3]	2.135[4]	2.249[5]	[126]
$Mo_2Fe(dpa)_4Cl_2$	R27	[C]	2	2.706(1)	2.150(1)	2.648(2)	2.328(1)	2.196[2]	2.124[2]	2.204[3]	[127]
$Mo_2Co(dpa)_4Cl_2$	R28	3.00	3/2	2.720(1)	2.1027(5)	2.6170(7)	2.430(1)	2.215[2]	2.121[2]	2.102[2]	[124]

$Mo_2Ni(dpa)_4Cl_2$	R29	1.09	1	2.627(2)	2.107(2)	2.524(4)	2.394(3)	2.174[3]	2.115[3]	2.146[3]	[37]
$Mo_2Ni(dpa)_4(OTf)_2$	R30	1.02	1	2.364(4)	2.110(8)	2.485(8)	2.086(5)	2.157[5]	2.157[1]	2.114[2]	[134]
$Mo_2Ni(dpa)_4(NCS)_2$	R31	1.09	1	2.334(2)	2.1073(9)	2.548(1)	2.025(2)	2.2014[2]	2.107[4]	2.131[3]	[134]
$Mo_2Ni(dpa)_4(NCSe)_2$	R32	1.14	1	2.403(6)	2.0966(8)	2.546(1)	2.016(6)	2.211[4]	2.09[4]	2.121[4]	[134]
$Mo_2Ni(dpa)_4(NCS)_2$ (Peng)	R33	N.R	N.R	2.333(4)	2.104(5)	2.546(6)	2.105(3)	2.199[3]	2.128[3]	2.105[3]	[118]
$[Mo_2Ni(dpa)_4Cl_2]OTf$	R34	1.75	3/2	2.545(2)	2.129(3)	2.552(4)	2.394(3)	2.163[4]	2.080[4]	2.156[5]	[37]
$[Mo_2Ru(dpa)_4Cl_2]OTf$	R35	[A]	1/2	2.4637(5)	2.2130(3)	2.3010(2)	2.4586(5)	2.176[2]	2.088[2]	2.121[2]	[131]
$W_2Fe(dpa)_4Cl_2$	R36	[C]	2	2.684(1)	2.199(1)	2.718(1)	2.335(1)	2.185[2]	2.106[2]	2.191[9]	[127]
$W_2Cr(dpa)_4Cl_2$	R37	2.98	2	2.736(1)	2.1978(3)	2.6497(8)	2.529(1)	2.178[3]	2.099[3]	2.134[3]	[132]
$Mo_2Fe(npo)_4(NCS)_2$	R38	2.99	2	2.351(7)	2.122(8)	2.710(9)	2.066(8)	O 2.059[5][D] N 2.210[7]	2.151[9]	O: 2.078[7][D] N: 2.234[8]	[118]
$Mo_2Co(npo)_4(NCS)_2$	R39	2.70	3/2	2.33(1)	2.117(1)	2.67(1)	2.03(1)	O: 2.062[7][D] N: 2.202[8]	2.150[17]	O: 2.08[1][D] N: 2. 218[5]	[118]
$Mo_2Ni(npo)_4(NCS)_2$	R40	1.00	1	2.023(1)	2.067(8)	2.64(1)	2.27(1)	O: 2.077[6][D] N: 2.184[7]	2.143[9]	O: 2.068[9] [D] N: 2.181[7]	[118]
$Ru_2Ni(dpa)_4Cl_2$	R41	2.27	2	2.513(9)	2.341(4)	2.349(9)	2.46(1)	2.106[3]	2.012[8]	2.102[3]	[113]
$[Ru_2Ni(dpa)_4Cl_2]PF_6$	R42	3.32	5/2	2.496(6)	2.263(6)	2.513(9)	2.25(1)	2.109[9]	2.017[4]	2.135[4]	[113]

$Ru_2Cu(dpa)_4Cl_2$	R43	2.00	3/2	2.624(3)	2.246(3)	2.575(3)	2.296(3)	2.136[4]	2.046[3]	2.173[6]	[113]
$[Ru_2Cu(dpa)_4Cl_2]PF_6$	R44	2.31	2	2.53(1)	2.312(9)	2.51(1)	2.33(2)	2.09[1]	2.012[6]	2.115[6]	[113]
$[Ru_2Rh(dpa)_4Cl_2]PF_6$	R45	0.92	1	2.578(3)	2.267(2)	2.610(3)	2.222(3)	2.12[2]	2.018[8]	2.16[2]	[120]
$[Ru_2Ir(dpa)_4Cl_2]PF_6$	R46	1.07	1	2.6757(7)	2.241(3)	2.512(3)	2.6757(7)	2.082[2]	2.070[5]	2.082[2]	[120]
$[Cu_2Pd(npa)_4Cl]PF_6$	R47	0.50	1/2	2.388(7)	2.489(4)	2.426(3)	N/A	2.03[2]	1.99[2]	2.03[2]	[114]
$[Cu_2Pt(npa)_4Cl]PF_6$	R48	0.50	1/2	2.404(5)	2.486(3)	2.436(2)	N/A	2.089(7)	2.007(6)	2.023[2]	[114]

[A] EPR spectroscopy was used for these compounds. These spectra were taken as frozen solution samples.
[B] And EPR spectrum for each compound was collected and compared against a known HEMAC to confirm spin values.
[C] Mössbauer spectroscopy confirmed the presence of a high spin Fe^{II} species.
[D] The npo ligand is bound in a 2 2 trans orientation on the metal chain, the M–O and M–N distances have been listed separately.

Table 2.10 Asymmetric $M_AM_BM_C$ HEMAC bond metrics and magnetic data. M_A represents the majority metal, M_B represents the heterometal, N_I represents the inner nitrogen, N_O represents the outer nitrogen atoms. All bond distances are reported in Å. The χT values are reported at room temperature, with the corresponding spin value at this temperature in the adjacent column.

Compound	Code	χT	Spin	$M_A - Ax$	$M_A - M_A$	$M_A - M_B$	$M_B - Ax$	$M_A - N_O$	$M_A - N_I$	$M_B - N_O$	Ref
$MoWCr(dpa)_4Cl_2$	R49	2.86	2	2.7792(8)	2.1548(4)	2.6742(5)	2.5228(8)	2.218[2]	2.106[2]	2.128[2]	[125]
$NiCoRh(dpa)_4Cl_2$	R50	0.20	1/2	2.6902(9)	2.3533(5)	2.3485(5)	2.6152(9)	2.014[3]	1.924[3]	2.002[3]	[116]
$[NiCoRh(dpa)_4Cl]^+$	R51	0.23	1/2	2.424(1)	2.3527(7)	2.3455(7)	2.428(1)	2.058[4]	1.916[4]	2.058[4]	[116]

3.1.1.5 Structural Trends in Heterotrimetallic Chains

Spin state assignments for specific metals within HEMACs generally can be made by analysis of the M–N distances. The Co-containing complexes **R10**, **R15**, and **R28** help to illustrate this point. With Co–N distances of 2.16 Å and 2.10 Å, respectively, compounds **R10** and **R28** can clearly be described as containing high-spin Co^{2+} ions.[112, 124] For the former symmetric compound, antiferromagnetic coupling of the outer two Co^{2+} ions yields a significant decrease in $\chi \cdot T$ toward 0 emu K mol^{-1} at low temperature. The assignment of the spin state in the asymmetric **R28** is more straightforwardly supported by SQUID magnetometry with $\chi \cdot T$ = 3.00 emu K mol^{-1} at room temperature consistent with an S = 3/2 spin center with significant orbital contribution to the susceptibility.[124] Compound **R15** is structurally more complex, and displays magnetic properties consistent with an S = 1/2 → S = 3/2 spin crossover. Consistent with this assignment, the crystal structure of **R15** at 100 K shows Co–N bond distances at 2.05 Å, ~ 0.05-0.10 Å shorter than in **R10** or **R28**, as expected for a low-spin Co^{2+} ion. The room temperature crystal structure of **R15** was also recorded, having Co–N distances of 2.13 Å. Compound **R15** and **R28** provide an enlightening comparison. The former compound, having a Cr≡Cr···Co chain, can achieve a low-spin Co^{2+} ground state below ~100 K while the latter compound with a Mo≡Mo···Co chain remains high-spin at all temperatures. This puzzling result led Berry and coworkers to propose that the Cr≡Cr "ligand" provides a stronger ligand–field than the Mo≡Mo "ligand". However, further analysis of the crystal structures provides a differeny and more satisfactory explanation. In **R15**, the Cr–N bond distances are uniformly shorter than the Mo – N distances in **R28** by 0.11 – 0.17 Å. The lengthening of the M_A–N bond distances as M_A is changed from Cr to Mo most clearly impact how short the Co–N bond distances can be. Thus, it is most likely these longer Mo–N distances that cause the pyridine groups in the $Mo_2(dpa)_4$ ligand to enforce a weaker ligand field to Co^{2+}.

Aside from the commonly used dpa ligand, Peng and coworkers have introduced two other ligands shown in Figure 2.15. The impact that the choice of ligands has on the torsion angle in each chain is illustrated in Figure 2.16. With dpa, the torsion angle ranges from 20.89° to 25.35°. However, with npa this angle decreases to approximately 21°.[114] When the equatorial paddlewheel ligand is changed to the fused ring npo, the ligand becomes planar with respect to the metal backbone. The planarity of the npo ligand as

opposed to the helical dpa ligand is hypothesized to support current values in single-molecule measurements in the npo-supported **R38**-**R40**.[118]

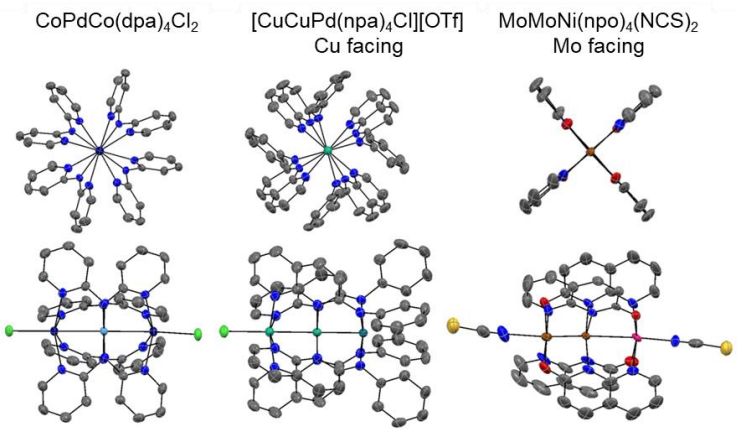

Figure 2.16. End-on (top) and side facing (bottom) views of HEMACs supported by (L to R): dpa, npa, and npo ligands (represented by **R1**, **R47**, **R33**, respectively).[112, 114, 118] All H atoms, molecules of solvation, and counter anions have been omitted for clarity. In any case of disorder, the dominant orientation is shown. In all end-on views, the axial ligands have also been omitted.

The compounds synthesized in the Berry lab (**R13-32**, **34-37**,**49**) all contain a quadruply bonded bimetallic core of Group VI metals. These quadruple bond core distances are within the expected range.[168-177] For Cr_2 this distance spans a range of nearly 0.4 Å from 1.78 to 2.15 Å.[170, 173, 178] An Mo_2 bond is typically between 2.07 Å and 2.16 Å while the W_2 quadruple bond is slightly longer and is between 2.18 Å and 2.28 Å in length.[1, 179-180] Comparing the M_A–M_B distances, all fall within a similar range from 2.6170(7) Å for M_B = Co to 2.797(5) Å for M_B = Mn.[37, 123-124, 126-127, 132]. The exception being the M = Ni series all of which present remarkably short Mo–Ni and Cr–Ni bond distances of 2.524(4) Å and 2.582(2) Å, respectively.[37, 121]

2.3.1.2 Heterotrimetallic Triangles

Betley and coworkers have reported the synthesis and characterization of two Co/Fe (**R52**, **R53**) and two Mn/Fe (**R54**, **R55**) triangular clusters.[135-136] The Co/Fe compounds were supported by the $MeC(CH_2NHPh\text{-}o\text{-}NH_2)_3$ ligand (C_1) while the Mn/Fe species were supported by the $[1,3,5\text{–}C_6H_9(NPh\text{-}o\text{-}NSi^tBuMe_2)_3]^{6-}$ ligand (C_2). The ligands are presented in Figure 2.17 while an example of each triangle is shown in Figure 2.18. These ligands have also been used to support homotrinuclear clusters.[181-182] The

ligand scaffold is hexadentate and enforces a coordination environment conducive to the formation of trinuclear or hexanuclear clusters. The synthesis of these triangles is accomplished through both metal atom substitution as well as the metalloligand approach. When synthesizing triangles supported by the C_1 ligand, Betley and coworkers utilize a thawing THF solution containing a $[(C_1)Fe_3(\mu\text{–}Cl)]_2$ hexamer to which solid $CoCl_2$ is added. By varying the number of equivalents of $CoCl_2$ added, either a Co_2Fe or a Fe_2Co triangle can is obtained (Scheme 2.14A). When using the C_2 ligand however, a bimetallic C_2 containing Mn or Fe as well as C_2 is used and the third metal is added in a separate synthetic step (Scheme 2.14B). Table 2.11 presents the bond metrics for these four triangles.

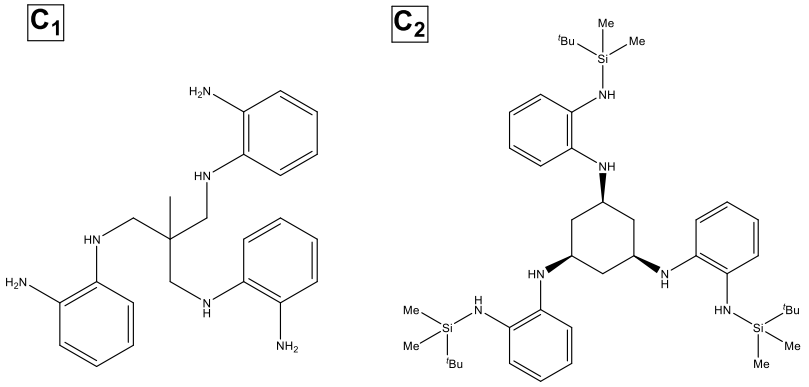

Figure 2.17. Ligands used to support trimetallic triangular compounds[135-136].

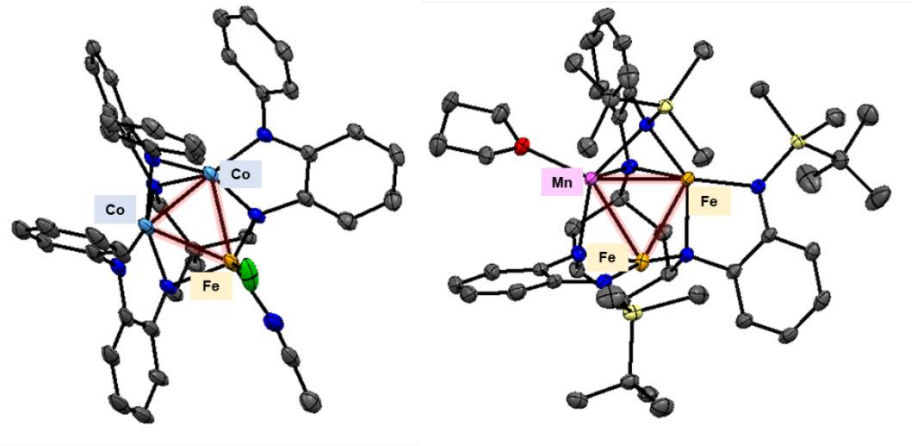

Figure 2.18 Triangle compounds **R53** (left) and **R54** (right), synthesized by the Betley lab. The metal triangle motif has been emphasized in red.

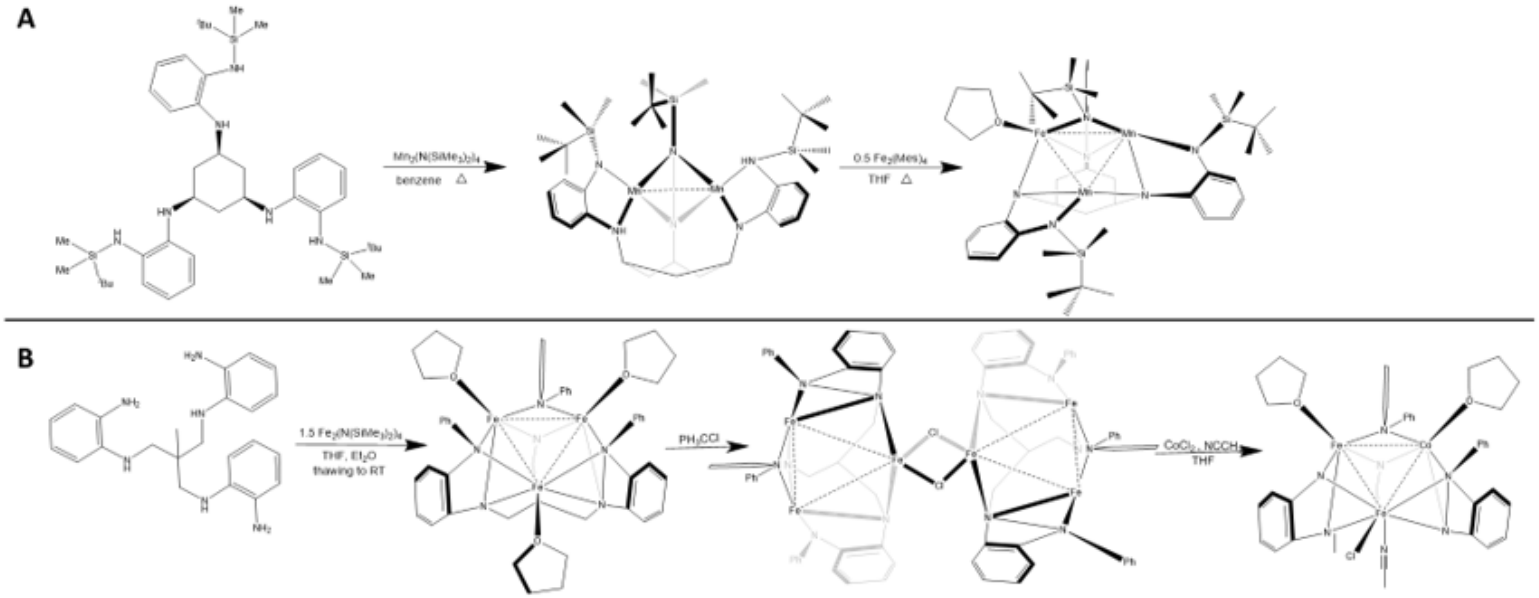

Scheme 2.14 Synthetic procedure used to make heterotrimetallic triangles in the Betley lab.[135-136]

Table 2.11 Bond metrics for heterometallic triangle compounds synthesized in the Betley lab.

Compound	Code	M1 – M2	M2 – M3	M1 – M3	Ref
$Fe_2Co(\mathbf{C_1})$	**R52**	2.5391(7)	2.5493(8)	2.2934(8)	[136]
$Co_2Fe(\mathbf{C_1})$	**R53**	2.5253(6)	2.5348(6)	2.2971(5)	[136]
$Fe_2Mn(\mathbf{C_2})(THF)$	**R54**	2.7247(5)	2.8687(5)	2.7485(5)	[135]
$Mn_{(3-x)}Fe_x(\mathbf{C_2})$	**R55**	2.7681(6)	3.0176(6)	2.8030(6)	[135]

Structurally, these compounds pose a challenge to crystallographic methods in that the metal ions differ by only one electron in each pairing. Thus, the metal atom identity cannot be determined unambiguously by X-ray crystallography alone. In the **R52** and **R53** pairing, paramagnetic ^{1}H NMR spectra of both compounds were unique, suggesting different metal compositions. Structurally, **R52** and **R53** display an isosceles triangle with one short M–M distance and two longer ones. The structure is interpreted as containing a bonded $[M_2]^{5+}$ unit and an isolated M^{2+} ion. Compound **R52** was crystallographically refined using equal populations of Co and Fe in the $[M_2]^{5+}$ site while two Co atoms were refined in the $[M_2]^{5+}$ site in **R53**.[136] These assignments were supported by comparing their Mössbauer spectra to that of the Fe_3 analog. In the homometallic species, there are three quadrupole doublets of equal intensity with one having a higher intensity than the other two. In **R52**, again three doublets are seen with similar isomer shifts to the Fe_3 species, but with a ratio of 1.3:1 between the two lower isomer shift species and the higher one. In **R53**, only the higher isomer shift signal is present, consistent with the placement of the two Co atoms in the $[M_2]^{5+}$positions. For the Mn/Fe pairings of **R54** and **R55**, Betley and coworkers utilized Mössbauer spectroscopy, EPR spectroscopy, X-ray fluorescence spectroscopy, and anomalous X-ray scattering to make assignments. Compound **R54** produces a Mössbauer spectra with two distinct signals, indicative of two irons in chemically different environments. X-ray fluorescence spectroscopy further suggested an Fe:Mn ratio of 2:1. Compound **R55** is less straightforward, although and EPR spectrum confirmed the existence of a $[Mn_2]$ unit, it was unclear if this sample also contained an impurity of different metallic composition. A Mössbauer spectrum also suggested the presence of two chemically distinct Fe species. However, a single iron sample could produce two signals if the Fe is disordered over two distinct geometric positions. X-ray diffraction experiments near the absorption edges of Mn or Fe allowed anomalous scattering to be used to determine that there is one Mn site and Fe site and one mixed site present in **R54**.[136]

2.3.2 Electronic Structure of Heterotrimetallic Compounds

2.3.2.1 Electronic Structure of Symmetric and Asymmetric Heterotrimetallic Chains

2.3.2.1.1 Electronic Structure of Symmetric Heterotrimetallic Chains

The electronic structure of symmetric HEMACs can be best described as consisting of two high spin M(II) centers bridged by a d^8 diamagnetic metal center; either Ni^{2+}, Pd^{2+}, or Pt^{2+}. A molecular orbital diagram for **R10** is presented in Figure 2.19. Orbitals of σ symmetry have been emphasized and drawn out. The π and δ symmetry orbitals are localized, signifying no multiple bonding is present. Furthermore, in order to accommodate two high spin Co^{2+} centers (S = 3/2), electrons are forced to occupy $d_{x^2-y^2}$ orbitals that are mainly M-L antibonding. These two Co centers are coupled antiferromagnetically to give an overall S = 0 state, however, shoes the S = 3 state that represents the highest state in the spin ladder.

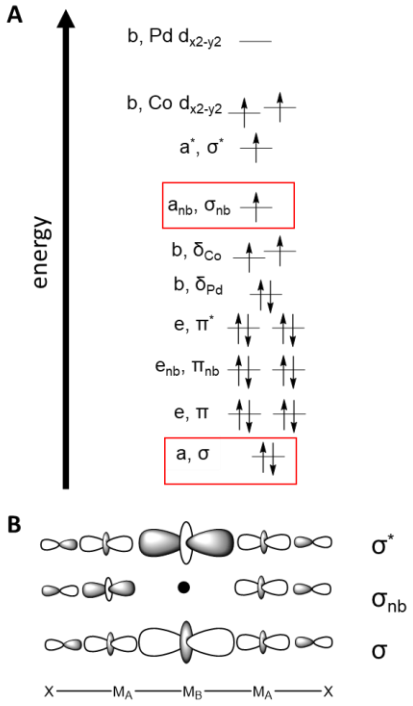

Figure 2.19. (A) Qualitative MO diagram for **R10** and (B) the σ symmetry orbitals that contribute to the 3c/3e- bond in the compound.[112]

2.3.2.1.2 Electronic Structure of Asymmetric Heterotrimetallic Compounds

Compounds that contain a multiply bonded Cr_2 unit have consistently challenged computational methods. Asymmetric $Cr_2M(dpa)_4X_2$ compounds are therefore similarly problematic from a computational standpoint. McGrady and coworkers initially reported a method to approximate the geometries of Cr_2M species using a broken-symmetry density functional theory (BS-DFT) approach. Their approach was to optimize the geometries based on a βαα spin-coupling scheme rather than the more physically meaningful

αβα scheme. The βαα avoids the bias toward Cr–Cr dissociation that is seen in the αβα models but does not capture the double exchange-like σ dissociation via the Cr_2M σ_{nb} orbital. Nevertheless, despite being higher in energy than the αβα configuration, the agreement in Cr–Cr as well as Cr–M lengths is remarkable.[183] In order to capture the multiconfigurational nature of $Cr_2M(dpa)_4X_2$ complexes, CASSCF and CASPT2 approaches have been employed by López and coworkers to correlate trends in effective bond order (EBO) in the series of Cr_2M HEMACs as well as the homometallic $Cr_3(dpa)_4Cl_2$.[184] The CASSCF results were analyzed according to the EBO formalism with $EBO = \frac{\eta_b - \eta_a}{2}$ where η are the occupation numbers of the bonding and antibonding combinations of the orbitals. The CASSCF wavefunctions for Cr_2M compounds show a set of bonding and antibonding orbitals localized on the Cr_2 unit that were used to calculate EBO values. These values may be compared to the EBO of 2.14 for the isolated $Cr_2(dpa)_4$ molecule to assess how the M atom affects the Cr≡Cr bond.

Based on the Cr≡Cr bond distances, 1.94 Å for $Cr_2(dpa)_4$[185] and 2.02 – 2.07 Å for the $Cr_2M(dpa)_4Cl_2$ molecules,[127] we expect to see a moderate impact of M on the Cr≡Cr bonding. Indeed, the Cr≡Cr bonding. Indeed, the Cr≡Cr EBO values are reduced to 1.67, 1.71, 1.66, for $Cr_2M(dpa)_4Cl_2$ with M_A = Mn, Fe, and Ni, respectively.[121, 123, 126] Moreover, the change in EBO may be further analyzed taking into account the individual σ, π, and δ component of the Cr≡Cr bond. Surprisingly, the major loss in EBO appears to stem from loss of Cr–Cr π bonding where the π contribution to EBO is 1.20 in $Cr_2(dpa)_4$ but only 0.92 in $Cr_2Mn(dpa)_4Cl_2$ with the other heterometallic compounds behaving similarly.[184] This result is surprising in view of the BS-DFT results that indicated clearly a σ-bonding pathway for electron delocalization throughout the Cr_2M chains. The CASSCF results indicate essentially no Cr–M bonding interactions.[184] Figure 2.20 demonstrates these differences quite clearly, showing in (A) the BS-DFT σ_{nb} orbital for $Cr_2Mn(dpa)_4Cl_2$, as well as the three σ-symmetry orbitals for $Cr_2Fe(dpa)_4Cl_2$ derived from CASSCF (14,13) calculations. The DFT σ_{nb} orbital displays clear delocalization across the three metal atoms, and its occupation by a single electron with two electrons occupying the σ bonding combination have been described as a 3c/3e$^-$ σ bond.[183] The CASSCF orbitals are localized either on the Cr_2 unit or on the appended Fe atom, and López and coworkers consequently describe no bonding between Cr and Fe in this system.[184] Currently, these contrary results have not been reconciled.

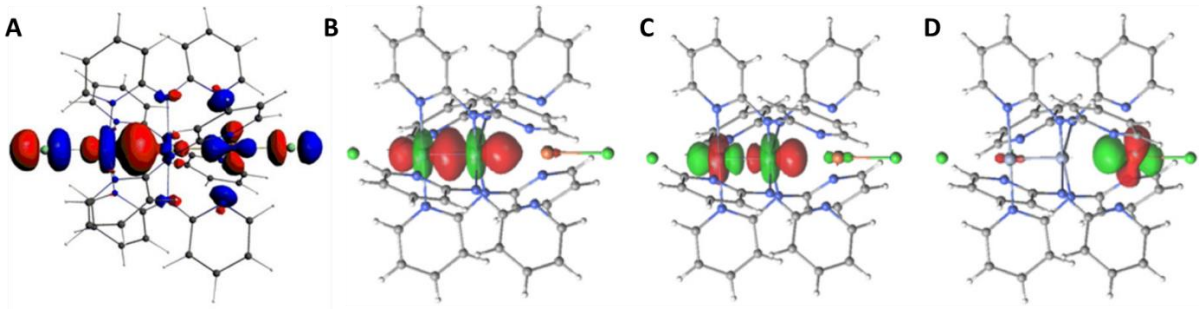

Figure 2.20 The σ_{nb} orbital of **R13** derived from DFT calculations (A), The three orbitals of σ symmetry for **R14** derived from CASSCF calculations (B-D).[183-184] (A) Reprinted from Arcisauskaite, V.; Spivak, M.; McGrady, J. E., Structure and bonding in trimetallic arrays containing a Cr–Cr quadruple bond: A challenge to density functional theory. *Inorg. Chim. Acta* **2015,** *424*, 293-299 with permission from Elsevier.(B-D; Reprinted (adapted) with permission from Spivak, M.; López, X.; de Graaf, C., Trends in the Bond Multiplicity of Cr_2, Cr_3 and Cr_2M (M = Zn, Ni, Fe, Mn) Complexes Extracted from Multiconfigurational Wave Functions. *J. Phys. Chem. A* **2019**. Copyright 2019 American Chemical Society.

In contrast to the Cr_2M compounds, whose multireference nature complicates computational assessment of bonding, treatment of Mo_2M complexes at the DFT level is straightforward. Calculations have been reported for $Mo_2M(dpa)_4Cl_2$ compounds with M = Cr,[132] Fe,[127] Ni,[37] and Ru,[130] for cationinc $Mo_2M(dpa)_4Cl_2$ complexes with M = Ni,[37] and Ru,[131] as well as for compounds with different axial ligands, $Mo_2Ni(dpa)_4X_2$ with X = OTf, NCS, and NCSe.[134] For the compounds containing first-row transition metals, the general feature is a 3c/3e$^-$ σ-bonding interaction that spans all three metal centers.[37, 127, 132] The Mo_2Ru and W_2Ru compounds have 3c/3e$^-$ σ-bonding, interactions, but also 3c/4e$^-$ π bonding interactions in addition.[130] One-electron oxidation of $Mo_2Ru(dpa)_4Cl_2$ adds an additional 3c/3e$^-$ δ bonding interaction.[130-131]

Compared to symmetric HEMACs, the asymmetric HEMACs synthesized present a similar electronic structure to that described above. However, those formed with a Group 6 metal core contain a quadruple bond that contains σ, π, and δ bonding. Figure 2.21 illustrates the construction of an MO diagram for the asymmetric **R29**. As with the MO diagram for **R10**, the σ symmetry orbitals have been emphasized. These orbitals can be considered a 3c/3e- when the σ bonding orbital is doubly occupied and the σ non-bonding orbital is singly occupied.

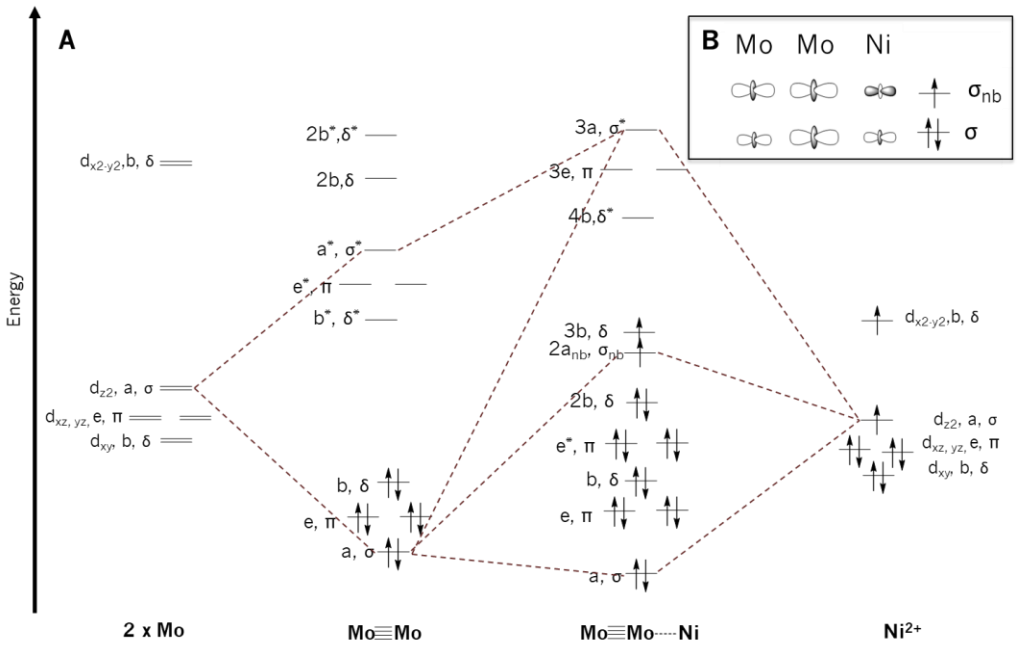

Figure 2.21 Construction of a molecular orbital diagram for **R29**. Orbitals contributing to the 3c/3e bond.

2.3.2.1.3 Computational Predictions for Heterotrimetallic Compounds

The 3c/3e- bond in heterometallic chains is similar to that proposed in the homometallic $Co_3(dpa)_4Cl_2$ and $Cr_3(dpa)_4Cl_2$ by Bénard et al.[138-139, 148, 153, 186] The composition of the σ symmetry orbitals depends strongly on the metal identities as shown in Figure 2.22. Moving across the first-row transition metals in the $Mo_2M(dpa)_4Cl_2$ series, there is a noticeable decrease in contribution from the outermost Mo and M_B species, while the Cl atom bound to the heterometal increases significantly in contribution. The orbital contributions for the occupied α spin σ_{nb} orbitals remain relatively constant. However, in the unoccupied β spin σ_{nb} orbital, the overall character is dominated by the heterometal (in excess of 50%). There is also a slight decrease in terminal Mo character and a slight increase in inner Mo character. Given that the compounds presented here contain two different metals, the polarization of these compounds is logical, which is manifested in metal orbital contribution. The consequence of this polarization is the lowering in energy of the σ and σ_{nb} orbitals allowing us to further consider the $M_2(dpa)_4$ core as a ligand with respect to the heterometal. The σ orbitals decrease in energy by 0.32 eV for the α component and by 0.49 eV for the β. The σ_{nb} energy decreases in value by a larger magnitude, 1.22 eV for the α component and 1.61 eV for the β.

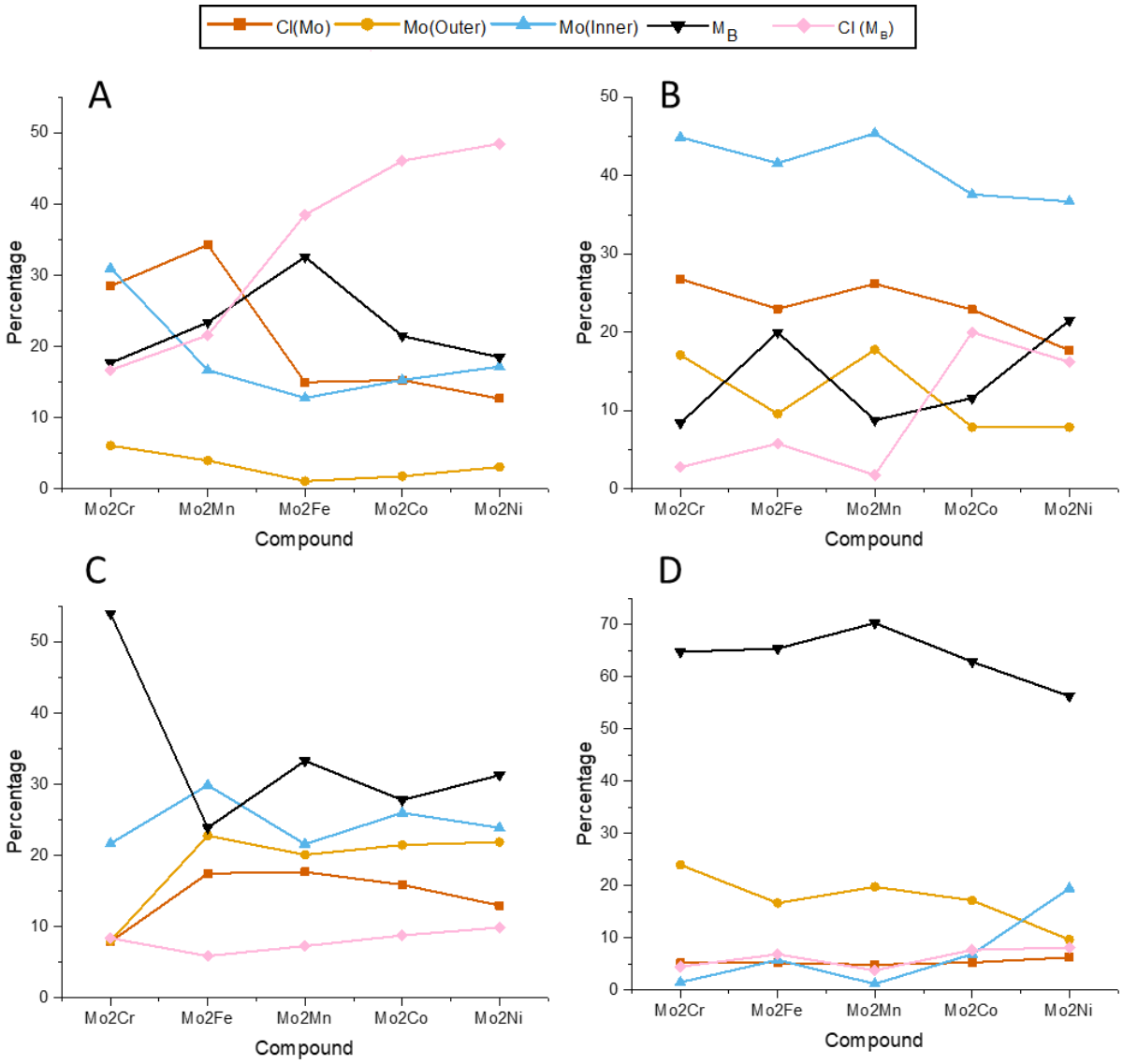

Figure 2.22 Contributions of the Mo_{Outer}, Mo_{inner}, heterometal, and terminal Cl atoms for a series of $Mo_2M_B(dpa)_4Cl_2$ HEMACs in the three center three electron bond; (A) σ α, (B) σ β, (C) σ_{nb} α, (D) σ_{nb} β.

3.2.2 Electronic Structure of Heterotrimetallic Triangle Compounds

Turning to the triangular species (**R52**-**R55**) from Betley and coworkers, despite having a different geometry, the predominant pathway of metal-metal bonding remains via σ interactions.[135-136] Specifically, analyses have been performed on the homometallic C_1Fe_3 cation, which helps provide insight into the electronic structures of **R52** and **R53**.[182] The homometallic species presents as a $[M_2]^{5+}$ core that is antiferromagnetically coupled to the third isolated metal In the case of the oxidized $\mathbf{C_1}Fe_3^{+}$, the $[Fe_2]^{5+}$ core

contains 11 valence electrons, which fill to give an S = 3/2 species. The third metal is treated as an independent high spin Fe^{2+} site. The $[M_2]^{5+}$ cores for **R52** and **R53** are $[FeCo]^{5+}$ and $[Co_2]^{5+}$ with 12 and 13 valence electrons, respectively. This gives an S = 1 ground state for **R52** and an S = 3/2 ground state for **R53**.[136] For all three of these species however, the HOMO and LUMO are both are of σ symmetry within the $[M_2]^{5+}$ core and are shown in Figure 2.23 This orbital treatment was not conducted on **R54** or **R55** but should be similar and the ground spin states were not determined.[135]

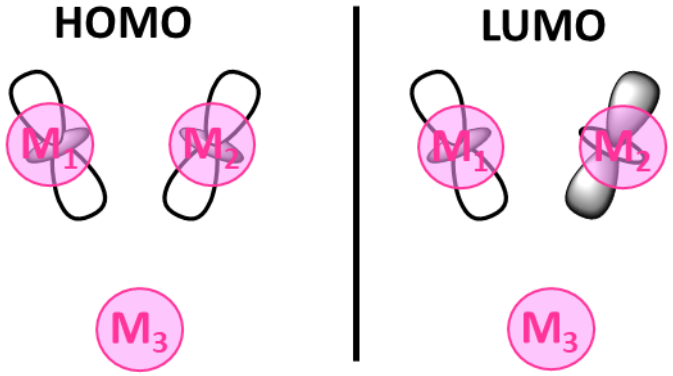

Figure 2.23 HOMO and LUMO for the highly coupled bimetallic $[M_AM_B]^{5+}$ "core" of the triangle compound.[136]

3.3 Magnetic Properties of Heterotrimetallic Compounds

While some heterotrimetallic compounds illustrate one isolated magnetic center, others present weak to moderate antiferromagnetic coupling. Uniquely **R18** illustrates ferromagnetic coupling. In both types of coupling d_{z^2}orbital overlap determines both the type of coupling, and the strength of the coupling constant, J.

3.3.1 Isolated Magnetic Centers

For asymmetric chains containing a quadruply bonded $M_A{\equiv}M_A$ unit, the magnetic properties depend solely on the M_B identity. With the exception of **R15** and **R21**, all $M_A{\equiv}M_A{\cdots}M_B$ HEMACs present magnetic behavior consistent with an isolated high spin M(II) center. For **R15** and **R21**, which both contain a Cr_2 core and a Co heterometal, spin crossover behavior is observed. At low temperatures the χT value for

R15 is 0.50 cm^3 K mol^{-1}, which remains constant as a plateau until 125 K where it rises to 2.5 emu^3 K mol^{-1} at room temperature. This is indicative of spin crossover equilibrium involving Co^{2+} transitioning from LS S = ½ at low temperature to S = 3/2 at higher temperatures. The magnetic data were modeled with T_C at 210 K, ΔH - 5.7 kJ/mol, ΔS = 27 J K^{-1} mol^{-1} as the parameters for spin equilibrium. As discussed in section 3.2.3, this is also illustrated in the structural metrics for **R15**. For **R21** only a room temperature value of χT was recorded via the Evans NMR method, 1.37 emu K mol^{-1}. This value is between what is expected for S = ½ and S = 3/2 and therefore it was suggested that this compound also undergoes spin crossover which was supported by variable temperature crystallographic data. Interestingly, **R22** has χT = 0.32 emu K mol^{-1} at room temperature indicating a low-spin configuration for the Co^{2+} ion. As **R15**, **R21**, and **R22** have axial Cl^-, N_3^-, and CH_3CN ligands, respectively, the spin-state of the Co^{2+} ion can be tuned by the π-donor/acceptor properties of the axial ligands in this Cr_2Co system.

The facile synthesis of these chains allows for systematic comparisons amongst a series. Our lab has synthesized **R25** and **R37** and compared them to the homometallic $Cr_3(dpa)_4Cl_2$ to better understand the effect of the heavier $Mo_2(dpa)_4$ and $W_2(dpa)_4$ "ligands" on the Cr^{2+} ion.[132-133] All three species display similar magnetic behavior as a function of their similar electronic structures. The isolated high spin S = 2 Cr^{2+} ion presented slow magnetic relaxation as a result of axial magnetic anisotropy. This was quantified using magnetic susceptibility measurements and further supported with high field EPR data. Variable temperature magnetic susceptibility measurements on both the heterometallic species and the homometallic analog presented increasing zero field splitting (ZFS) moving down the Group VI bimetallic cores. The magnitude of the ZFS parameter for **R37**, 3.617 remains the largest reported for a high spin Cr^{2+} species (with the exception of chromocene, which has a fundamentally different electronic structure.)[133]

3.3.2 Spin Coupled Magnetic Centers

For the symmetric M_A–M_B–M_A species, the magnetic properties are similar to one another, only differentiated by the strength of the coupling constant between the two metal termini. The central M_B of either Ni^{II}, Pd^{II}, or Pt^{II} is in a d^8 configuration in a square planar environment, thus rendering the central metal diamagnetic. This leaves the only the two terminal metals to couple with one another. The 300 K χT

values are all slightly less than would be expected for two isolated centers, indicating that the two terminal metals are indeed coupled and in an antiferromagnetic fashion. Table 2.12 summarizes the parameters derived from modeling this magnetic susceptibility data for each symmetric chain. All of the symmetric species are diamagnetic in the ground state, which is illustrated by a tendency toward $\chi T = 0$ emu K/mol in their magnetic susceptibility plots at low temperatures.

Table 2.12. Magnetic properties of the symmetric HEMACs made by Peng and coworkers. M_A spin denotes the terminal metal atoms. g values were determined via EPR spectroscopy or SQUID magnetometry. SQUID magnetometry data were taken at 300 K and are reported in $cm^3\ K^{-1}\ mol^{-1}$

Code	χT	M_A spin	J (cm^{-1})	g values	Ref
R1	7.08	5/2	- 6.85	1.94	[117]
R2	5.73	5/2	- 14.9	1.91	[117]
R3	3.69	5/2	- 33.1	1.91	[117]
R4	4.57	2	- 11.8	2.11	[119]
R5	4.30	2	- 23.5	2.24	[119]
[R5]+	N/R	Fe^{II} = 2 Fe^{III} = 5/2	- 29.1	2.00* Fe^{II},2.05 Fe^{III} EPR: g_x =1.84, g_y = 1.47, g_z = 1.40	[119]
[R5]2+	N/R	5/2	- 29.1	2.00*	[119]
R6	1.87	2	- 39.7	2.00*	[119]
[R6]2+	N/R	5/2	- 49.9	2.00*	[119]
R7	5.55	Fe^{II} = 2 Fe^{III} = 5/2	- 13.6	2.01 Fe^{II},2.11 Fe^{III} EPR: g_x =1.91, g_y = 1.35, g_z = 1.34	[119]
R8	3.70	Fe^{II} = 2 Fe^{III} = 5/2	- 48.5	2.10 Fe^{II},2.12 Fe^{III} EPR: g_x =1.66, g_y = 1.50, g_z = 1.49	[119]
R9	6.20	5/2	- 11.4	2.04	[119]
R10	3.09	3/2	- 46. 24	2.20	[112]
R11	0.50	1/2	- 3.73	2.02 EPR: $g_{\parallel}$ = 2.25, $g_{\perp}$ = 2.10	[111]
R12	0.50	1/2	- 0.39	2.00 EPR: $g_{\parallel}$ = 2.28, $g_{\perp}$ = 2.07	[111]

* these g values were fixed at 2.00

While the majority of these symmetric chains show moderate antiferromagnetic coupling, **R11** and **R12** are modeled as having near negligible coupling constants. In considering the trio of $MnMMn(dpa)_4Cl_2$ compounds (M = Ni, Pd, or Pt; compounds **R1**-**R3**), Peng and coworkers noted a decrease in coupling constant value moving from **R1** to **R3**. This result led to a more thorough theoretical consideration of two possible coupling mechanisms. The first is through a σ pathway of overlapping d_{z^2} orbitals while the second stems from superexchange via the bridging dpa ligands. In contrast to the Mn^{2+} compounds, Cu^{2+} compounds **R11** and **R12** show a decrease in *J* moving from **R11** to **R12**.In this case, unpaired electrons are present in orbitals of δ symmetry only, meaning that only ligand mediated superexchange is possible. This type of coupling is inherently weaker than direct exchange due to a longer orbital pathway.[111] In **R1**-**R3** unpaired electrons are present in both σ and δ symmetry orbitals allowing both direct exchange through Md_{z^2} orbitals and superexchange.[117] These observations are in agreement with a prior theoretical investigation from Bénard and coworkers on the hypothetical $NiPdNi(dpa)_4Cl_2$ molecule compared against the known $Ni_3(dpa)_4Cl_2$ EMAC. This analysis predicted a larger antiferromagnetic coupling constant for $NiPdNi(dpa)_4Cl_2$ on the basis of increased d_{z^2} overlap between Ni and Pd in comparison to d_{z^2} overlap between Ni atoms only in $Ni_3(dpa)_4Cl_2$. The Pd orbitals are more diffuse than Ni orbitals and allow for greater communication between the two termini.

Asymmetric HEMACS that contain a paramagnetic M_AM_A core (**R41**-**R48**) engage in spin coupling with M_B ions. Notably, the pair of **R47** and **R48** are best modeled as having remarkably strong antiferromagnetic coupling (*J* = - 498.90 cm^{-1} and - 501.24 cm^{-1}, respectively) between adjacent Cu^{2+} ions. In the χT plots, the χT at room temperature is reported as 0.5 emu K mol^{-1}. Given the only magnetic centers are two adjacent M_A Cu^{II} centers, this value is lower than would be expected for two isolated Cu^{II} centers (0.75 emu K mol^{-1}). Thus, remarkably strong antiferromagnetic coupling is present. This was further supported computationally with predicted *J* values for **R47** and **R48** of -572.51 cm^{-1} and -556.75 cm^{-1}. The theoretical results also support the proposed mechanism, which involves superexchange via the bridging npa ligand. This behavior is similar to that of the $Cu_3(dpa)_4Cl_2$, that reports a lower bond on the value of J as > 500 cm^{-1}. [187] This was later supported computationally.[188] Neither species is diamagnetic despite the large J values. This is attributed to the helicity of the bridging dpa ligand. [187]

Recently, Berry and coworkers reported the first ferromagnetic HEMAC in the form of **R18**, the one electron oxidized analog of **R17**. Both the neutral and one-electron oxidized compounds were examined via variable temperature SQUID magnetometry.[37] The neutral species presented χT data consistent with an isolated $S = 1$ Ni^{2+} center. However, upon oxidation, the χT value rose to 1.75 emu cm^3 K mol^{-1} indicative of an $S = 3/2$ species. This suggested that oxidation of the $[Mo_2]^{4+}$ core, which was expected based on electrochemical data of **R17**, gave rise to two magnetic centers (the Mo_2^{5+} and Ni^{2+} sites) that are coupled ferromagnetically, with J of at least 150 cm^{-1}. This result was initially surprising as two of the unpaired electrons were found to be located on a Mo_2 d_{xy} orbital and a Ni $d_{x^2-y^2}$ orbital, which should be of appropriate orientation (and energy) to overlap. The observed ferromagnetic interaction was then justified by considering the third unpaired electron, which is housed in a σ_{nb} orbital, which is rigorously orthogonal to both the Mo_2 and Ni δ symmetry orbitals as shown in Figure 2.24. DFT calculations supported stabilization of this $S = 3/2$ ground state by 340 cm^{-1} against the lowest energy $S = 1/2$ system, an energy difference corresponding to 3J, in good agreement with the experimentally determined lower bound of 150 cm^{-1}.

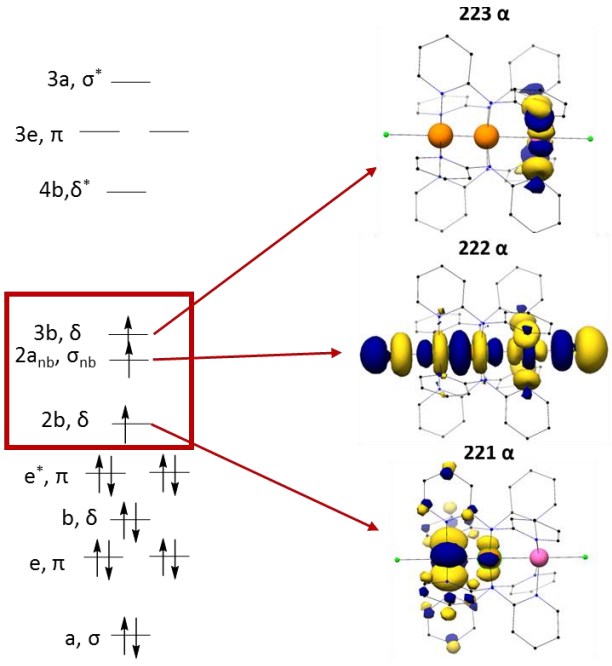

Figure 2.24 MO diagram for **R18** with emphasis placed on the SOMOs.

Two of the four heterometallic triangles synthesized in the Betley lab have been examined via a combination of EPR and SQUID magnetometry in order to understand the magnetic intricacies within each structure. SQUID magnetometry data were reported for **R52** and **R53**. For compound **R52**, the χT value reaches as a maximum of 5.78 cm^3 K mol^{-1} at 300 K and decreases to 1.55 cm^3 K mol^{-1} at 5K. These data were modeled assuming the presence of an $S = 1$ $[FeCo]^{5+}$ core and a high spin Fe^{2+} center that are weakly antiferromagnetically coupled with a coupling constant of -4.25 cm^{-1}. The same is true for **R53**, which has χT value 4.53 cm^3 K mol^{-1} at 300 K and decreases to 2.33 cm^3 K mol^{-1} at 5K supporting an $S = 3/2$ ground state. The coupling constant between the $[Co_2]^{5+}$ $S = 1/2$ core, with the high spin Fe^{2+} center was determined to be -6.35 cm^{-1}. [136] At room temperature these spins uncouple and the χT values match well for two independent $S = 1$ and $S = 2$ center for **R52** and two independent $S = 1/2$ and $S = 2$ centers for **R53**.

3.4 Electron Transport Properties of Heterotrimetallic Compounds

3.4.1 Significance of the σ Orbital Pathway

The delocalization of electrons across a molecular structure is one of the key principles in molecular electronics. In many organic electronics, electrons travel freely in a conjugated π network. The same is not true for metal chain compounds; instead it is the σ pathway via the d_{z^2} orbitals. In support of this idea, McGrady and coworkers have conducted detailed computational analyses of the homometallic $Cr_3(dpa)_4(NCS)_2$ and $Co_3(dpa)_4(NCS)_2$ structures.[189-191] Experimentally, the Cr_3,Co_3 and the Ni_3 species present molecular conductivity.[192-194] However, the Cr_3 has enhanced conductivity on what was initially believed to be π orbitals present in Cr_3 but not Co_3 or Ni_3. McGrady and coworkers computed a transmission spectrum of the Cr_3 and found that the π orbitals fell far too low in energy to play a noticeable role and act as the dominant electron transport channel. Instead, it is the σ_{nb} symmetry orbitals that provide the pathway for electron transport. In the σ_{nb} orbitals Cr_3 the d_{z^2} orbitals are localized on the two terminal metals with little contribution from the central Cr. However, slight deviations from an ideal D_4 symmetry allow the central Cr to contribute, strengthening the overall transport property and allowing enhanced conductivity (Scheme 2.15). This does not happen with Co_3 or Ni_3 hence, the lesser conductivity. This pathway proves significant in heterotrimetallic compounds as well.

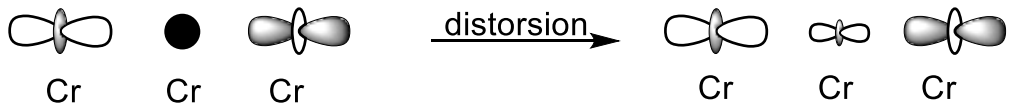

Scheme 2.15 σ_{nb} orbitals for an ideal D_4 $Cr_3(dpa)_4(NCS)_2$ (left) become distorted (right) allowing central Cr character to be introduced.[189]

2.3.4.2 Computational Investigations of Heterotrimetallic Compounds as Components in Molecular Electronics

One of the primary long-term goals for metal chain compounds is to develop them as potential compounds for molecular electronics. Extended metal atom chains (EMACs) provide a testing ground for the hypothesis; they contain a conductive core, a sheath of organic ligand, and axial ligands capping the chain, enabling the chain to be adhered to a surface. On a superficial level, these chains resemble a macroscopic wire on a much smaller scale (Figure 2.25).[49-50, 122, 159, 161, 195-196] Utilizing a modified scanning tunneling microscopy break junction (STM-BJ), experimentally testing this hypothesis is possible. In this method, a gold STM tip is smashed into a gold substrate until a conductance value greater than 10 G_o (where G_o is a single quantum of conductance) is achieved. The gold substrate has been previously bathed in a solution of the analyte. The solution may contain a nonconducting alkanethiol that is the same length as the analyte in order to better space out the analyte molecules. The tip is then slowly removed and eventually the gold-gold physical contact ruptures and the conductance of a single molecule of the analyte can be observed as it too is elongated and ruptured. These measurements are taken thousands of times on different portions of the gold substrate. The result is a histogram of conductance measurements that allow for an interpretation of conductance to be made.[197-201]

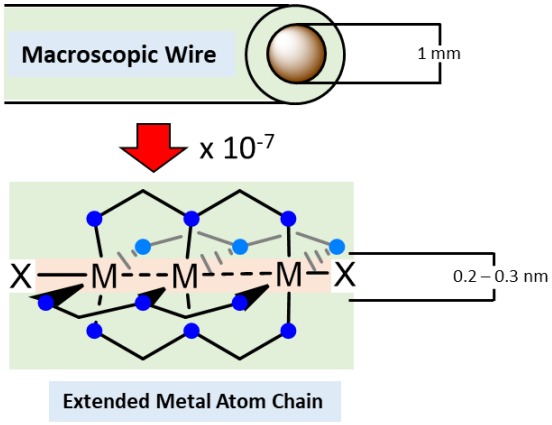

Figure 2.25. Macroscopic wires and the analogous molecular wires made with extended metal chains.

EMACs ranging from three metal atoms in length to eleven metal atoms in length have been studied using the STM-BJ technique. Early work focused on a trio of Cr, Co, and Ni chains. This trio has been studied in both the trimetallic and pentametallic states.[193-194, 196] In both cases, the Cr chain has had the highest conductance followed by Co and Ni. This is rationalized based on *d* orbital overlap; the greater the overlap, the greater the conductance. Furthermore, moving from the trimetallic to the pentametallic chains, conductance values decrease. This is reasonable given resistance is proportional to length and thus the longer pentametallic chains have the greatest resistance. These results are supported computationally using a non-equilibrium Green's function to predict transmission spectra for each chain. These transmission spectra allow for the determination of the dominant electron transport channel (i.e. molecular orbital) and its symmetry.[142, 189] In addition, the supporting dpa ligand was found to not contribute significantly to conductance, which furthers the analogy to a macroscopic wire as well as confirms the primary electron transport occurs via the metal atom chain.

While EMACs of varying composition length have been explored as molecular wires, their heterometallic counterparts have not yet received the same experimental treatment. However, their potential properties have been computationally explored in the context of molecular electronics. The physical asymmetry of $M_AM_AM_B$ HEMACs suggests that they could have an asymmetric current response. Given that EMACs behave as wires, it is not unreasonable to hypothesize that these asymmetric HEMACs would have current rectification behavior. Using a non-equilibrium Green's function calculations, the McGrady group examined $Mo_2M(dpa)_4(NCS)_2$ (M = Cr, Mn, Co) as well as $Ru_2M(dpa)_4(NCS)_2$ (M = Ni, Cu)

in the context of current rectification by generating transmission plots of each compound. Theoretical current-voltage response curves were also generated for the Mo_2M series. Current for a wire flows equally in both directions (Figure 2.26A) whereas for a rectifier, current flows preferentially in on direction (Figure 2.26B). In a current voltage response curve, the slope is indicative of the resistance and thus a rectifier will have a horizontal portion indicating near infinite resistance. When turning to the transmission diagrams, it was discovered that physical asymmetry was a requirement but not the only property of a chain needed for current rectification.[202-203] More important is the symmetry of the conductance channels and their proximity to the fermi level of the electrode. As such, the rectification capability is strongest in Mo_2Co followed by Mo_2Cr with Mo_2Mn having negligible rectification capabilities.[202] With these computational results in mind, there is now a strong motivation to experimentally validate these results.

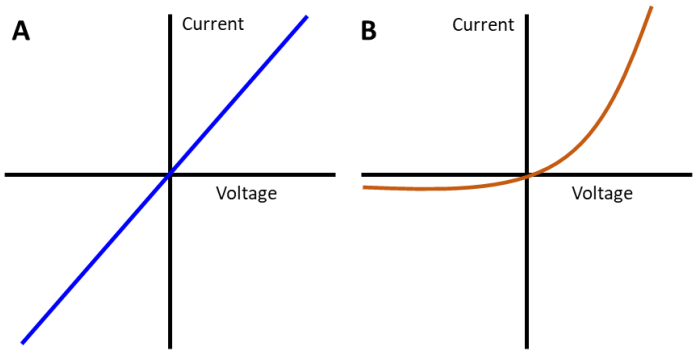

Figure 2.26 Idealized current voltage I/V curves for (A) wire and (B) rectifier

2.4. Paramagnetic Heteropolymetallic Complexes (More than Three Metals)

Extensive work focusing on extending the length of metal chain compounds beyond three metal atoms has been performed on homometallic extended metal atom chains (EMACs), which have been synthesized from five to eleven metal atoms in length.[1, 49, 196, 204-210] A similar body of work is currently being developed for heterometallic chains containing at least one metal-metal bond.[37, 111-121, 123-132, 134] A goal of this research area is to explore the attractive optical, magnetic, and conductance properties of the compounds.[37, 50, 111-113, 117-118, 122-123, 126, 133, 164-167, 195, 211-214] The primary means of electron communication in the longer chains like in the shorter bimetallic and trimetallic series is via overlap of σ symmetry d_{z^2} overlap. [215-216] Within

this section, both discrete molecular chain and several quasi 1D or “infinite” polymeric chain compounds are described.

2.4.1. Synthetic Methods and Structural Data for Polymetallic Chains

2.4.1.2 Molecular Chains

Peng and coworkers have reported four discrete compounds including heterometallic chains.[217-219] These chains contain two different metals and are supported by either the bna (bisnaphthyridylamido) or tdpa (tripyridyldiamido) ligand, which are shown in Figure 2.27. These pentametallic compounds are made by self–assembly at high temperatures (Scheme 2.16A). For tdpa-supported complexes **P1** and **P2** the bimetallic $Ru_2(OAc)_4Cl$ or $Mo_2(OAc)_4$ precursors are used in addition to $Ni(OAc)_2{\cdot}4H_2O$. The reagents are mixed with the ligand in molten naphthalene. An excess of NaNCS is then added as a source for the NCS axial ligand. For the bna-supported complexes, bimetallic $Mo_2(OAc)_4$ is first allowed to react with the Hbna ligand in molten naphthalene for several hours after which $Ni(OAc)_2{\cdot}6H_2O$ and LiCl are added to the reaction mixture (Scheme 2.16B). Presumably, the reaction proceeds via an Mo_2 intermediate but none was isolated. The resulting chains **P3** and **P4** are tricationic and three equivalents of KPF_6 are added in a final step to provide suitable cations.[219] The bond metrics for these compounds are presented in Table 2.13

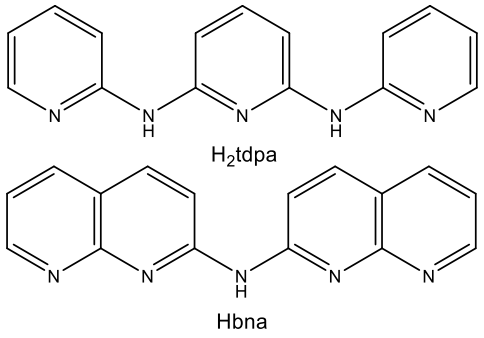

Figure 2.27 Ligands used to support pentametallic chains; H_2tdpa and Hbna

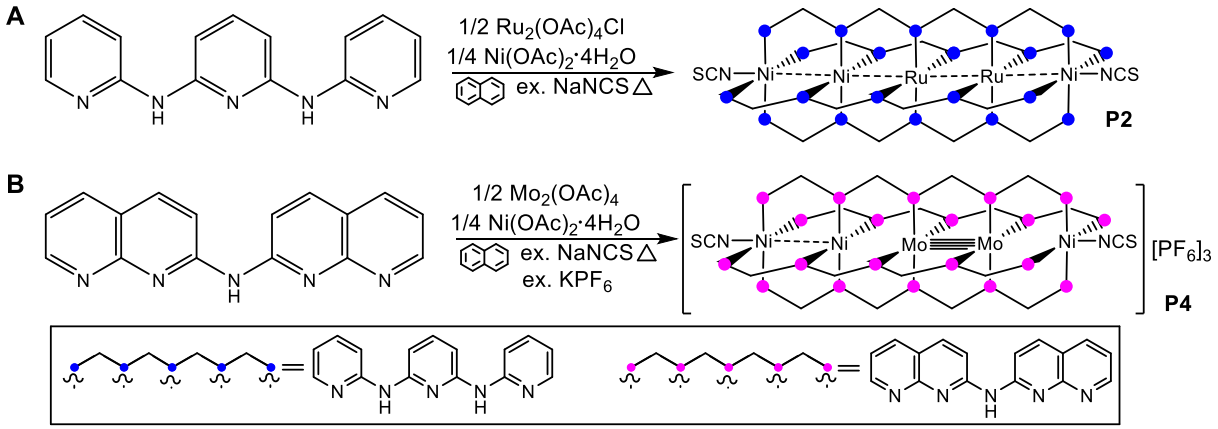

Scheme 2.16. Synthetic conditions for formation of heteropentanuclear chains **P2** (A) and **P4** (B)

Structurally, the four heteropentauclear complexes **(P1-P4)** share one notable similarity; a metal–metal multiple-bonded bimetallic unit of either Ru_2 or Mo_2. For **P2-P4**, which contain a $M_{A2}M_{B3}$ stroichiometry the M_2 unit contains the middle atom of the chain For **P1**, a central Ni atom is flanked on either side by Mo_2 units, yielding a stoichiometry of Mo_4Ni. The M_2 placement has an interesting effect of the helicity of the pentametallic chain, which is easily seen in the end-on view of **P1** in comparison to **P2** (Figure 2.28). The torsion angles of **P1** is quite small, ranging from 10.5° to 11.3°. While complexes **P2** – **P4** have torsion angles nearly double those of **P1** ranging from 19.970° to 25.579°.[217-219] All of the Mo_2 bond distances are in the "normal" range of quadruple bonds (between 2.07 Å and 2.16 Å).[179] For complex **P2**, crystallographic differention between the disordered metal atoms at positions M2 and M4 was note possible and thus, these distances were arbitrarily fixed and it is therefore not possible to compare Ru_2 distances to the other Ru_2 containing compounds. Complex **P5** does not have this disorder and thus we may make several comparisons. The Ru–Ru distance of 2.318(2) is within the range for a Ru=Ru bond rather than a Ru_2 with a 2.5 bond order. [220]

Table 2.13 Structural data for the pentametallic chains synthesized by the Peng lab. The name of each compound reads the metal composition from left to right.

M_1—M_2—M_3—M_4—M_5

Compound	Code	M_1–M_2	M_2–M_3	M_3–M_4	M_4–M_5	Ref.
$Mo_2NiMo_2(tpda)_4(NCS)_2$[A]	P1	2.1021(7)	2.516(4)	2.516(4)	2.1021(7)	[218]
$Ni_2Ru_2Ni(tpda)_4(NCS)_2$	P2	2.090(8) 2.397(1)	1.961(8) 2.290(1)	2.031(7) 2.261(1)	2.011(8) 2.0383(1)	[221]
$[Ni_2Mo_2Ni(bna)_4Cl_2][PF_6]_3$	P3	2.311(5)	2.369(5)	2.133(2)	2.514(2)	[219]
$[Ni_2Mo_2Ni(bna)_4(NCS)_2][PF_6]_3$	P4	2.334(4)	2.408(3)	2.109(2)	2.535(2)	[219]
$[Ni_2Ru_2Ni(bna)Cl_2][PF_6]_3$	P5	2.376(2)	2.318(2)	2.3122(2)	2.362(2)	[219]

[A] M1 – M2 is crystallographically equivalent to M3–M4, and M2–M3 is crystallographically equivalent to M4 – M5.

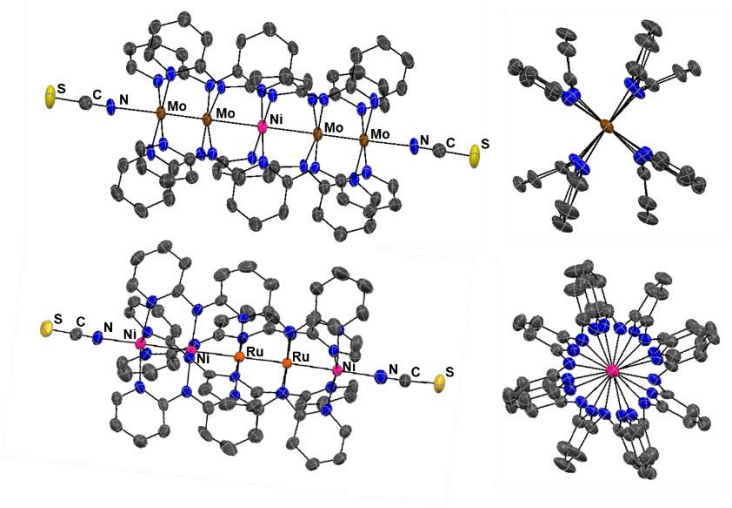

Figure 2.28 Crystal structure images of **P1** (top) and **P2** (bottom) pentametallic chains illustrating the effect of the metal-metal multiple bond location on torsion angle. All molecules of solvation and H atoms have been removed for clarity. In both end–on views, the axial–NCS ligands have been omitted.[217, 219]

4.1.2 Quasi 1-Dimensional Polymeric Chains

Ebihara, Uemura, and coworkers have synthesized both molecular and poymeric chain compounds containing Rh, Ru, Pt, and Cu.[47, 222-224] Given the similarity in synthesis for finite chain **P9**, it will be discussed in this section. The chains are constructed of a bimetallic Ru_2,Rh_2, PtRh, or Pt_2 bimetallic species and a $(Pt_2)_4$ or PtCuPt unit. The Ru_2 and Rh_2 units are supported by four acetate paddlewheel ligands while the Pt_2,PtRh, and PtCuPt units are supported by a combination of pivalamidate (piam) ligands and dangling NH_3 ligands (with the exception of (**P7**). The general synthetic method for both finite and infinite chains

involves adding a solution of $Ru_2(OAc)_4NO_3$ or $Rh_2(OAc)_4$ to a solution of either $[Pt_2(piam)_2(NH_3)_4]_2(PF_6)_2$ or $[Pt_2Cu(piam)_4(NH_3)_4](PF_6)_2$ with excess $NaPF_6$. The single molecular chain, compound, **P9**, uses a perchlorate anion and a trifluoroacetate anion as the counter anions instead of hexafluorophosphate.[223] In this chain, hydrogen bonding interactions from the hydrogen atoms of the amine ligands (on the CuPtCu units) prevents the chain from growing past 8 metal atoms in length.[223] A general overview of these synthetic methods is presented in Scheme 2.16. The structural data for these compounds are presented in Table 2.14.

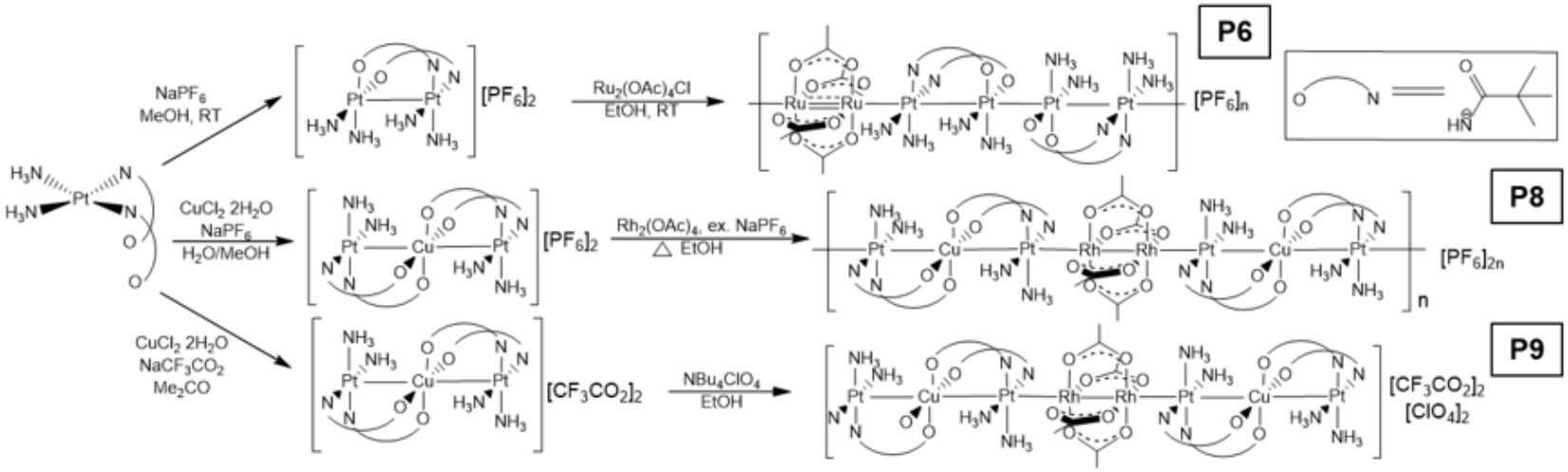

Scheme 2.17 Outline of the synthetic methods utilized by Uemura, Ebihara, and coworkers.

Table 2.14 Bond metrics for the compounds synthesized by Ebihara, Uemura, and coworkers. Two structure types are possible in these chains.

Structure Type A:

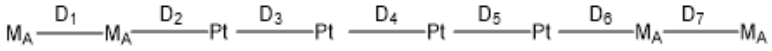

Structure Type B:

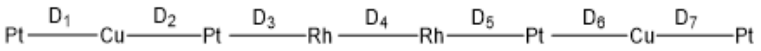

Compound	Code	Type	D_1 & D_7	D_2 & D_6	D_3 & D_5	D_4	Ref
$[\{Ru_2(OAc)_4\}\{Pt_2(piam)_2(NH_3)_4\}_2]_n(PF_6)_n$	**P6**	A	2.257(3)	2.789(2)	2.926(2)	3.096(2)	[224]
$[\{PtRh(Cl_3CCONH)_2(NH_3)_2Cl_{2.5}\}_2[Pt_2(piam)_2(NH_3)_4]_2(PF_6)_6 \cdot 2MeOH \cdot 2H_2O]_n$	**P7**	A	2.605(2) 2.602(2)	2.742(2) 2.715(2)	2.845(2) 2.806(2)	2.979(2)	[222]
$[\{Rh_2(OAc)_4\}\{Pt_2Cu(piam)_4(NH_3)_4\}_2]_n(PF_6)_{2n}$	**P8A**[a]	B	2.7034(9)	2.7034(9)	2.775(1)	2.370(1)	[223]
$[\{Rh_2(OAc)_4\}\{Pt_2Cu(piam)_4(NH_3)_4\}_2]_n(PF_6)_{2n}$	**P8B**[a]	B	2.6716(3)	2.6716(3)	2.7702(4)	2.3733(6)	[223]
$[\{Rh_2(OAc)_4\}\{Pt_2Cu(piam)_4(NH_3)_4\}_2]_n(PF_6)_{2n} \cdot 6nMe_2CO$	**P8C**[a]	B	2.6540(5)	2.6540(5)	2.7954(6)	2.3901(7)	[223]
$[\{Rh_2(OAc)_4\}\{Pt_2Cu(piam)_4(NH_3)_4\}_2](g_2)_2(ClO_4)_2 \cdot 2H_2O$	**P9**	B	2.6560(6)	2.7094(6)	2.8155(5)	2.3826(8)	[223]

[a] These crystal structures are all different solvent adducts of one another.

Structurally, these heterometallic chain compounds can be divided into one of two types, A or B as listed in Table 2.13. In the A structure type a bimetallic unit of either $Ru_2(OAc)_4^+$ $[PtRh(piam)_4(NH_3)_2Cl_2]^+$, or $[PtRh(Cl_3CCONH)_2(NH_3)_2Cl_2]$ is bound to a tetrametallic $[Pt_2(piam)_2(NH_3)_4]_2^{4+}$ unit. In structure type B, a bimetallic $Rh_2(OAc)_4$ unit is linked to a $[PtCuPt(piam)_4(NH_3)_4]^{2+}$ trimer. Both types start with a bimetallic species, either $Rh_2OAc)_4$ or $Ru_2(OAc)_4Cl$ as the first building block and from compound to compound. In the infinite chain **P8A**, **B**, and **C**, the Rh–Rh distances range from 2.3733(6) Å to 2.3901(7) Å, quite similar to the Rh–Rh distance in $Rh_2(OAc)_4(OH_2)_2$ of 2.3855(5) Å.[225] In the molecular chain **P9**, this distance is 2.3826 Å, also in good agreement with the isolated bimetallic $Rh_2(OAc)_4(OH_2)$. We may also compare the Ru–Ru in **P6** (2.257(3) Å) to that in an isolated $Ru_2(OAc)_4Cl$ species (2.281(3) Å),[1] In the second building block, the Pt–Cu distances in the Pt–Cu–Pt trimer are within 0.05 Å of one another and are similar in distance to an isolated Pt–Cu–Pt chain (2.6870(6) Å).[RE] We may also compare the Pt–Cu distances in several Pt–Cu–Pt species synthesized by Lippert.[39, 43, 226-227] In the tetrametallic $[Pt_4(piam)_4(NH_3)_8]^{4+}$ units with **P6** and **P7**, the Pt–Pt distances are in between that of an independent are in between that of an independent $[Pt_2(piam)_2(NH_3)_4](PF_6)_2{\cdot}2H_2O$ binuclear complex and the tetramer. It is also important to note that many of the equatorial ligands have hydrogen bonding interactions that aid in holding the building blocks together. For example, in **P6**, the O atoms on the $[Ru_2(OAc)_4]^+$ have hydrogen bonding interactions to the N–H of the piam ligand and the NH_3 ligands on the $[Pt_2(piam)_2(NH_3)_4]_2$ (Figure 2.29).[224]

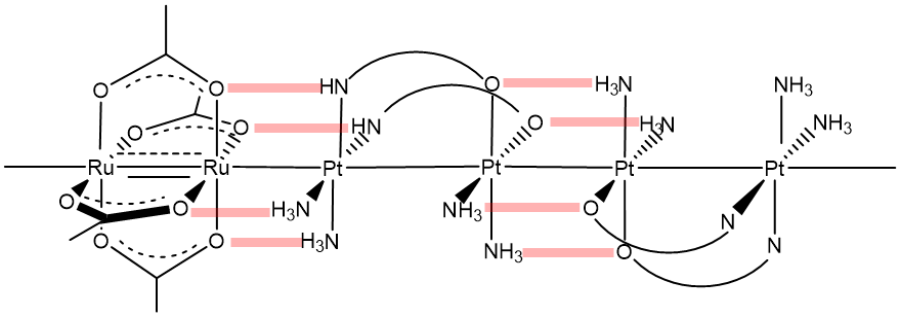

Figure 2.29 Hydrogen bonding interactions (emphasized in red) found in heterometallic chain compounds.

2.4.3 Electronic Structure of Heteropolymetallic Compounds

Although each class of compounds described previously has their own unique electronic structure, a commonality does exist between almost all but one of the compounds presented in these chains, infinite

or finite. As was seen with the shorter bimetallic and trimetallic species, the σ-symmetry d_{z^2} orbital overlap dominates the metal-metal bonding in these compounds.

The heteropentametallic chains explored by Peng and coworkers each present a unique structure with some commonalities between them. There are two types of structures that Peng and coworkers have established, symmetric ($M_AM_AM_BM_AM_A$) and asymmetric ($M_AM_BM_BM_AM_A$). Only compound **P1** is symmetric. Figure 2.30 illustrates the expected combinations of σ-type orbitals in this chain. The Ni d_{z^2} orbital can be destabilized by interaction with the filled Mo_2 σ bonding orbitals, leading to the occupation of the three lowest σ-symmetry orbital combinations, shown in Figure 2.30. Interestingly, the central tdpa pyridine rings are pointed off-axis with respect to the Ni–N bonds (see the view along the M_5 axis in Figure 2.28). These less-than-optimal Ni–N bonding interactions lower the Ni $d_{x^2-y^2}$ orbital enough to allow the central Ni atom **P1** to have a high-spin ground state.[218] Peng and coworkers Mo–Ni δ bonding could contribute to the high-spin state of **P1** but at a distance of >2.5 Å, such an interaction is unlikely. Compounds **P2**-**P4** are asymmetric in nature and computational investigations were performed $Ni_2Ru_2Ni(tpda)_4(NCS)_2$.[221] The electronic structure is consistent with the presence of three magnetic centers. The terminal Ni_2 unit features of d^8 Ni^{2+} ions, one of which is five coordinate with $S = 1$ and on is square planar with $S = 0$. The $S = 1$ Ni ion holds two unpaired electrons d_{z^2} and $d_{x^2-y^2}$ orbitals. The $[Ru_2]^{5+}$ species is the second magnetic site with $S = 3/2$ and electrons present in the δ^* and π^* orbitals. An additional unpaired electron is present in the terminal d^9 Ni^+ $d_{x^2-y^2}$ orbital.

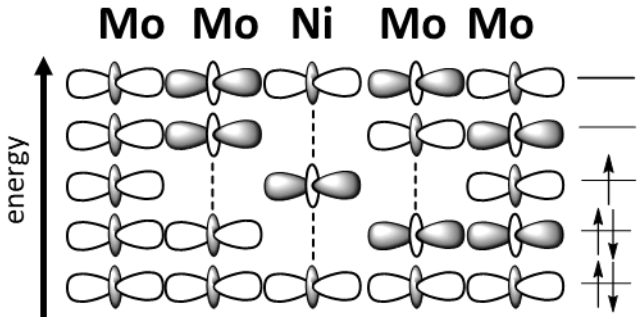

Figure 2.30 Orbitals of σ-type symmetry for symmetric pentametallic HEMACs from Peng and coworkers.

The chain compounds reported by Ebihara, Uemura, and coworkers were inspired by the mixed-valent "platinum blue", a linear, tetranuclear, Pt chain with an average oxidation state of $Pt^{2.25}$ and contains

one unpaired electron delocalized across four Pt centers via a σ pathway of d_{z^2} orbitals.[228-229] In **P6** and **P7** this motif remains in compounds featuring a Pt_4 building block. Furthermore, the LUMO for the majority of the bimetallic building blocks (Rh_2, Ru_2, PtRh) is a σ^* orbital. Therefore, a pathway uniting the doubly or singly occupied d_{z^2} orbitals of the Pt_4 building blocks and the unoccupied σ^* orbitals of the M_2 building block exists, supporting both bonding interactions as well as electron communication.

In **P6** the unpaired electrons are localized on the $[Ru_2]^{5+}$ core while in **P8** and **P9** they are localized on the $[Rh_2]^{4+}$ core. Based on magnetic susceptibility data for **P6**, the electronic structure is analogous to that of $Ru_2(OAc)_4Cl$ with a $\sigma^2\pi^4\delta^2\delta^{*2}\pi^{*2}$ triplet ground state. [216, 224] The LUMO for the bimetallic building blocks as well as the [Pt–Cu–Pt] bridged compound remains on a σ^* orbital, composed of d_{z^2} orbitals. Ebihara, Uemura and coworkers have found that simple, yet accurate molecular orbital depictions of these chains can be obtained by determining and energetically ranking all combinations of d_{z^2} orbitals.

4.2 Magnetic Properties of Heteropolymetallic Compounds

The magnetic behavior of these compounds can be categorized into three general classes: isolated magnetic centers, ferromagnetically coupled centers, and antiferromagnetically coupled centers. As will be discussed in section 4.2, despite the differences in magnetic behavior the vast majority of electron communication occurs through the σ pathway. This is also seen in the trimetallic complexes, described in section 3.

4.3.1 Isolated Magnetic Centers

Despite the apparent similarities between the pentametallic chains **P1**-**P5** all three types of magnetic behavior are represented. Compound **P1** is the only one to present a single isolated magnetic center. This is easily justified however, when considering the terminal Mo_2 diamagnetic units are not magnetically active leaving just the central high-spin $[Ni]^{2+}$ ion. [218]

4.3.2. Intramolecular Spin Coupling

When a diamagnetic $[Mo_2]$ unit is bookended by one Ni ion on one side as in **P3** and **P4**, the single five-coordinate Ni is paramagnetic with $S = 1$ and the terminal $[Ni_2]^{3+}$ unit is also paramagnetic with $S = 3/2$. Intrachain communication occurs in the form of antiferromagnetic coupling between the two termini.

Two possible mechanisms for pin couple have been considered: direct exchange via the d_{z^2} orbitals or superexchange via the ligands supporting the chain. Since the magnitude of the coupling, J ~ -45 cm^{-1}, is larger than in the homometallic $[Ni_5(bna)_4Cl_2]^{n+}$ compounds, the authors suggest a σ pathway. [219] For **P2** weak ferromagnetic coupling is suggested by the magnetometry data as indicated by the slight rise in μ_{eff} from 3.67 emu mol K^{-1} (300K) to 4.41 emu mol K^{-1} (41 K).[221] The nature of the spin coupling is ambiguous since the compound contains three spin centers and the susceptibility data have not been modeled.[221]

The infinite chain compounds from Ebihara and Uemura present spin coupling between each discrete octameric unit. Compound **P7** for example, is composed of [Pt2] and [PtRh] units, at 250 K, the complex at a μeff of 0.5 cm3 K mol-1.[222] this value decreases to 0.04 cm3 K mol-1 as the temperature tends toward zero. Compound **P5** contains a $[Ru_2]^{5+}$ bimetallic unit. Variable temperature magnetic susceptibility data provided a χT value of 0.95 cm^3 K mol^{-1} at room temperature, consistent with that of a $[Ru_2]^{II/III}$ unit with an S = 1 ground state.[224] Additionally, substantial zero field splitting (D = 220 cm^{-1}, consistent with other $Ru_2^{II/III}$ species as well as weak antiferromagnetic coupling (zJ = -3 cm^{-1}) between [Ru2] units were found. Most recently, $[Rh_2]$ chains bridged by [Pt–Cu–Pt] units were characterized magnetically. Two of the solvent adducts of **P8** were examined to understand if solvent in the crystal lattice had any impact on magnetic chain communication. These adducts present χT values of 0.441 cm^3 K mol^{-1} and 0.412 cm^3 K mol^{-1} at 300K, decreasing slightly at lower temperatures.[230] This is suggestive of one unpaired electron, housed in the $d_{x^2-y^2}$ orbital of the Cu^{2+} ion.[223, 230] These electrons present weak antiferromagnetic coupling (J = - 0.35 cm^{-1} in the first sample, J = - 0.47 cm^{-1} in the second.) The discrete octanuclear chain **P9** showed a similar χT value of 0.412 cm3 K mol-1 at 300 K with slight decreasing behavior at lower temperatures. As with the infinite chains above, the unpaired electron lives in a $d_{x^2-y^2}$ orbital on the Cu atom. The data were fit with a weak antiferromagnetic coupling constant of J = 0.45 cm-1 between octameric units. This coupling occurs between neighboring chains that are approximately 10.2 Å apart.

4.3.3 Intermolecular Spin Coupling

As mentioned in Section 2.2.1, the geometry of the crystallized dimer in compounds made by Doerrer and coworkers, dictates their magnetic behavior. For compounds that exist in the square geometry, the magnetic data suggest that each bimetallic paddlwheel behaves independently with one

high spin metal (II) ion. The rationale for the isolated behavior lies in the communication via Pt d_{z^2} orbitals. When these species dimerize they do so with Pt atoms facing each other. When the Pt atoms are in close enough proximity, unpaired electrons on the terminal 3d metals can communicate via this pathway and couple. The square geometry does not have this magnetic pathway available. The other three geometries do, however, and antiferromagnetic coupling is observed; as a dimer, each compound is expected to have a singlet ground state. It is also important to notice the disparity in χT values observed in the solid state and in solution. This is attributable to propensity of these heterobimetallics to crystallize into dimers while this behavior is not possible in solution. The coupling constants (where reported) have been compiled in Table 6.

Table 2.15 Coupling constants in heterobimetallic complexes in the Doerrer lab.

Compound	*J* (cm^{-1})	Ref
B2	– 10	95
B3	– 60	95
B4	– 12.7	95
B5	– 50.8	98
B6	– 6	98
B7	– 12.6	98
B17	– 6.7	104
B18	– 8.8	104
B19	– 30.7	104

Doerrer and coworkers note in these pairings, the Ni containing compound consistently has a greater magnitude coupling constant. Perhaps the most surprising compound in this class is **B20**, which behaves as a one–dimensional infinite chain linked in a zig–zag pattern through thiocyanate ligands. The χT value at 300 K is 2.33 $cm^3\ K\ mol^{-1}$ whereas beginning at 45 K it dramatically rises to 10.94 $cm^3\ K\ mol^{-1}$. These data are consistent with Cr(III) centers that are ferromagnetically coupled that was determined with J = 1.18 cm^{-1}. Additionally, under low temperature and low field conditions, **B20** presented strong field dependence indicative of three–dimensional ordering. Furthermore, at 1.8 K, butterly–shaped hysteresis loops were found. This hysteresis behavior was later attributed to disruptions in the rearrangement of the chain as a result of the tilting of the magnetic axis of Cr(III) as the magnetic field is changed.[99]

4.4 Electron Transport Properties of Heteropolymetallic Complexes

Complex **P2** has been studied the STM-bj measurement technique described in Section 3.4. In comparison to its [Ni_5] and [Ru_5] analogs, compound **P2** has a resistance value of 6.1±1 MΩ; greater than [Ru_5] 4.2±0.9 MΩ but less than the [Ni_5] 23.3±4.1 MΩ which was attributed to the HOMO-LUMO gap in each chain; the lesser the gap, the lesser the resistance. A current–voltage response curve was also constructed for **P2**. In contrast to the homometallic analogs which show a continuous line, analogous to the one in Figure 2.26, **P2** presented negative differential resistance (NDR). This is seen in the current-voltage response curve with sudden spikes on the curve. In contrast to a traditional resistor in which an increase in applied voltage leads to an increase in current response, the opposite occurs with NDR. The rationale behind this behavior, which is valuable in molecular electronics remains poorly understood.[217]

5. Summary and Outlook

Moving from heterobimetallics to heterometallic chains of higher nuclearity, several prominent trends become apparent. From a synthetic aspect, both the metalloligand approach and self-assembly methods in conjunction with HSAB allow for the highly selective syntheses of heterobimetallic and heterotrimetallic chains in which metal atom pairings can be investigated with atomic precision. Currently, quasi 1D chains may be synthesized by first forming building blocks using methods enabling selectivity and control but the metalloligand and self-assembly approach have not been investigated for chains of higher nuclearity. Development of such methods could prove valuable.

Many of the species that present magnetic or electron transport behavior do so through the use of the σ pathway comprised of d_{z^2} orbitals. The application of d^8 square planar ions (or more generally diamagnetic species) such as Pt^{2+} has proved useful in all three classes of paramagnetic heterometallic metal–metal bonded complexes in this review. Their incorporation allows for long range communication between magnetic units to occur. This is seen in the heterobimetallic complexes for Doerrer and coworkers in which Pt–Pt interactions on neighboring complexes allows for magnetic coupling between two neighboring units to occur. As evidenced in Doerrer's own quasi 1D chain (**B20**), the appropriate choice of bridging ligand and metal-metal pairing allows for long range interactions. Continued development into the incorporation of other diamagnetic mediators between magnetic centers may be a way to incorporate existing heterobi- and heterotrimetallic chains into longer quasi 1D chain systems.

Beginning in 2007, the field of paramagnetic metal-metal bonded compounds has undergone a renaissance. This renaissance has included heterobimetallic compounds capable of enabling unique reactivity,[51] heterotrimetallic chain compounds exhibiting unusually large ferromagnetic coupling,[37], heterotrimetallic compounds in triangular arrangements,[135-136], and heterobimetallic compounds that crystallize into tetramers with long range coupling.[96, 98]

References

1. Cotton, F. A.; Murillo, C. A.; Walton, R. A., *Multiple Bonds between Metal Atoms*. Springer New York: 2005.

2. Liddle, S. T., Molecular metal-metal bonds : compounds, synthesis, properties. **2015**.

3. Constable, E. C.; Housecroft, C. E., Coordination chemistry: the scientific legacy of Alfred Werner. *Chem. Soc. Rev.* **2013,** *42*, 1429-1439.

4. Abel, E. W.; Singh, A.; Wilkinson, G., 265. Some π-cyclopentadienyl-molybdenum and -tungsten carbonyls. *J. Chem. Soc.* **1960**, 1321-1324.

5. Coffey, C. E.; Lewis, J.; Nyholm, R. S., 339. Metal–metal bonds. Part I. Compounds of gold(0) with the carbonyls of manganese, iron, and cobalt. *J. Chem. Soc.* **1964**, 1741-1749.

6. Bennett, M. J.; Caulton, K. G.; Cotton, F. A., Structure of tetra-n-butyratodiruthenium chloride, a compound with a strong metal-metal bond. *Inorg. Chem.* **1969,** *8*, 1-6.

7. Dahl, L. F.; Connelly, N. G., Organometallic chalcogen complexes. XX. Stereochemical characterization of an oxidized iron-sulfur dimer, [Fe(h5-C5H5)(CO)(SCH3)]2+. Paramagnetic cation effectively containing a one-electron metal-metal bond. *J. Am. Chem. Soc.* **1970,** *92*, 7472-7474.

8. Pauling, L., The nature of the chemical bond: application of results obtained from the quantum mechanics and from a theory of paramagnetic susceptibility to the structures of molecules. *J. Am. Chem. Soc.* **1931,** *53*, 1367-1400.

9. Zener, C., Interaction between the *d*-Shells in the Transition Metals. II. Ferromagnetic Compounds of Manganese with Perovskite Structure. *Phys. Rev.* **1951,** *82*, 403-405.

10. Münck, E.; Papaefthymiou, V.; Surerus, K. K.; Girerd, J. J., Double Exchange in Reduced Fe_3S_4 Clusters and Novel Clusters with MFe_3S_4 Cores. In *Metal Clusters in Proteins*, American Chemical Society: 1988; Vol. 372, pp 302-325.

11. Ding, X. Q.; Bominaar, E. L.; Bill, E.; Winkler, H.; Trautwein, A. X.; Drüeke, S.; Chaudhuri, P.; Wieghardt, K., Mössbauer and electron paramagnetic resonance study of the double-exchange and Heisenberg-exchange interactions in a novel binuclear Fe(II/III) delocalized-valence compound. *J. Chem Phys.* **1990,** *92*, 178-186.

12. Cotton, F. A.; Curtis, N. F.; Harris, C. B.; Johnson, B. F. G.; Lippard, S. J.; Mague, J. T.; Robinson, W. R.; Wood, J. S., Mononuclear and Polynuclear Chemistry of Rhenium (III): Its Pronounced Homophilicity. *Science* **1964,** *145*, 1305.

13. Krapp, A.; Lein, M.; Frenking, G., *The strength of the σ-, π- And δ-bonds in $Re_2Cl_8^{2-}$*. 2008; Vol. 120.

14. Saito, K.; Nakao, Y.; Sato, H.; Sakaki, S., Theoretical Study of Rhenium Dinuclear Complexes: Re−Re Bonding Nature and Electronic Structure. *J. Phys. Chem. A* **2006,** *110*, 9710-9717.

15. Enemark, J. H.; Feltham, R. D., Principles of structure, bonding, and reactivity for metal nitrosyl complexes. *Coord. Chem. Rev.* **1974,** *13*, 339-406.

16. Pauling, L., Atomic Radii and Interatomic Distances in Metals. *J. Am. Chem. Soc.* **1947,** *69*, 542-553.

17. Cordero, B.; Gómez, V.; Platero-Prats, A. E.; Revés, M.; Echeverría, J.; Cremades, E.; Barragán, F.; Alvarez, S., Covalent radii revisited. *Dalton Trans.* **2008,** *21*, 2832-2838.

18. Pyykkö, P.; Atsumi, M., Molecular Single-Bond Covalent Radii for Elements 1–118. *Chem. Eur. J.* **2009,** *15*, 186-197.

19. Pyykkö, P.; Atsumi, M., Molecular Double-Bond Covalent Radii for Elements Li–E112. *Chem. Eur. J.* **2009,** *15*, 12770-12779.

20. Pyykkö, P.; Riedel, S.; Patzschke, M., Triple-Bond Covalent Radii. *Chem. Eur. J.* **2005,** *11*, 3511-3520.

21. Cotton, F. A.; Frenz, B. A.; Stults, B. R.; Webb, T. R., Investigations of quadruple bonds by polarized crystal spectra. I. The interpretation of the spectrum of tetra(n-butylammonium) octachlorodirhenate. The disordered crystal structure. *J. Am. Chem. Soc.* **1976,** *98*, 2768-2773.

22. Glaser, T., Rational design of single-molecule magnets: a supramolecular approach. *Chem Commun.* **2011,** *47*, 116-130.

23. Malrieu, J. P.; Caballol, R.; Calzado, C. J.; de Graaf, C.; Guihéry, N., Magnetic Interactions in Molecules and Highly Correlated Materials: Physical Content, Analytical Derivation, and Rigorous Extraction of Magnetic Hamiltonians. *Chem. Rev.* **2014,** *114*, 429-492.

24. Frost, J. M.; Harriman, K. L. M.; Murugesu, M., The rise of 3-d single-ion magnets in molecular magnetism: towards materials from molecules? *Chem. Sci.* **2016,** *7*, 2470-2491.

25. Aromí, G.; Gamez, P.; Roubeau, O., Molecular Magnetism. In *Spin States in Biochemistry and Inorganic Chemistry*, John Wiley & Sons, Ltd: 2015; pp 263-296.

26. Anderson, P. W.; Hasegawa, H., Considerations on Double Exchange. *Phys. Rev.* **1955,** *100*, 675-681.

27. Palii, A.; Tsukerblat, B.; Clemente-Juan, J. M.; Coronado, E., Magnetic exchange between metal ions with unquenched orbital angular momenta: basic concepts and relevance to molecular magnetism. *International Reviews in Physical Chemistry* **2010,** *29*, 135-230.

28. Soncini, A.; Mallah, T.; Chibotaru, L. F., Molecular Spintronics in Mixed-Valence Magnetic Dimers: The Double-Exchange Blockade Mechanism. *J. Am. Chem. Soc.* **2010,** *132*, 8106-8114.

29. Kahn, O., *Molecular magnetism*. VCH: 1993.

30. Anderson, P. W., Antiferromagnetism. Theory of Superexchange Interaction. *Phys. Rev.* **1950,** *79*, 350-356.

31. Kramers, H. A., L'interaction Entre les Atomes Magnétogènes dans un Cristal Paramagnétique. *Physica* **1934,** *1*, 182-192.

32. Kanamori, J., Superexchange interaction and symmetry properties of electron orbitals. *Journal of Physics and Chemistry of Solids* **1959,** *10*, 87-98.

33. Gamelin, D. R.; Bominaar, E. L.; Kirk, M. L.; Wieghardt, K.; Solomon, E. I., Excited-State Contributions to Ground-State Properties of Mixed-Valence Dimers: Spectral and Electronic-Structural Studies of $[Fe_2(OH)_3(tmtacn)_2]^{2+}$ Related to the $[Fe_2S_2]^{+}$ Active Sites of Plant-Type Ferredoxins. *J. Am. Chem. Soc.* **1996,** *118*, 8085-8097.

34. Glaser, T.; Kesting, F.; Beissel, T.; Bill, E.; Weyhermüller, T.; Meyer-Klaucke, W.; Wieghardt, K., Spin-Dependent Delocalization in Three Isostructural Complexes $[LFeNiFeL]^{2+/3+/4+}$ (L = 1,4,7-(4-tert-Butyl-2-mercaptobenzyl)-1,4,7-triazacyclononane). *Inorg. Chem.* **1999,** *38*, 722-732.

35. Payne, S. C.; Hagen, K. S., Steric Control of Reactivity of Non-Heme μ-Hydroxo Diiron(II) Complexes with Oxygen: Isolation of a Strongly Coupled μ-Oxo Fe(II)Fe(III) Dimer. *J. Am. Chem. Soc.* **2000,** *122*, 6399-6410.

36. Chibotaru, L. F.; Girerd, J. J.; Blondin, G.; Glaser, T.; Wieghardt, K., Electronic Structure of Linear Thiophenolate-Bridged Heteronuclear Complexes $[LFeMFeL]^{n+}$ (M = Cr, Co, Fe; n = 1–3): A Combination of Kinetic Exchange Interaction and Electron Delocalization. *J. Am. Chem. Soc.* **2003,** *125*, 12615-12630.

37. Chipman, J. A.; Berry, J. F., Extraordinarily Large Ferromagnetic Coupling ($J \geq 150\ cm^{-1}$) by Electron Delocalization in a Heterometallic Mo≡Mo–Ni Chain Complex. *Chem. Eur. J.* **2018,** *24*, 1494-1499.

38. Lippert, B.; Schubert, U., The x-ray structure of a heteronuclear (Pt, Mn) complex of 1-methylthymine and its vibrational spectra. *Inorg. Chim. Acta* **1981,** *56*, 15-20.

39. Lippert, B.; Thewalt, U.; Schoellhorn, H.; Goodgame, D. M. L.; Rollins, R. W., Formation, crystal structure, and EPR spectroscopic properties of a heteronuclear (Pt_2,Cu) mixed-nucleobase (1-methylcytosine, 1-methyluracil) complex: bis[(.mu.-1-methyluracilato-N_3,O_4)(.mu.-1-methylcytosine-N3,O2)-cis-diammineplatinum(II)]copper(II) tetranitrate-6-water. *Inorg. Chem.* **1984,** *23* , 2807-2813.

40. Lippert, B.; Schoellhorn, H.; Thewalt, U., Formation of platinum [Pt2.25]4-1-methyluracil blue through silver(I) oxidation of [Pt2.0]2 and isolation of a heteronuclear (Pt2,Ag2) precursor. *Inorg. Chem.* **1987,** *26*, 1736-1741.

41. Micklitz, W.; Mueller, G.; Huber, B.; Riede, J.; Rashwan, F.; Heinze, J.; Lippert, B., Trinuclear, mixed Pt_2Pd-1-methyluracil and -1-methylthymine blues with +2.33 average metal oxidation state. Preparation, crystal structures, and solution studies. *J. Am. Chem. Soc.* **1988,** *110*, 7084-7092.

42. Schreiber, A.; Krizanovic, O.; Fusch, E. C.; Lippert, B.; Lianza, F.; Albinati, A.; Hill, S.; Goodgame, D. M. L.; Stratemeier, H.; Hitchman, M. A., Heteronuclear Complexes Derived from trans-a2PtL_2 (a = NH_2 or CH_3NH_2, L = 2-Pyridonate). Distorted Coordination Geometries of All Three Metals in trans-$[a_2PtL_2CuL_2Pt(a_2)]^{2+}$ and an Extraordinary Short Hydrogen Bond in trans-$[a_2PtL(LH)]^{+}$. *Inorg. Chem.* **1994,** *33*, 6101-6110.

43. Erxleben, A.; Albinati, A.; Lippert, B., Heteronuclear Pt–Pd, Pt_2Cu and Pt_2Ni complexes with bridging acetamidate: crystal structures and spectroscopic studies. *Dalton Trans.* **1996**, 1823-1828.

44. Fusch, G.; Fusch, E. C.; Erxleben, A.; Hüttermann, J.; Scholl, H.-J.; Lippert, B., Heteronuclear μ-1-methylcytosinato-N3,N4 complexes containing very short Pt → Cu dative bonds. *Inorg. Chim. Acta* **1996,** *252*, 167-178.

45. Hegmans, A.; Zangrando, E.; Freisinger, E.; Pichierri, F.; Randaccio, L.; Mealli, C.; Gerdan, M.; Trautwein, A. X.; Lippert, B., Pt as Mediator of Strong Antiferromagnetic Coupling between Two CuII Ions in a Heteronuclear $Cu^{II}Pt^{II}Cu^{II}$ Complex of the Model Nucleobase 1-Methylcytosinate. *Chem. Eur. J.* **1999,** *5*, 3010-3018.

46. Goodgame, D. M. L.; Hitchman, M. A.; Lippert, B., Ligating properties of platinum(II) ions in mixed-metal (Pt_2M) trimers (M = copper(II), nickel(II), cobalt(II), iron(II)). *Inorg. Chem.* **1986,** *25*, 2191-2194.

47. Uemura, K.; Fukui, K.; Nishikawa, H.; Arai, S.; Matsumoto, K.; Oshio, H., Paramagnetic Platinum–Rhodium Octamers Bridged by Halogen Ions To Afford a Quasi-1D System. *Angew. Chemie. Int. Ed.* **2005,** *44*, 5459-5464.

48. Scott, T. A.; Abbaoui, B.; Zhou, H.-C., Crystallographic Evidence for Chromium–Platinum Interaction. *Inorg. Chem.* **2004,** *43*, 2459-2461.

49. Berry, J. F., Metal–Metal Bonds in Chains of Three or More Metal Atoms: From Homometallic to Heterometallic Chains. In *Metal-Metal Bonding*, Parkin, G., Ed. Springer Berlin Heidelberg: Berlin, Heidelberg, 2010; pp 1-28.

50. Hua, S.-A.; Cheng, M.-C.; Chen, C.-h.; Peng, S.-M., From Homonuclear Metal String Complexes to Heteronuclear Metal String Complexes. *Eur. J. Inorg. Chem.* **2015,** *2015*, 2510-2523.

51. Thomas, C. M., Metal-Metal Multiple Bonds in Early/Late Heterobimetallic Complexes: Applications Toward Small Molecule Activation and Catalysis *Comments on Inorganic Chemistry* **2011,** *32*, 14-38.

52. Krogman, J. P.; Thomas, C. M., Metal–metal multiple bonding in C_3-symmetric bimetallic complexes of the first row transition metals. *Chem Commun.* **2014,** *50*, 5115-5127.

53. Rudd, P. A.; Liu, S.; Planas, N.; Bill, E.; Gagliardi, L.; Lu, C. C., Multiple Metal–Metal Bonds in Iron–Chromium Complexes. *Angew. Chemie. Int. Ed.* **2013,** *52*, 4449-4452.

54. Zall, C. M.; Clouston, L. J.; Young, V. G.; Ding, K.; Kim, H. J.; Zherebetskyy, D.; Chen, Y.-S.; Bill, E.; Gagliardi, L.; Lu, C. C., Mixed-Valent Dicobalt and Iron–Cobalt Complexes with High-Spin Configurations and Short Metal–Metal Bonds. *Inorg. Chem.* **2013,** *52*, 9216-9228.

55. Clouston, L. J.; Siedschlag, R. B.; Rudd, P. A.; Planas, N.; Hu, S.; Miller, A. D.; Gagliardi, L.; Lu, C. C., Systematic Variation of Metal–Metal Bond Order in Metal–Chromium Complexes. *J. Am. Chem. Soc.* **2013,** *135*, 13142-13148.

56. Tereniak, S. J.; Carlson, R. K.; Clouston, L. J.; Young, V. G.; Bill, E.; Maurice, R.; Chen, Y. S.; Kim, H. J.; Gagliardi, L.; Lu, C. C., Role of the Metal in the Bonding and Properties of Bimetallic Complexes Involving Manganese, Iron, and Cobalt. *J. Am. Chem. Soc.* **2014,** *136*, 1842-1855.

57. Clouston, L. J.; Bernales, V.; Carlson, R. K.; Gagliardi, L.; Lu, C. C., Bimetallic Cobalt–Dinitrogen Complexes: Impact of the Supporting Metal on N_2 Activation. *Inorg. Chem.* **2015,** *54*, 9263-9270.

58. Eisenhart, R. J.; Clouston, L. J.; Lu, C. C., Configuring Bonds between First-Row Transition Metals. *Acc. Chem. Res* **2015,** *48*, 2885-2894.

59. Eisenhart, R. J.; Carlson, R. K.; Clouston, L. J.; Young, V. G.; Chen, Y.-S.; Bill, E.; Gagliardi, L.; Lu, C. C., Influence of Copper Oxidation State on the Bonding and Electronic Structure of Cobalt–Copper Complexes. *Inorg. Chem.* **2015,** *54*, 11330-11338.

60. Clouston, L. J.; Bernales, V.; Cammarota, R. C.; Carlson, R. K.; Bill, E.; Gagliardi, L.; Lu, C. C., Heterobimetallic Complexes That Bond Vanadium to Iron, Cobalt, and Nickel. *Inorg. Chem.* **2015,** *54*, 11669-11679.

61. Miller, D. L.; Siedschlag, R. B.; Clouston, L. J.; Young, V. G.; Chen, Y.-S.; Bill, E.; Gagliardi, L.; Lu, C. C., Redox Pairs of Diiron and Iron–Cobalt Complexes with High-Spin Ground States. *Inorg. Chem.* **2016,** *55*, 9725-9735.

62. Moore, J. T.; Chatterjee, S.; Tarrago, M.; Clouston, L. J.; Sproules, S.; Bill, E.; Bernales, V.; Gagliardi, L.; Ye, S.; Lancaster, K. M.; Lu, C. C., Enhanced Fe-Centered Redox Flexibility in Fe–Ti Heterobimetallic Complexes. *Inorg. Chem.* **2019**.

63. Greenwood, B. P.; Forman, S. I.; Rowe, G. T.; Chen, C.-H.; Foxman, B. M.; Thomas, C. M., Multielectron Redox Activity Facilitated by Metal–Metal Interactions in Early/Late Heterobimetallics: Co/Zr Complexes Supported by Phosphinoamide Ligands. *Inorg. Chem.* **2009,** *48*, 6251-6260.

64. Thomas, C. M.; Napoline, J. W.; Rowe, G. T.; Foxman, B. M., Oxidative addition across Zr/Co multiple bonds in early/late heterobimetallic complexes. *Chem Commun.* **2010,** *46*, 5790-5792.

65. Krogman, J. P.; Foxman, B. M.; Thomas, C. M., Activation of CO_2 by a Heterobimetallic Zr/Co Complex. *J. Am. Chem. Soc.* **2011,** *133*, 14582-14585.

66. Setty, V. N.; Zhou, W.; Foxman, B. M.; Thomas, C. M., Subtle Differences Between Zr and Hf in Early/Late Heterobimetallic Complexes with Cobalt. *Inorg. Chem.* **2011,** *50*, 4647-4655.

67. Napoline, J. W.; Krogman, J. P.; Shi, R.; Kuppuswamy, S.; Bezpalko, M. W.; Foxman, B. M.; Thomas, C. M., Activation of E–H and E–E (E = S, O) Bonds by Heterobimetallic Zr/Co Complexes: Evidence for Both One- and Two-Electron Processes. *Eur. J. Inorg. Chem.* **2013,** *2013*, 3874-3882.

68. Krogman, J. P.; Bezpalko, M. W.; Foxman, B. M.; Thomas, C. M., Synthesis, Structure, and Reactivity of an Anionic Zr–Oxo Relevant to CO_2 Reduction by a Zr/Co Heterobimetallic Complex. *Inorg. Chem.* **2013,** *52*, 3022-3031.

69. Zhou, W.; Marquard, S. L.; Bezpalko, M. W.; Foxman, B. M.; Thomas, C. M., Catalytic Hydrosilylation of Ketones Using a Co/Zr Heterobimetallic Complex: Evidence for an Unusual Mechanism Involving Ketyl Radicals. *Organometallics* **2013,** *32*, 1766-1772.

70. Napoline, J. W.; Bezpalko, M. W.; Foxman, B. M.; Thomas, C. M., N–H activation of hydrazines by a heterobimetallic Zr–Co complex: promotion of one-electron chemistry at Zr. *Chem Commun.* **2013,** *49*, 4388-4390.

71. Kuppuswamy, S.; Powers, T. M.; Krogman, J. P.; Bezpalko, M. W.; Foxman, B. M.; Thomas, C. M., Vanadium–iron complexes featuring metal–metal multiple bonds. *Chem. Sci.* **2013,** *4*, 3557-3565.

72. Kuppuswamy, S.; Bezpalko, M. W.; Powers, T. M.; Wilding, M. J. T.; Brozek, C. K.; Foxman, B. M.; Thomas, C. M., A series of C_3-symmetric heterobimetallic Cr–M (M = Fe, Co and Cu) complexes. *Chem. Sci.* **2014,** *5*, 1617-1626.

73. Wu, B.; Hernández Sánchez, R.; Bezpalko, M. W.; Foxman, B. M.; Thomas, C. M., Formation of Heterobimetallic Zirconium/Cobalt Diimido Complexes via a Four-Electron Transformation. *Inorg. Chem.* **2014,** *53*, 10021-10023.

74. Zhou, W.; Saper, N. I.; Krogman, J. P.; Foxman, B. M.; Thomas, C. M., Effect of ligand modification on the reactivity of phosphinoamide-bridged heterobimetallic Zr/Co complexes. *Dalton Trans.* **2014,** *43*, 1984-1989.

75. Kuppuswamy, S.; Cass, T. R.; Bezpalko, M. W.; Foxman, B. M.; Thomas, C. M., Synthesis and investigation of the metal–metal interactions in heterobimetallic Cr/Rh and Cr/Ir complexes. *Inorg. Chim. Acta* **2015,** *424*, 167-172.

76. Krogman, J. P.; Foxman, B. M.; Thomas, C. M., Formation and Subsequent Reactivity of a N_2-Stabilized Cobalt–Hydride Complex. *Organometallics* **2015,** *34*, 3159-3166.

77. Krogman, J. P.; Bezpalko, M. W.; Foxman, B. M.; Thomas, C. M., Multi-electron redox processes at a Zr(iv) center facilitated by an appended redox-active cobalt-containing metalloligand. *Dalton Trans.* **2016,** *45*, 11182-11190.

78. Wu, B.; Wilding, M. J. T.; Kuppuswamy, S.; Bezpalko, M. W.; Foxman, B. M.; Thomas, C. M., Exploring Trends in Metal–Metal Bonding, Spectroscopic Properties, and Conformational Flexibility in a Series of Heterobimetallic Ti/M and V/M Complexes (M = Fe, Co, Ni, and Cu). *Inorg. Chem.* **2016,** *55*, 12137-12148.

79. Culcu, G.; Iovan, D. A.; Krogman, J. P.; Wilding, M. J. T.; Bezpalko, M. W.; Foxman, B. M.; Thomas, C. M., Heterobimetallic Complexes Comprised of Nb and Fe: Isolation of a Coordinatively Unsaturated NbIII/Fe0 Bimetallic Complex Featuring a Nb≡Fe Triple Bond. *J. Am. Chem. Soc.* **2017,** *139*, 9627-9636.

80. Zhang, H.; Wu, B.; Marquard, S. L.; Litle, E. D.; Dickie, D. A.; Bezpalko, M. W.; Foxman, B. M.; Thomas, C. M., Investigation of Ketone C═O Bond Activation Processes by Heterobimetallic Zr/Co and Ti/Co Tris(phosphinoamide) Complexes. *Organometallics* **2017,** *36*, 3498-3507.

81. Barden, B. A.; Culcu, G.; Krogman, J. P.; Bezpalko, M. W.; Hatzis, G. P.; Dickie, D. A.; Foxman, B. M.; Thomas, C. M., Assessing the Metal–Metal Interactions in a Series of Heterobimetallic Nb/M Complexes (M = Fe, Co, Ni, Cu) and Their Effect on Multielectron Redox Properties. *Inorg. Chem.* **2019,** *58*, 821-833.

82. Marquard, S. L.; Bezpalko, M. W.; Foxman, B. M.; Thomas, C. M., Interaction and Activation of Carbon–Heteroatom π Bonds with a Zr/Co Heterobimetallic Complex. *Organometallics* **2014,** *33*, 2071-2079.

83. Marquard, S. L.; Bezpalko, M. W.; Foxman, B. M.; Thomas, C. M., Stoichiometric C═O Bond Oxidative Addition of Benzophenone by a Discrete Radical Intermediate To Form a Cobalt(I) Carbene. *J. Am. Chem. Soc.* **2013,** *135*, 6018-6021.

84. Wu, B.; Gramigna, K. M.; Bezpalko, M. W.; Foxman, B. M.; Thomas, C. M., Heterobimetallic Ti/Co Complexes That Promote Catalytic N–N Bond Cleavage. *Inorg. Chem.* **2015,** *54*, 10909-10917.

85. Cammarota, R. C.; Clouston, L. J.; Lu, C. C., Leveraging molecular metal–support interactions for H_2 and N_2 activation. *Coord. Chem. Rev.* **2017,** *334*, 100-111.

86. Siedschlag, R. B.; Bernales, V.; Vogiatzis, K. D.; Planas, N.; Clouston, L. J.; Bill, E.; Gagliardi, L.; Lu, C. C., Catalytic Silylation of Dinitrogen with a Dicobalt Complex. *J. Am. Chem. Soc.* **2015,** *137*, 4638-4641.

87. Zhou, W.; Napoline, J. W.; Thomas, C. M., A Catalytic Application of Co/Zr Heterobimetallic Complexes: Kumada Coupling of Unactivated Alkyl Halides with Alkyl Grignard Reagents. *Eur. J. Inorg. Chem.* **2011,** *2011*, 2029-2033.

88. Coombs, J.; Perry, D.; Kwon, D.-H.; Thomas, C. M.; Ess, D. H., Why Two Metals Are Better Than One for Heterodinuclear Cobalt–Zirconium-Catalyzed Kumada Coupling. *Organometallics* **2018,** *37*, 4195-4203.

89. Greenwood, B. P.; Rowe, G. T.; Chen, C.-H.; Foxman, B. M.; Thomas, C. M., Metal–Metal Multiple Bonds in Early/Late Heterobimetallics Support Unusual Trigonal Monopyramidal Geometries at both Zr and Co. *J. Am. Chem. Soc.* **2010,** *132*, 44-45.

90. Cooper, B. G.; Napoline, J. W.; Thomas, C. M., Catalytic Applications of Early/Late Heterobimetallic Complexes. *Catalysis Reviews* **2012,** *54*, 1-40.

91. Sunderland, T. L.; Berry, J. F., Metal-Metal Single Bonds with the Magnetic Anisotropy of Quadruple Bonds: A Systematic Series of Heterobimetallic Bismuth(II)-Rhodium(II) Formamidinate Complexes. *Chem. Eur. J.* **2016**.

92. Sunderland, T. L.; Berry, J. F., Expanding the family of heterobimetallic Bi-Rh paddlewheel carboxylate complexes via equatorial carboxylate exchange. *Dalton Trans.* **2016,** *45*.

93. Dikarev, E. V.; Gray, T. G.; Li, B., Heterobimetallic Main-Group–Transition-Metal Paddle-Wheel Carboxylates. *Angew. Chemie. Int. Ed.* **2005,** *44*, 1721-1724.

94. Filatov, A. S.; Napier, M.; Vreshch, V. D.; Sumner, N. J.; Dikarev, E. V.; Petrukhina, M. A., From Solid State to Solution: Advancing Chemistry of Bi–Bi and Bi–Rh Paddlewheel Carboxylates. *Inorg. Chem.* **2012,** *51*, 566-571.

95. Dahl, E. W.; Baddour, F. G.; Fiedler, S. R.; Hoffert, W. A.; Shores, M. P.; Yee, G. T.; Djukic, J.-P.; Bacon, J. W.; Rheingold, A. L.; Doerrer, L. H., Antiferromagnetic coupling across a tetrametallic unit through noncovalent interactions. *Chem. Sci.* **2012,** *3*, 602-609.

96. Baddour, F. G.; Fiedler, S. R.; Shores, M. P.; Bacon, J. W.; Golen, J. A.; Rheingold, A. L.; Doerrer, L. H., Pt···Pt vs Pt···S Contacts Between Pt-Containing Heterobimetallic Lantern Complexes. *Inorg. Chem.* **2013,** *52*, 13562-13575.

97. Beach, S. A.; Doerrer, L. H., Heterobimetallic Lantern Complexes and Their Novel Structural and Magnetic Properties. *Acc. Chem. Res* **2018,** *51*, 1063-1072.

98. Baddour, F. G.; Fiedler, S. R.; Shores, M. P.; Golen, J. A.; Rheingold, A. L.; Doerrer, L. H., Heterobimetallic Lantern Complexes That Couple Antiferromagnetically through Noncovalent Pt···Pt Interactions. *Inorg. Chem.* **2013,** *52*, 4926-4933.

99. Guillet, J. L.; Bhowmick, I.; Shores, M. P.; Daley, C. J. A.; Gembicky, M.; Golen, J. A.; Rheingold, A. L.; Doerrer, L. H., Thiocyanate-Ligated Heterobimetallic {PtM} Lantern Complexes Including a Ferromagnetically Coupled 1D Coordination Polymer. *Inorg. Chem.* **2016,** *55*, 8099-8109.

100. Wu, B.; Bezpalko, M. W.; Foxman, B. M.; Thomas, C. M., A heterobimetallic complex featuring a Ti–Co multiple bond and its application to the reductive coupling of ketones to alkenes. *Chem. Sci.* **2015,** *6*, 2044-2049.

101. Zhang, H.; Hatzis, G. P.; Moore, C. E.; Dickie, D. A.; Bezpalko, M. W.; Foxman, B. M.; Thomas, C. M., O_2 Activation by a Heterobimetallic Zr/Co Complex. *J. Am. Chem. Soc.* **2019,** *141*, 9516-9520.

102. Gramigna, K. M.; Dickie, D. A.; Foxman, B. M.; Thomas, C. M., Cooperative H2 Activation across a Metal–Metal Multiple Bond and Hydrogenation Reactions Catalyzed by a Zr/Co Heterobimetallic Complex. *ACS Catalysis* **2019,** *9*, 3153-3164.

103. Eisenhart, R. J.; Rudd, P. A.; Planas, N.; Boyce, D. W.; Carlson, R. K.; Tolman, W. B.; Bill, E.; Gagliardi, L.; Lu, C. C., Pushing the Limits of Delta Bonding in Metal–Chromium Complexes with Redox Changes and Metal Swapping. *Inorg. Chem.* **2015,** *54*, 7579-7592.

104. Beach, S. A.; Zuckerman, L. A.; Portillo, R. I.; Shores, M. P.; Rheingold, A. L.; Doerrer, L. H., Heterobimetallic {PtMn} and {PtFe} Lantern Complexes with Exceptionally Long Metallophilic Contacts. *Inorg. Chim. Acta* **2019**.

105. Sunada, Y.; Sue, T.; Matsumoto, T.; Nagashima, H., Titanium(IV) phosphinoamide as a unique bidentate ligand for late transition metals II: TiRu heterobimetallics bearing a bridging chlorine atom. *J. Organomet. Chem.* **2006,** *691*, 3176-3182.

106. Nagashima, H.; Sue, T.; Oda, T.; Kanemitsu, A.; Matsumoto, T.; Motoyama, Y.; Sunada, Y., Dynamic Titanium Phosphinoamides as Unique Bidentate Phosphorus Ligands for Platinum. *Organometallics* **2006,** *25*, 1987-1994.

107. Tsutsumi, H.; Sunada, Y.; Shiota, Y.; Yoshizawa, K.; Nagashima, H., Nickel(II), Palladium(II), and Platinum(II) η3-Allyl Complexes Bearing a Bidentate Titanium(IV) Phosphinoamide Ligand: A Ti←M2 Dative Bond Enhances the Electrophilicity of the π-Allyl Moiety. *Organometallics* **2009,** *28*, 1988-1991.

108. Halder, P.; SantaLucia, D. J.; Park, S. V.; Berry, J. F., From Pincer to Paddlewheel: C–H and C–S Bond Activation at Bis(2-pyridylthio)methane by Palladium(II). *Inorg. Chem.* **2019,** *58* (4), 2270-2274.

109. Gennari, M.; Givaja, G.; Castillo, O.; Hermosilla, L.; Gómez-García, C. J.; Duboc, C.; Lledós, A.; Mas-Ballesté, R.; Zamora, F., On the Road to MM′X Polymers: Redox Properties of Heterometallic Ni···Pt Paddlewheel Complexes. *Inorg. Chem.* **2014,** *53*, 10553-10562.

110. Yang, E. C.; Cheng, M. C.; Tsai, M. S.; Peng, S. M., Structure of a linear unsymmetrical trinuclear cobalt(II) complex with a localized CO–CO bond: dichlorotetrakis[μ3-bis(2-pyridyl)amido]tricobalt(II). *Journal of the Chemical Society, Chem. Commun.* **1994**, 2377-2378.

111. Liu, I. P.-C.; Lee, G.-H.; Peng, S.-M.; Bénard, M.; Rohmer, M.M., Cu–Pd–Cu and Cu–Pt–Cu Linear Frameworks: Synthesis, Magnetic Properties, and Theoretical Analysis of Two Mixed-Metal Complexes of Dipyridylamide (dpa), Isostructural, and Isoelectronic with $[Cu_3(dpa)_4Cl_2]^+$. *Inorg. Chem.* **2007,** *46*, 9602-9608.

112. Rohmer, M. M.; Liu, I. P. C.; Lin, J. C.; Chiu, M. J.; Lee, C. H.; Lee, G. H.; Bénard, M.; López, X.; Peng, S. M., Structural, Magnetic, and Theoretical Characterization of a Heterometallic Polypyridylamide Complex. *Angew. Chemie. Int. Ed.* **2007,** *46*, 3533-3536.

113. Huang, G. C.; Bénard, M.; Rohmer, M. M.; Li, L. A.; Chiu, M. J.; Yeh, C. Y.; Lee, G. H.; Peng, S. M., $Ru_2M(dpa)_4Cl_2$ (M = Cu, Ni): Synthesis, Characterization, and Theoretical Analysis of Asymmetric Heterometal String Complexes of the Dipyridylamide Family. *Eur. J. Inorg. Chem.* **2008**, 1767-1777.

114. Liu, I. P.-C.; Chen, C.-H.; Chen, C.-F.; Lee, G.-H.; Peng, S.-M., Asymmetric heterometal string complexes: stereochemical control of the unique isomer of (4,0)[CuCuPd$(npa)_4$Cl][PF_6] and (4,0)[CuCuPt(npa)4Cl][PF_6]. *Chem Commun.* **2009**, 577-579.

115. Xiang, J.; Jia, L. H.; Wang, B. W.; Yiu, S. M.; Peng, S. M.; Wong, W. Y.; Gao, S.; Lau, T. C., The synthesis, structures and magnetic properties of polynuclear Ru^{III}3d(3d = Mn II/III , Ni II , Cu II) compounds based on $[Ru^{III}(Q)_2(CN)_2]$. *Dalton Trans.* **2013,** *42*, 3876-3887.

116. Cheng, M. C.; Mai, C.L.; Yeh, C. Y.; Lee, G. H.; Peng, S. M., Facile synthesis of heterotrimetallic metal–string complex $[NiCoRh(dpa)_4Cl_2]$ through direct metal replacement. *Chem Commun.* **2013,** *49* (72), 7938-7940.

117. Yu, L. C.; Lee, G. H.; Sigrist, M.; Lin, T. S.; Peng, S. M., Structure and Antiferromagnetism of Trinuclear Heterometallic Strings Containing Mn^{II}-M^{II}-Mn^{II} Frameworks (M = Ni, Pd, Pt. *Eur. J. Inorg. Chem.* **2016,** 4250-4256.

118. Chang, W. C.; Chang, C. W.; Sigrist, M.; Hua, S. A.; Liu, T. J.; Lee, G. H.; Jin, B. Y.; Chen, C. H.; Peng, S. M., Nonhelical heterometallic $[Mo_2M(npo)_4(NCS)_2]$ string complexes (M = Fe, Co, Ni) with high single-molecule conductance. *Chem Commun.* **2017,** *53*, 8886-8889.

119. Liu, Y. C.; Hua, S. A.; Cheng, M. C.; Yu, L. C.; Demeshko, S.; Dechert, S.; Meyer, F.; Lee, G. H.; Chiang, M. H.; Peng, S. M., Electron Delocalization of Mixed-Valence Diiron Sites Mediated by Group 10 Metal Ions in Heterotrimetallic Fe-M-Fe (M=Ni, Pd, and Pt) Chain Complexes. *Chem. Eur. J.* **2018,** *24*, 11649-11666.

120. Cheng, M. C.; Hua, S. A.; Lv, Q.; Sigrist, M.; Lee, G. H.; Liu, Y.-C.; Chiang, M. H.; Peng, S. M., Stepwise synthesis of the heterotrimetallic chains $[MRu_2(dpa)_4X_2]^{0/1+}$ using group 7 to group 12 transition metal ions and $[Ru_2(dpa)_4Cl]$. *Dalton Trans.* **2018,** *47*, 1422-1434.

121. Aydin-Cantürk, D.; Nuss, H., Synthesis, Structure Determination, and Magnetic Properties of the New Heterometallic Chain Compound CrCrNi(di-2,2′-pyridylamido)$_4Cl_2$·Et_2O. *Zeitschrift für anorganische und allgemeine Chemie* **2011,** *637*, 543-546.

122. Berry, J. F.; Cotton, F. A.; Daniels, L. M.; Murillo, C. A., A Trinickel Dipyridylamido Complex with Metal–Metal Bonding Interaction: Prelude to Polynickel Molecular Wires and Devices? *J. Am. Chem. Soc.* **2002,** *124*, 3212-3213.

123. Nippe, M.; Berry, J. F., Introducing a Metal–Metal Multiply Bonded Group as an "Axial Ligand" to Iron: Synthetic Design of a Linear Cr–Cr···Fe Framework. *J. Am. Chem. Soc.* **2007,** *129*, 12684-12685.

124. Nippe, M.; Victor, E.; Berry, J. F., Do Metal–Metal Multiply-Bonded "Ligands" Have a trans Influence? Structural and Magnetic Comparisons of Heterometallic Cr≡Cr···Co and Mo≡Mo···Co Interactions. *Eur. J. Inorg. Chem.* **2008**, 5569-5572.

125. Nippe, M.; Timmer, G. H.; Berry, J. F., Remarkable regioselectivity in the preparation of the first heterotrimetallic Mo≡W-Cr chain. *Chem Commun.* **2009**, 4357-4359.

126. Nippe, M.; Wang, J.; Bill, E.; Hope, H.; Dalal, N. S.; Berry, J. F., Crystals in Which Some Metal Atoms are More Equal Than Others: Inequalities From Crystal Packing and Their Spectroscopic/Magnetic Consequences. *J. Am. Chem. Soc.* **2010,** *132*, 14261-14272.

127. Nippe, M.; Bill, E.; Berry, J. F., Group 6 Complexes with Iron and Zinc Heterometals: Understanding the Structural, Spectroscopic, and Electrochemical Properties of a Complete Series of MM···M′ Compounds. *Inorg. Chem.* **2011,** *50*, 7650-7661.

128. Nippe, M.; Turov, Y.; Berry, J. F., Remote Effects of Axial Ligand Substitution in Heterometallic Cr≡Cr···M Chains. *Inorg. Chem.* **2011,** *50*, 10592-10599.

129. Turov, Y.; Berry, J. F., Synthesis, characterization and thermal properties of trimetallic N_3-Cr-Cr-M-N_3 azide complexes with M = Cr, Mn, Fe, and Co. *Dalton Trans.* **2012,** *41*, 8153-8161.

130. Brogden, D. W.; Berry, J. F., Heterometallic Multiple Bonding: Delocalized Three-Center σ and π Bonding in Chains of 4d and 5d Transition Metals. *Inorg. Chem.* **2014,** *53*, 11354-11356.

131. Brogden, D. W.; Berry, J. F., Heterometallic Second-Row Transition Metal Chain Compounds in Two Charge States: Syntheses, Properties, and Electronic Structures of $[Mo–Mo–Ru]^{6+/7+}$ Chains. *Inorg. Chem.* **2015,** *54*, 7660 - 7665.

132. Brogden, D. W.; Christian, J. H.; Dalal, N. S.; Berry, J. F., Completing the series of Group VI heterotrimetallic $M_2Cr(dpa)_4Cl_2$ (M_2 = Cr_2, Mo_2, MoW and W_2) compounds and investigating their metal–metal interactions using density functional theory. *Inorg. Chim. Acta* **2015,** *424*, 241-247.

133. Christian, J. H.; Brogden, D. W.; Bindra, J. K.; Kinyon, J. S.; van Tol, J.; Wang, J.; Berry, J. F.; Dalal, N. S., Enhancing the Magnetic Anisotropy of Linear Cr(II) Chain Compounds Using Heavy Metal Substitutions. *Inorg. Chem.* **2016,** *55*, 6376-6383.

134. Chipman, J. A.; Berry, J. F., Facile Axial Ligand Substitution in Linear Mo≣Mo–Ni Complexes. *Inorg. Chem.* **2018,** *57*, 9354-9363.

135. Powers, T. M.; Gu, N. X.; Fout, A. R.; Baldwin, A. M.; Hernández Sánchez, R.; Alfonso, D. M.; Chen, Y.-S.; Zheng, S.-L.; Betley, T. A., Synthesis of Open-Shell, Bimetallic Mn/Fe Trinuclear Clusters. *J. Am. Chem. Soc.* **2013,** *135*, 14448-14458.

136. Eames, E. V.; Hernández Sánchez, R.; Betley, T. A., Metal Atom Lability in Polynuclear Complexes. *Inorg. Chem.* **2013,** *52*, 5006-5012.

137. Brogden, D. W.; Berry, J. F., Coordination Chemistry of 2,2'-Dipyridylamine: The Gift That Keeps on Giving. *Comments on Inorganic Chemistry* **2016,** *36*, 17-37.

138. Benbellat, N.; Rohmer, M.-M.; Benard, M., Electronic origin of the structural versatility in linear trichromium complexes of dipyridylamide. *Chem. Commun.* **2001**, 2368-2369.

139. Rohmer, M.-M.; Bénard, M., Structural Versatility in Polyoxometalates and in Some Linear Trimetallic Complexes: An Electronic Interpretation. *J. Cluster Sci.* **2002,** *13*, 333-353.

140. Hsiao, C.-J.; Lai, S.-H.; Chen, I.-C.; Wang, W.-Z.; Peng, S.-M., Metal-metal bonding and structures of metal string complexes $Cr_3(dpa)_4Cl_2$, $Cr_3(dpa)_4(NCS)_2$, and $Cr_3(dpa)_4Cl_2(PF_6)$ from IR, Raman, and surface-enhanced Raman spectra. *J. Phys. Chem. A* **2008,** *112*.

141. Wang, J.; Wang, Z.; Clark, R. J.; Ozarowski, A.; van Tol, J.; Dalal, N. S., A high-frequency EPR characterization of the S=2 linear tri-atomic chain in $Cr_3(dpa)_4Cl_2 \cdot CH_2Cl_2$. *Polyhedron* **2011,** *30*, 3058-3061.

142. Mohan, P. J.; Georgiev, V. P.; McGrady, J. E., Periodic trends in electron transport through extended metal atom chains: comparison of $Ru_3(dpa)_4(NCS)_2$ with its first-row analogues. *Chem. Sci.* **2012,** *3*, 1319-1329.

143. Cheng, C. H.; Wang, W. Z.; Peng, S. M.; Chen, I. C., Excited state dynamics of symmetric and asymmetric $Cr_3(dpa)_4Cl_2$ measured using femtosecond transient absorption spectroscopy. *Phys. Chem. Chem. Phys.* **2017,** *19*, 25471-25477.

144. Berry, J. F.; Cotton, F. A.; Lu, T.; Murillo, C. A.; Roberts, B. K.; Wang, X., Molecular and Electronic Structures by Design: Tuning Symmetrical and Unsymmetrical Linear Trichromium Chains. *J. Am. Chem. Soc.* **2004,** *126*, 7082-7096.

145. Li, H.; Lee, G.-H.; Peng, S.-M., Synthesis and crystal structure of trichromium metal string complex. *Journal of Molecular Structure* **2004,** *707*, 179-186.

146. Berry, J. F.; Cotton, F. A.; Murillo, C. A.; Chan, Z.-K.; Yeh, C.-W.; Chen, J.-D., Linear Trichromium, Tricobalt, Trinickel, and Tricopper Complexes of 2,2′-Dipyridylamide. In *Inorganic Syntheses: Volume 36*, John Wiley & Sons, Inc.: 2014; pp 102-110.

147. Cotton, F. A.; Daniels, L. M.; Jordan; Murillo, C. A., Symmetrical and Unsymmetrical Compounds Having a Linear Co_3^{6+} Chain Ligated by a Spiral Set of Dipyridyl Anions. *J. Am. Chem. Soc.* **1997,** *119*, 10377-10381.

148. Rohmer, M.-M.; Bénard, M., Bond Stretch Isomerism Still Elusive in Linear Trimetallic Complexes. DFT Calculations on Co3(dipyridylamine)4Cl2. *J. Am. Chem. Soc.* **1998,** *120*, 9372-9373.

149. Albert Cotton, F.; A. Murillo, C.; Wang, X., Can crystal structure determine molecular structure? For $Co_3(dpa)_4Cl_2$, yes. *Dalton Trans.* **1999**, 3327-3328.

150. Clérac, R.; Cotton, F. A.; Dunbar, K. R.; Lu, T.; Murillo, C. A.; Wang, X., New Linear Tricobalt Complex of Di(2-pyridyl)amide (dpa), $[Co_3(dpa)_4(CH_3CN)_2][PF_6]_2$. *Inorg. Chem.* **2000,** *39*, 3065-3070.

151. Clérac, R.; Cotton, F. A.; Daniels, L. M.; Dunbar, K. R.; Kirschbaum, K.; Murillo, C. A.; Pinkerton, A. A.; Schultz, A. J.; Wang, X., Linear Tricobalt Compounds with Di(2-pyridyl)amide (dpa) Ligands: Temperature Dependence of the Structural and Magnetic Properties of Symmetrical and Unsymmetrical Forms of $Co_3(dpa)_4Cl_2$ in the Solid State. *J. Am. Chem. Soc.* **2000,** *122*, 6226-6236.

152. Clérac, R.; Cotton, F. A.; Daniels, L. M.; Dunbar, K. R.; Murillo, C. A.; Wang, X., Structural and magnetic properties of $Co_3(dpa)_4Br_2$ *Dalton Trans.* **2001**, 386-391.

153. Rohmer, M.-M.; Strich, A.; Bénard, M.; Malrieu, J.-P., Metal–Metal Bond Length Variability in Co3(dipyridylamide)4Cl2: Bond-Stretch Isomerism, Crystal Field Effects, or Spin Transition Process? A DFT Study. *J. Am. Chem. Soc.* **2001,** *123*, 9126-9134.

154. Lai, S.-H.; Hsiao, C.-J.; Ling, J.-W.; Wang, W.-Z.; Peng, S.-M.; Chen, I. C., Metal–metal bonding in metal–string complexes M3(dpa)4X2 (M=Ni, Co, dpa=di(2-pyridyl)amido, and X=Cl, NCS) from resonance Raman and infrared spectroscopy. *Chem. Phys. Let.* **2008,** *456*, 181-185.

155. Cotton, F. A.; Murillo, C. A.; Wang, Q., Symmetrical linear Co_3^{6+} chains cocooned by two polypyridylamide ligands: How do they compare to open chains? *Inorg. Chim. Acta* **2010,** *363*, 4175-4180.

156. Pyrka, G. J.; El-Mekki, M.; Pinkerton, A. A., Structure of the linear trinuclear copper complex, dichlorotetrakis-(di-2-pyridylamido)tricopper. *J. Chem. Soc. Chem. Commun.* **1991**, 84-85.

157. Berry, J. F.; Cotton, F. A.; Lei, P.; Murillo, C. A., Further Structural and Magnetic Studies of Tricopper Dipyridylamido Complexes. *Inorg. Chem.* **2003,** *42*, 377-382.

158. Zhu, L. G.; Peng, S. M.; Lee, G. H., Axial Extension of Metal String Complexes: Crystal Structure of $\{Ni_3(dpa)_4[Ag(CN)_2]_2\}$. *Chem. Lett.* **2002,** *31*, 1210-1211.

159. Berry, J. F.; Albert Cotton, F.; Murillo, C. A., Making connections with molecular wires: extending tri-nickel chains with axial cyanide, dicyanamide, and phenylacetylide ligands. *Dalton Trans.* **2003**, 3015-3021.

160. Tsao, T. B.; Lee, G. H.; Yeh, C. Y.; Peng, S. M., Supramolecular assembly of linear trinickel complexes incorporating metalloporphyrins: a novel one-dimensional polymer and oligomer. *Dalton Trans.* **2003**, 1465-1471.

161. Berry, J. F.; Cotton, F. A.; Lu, T.; Murillo, C. A.; Wang, X., Enhancing the Stability of Trinickel Molecular Wires and Switches: Ni_3^{6+}/Ni_3^{7+}. *Inorg. Chem.* **2003,** *42*, 3595-3601.

162. Kiehl, P.; Rohmer, M. M.; Bénard, M., Electron Delocalization in Nickel Metallic Wires: A DFT Investigation of $Ni_3(dpa)_4Cl_2$ and $[Ni_3(dpa)_4]^{3+}$ (dpa = Dipyridylamide) and Extension to Higher Nuclearity Chains. *Inorg. Chem.* **2004,** *43*, 3151-3158.

163. Miao, X.-H.; Zhu, L.-G., Synthesis, Structure, and Cyclic Voltammetric Property of Metal String Complex $[Ni_3(dpa)_4(ClO_4)(Cl)]\cdot CH_2Cl_2$. *Zeitschrift für anorganische und allgemeine Chemie* **2010,** *636* (5), 878-881.

164. Kuo, C. K.; Chang, J. C.; Yeh, C. Y.; Lee, G. H.; Wang, C. C.; Peng, S. M., Synthesis, structures, magnetism and electrochemical properties of triruthenium-acetylide complexes. *Dalton Trans.* **2005**, 3696-3701.

165. Kuo, C. K.; Liu, I. P. C.; Yeh, C. Y.; Chou, C. H.; Tsao, T. B.; Lee, G. H.; Peng, S. M., Oxidation of Linear Trinuclear Ruthenium Complexes $[Ru_3(dpa)_4Cl_2]$ and $[Ru_3(dpa)_4(CN)_2]$: Synthesis, Structures, Electrochemical and Magnetic Properties. *Chem. Eur. J.* **2007,** *13*, 1442-1451.

166. Chiu, Y. C.; Ho, K. Y.; Chen, A. I. C.; Hua, S. A.; Cheng, M. C.; Peng, S. M., IR, Raman, and Surface enhanced Raman Spectroscopic Study on Triruthenium Dipyridylamide Diruthenium Nickel Dipyridylamide Family: Metal metal Bonding and Structures. *J. Chin. Chem. Soc.* **2014,** *61*, 1289-1296.

167. Huang, G.C.; Po-Chun Liu, I.; Kuo, J.H.; Huang, Y.L.; Yeh, C.Y.; Lee, G.H.; Peng, S.M., *Further investigations of linear trirhodium complexes: Experimental and theoretical studies of [Rh3(dpa)4Cl2] and [$Rh_3(dpa)_4Cl_2$](BF_4) [dpa = bis(2-pyridyl)amido anion]*. 2009; p 2623-9.

168. Cotton, F. A.; Rice, G. W., Further studies of chromium-chromium bond lengths in quadruply bonded dinuclear compounds. *Inorg. Chem.* **1978,** *17*, 2004-2009.

169. Cotton, F. A.; Niswander, R. H.; Sekutowski, J. C., Homologous chromium, molybdenum, and tungsten compounds with very short quadruple bonds. *Inorg. Chem.* **1978,** *17*, 3541-3545.

170. Cotton, F. A.; Extine, M.; Rice, G. W., Sensitivity of the chromium-chromium quadruple bond in dichromium tetracarboxylates to axial coordination and changes in inductive effects. *Inorg. Chem.* **1978,** *17*, 176-186.

171. Cotton, F. A.; Ilsley, W. H.; Kaim, W., Homologous chromium, molybdenum, and tungsten derivatives of 6-chloro-2-hydroxypyridine. Inductive effects on the metal-metal bond length. *Inorg. Chem.* **1980,** *19*, 1453-1457.

172. Cotton, F. A.; Ilsley, W. H.; Kaim, W., A mixed-ligand complex of quadruply bonded ditungsten(II): bis(2,4-dimethyl-6-oxopyrimidine)bis(1,3-diphenyltriazeno)ditungsten. *Inorg. Chem.* **1980,** *19*, 1450-1452.

173. Cotton, F. A.; Ilsley, W. H.; Kaim, W., Sensitivity of the chromium-chromium quadrupole bond to axial interactions in dichromium(II) compounds. *J. Am. Chem. Soc.* **1980,** *102*, 3464-3474.

174. Sattelberger, A. P.; McLaughlin, K. W.; Huffman, J. C., Metal-metal bonded complexes of the early transition metals. 2. Synthesis of quadruply bonded tungsten(II) trifluoroacetate complexes. *J. Am. Chem. Soc.* **1981,** *103*, 2880-2882.

175. Baral, S.; Cotton, F. A.; Ilsley, W. H., Tetraamidodichromium(II) compounds and their dihalomethane adducts. Structures of $Cr_2[(2,6\text{-xylyl})NC(CH_3)O]_4*1.5C_6H_5CH_3$ and $M_2[(2,6\text{-xylyl})NC(CH_3)O]_4*2CH_2Br_2$, M = chromium, molybdenum. *Inorg. Chem.* **1981,** *20*, 2696-2703.

176. Mitschler, A.; Rees, B.; Wiest, R.; Benard, M., Electron deformation density for the "supershort" chromium-chromium quadruple bond: a joint experimental and theoretical study. *J. Am. Chem. Soc.* **1982,** *104*, 7501-7509.

177. Cotton, F. A.; Huang, P.; Murillo, C. A.; Timmons, D. J., A complete series of $W_2(hpp)_4Cl_n$(n=0,1,2) compounds. *Inorganic Chemistry Communications* **2002,** *5*, 501-504.

178. Duncan Lyngdoh, R. H.; Schaefer, H. F.; King, R. B., Metal–Metal (MM) Bond Distances and Bond Orders in Binuclear Metal Complexes of the First Row Transition Metals Titanium Through Zinc. *Chem. Rev.* **2018,** *118*, 11626-11706.

179. Cotton, F. A.; Daniels, L. M.; Hillard, E. A.; Murillo, C. A., The Lengths of Molybdenum to Molybdenum Quadruple Bonds: Correlations, Explanations, and Corrections. *Inorg. Chem.* **2002,** *41*, 2466-2470.

180. Eglin, J. L.; Smith, L. T.; Staples, R. J., Tungsten to tungsten quadruple bonds: over 30 years of research, 50 structurally characterized compounds and 100 known compounds. *Inorg. Chim. Acta* **2003,** *351*, 217-224.

181. Eames, E. V.; Betley, T. A., Site-Isolated Redox Reactivity in a Trinuclear Iron Complex. *Inorg. Chem.* **2012,** *51*, 10274-10278.

182. Eames, E. V.; Harris, T. D.; Betley, T. A., Modulation of magnetic behavior via ligand-field effects in the trigonal clusters (PhL)Fe_3L*3 (L* = thf, py, PMe2Ph). *Chem. Sci.* **2012,** *3*, 407-415.

183. Arcisauskaite, V.; Spivak, M.; McGrady, J. E., Structure and bonding in trimetallic arrays containing a Cr–Cr quadruple bond: A challenge to density functional theory. *Inorg. Chim. Acta* **2015,** *424*, 293-299.

184. Spivak, M.; López, X.; de Graaf, C., Trends in the Bond Multiplicity of Cr_2, Cr_3 and Cr_2M (M = Zn, Ni, Fe, Mn) Complexes Extracted from Multiconfigurational Wave Functions. *J. Phys. Chem. A* **2019**.

185. Cotton, F. A.; Daniels, L. M.; Murillo, C. A.; Pascual, I.; Zhou, H. C., Remarkable Effects of Axial π* Coordination on the Cr–Cr Quadruple Bond in Dichromium Paddlewheel Complexes. *J. Am. Chem. Soc.* **1999,** *121*, 6856-6861.

186. Rohmer, M.M.; Benard, M., Bond-stretch isomerism in strained inorganic molecules and in transition metal complexes: a revival? *Chem. Soc. Rev.* **2001,** *30*, 340-354.

187. Wu, L. P.; Field, P.; Morrissey, T.; Murphy, C.; Nagle, P.; Hathaway, B.; Simmons, C.; Thornton, P., Crystal structure and electronic properties of dibromo- and dichloro-tetrakis[μ3-bis(2-pyridyl)amido]tricopper(II) hydrate. *Dalton Trans.* **1990**, 3835-3840.

188. Bénard, M.; Berry, J. F.; Cotton, F. A.; Gaudin, C.; López, X.; Murillo, C. A.; Rohmer, M. M., Structure and Magnetism of $[M_3]^{6/7+}$ Metal Chain Complexes from Density Functional Theory: Analysis for Copper and Predictions for Silver. *Inorg. Chem.* **2006,** *45*, 3932-3940.

189. Georgiev, V. P.; McGrady, J. E., Influence of Low-Symmetry Distortions on Electron Transport through Metal Atom Chains: When Is a Molecular Wire Really "Broken"? *J. Am. Chem. Soc.* **2011,** *133*, 12590-12599.

190. Pantazis, D. A.; McGrady, J. E., A Three-State Model for the Polymorphism in Linear Tricobalt Compounds. *J. Am. Chem. Soc.* **2006,** *128*, 4128-4135.

191. Pantazis, D. A.; Murillo, C. A.; McGrady, J. E., A re-evaluation of the two-step spin crossover in the trinuclear cation $[Co_3(\text{dipyridylamido})_4Cl_2]^+$. *Dalton Trans.* **2008**, 608-614.

192. Berry, J. F.; Cotton, F. A.; Lei, P.; Lu, T.; Murillo, C. A., Additional Steps toward Molecular Scale Wires: Further Study of $Ni_5^{10/11+}$ Chains Embraced by Polypyridylamide Ligands. *Inorg. Chem.* **2003,** *42*, 3534-3539.

193. Lin, S.-Y.; Chen, I. W. P.; Chen, C.-h.; Hsieh, M.-H.; Yeh, C.Y.; Lin, T.W.; Chen, Y.H.; Peng, S.M., Effect of Metal–Metal Interactions on Electron Transfer: an STM Study of One-Dimensional Metal String Complexes. *The J. Phys. Chem. B* **2004,** *108*, 959-964.

194. Chen, I. W. P.; Fu, M.D.; Tseng, W.H.; Yu, J.Y.; Wu, S.-H.; Ku, C.J.; Chen, C.H.; Peng, S.M., Conductance and stochastic switching of ligand-supported linear chains of metal atoms.*Angew. Chem. Int. Ed.* **2006,** *45*, 5814-8.

195. Berry, J. F.; Cotton, F. A.; Murillo, C. A.; Roberts, B. K., An Efficient Synthesis of Acetylide/Trimetal/Acetylide Molecular Wires. *Inorg. Chem.* **2004,** *43*, 2277-2283.

196. Yeh, C. Y.; Wang, C. C.; Chen, C. H.; Peng, S. M., Molecular Metal Wires Built from a Linear Metal Atom Chain Supported by Oligopyridylamido Ligands. In *Redox Systems Under Nano-Space Control*, Hirao, T., Ed. Springer Berlin Heidelberg: Berlin, Heidelberg, 2006; pp 85-117.

197. Millar, D.; Venkataraman, L.; Doerrer, L. H., Efficacy of Au–Au Contacts for Scanning Tunneling Microscopy Molecular Conductance Measurements. *J. Phys. Chem. C* **2007,** *111*, 17635-17639.

198. Quek, S. Y.; Venkataraman, L.; Choi, H. J.; Louie, S. G.; Hybertsen, M. S.; Neaton, J. B., Amine–Gold Linked Single-Molecule Circuits: Experiment and Theory. *Nano Letters* **2007,** *7*, 3477-3482.

199. Park, Y. S.; Whalley, A. C.; Kamenetska, M.; Steigerwald, M. L.; Hybertsen, M. S.; Nuckolls, C.; Venkataraman, L., Contact Chemistry and Single-Molecule Conductance: A Comparison of Phosphines, Methyl Sulfides, and Amines. *J. Am. Chem. Soc.* **2007,** *129*, 15768-15769.

200. Quek, S. Y.; Kamenetska, M.; Steigerwald, M. L.; Choi, H. J.; Louie, S. G.; Hybertsen, M. S.; Neaton, J. B.; Venkataraman, L., Mechanically controlled binary conductance switching of a single-molecule junction. *Nature Nanotech.* **2009,** *4*, 230.

201. Su, T. A.; Neupane, M.; Steigerwald, M. L.; Venkataraman, L.; Nuckolls, C., Chemical principles of single-molecule electronics. *Nature Rev. Mat.* **2016,** *1*, 16002.

202. DeBrincat, D.; Keers, O.; McGrady, J. E., Can heterometallic 1-dimensional chains support current rectification? *Chem Commun.* **2013,** *49*, 9116-9118.

203. Weng, T.; DeBrincat, D.; Arcisauskaite, V.; McGrady, J. E., In search of structure-function relationships in transition-metal based rectifiers. *Inorg. Chem. Front.* **2014,** *1*, 468-477.

204. Kuo, J. H.; Tsao, T. B.; Lee, G. H.; Lee, H. W.; Yeh, C. Y.; Peng, S. M., An Extended Metal Chain with the 2,7-Bis(dipyridyldiamino)-1,8-naphthyridine (H4bdpdany) Ligand – The Longest Even-Numbered Metal Chain Complex. *Eur. J. Inorg. Chem.* **2011,** *2011*, 2025-2028.

205. Ismayilov, R. H.; Wang, W. Z.; Lee, G. H.; Yeh, C. Y.; Hua, S. A.; Song, Y.; Rohmer, M. M.; Bénard, M.; Peng, S. M., Two Linear Undecanickel Mixed-Valence Complexes: Increasing the Size and the Scope of the Electronic Properties of Nickel Metal Strings. *Angew. Chemie. Int. Ed.* **2011,** *50*, 2045-2048.

206. Huang, G.-C.; Hua, S.-A.; Liu, I. P.-C.; Chien, C.-H.; Kuo, J.-H.; Lee, G.-H.; Peng, S.-M., Further studies of [Ni4(DAniDANy)4] (DAniDANy2−=N,N'-bis-p-anisyl-2,7-diamido-1,8-naphthyridine) and its one-electron oxidation product: Metal-metal sigma bonding in Ni49+ complex. *Comptes Rendus Chimie* **2012,** *15*, 159-162.

207. Tsou, L. H.; Sigrist, M.; Chiang, M. H.; Horng, E. C.; Chen, C. H.; Huang, S. L.; Lee, G. H.; Peng, S. M., Asymmetric tetranuclear nickel chains with unidirectionally ordered 2-(α-(5-phenyl)pyridylamino)-1,8-naphthyridine ligands. *Dalton Trans.* **2016,** *45* , 17281-17289.

208. Chen, P. J.; Sigrist, M.; Horng, E. C.; Lin, G. M.; Lee, G. H.; Chen, C. H.; Peng, S. M., A ligand design with a modified naphthyridylamide for achieving the longest EMACs: the 1st single-molecule conductance of an undeca-nickel metal string. *Chem Commun.* **2017,** *53*, 4673-4676.

209. Nicolini, A.; Galavotti, R.; Barra, A.L.; Borsari, M.; Caleffi, M.; Luo, G.; Novitchi, G.; Park, K.; Ranieri, A.; Rigamonti, L.; Roncaglia, F.; Train, C.; Cornia, A., Filling the Gap in Extended Metal Atom Chains: Ferromagnetic Interactions in a Tetrairon(II) String Supported by Oligo-α-pyridylamido Ligands. *Inorg. Chem.* **2018,** *57*, 5438-5448.

210. Ismayilov, R. H.; Wang, W. Z.; Lee, G. H.; Peng, S. M.; Suleimanov, B. A., Synthesis, crystal structure and properties of a pyrimidine modulated tripyridyldiamino ligand and its complexes. *Polyhedron* **2017,** *122*, 203-209.

211. Tsai, T. W.; Huang, Q. R.; Peng, S. M.; Jin, B. Y., Smallest Electrical Wire Based on Extended Metal-Atom Chains. *J. Phys. Chem. C* **2010,** *114*, 3641-3644.

212. Shih, K. N.; Huang, M. J.; Lu, H. C.; Fu, M. D.; Kuo, C. K.; Huang, G. C.; Lee, G. H.; Chen, C. H.; Peng, S. M., On the tuning of electric conductance of extended metal atom chains via axial ligands for $[Ru_3(dpa)_4X_2]^{0/+}$ (X = NCS, CN). *Chem Commun.* **2010,** *46*, 1338-1340.

213. Liu, I. P. C.; Chen, C. H.; Peng, S. M., Award Accounts : The Road to Molecular Metal Wires : The Past and Recent Advances of Metal String Complexes. *Bulletin of Japan Society of Coordination Chemistry* **2012**, 3-10.

214. Berry, J. F.; Cotton, F. A.; Murillo, C. A., A Trinuclear EMAC-Type Molecular Wire with Redox-Active Ferrocenylacetylide "Alligator Clips" Attached. *Organometallics* **2004,** *23*, 2503-2506.

215. Bera, J. K.; Dunbar, K. R., Chain Compounds Based on Transition Metal Backbones: New Life for an Old Topic. *Angew. Chemie. Int. Ed.* **2002,** *41*, 4453-4457.

216. Uemura, K., One-dimensional complexes extended by unbridged metal–metal bonds based on a HOMO–LUMO interaction at the d_{z2} orbital between platinum and heterometal atoms. *Dalton Trans.* **2017,** *46*, 5474-5492.

217. Huang, M. J.; Hua, S. A.; Fu, M.-D.; Huang, G. C.; Yin, C.; Ko, C. H.; Kuo, C. K.; Hsu, C.-H.; Lee, G. H.; Ho, K. Y.; Wang, C. H.; Yang, Y. W.; Chen, I. C.; Peng, S. M.; Chen, C. H., The First Heteropentanuclear Extended Metal-Atom Chain: $[Ni^{+}\text{-}Ru_2^{5+}\text{-}Ni^{2+}\text{-}Ni^{2+}(tripyridyldiamido)_4(NCS)_2]$. *Chem. Eur. J.* **2014,** *20*, 4526-4531.

218. Hung, W. C.; Sigrist, M.; Hua, S. A.; Wu, L. C.; Liu, T. J.; Jin, B. Y.; Lee, G. H.; Peng, S. M., A heteropentanuclear metal string complex $[Mo_2NiMo_2(tpda)_4(NCS)_2]$ with two linearly aligned quadruply bonded Mo2 units connected by a Ni ion and a meso configuration of the complex. *Chem Commun.* **2016,** *52*, 12380-12382.

219. Hsu, S. C.; Lin, G.-M.; Lee, G. H.; Chen, C. H.; Peng, S. M., Pentanuclear Heterometallic String Complexes with High-Bond-order Units $[Ni_2^{3+}\text{–}Mo_2^{4+}\text{–}Ni^{2+}(bna)_4X_2]^{3+}$ (X = Cl, NCS). *J. Chin. Chem. Soc.* **2017,** *65*, 122-132.

220. Chakravarty, A., Chemistry of diruthenium compounds having metal-metal multiple bonds. *Proc. Indian Natil. Sci. Acad.* **1986,** *52*, 749-763.

221. Huang, M.-J.; Hua, S.A.; Fu, M.-D.; Huang, G.C.; Yin, C.; Ko, C.H.; Kuo, C.K.; Hsu, C.H.; Lee, G.H.; Ho, K.Y.; Wang, C.H.; Yang, Y.W.; Chen, I. C.; Peng, S.M.; Chen, C.H., The first heteropentanuclear extended metal-atom chain: $[Ni^{+}\text{-}Ru_2^{5+}\text{-}Ni^{2+}\text{-}Ni^{2+}$ (tripyridyldiamido)$_4$(NCS)$_2$]. *Chemistry (Weinheim an der Bergstrasse, Germany)* **2014,** *20* (16), 4526-31.

222. Uemura, K.; Fukui, K.; Yamasaki, K.; Matsumoto, K.; Ebihara, M., Synthesis, Crystal Structure, and Characterization of a Heterometallic One-Dimensional Complex with Metal–Metal Bonds. *Inorg. Chem.* **2010,** *49*, 7323-7330.

223. Uemura, K.; Ebihara, M., Paramagnetic One-Dimensional Chains Comprised of Trinuclear Pt–Cu–Pt and Paddlewheel Dirhodium Complexes with Metal–Metal Bonds. *Inorg. Chem.* **2013,** *52*, 5535-5550.

224. Uemura, K.; Uesugi, N.; Matsuyama, A.; Ebihara, M.; Yoshikawa, H.; Awaga, K., Integration of Paramagnetic Diruthenium Complexes into an Extended Chain by Heterometallic Metal–Metal Bonds with Diplatinum Complexes. *Inorg. Chem.* **2016,** *55*, 7003-7011.

225. Cotton, F. A.; DeBoer, B. G.; LaPrade, M. D.; Pipal, J. R.; Ucko, D. A., The crystal and molecular structures of dichromium tetraacetate dihydrate and dirhodium tetraacetate dihydrate. *Acta Crystallographica Section B* **1971,** *27*, 1664-1671.

226. Mutikainen, I.; Orama, O.; Pajunen, A.; Lippert, B., The crystal structure of a heteronuclear Pt_2CuL_4 complex of 1-methyluracil, $Cu[Pt(NH_3)_2(C_5H_5N_2O_2)_2]_2SO_4{\cdot}8H_2O$. *Inorg. Chim. Acta* **1987,** *137*, 189-193.

227. Schreiber, A.; Krizanovic, O.; Fusch, E. C.; Lippert, B.; Lianza, F.; Albinati, A.; Hill, S.; Goodgame, D. M. L.; Stratemeier, H.; Hitchman, M. A., Heteronuclear Complexes Derived from trans-a_2PtL_2(a=NH_3 or CH_3NH_2, L=2-Pyridonate). Distorted Coordination Geometries of All Three Metals in trans-$[a_2PtL_2CuL_2Pt(a_2)]^{2+}$ and an Extraordinary Short Hydrogen Bond in trans-$[a_2PtL(LH)]^{+}$. *Inorg. Chem.* **1994,** *33*, 6101-6110.

228. Barton, J. K.; Szalda, D. J.; Rabinowitz, H. N.; Waszczak, J. V.; Lippard, S. J., Solid state structure, magnetic susceptibility, and single crystal ESR properties of cis-diammineplatinum a pyridone blue. *J. Am. Chem. Soc.* **1979,** *101*, 1434-1441.

229. Barton, J. K.; Rabinowitz, H. N.; Szalda, D. J.; Lippard, S. J., Synthesis and crystal structure of cis-diammineplatinum a pyridone blue. *J. Am. Chem. Soc.* **1977,** *99*, 2827-2829.

230. Uemura, K., Magnetic behavior in heterometallic one-dimensional chains or octanuclear complex regularly aligned with metal–metal bonds as –Rh–Rh–Pt–Cu–Pt. *Journal of Molecular Structure* **2018,** *1162*, 31-36.

Chapter Three

Extraordinarily Large Ferromagnetic Coupling ($J \geq 150$ cm^{-1}) via Electron Delocalization in a Heterometallic Mo≡Mo–Ni Chain Complex

Jill A. Chipman and John F. Berry

This chapter is adapted from *Extraordinarily Large Ferromagnetic Coupling (J≥150 cm^{-1}) via Electron Delocalization in a Heterometallic Mo≡Mo–Ni Chain Complex*

Reprinted with permission from Chipman, J.A; Berry, J.F *Chem. Eur. J.* **2018,** *24*, 1494-1499.

3.1 Abstract

The new heterometallic chain compounds $Mo_2Ni(dpa)_4Cl_2$ (**1**) and $[Mo_2Ni(dpa)_4Cl_2]OTf$ (**2**) (dpa = 2,2'-dipyridylamine) have been prepared and studied by crystallography and magnetic susceptibility, among other methods. Oxidation of **1** to **2** removes an electron from the multiply-bonded Mo_2 unit, consistent with the formulation of 2 as containing a $(Mo_2)^{5+}\cdots(Ni)^{2+}$ core. While **1** contains an $S = 1$, pseudo-octahedral Ni(II) ion, **2** has an $S = 3/2$ ground state in which the two Ni(II) unpaired electrons are joined by an unpaired electron in a Mo—Mo δ orbital. The $S = 3/2$ ground state is persistent to 300 K, evidencing strong ferromagnetic coupling of the Mo_2 and Ni spins with $J \geq 150$ cm^{-1}. This ferromagnetic interaction occurs via delocalization of a σ_{nb} electron across all three metal atoms, forcing ferromagnetic alignment of electrons in orthogonal Ni and Mo_2 δ-symmetry orbitals. We anticipate that this new means of coupling spins can be used as a design principle for the preparation of new compounds with high spin ground states.

3.2 Introduction

Control of electron spins at the atomic level is a major goal in molecular magnetism.[1-4] Orbital overlap is an important guiding principle for achieving such control, as electrons in overlapping orbitals will couple antiferromagnetically via superexchange whereas electrons in orthogonal orbitals will couple ferromagnetically.[5] Electron delocalization is another fundamental design principle exemplified by the "double exchange" mechanism, whereby delocalization of one or more "itinerant" β-spin electrons leads to alignment of α-spin electrons on two adjacent metal centers (Scheme 3.1A).[6-10] In this mechanism, it is the strong antiferromagnetic interaction between the majority spins and the delocalized electron that leads to a high-spin ground state, an exact molecular analogy to the concept of ferrimagnetism in bulk materials.

The double exchange mechanism implies orbital overlap between the α-spins and the β-spin itinerant electron. But what if the orbitals housing these electrons were orthogonal? Can an α-spin itinerant electron cause alignment of α-spins in neighboring metal atoms via orbital orthogonality – spins that would otherwise couple antiferromagnetically (Scheme 3.1B)? We present an unusual heterotrimetallic Mo≣Mo–Ni chain complex in which this effect is observed: delocalization of a σ-symmetry electron across the Mo≣Mo–Ni chain causes ferromagnetic alignment of δ-symmetry electrons at both the Mo_2 and Ni centers.

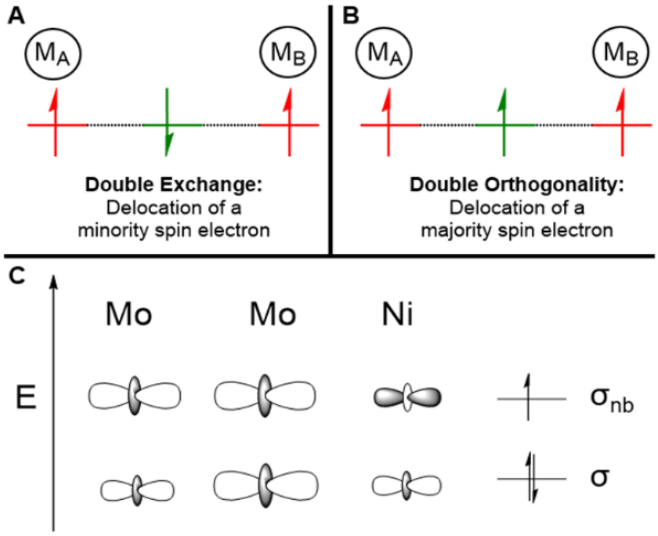

Scheme 3.1. Spin coupling mechanisms involving (A) electron delocalization of a minority spin electron (the double exchange mechanism) and (B) a majority spin electron as described in this work. (C) The 3-center/3 electron σ bond within the Mo≣Mo–Ni core.

Over the past decade, we [11-20] and others[21-30] have studied heterometallic extended metal atom chains (HEMACs), which contain a linear string of three or more metal centers supported by four triply-bridging ligands. Of specific interest to this work are trimetallic HEMACs of the form $M_A{\equiv}M_A{-}M_B$ in which a quadruply bonded pair of group VI metals is appended to a high-spin divalent first row transition metal. In these complexes, the M_A and M_B d_{z^2} orbitals overlap resulting in a 3-center/3-electron bond within the complex in which an unpaired electron occupies a 3-center σ_{nb} orbital as shown in Scheme 3.1C.[17, 31]

We have found $Mo{\equiv}Mo{-}M(dpa)_4X_2$ compounds to be more chemically robust than their $Cr{\equiv}Cr{-}M(dpa)_4X_2$ counterparts, which are unstable to chemical oxidation.[11] Additionally, a recent report of unusually large single molecule conductance behavior of $Mo{\equiv}Mo{-}Ni(dpa)_4(NCS)$[32] prompts an investigation into the electronic structures of $Mo{\equiv}Mo{-}Ni$ chain compounds. Oxidation of $M_A{\equiv}M_A{-}M_B$ HEMACS with M_A = Mo has been proposed to remove an electron from the Mo_2 δ-bonding orbital but until this report, we have been unable to stabilize such an oxidized complex.[12, 18-19, 33] The only HEMACs that have been amenable to chemical oxidation have had a different type of electronic structure.[21-22, 26-27] Thus, we were curious whether a $Mo{\equiv}Mo{-}M(dpa)_4X_2$ complex in which M is a first-row transition metal could be stable to one-electron oxidation.

3.3 Results and Discussion

Our lab has established synthetic methods for accessing $Mo_2M_B(dpa)_4Cl_2$ complexes where M_B is Cr, Mn, Fe, or Co.[12, 14-15, 19] $Mo_2Ni(dpa)_4Cl_2$, **1**, was prepared analogously through reaction of $Mo_2(dpa)_4$ with 1.5 equivalents of $NiCl_2$ in molten naphthalene (Scheme 3.2).

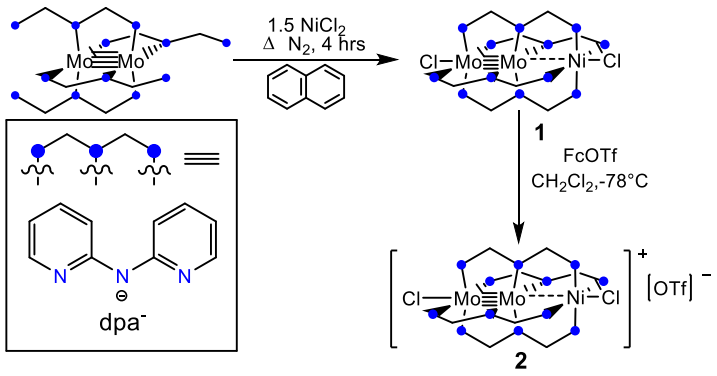

Scheme 3.2 Preparation of $Mo_2Ni(dpa)_4Cl_2$ (**1**) and $[Mo_2Ni(dpa)_4Cl_2]OTf$ (**2**)

Compound **1** contains a linear Mo≡Mo–Ni framework buttressed by a helical set of four dpa ligands. The cyclic voltammogram of **1** illustrates a quasi-reversible $Mo_2^{4+/5+}$ oxidation wave at $E_{1/2}$ = -0.418 V vs Fc/Fc^+, approximately 0.10 V more positive than for the other Mo≡Mo–M_B HEMACs.[12, 19] This observation is consistent with the increased electronegativity of Ni relative to the other M_B metals studied. Given the reversibility of this wave, it seemed plausible that a one-electron oxidized compound might also be stable. Indeed, upon dropwise addition of a solution of $FeCp_2OTf$ to a CH_2Cl_2 solution of **1** at –78 °C, an initially fleeting hint of maroon appeared, which became persistent over time. Addition of pentane yields a maroon colored solid, which was isolated and crystallized by slow diffusion of pentane into a CH_2Cl_2 solution at –78 °C. Deep purple needles of **2** were obtained in 59% yield.

The molecular structures of **1** and **2** are shown in Figure 3.1. From **1** to **2** both the Mo–Mo distance and the Mo–Ni distance increased by approximately 0.02 Å from 2.107(2) Å to 2.129(3) Å and 2.525(4) Å to 2.552(4) Å, respectively. There is a substantial contraction (0.08 Å) of the Mo–Cl distance and no change in the Ni–Cl distance (Table 3.1). Overall, these changes support the idea that the oxidation is localized to the Mo_2 unit. To investigate this hypothesis further, we turned to UV-vis/NIR spectroscopy to characterize **1** and **2** in solution.

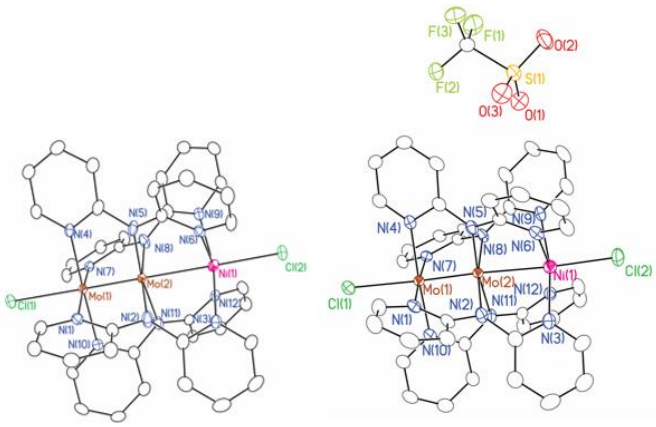

Figure 3.1. Crystal structures of **1** (left) and **2** (right.) Hydrogen atoms and any solvent molecules have been removed for clarity.

Table 3.1. Changes in bond distances between **1** and **2**.

Bond	Length in **1** (Å)	Length in **2** (Å)	Change (Å)
Mo–Mo	2.107(2)	2.129(3)	+ 0.022
Mo–Ni	2.524(4)	2.552(4)	+ 0.020
Mo–Cl	2.627(2)	2.545(2)	- 0.082
Ni–Cl	2.394(3)	2.394(3)	0.000
Mo–N_{inner}(av)	2.174[3]	2.080[4]	- 0.093
Mo–N_{outer}(av)	2.115[3]	2.163[4]	+ 0.048
Ni–N(av)	2.146[3]	2.156[5]	+ 0.010

UV-vis spectra of **1** and **2** are given in Figure 3.2. The spectrum of **1** is notably similar to those of other $Mo_2M_B(dpa)_4Cl_2$ compounds and allows us by analogy to assign the features at 494 nm (ε = 13,100) and 671 nm (ε = 2,400) as a MLCT transition and a Mo_2 δ – δ* transition, respectively. These findings are further supported through time dependent DFT (TDDFT) calculations. Compared to **1**, we observe a red shift in all the transitions in **2**. Of note are the features at 1074 nm, which are metal-to-metal charge transfer transitions that are made available by a hole in the Mo_2 δ orbital.

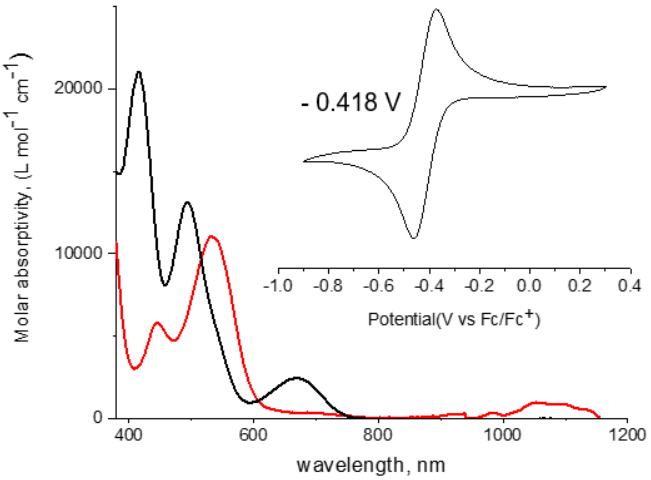

Figure 3.2. UV-vis and near IR spectrum of **1** (black) and **2** (red). Inset: cyclic voltammogram of **1**.

Magnetic susceptibility data for **1** and **2** are shown in Figure 3.3 with the data summarized in Table 3.2. The χ·T value for **1** at 300 K, 1.09 emu·K·mol^{-1}, agrees with the spin-only value for an S = 1 system of

1.0 emu·K·mol^{-1}. In the case of **2** the high temperature limit in our data is 1.75 emu·K·mol^{-1}, for which the only reasonable assignment is to an S = 3/2 system (spin only value of 1.875 emu·K·mol^{-1}). Thus, the data for **1** and **2** were modeled as S = 1 or S = 3/2 systems, respectively. For both **1** and **2**, a sharp downward feature is seen in the χ·T vs. T plot below 50 K, indicative of zero field splitting. The data for **1** and **2** were fitted with g_{iso} = 1.935(3); $|D|$= 9.19(3) cm^{-1}, and g_{iso} = 1.906(3); $|D|$ = 2.86(4) cm^{-1}, respectively.

For **2**, fitting the data as an S = 3/2 system suggests that **2** is a strongly ferromagnetically coupled system (S_{Ni} = 1/2 and S_{Ni} = 1; total S = 3/2). Although we were unable to directly obtain a fitted value for the Mo_2···Ni exchange parameter J, simulations of the data with coupled S_{Mo2} and S_{Ni} centers indicate a lower bound of 150 cm^{-1} (Figure 3.4) . These results contrast with previous examples of M_A–M_B–M_A HEMACs that exclusively display antiferromagnetic coupling between M_A centers.[22, 26-28]

Table 3.2. SQUID Magnetometer Fit Parameters for **1** and **2**.

	1	**2**
$g_\perp$	2.171(1)	2.299(3)
$g_\parallel$	1.817(4)	1.710(2)
|D|	9.19(3)	2.86(4)
ZJ	0.273(3)	0.9(4)
TIP	0.7(1)	
Residual	0.00138	0.00566

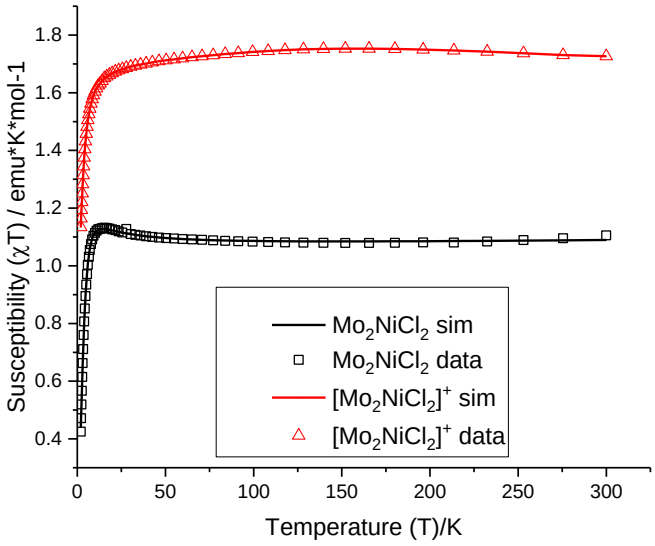

Figure 3.3. Variable temperature magnetic susceptibility data for **1** (black squares) and **2** (red triangles).

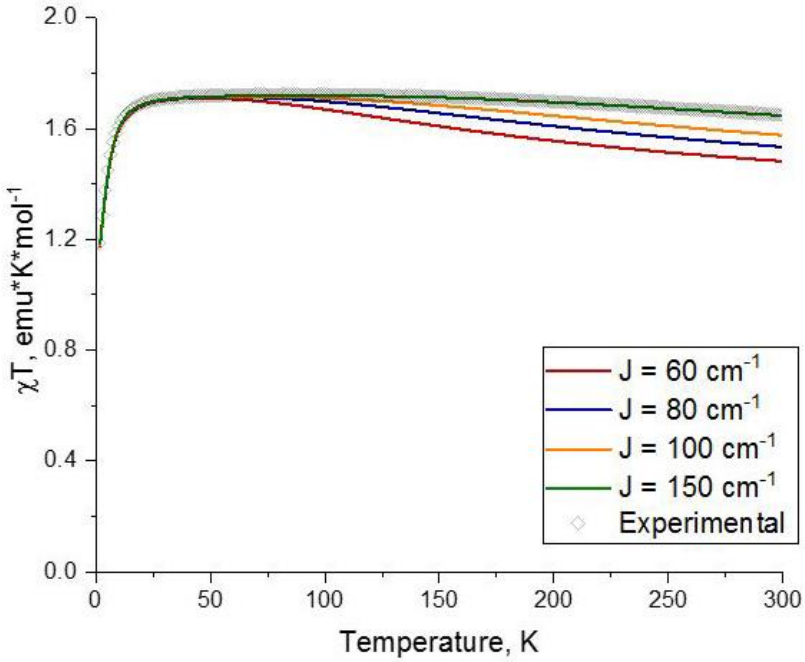

Figure 3.4. Simulations of the exchange parameter *J* against the experimental data for **2**.

In addition to magnetic susceptibility measurements, a frozen solution X-band EPR spectrum of **2** was collected (Figure 3.5). Compound **2** displays an axial signal with effective *g* values of $g_{\parallel,\mathrm{eff}}$ = 2.063 and $g_{\perp}$,eff = 3.897, which are characteristic of an $S = 3/2$ system where $D >>$ hv, and confirm the assignment of

the $S = 3/2$ ground state. The spectrum was modeled with $S = 3/2$, intrinsic $g_{\parallel}$ =2.060, $g_{\perp}$ = 2.069, and E/D = 0.039, indicative of nearly axial symmetry. An additional Mo (^{97}Mo and ^{95}Mo) hyperfine interaction was observable on the parallel component ($A_{\parallel}$= ~250 MHz.) This hyperfine interaction in **2** is strikingly large in comparison to other Mo–Mo bonded systems where A values range from 107–135 MHz.[34-37] The largest value in this range corresponds to $[Mo_2Ru(dpa)_4Cl_2]^+$, in which the unpaired electron is nearly completely localized on a single Mo center. Thus, there appears to be an even greater Mo spin population in **2**.

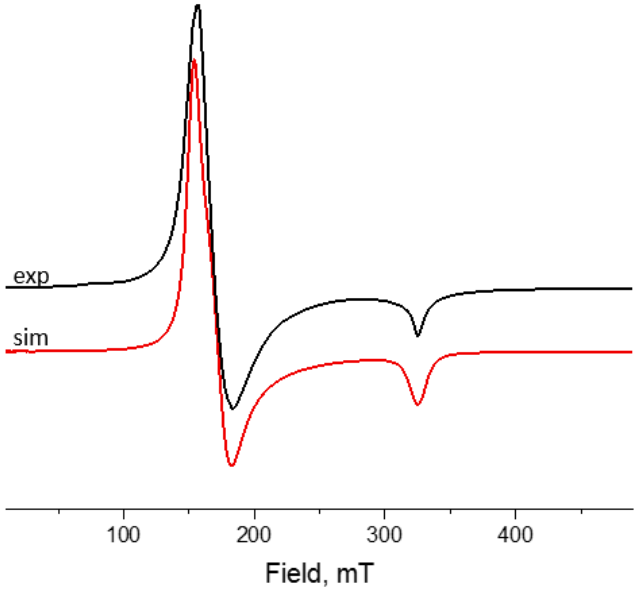

Figure 3.5. Simulated (red) and experimental (black) EPR spectra of **2** at 8 K. Simulation parameters are as follows: freq. 9.3846 GHz; $g_{\parallel}$ = 2.060, $g_{\perp}$ = 2.069, $A_{\parallel}$ = ~250 MHz; H-strain [700 200 225]; lw =11, points = 1024.

These experimental findings are supported by density functional theory (DFT) calculations. Single-point DFT calculations allow for comparison between the electronic structures of compounds **1** and **2** as well as other HEMAC compounds. As described above, **1** features a 3*c*/3*e* σ bond consisting of a doubly-occupied σ bonding orbital formed via overlap of the Mo_2 and Ni d_{z^2} orbitals plus single occupation of the corresponding σ_{nb} orbital. An additional unpaired electron is localized on a Ni $d_{x^2-y^2}$ type orbital that makes a strong antibonding interaction with the dpa N atoms.[38-42] This is similar to our previous bonding description for the series of $Mo_2M_B(dpa)_4Cl_2$ in which M_B represents a first-row transition metal.[18-19]

Upon oxidation, an electron is removed from the Mo_2 unit leaving an unpaired electron in the Mo_2 δ_{xy} orbital (Figure 3.6). Due to the helical twisting about the Mo–Mo–Ni axis, the Mo_2 δ_{xy} and Ni $d_{x^2-y^2}$ orbitals have the same symmetry and can overlap with each other, suggesting that we should see antiferromagnetic coupling between the Mo_2 and Ni centers. However, the σ_{nb} orbital is delocalized over all three metal atoms and is rigorously orthogonal to both of the Mo_2 and Ni δ symmetry orbitals. Thus, the prevailing interaction is a ferromagnetic one identical to what is depicted in Scheme 3.1B in which the red electrons are of δ symmetry and the green itinerant electron has σ symmetry. Notably, the lowest energy S = 1/2 state is predicted by DFT to be ~340 cm^{-1} higher in energy than the S = 3/2 ground state. This energy difference corresponds to 3J and is therefore in good agreement with our estimate for $J \geq 150$ cm^{-1} from the magnetic data.

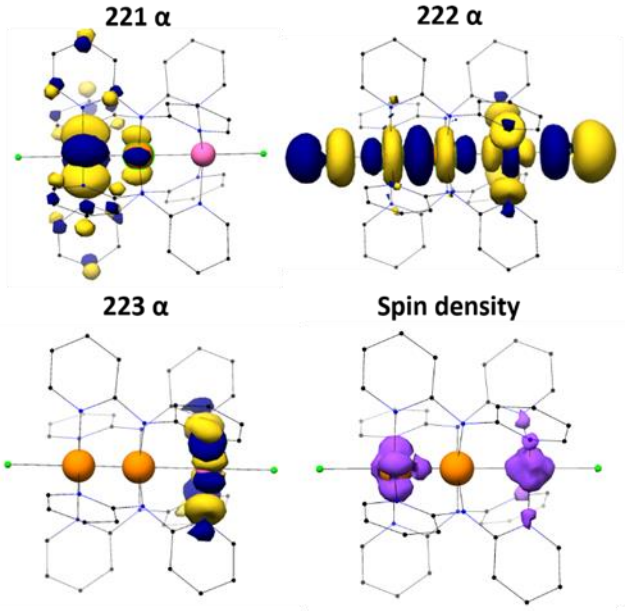

Figure 3.6. (A–C) Singly occupied orbitals contributing to the S = 3/2 ground state of **2** (orange balls represent the Mo atoms and the pink ball represents the Ni atom). (D) Spin density plot of **2**.

3.4 Summary

Thus, in reporting the first example of a one-electron oxidized $Mo_2M_B(dpa)_4Cl_2$ monocation in which M_B represents a first-row transition metal, we find that the cation displays unusual, strongly ferromagnetic coupling affording an S = 3/2 ground state that persists to room temperature. This conclusion is supported through EPR spectroscopy, SQUID magnetometry, as well as DFT computations.

The ferromagnetism arises via a new mechanism in which a delocalized itinerant electron couples ferromagnetically to electrons in orthogonal orbitals in neighboring spin centers. The resulting magnitude of the coupling ($J \geq 150$ cm^{-1}) suggests promise for the use of this effect in the design of novel magnetic materials.

3.5 Acknowledgements

This work was supported in part by the National Science Foundation. Computational facilities were supported by the NSF under Grant CHE-0840494. The Bruker Impact™ II mass spectrometer was funded via a bequest from Paul J. and Margaret M. Bender. We thank Dr. Tzuhsiung Yang for help interpreting the computational data, and Dr. Brian S. Dolinar for crystallographic advice.

3.6 Supporting Information

Materials and Methods

All reactions were carried out under a dry N_2 atmosphere using Schlenk techniques and glovebox methods. Pentane was purified using a Vacuum Atmospheres solvent purification system. Dichloromethane was freshly distilled under N_2 over CaH_2 prior to use. $FeCp_2OTf$ and $Mo_2(dpa)_4$ were prepared according to previous literature procedures.[35, 43] Naphthalene was purchased from Sigma-Aldrich and sublimed prior to use. Anhydrous hexanes were purchased from Sigma-Aldrich and degassed prior to use. $NiCl_2$ was purchased from Strem Chemicals and used as received. The ligand Hdpa was purchased from TCI and recrystallized from hot hexanes prior to use. Elemental analysis was carried out by Midwest Microlabs, LLC, Indianapolis, IN. IR spectra were taken on a BRUKER TENSOR 27 FTIR spectrometer using an attenuated total reflectance (ATR) adapter. Cyclic voltammograms (CVs) were taken on a BASI Epsilon EC instrument using CH_2Cl_2 solutions with 0.1 M NBu_4PF_6 and 1 mM substrate. The electrodes were as follows: glassy carbon (working), Pt wire (auxiliary), and Ag/Ag^+ in CH_3CN (reference). The potentials were referenced against the ferrocene/ferrocenium redox couple by external addition of ferrocene. The EPR measurement was carried out at 8K using a Bruker EleXeys EPR Spectrometer (E-500A console with ER 0495X SuperX bridge and SuperX cavity). The parameters were as follows: frequency = 9.3846 GHz, microwave power = 1.589 mW; field center 4000 G; time constant 20.48. MALDI mass spectra were obtained on Bruker Impact™ II MALDI mass spectrometer. Variable temperature magnetic susceptibilities of crystalline samples of **1** and **2** were recorded at the University of Wisconsin-Madison on a SQUID magnetometer

(MPMS 3 Quantum Design) in the temperature range 2-300 K with an applied field of 0.1 Tesla. Experimental susceptibility and magnetization data were corrected for the underlying diamagnetism using Pascal's constants and for the temperature independent paramagnetism contributions. The data were modeled using the program PHI.[34] The crystal structures were deposited in the CCDC with deposition numbers 1576876 for **1** and 1576877 for **2**.

Crystallography

Crystallographic data were measured at the Molecular Structure Laboratory of the Chemistry Department of the University of Wisconsin—Madison. Crystals were selected under oil under ambient conditions and attached to the tip of a MiTeGen MicroMount©. Each crystal was mounted under a stream of cold nitrogen at 100(1) K and centered in the X-ray beam using a video camera. The crystal evaluation and data collection were performed on a Bruker Quazar SMART APEXIII diffractometer with Mo K-α (λ = 0.71073 A) radiation with a detector to crystal distance of 5.0 cm. The data were collected using a routine to survey the entire sphere of reciprocal space, and were indexed by the SMART program.[44] The structures were solved using direct methods and refined by least-squares refinement on F^2 followed by difference Fourier synthesis.[45] All hydrogen atoms were included in the final structure factor calculation at idealized positions and were allowed to ride on the neighboring atoms with relative isotropic displacement coefficients. Due to crystallographic disorder, the metal atoms of **2** were unable to be refined anisotropically and were thus left refined isotropically.

Computational Methods

The initial coordinates for **1** and **2** were obtained from the crystallographic data for the compounds with the solvent molecules of crystallization removed and the dominant orientation for any disorder utilized. All calculations were carried out using the program package ORCA version 3.0.3.[46] The BP86 exchange-correlation functional,[47-48] including the ZORA approximation was used.[49] The Stuttgart-Dresden effective core potential (ECP), def2-SD,[50] was used along with valence basis sets def2-TZVP and density fitting basis set def2-TZVP/J for Mo atoms.[51-52] The def2-TZVP basis set and def2-TZVP/J auxiliary basis set was used for Ni.[53-54] The def2-SVP basis set and def2-SVP/J density fitting basis set were used for all other atoms.[53-54] Tight optimization and tight self-consistent field convergence criteria were employed along with grid4 for all calculations. Frequency calculations were formed following geometry optimizations to

ensure the structures were at local minimum. Löwdin population analysis was done to determine orbital populations.[55-56] Visualizations were performed with the UCSF Chimera package.[57] Symmetry labels presented in the molecular orbital diagrams were assigned by inspection to conform to the idealized C_4 point group.

$Mo_2Ni(dpa)_4Cl_2$ (**1**) Solid brick-red $Mo_2(dpa)_4$ (406.2 mg, 0.466 mmol) and $NiCl_2$ (97.0 mg, 0.745 mmol) were combined with naphthalene (5 g) in a Schlenk flask. The flask was placed in a sandbath that had been preheated to 220°C and the reaction mixture was stirred for 4 hours during which it became brown in color. After cooling to room temperature, the mixture was washed with hot hexanes (4 x 40 mL). The residual dark solid was dried under vacuum and subsequently extracted with CH_2Cl_2 (30 mL). The dark green extract was then layered with hexanes (70 mL). Dark colored X-ray quality blocks of **1** were obtained after 3 days. Yield 182.6 mg, 39%. Anal Cald for $Mo_2Ni(dpa)_4Cl_2$: C, 47.93; H, 3.22; N 16.77. Found: C,47.92; H, 3.19; N, 16.64. IR (ATR, cm^{-1}); 3069 w, 1601 w, 1592, w, 1563 w, 1544 w, 1459 s, 1417 s, 1347 m, 1311 s, 1284 w, 1260 w, 1154 m, 1058 w, 1015 m, 1014 m, 882 w, 856 w, 763 s, 750 w, 738 s, 690 w, 636 w.

$[Mo_2Ni(dpa)_4Cl_2]SO_3CF_3$ (**2**) $Mo_2Ni(dpa)_4Cl_2$ (87.4 mg, 0.0870 mmol), was dissolved in 40 mL of dichloromethane and cooled to -78 °C. Then, 6.80 mL of a navy blue 13 mM $FcSO_3CF_3$ solution, also at -78 °C was added dropwise to the brown $Mo_2Ni(dpa)_4Cl_2$ solution affording a deep maroon solution. This solution was allowed to stir at -78 °C for 30 minutes after which it was added to 200 mL of chilled pentane at -78 °C. A maroon precipitate formed with the orange/yellow supernatant. This mixture was then filtered, and the orange-yellow supernatant was discarded. The resulting solid was extracted with CH_2Cl_2 (2 x 15 mL) and layered to 100 mL with cold pentane at -78 °C. X-ray quality crystals of **2** formed after 1 week at -78 °C. Yield: 59.33 mg, 59.33%. Anal Cald for $Mo_2Ni(dpa)_4Cl_2 \cdot 2CH_2Cl_2$: C, 39.09; H, 2.75; N,12.72. Found C, 39.21, H, 2.89; N,12.74. IR (ATR, cm^{-1}) 1602 m, 1566 w, 1552 w, 1471 w, 1460 s, 1422 s, 1339 m, 1311 m, 1270 w, 1258 w, 1231 m, 1157 m, 1113 m 1058 m, 1017 w, 859 w, 767 s, 751 s, 743 w, 731 m, 726 m, 692 m, 670 m, 666 (m), 661 (m), 653 m, 648 m, 636 s.

Table S3.1. Crystallographic Data for $Mo_2Ni(dpa)_4Cl_2$ (**1**) and $[Mo_2Ni(dpa)_4Cl_2]SO_3CF_3$ (**2**) at 100 K.

Formula	**$Mo_2NiC_{40}H_{32}N_{12}\cdot C_4H_8O$**	**$[Mo_2NiC_{40}H_{32}N_{12}]SO_3CF_3\cdot 2(CH_2Cl_2)$**
Crystal system	monoclinic	triclinic
Space group	$P2_1/c$	$P\bar{1}$
a/Å	16.1186(6)	12.0215(3)
b/Å	15.7622(6)	14.4876(4)
c/Å	16.9848(7)	15.4157(4)
α/°	90	90.135(2)
β/°	98.435(2)	102.780(2)
γ/°	90	98.930(2)
V/Å^3	4268.6(3)	2584.7(1)
Z	4	2
ρ_{calc}g/cm^3	1.673	1.807
R_1[a] [I>=2σ (I)]	R_1 = 0.0363, wR_2 = 0.0806	R_1 = 0.0534, wR_2 = 0.1473
R_1[b] [all data]	R_1 = 0.0430, wR_2 = 0.0833	R_1 = 0.0650, wR_2 = 0.1537

[a] $R1 = \Sigma\big||F_o| - |F_c|\big|/\Sigma|F_o|$

[b] $wR2 = [\Sigma[w(F_o^2 - F_c^2)^2/\Sigma[(w(F_o^2)^2]]^{\frac{1}{2}}$, $w = 1/\sigma^2(F_o^2) + (aP)^2 + bP$ where $P = [\max(0 \text{ or } F_o^2) + 2(F_c^2)]/3$.

Table S3.2 Mayer Bond Orders for **1** and **2**

Compound	Mo – Mo	Mo – Ni
1	2.6969	0.5398
2	2.4810	0.5125

Table S3.3. Spin Populations for **1** and **2.**

Compound	Mo1	Mo2	Ni	Cl1	Cl2
1	0.052678	0.197549	1.319673	0.062822	0.095524
2	0.058296	0.960333	1.319171	0.056691	0.116705

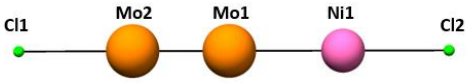

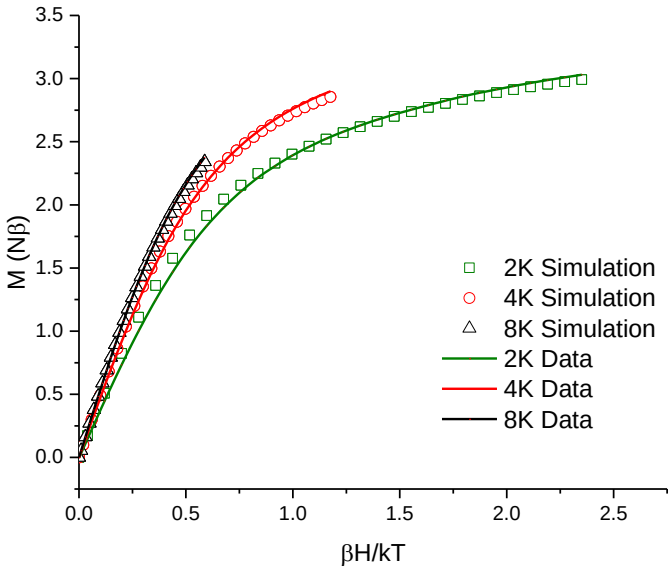

Figure S3.1. Reduced magnetization data for **2**. The data shown in Figure S1 were modeled with $S = 3/2$ in which $g_{\parallel} = 2.299(7)$ and $g_{\perp} = 2.072(8)$ with $|D| = 2.79(6)$ cm^{-1}.

Figure S3.2. Comparison of molecular orbital diagrams for **1** and **2.** Orbitals localized on the Mo_2 core are shown in red, blue labels correspond to Ni centered orbitals, and green labels represent delocalized orbitals across the Mo_2Ni unit.

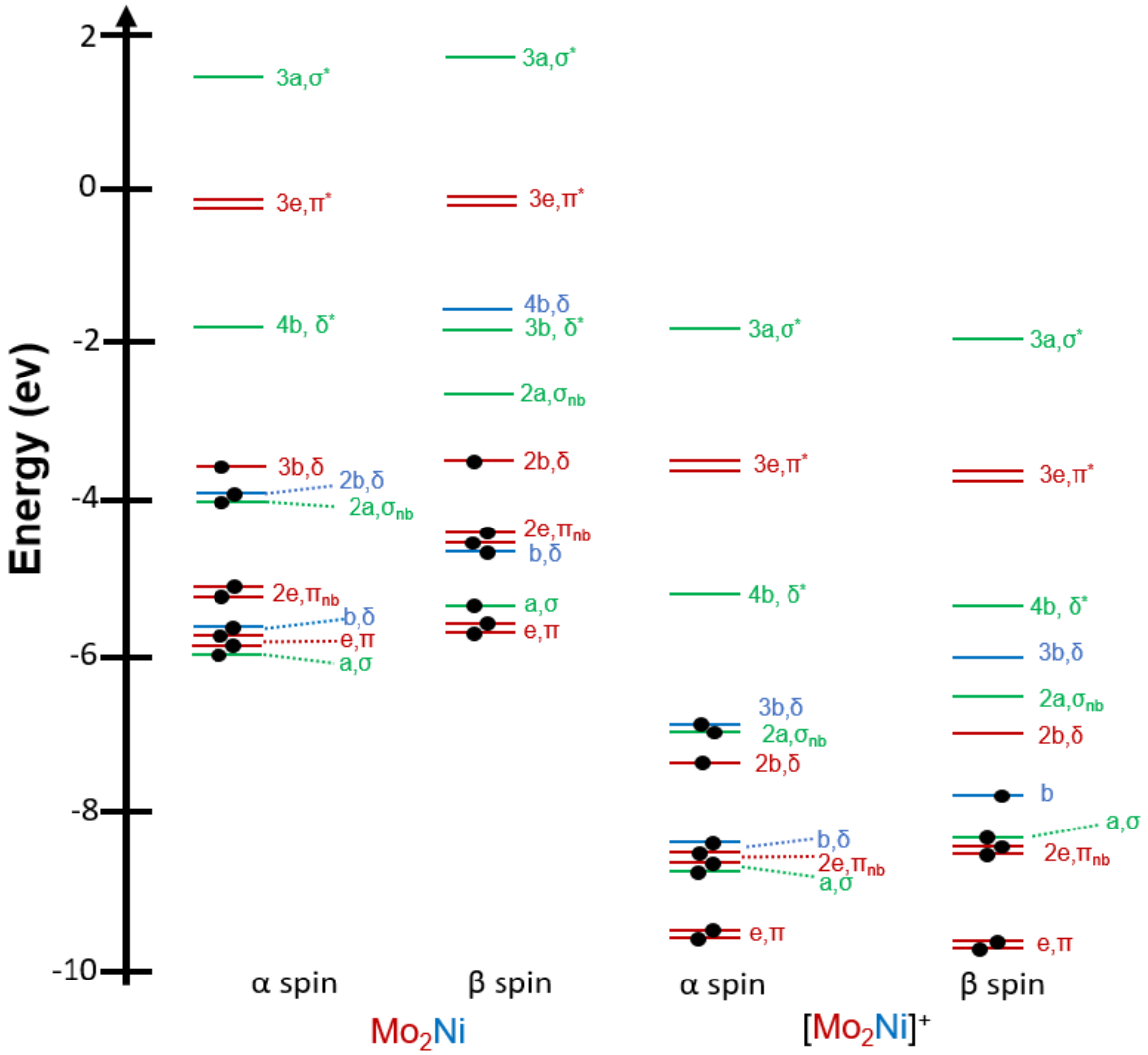

Figure S3.3. TDDFT transitions for **2** in the near IR region.

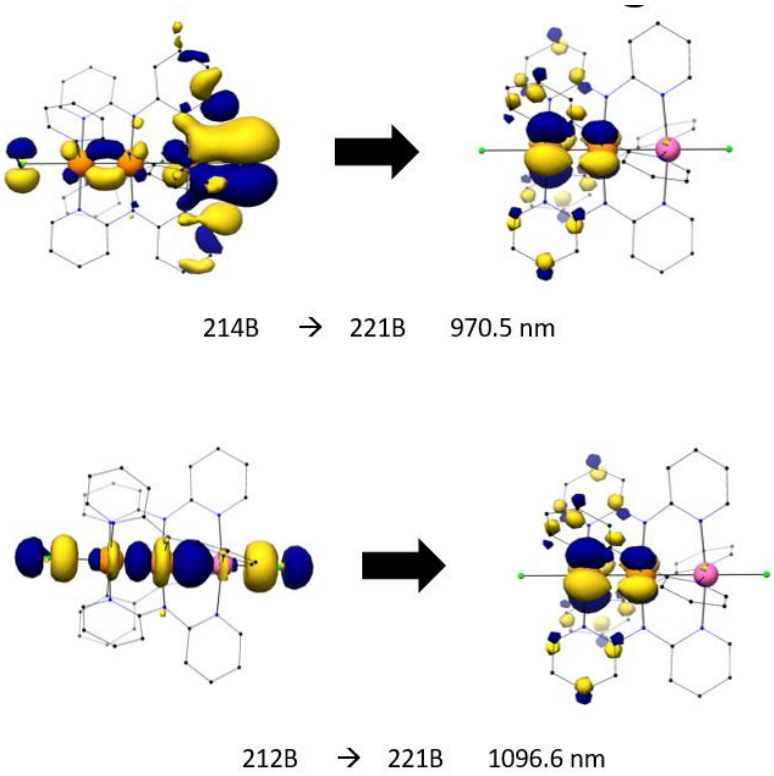

References

1. Glaser, T., Rational design of single-molecule magnets: a supramolecular approach. *Chem. Commun.* **2011,** *47*, 116-130.

2. Malrieu, J. P.; Caballol, R.; Calzado, C. J.; de Graaf, C.; Guihéry, N., Magnetic Interactions in Molecules and Highly Correlated Materials: Physical Content, Analytical Derivation, and Rigorous Extraction of Magnetic Hamiltonians. *Chem. Rev.* **2014,** *114*, 429-492.

3. Frost, J. M.; Harriman, K. L. M.; Murugesu, M., The rise of 3-d single-ion magnets in molecular magnetism: towards materials from molecules? *Chem. Sci.* **2016,** *7*, 2470-2491.

4. Aromí, G.; Gamez, P.; Roubeau, O., Molecular Magnetism. In *Spin States in Biochemistry and Inorganic Chemistry*, John Wiley & Sons, Ltd: 2015; pp 263-296.

5. Kahn, O., *Molecular magnetism*. VCH: 1993.

6. Reger, D. L.; Pascui, A. E.; Foley, E. A.; Smith, M. D.; Jezierska, J.; Wojciechowska, A.; Stoian, S. A.; Ozarowski, A., Dinuclear Metallacycles with Single M–X–M Bridges (X = Cl^-, Br^-; M = Fe(II), Co(II), Ni(II), Cu(II), Zn(II), Cd(II)): Strong Antiferromagnetic Superexchange Interactions. *Inorg. Chem.* **2017,** *56*, 2884-2901.

7. Bechlars, B.; D'Alessandro, D. M.; Jenkins, D. M.; Iavarone, A. T.; Glover, S. D.; Kubiak, C. P.; Long, J. R., High-spin ground states via electron delocalization in mixed-valence imidazolate-bridged divanadium complexes. *Nat Chem* **2010,** *2*, 362-368.

8. Powell, A. K., Molecular magnetism: A bridge to higher ground. *Nat Chem* **2010,** *2*, 351-352.

9. Zener, C., Interaction between the d-Shells in the Transition Metals. II. Ferromagnetic Compounds of Manganese with Perovskite Structure. *Phys. Rev.* **1951,** *82*, 403-405.

10. Gatteschi, D.; Sessoli, R.; Villain, J., Molecular Nanomagnets. Nature Publishing Group: 2006.

11. Nippe, M.; Berry, J. F., Introducing a Metal–Metal Multiply Bonded Group as an "Axial Ligand" to Iron: Synthetic Design of a Linear Cr–Cr···Fe Framework. *J. Am. Chem. Soc.* **2007,** *129*, 12684-12685.

12. Nippe, M.; Bill, E.; Berry, J. F., Group 6 Complexes with Iron and Zinc Heterometals: Understanding the Structural, Spectroscopic, and Electrochemical Properties of a Complete Series of M≣M···M′ Compounds. *Inorg. Chem.* **2011,** *50*, 7650-7661.

13. Nippe, M.; Timmer, G. H.; Berry, J. F., Remarkable regioselectivity in the preparation of the first heterotrimetallic Mo≣W···Cr chain. *Chem Commun.* **2009**, 4357-4359.

14. Nippe, M.; Victor, E.; Berry, J. F., Do Metal–Metal Multiply-Bonded "Ligands" Have a trans Influence? Structural and Magnetic Comparisons of Heterometallic Cr≣Cr···Co and Mo≣Mo···Co Interactions. *Eur. J. Inorg. Chem.* **2008**, 5569-5572.

15. Nippe, M.; Wang, J.; Bill, E.; Hope, H.; Dalal, N. S.; Berry, J. F., Crystals in Which Some Metal Atoms are More Equal Than Others: Inequalities From Crystal Packing and Their Spectroscopic/Magnetic Consequences. *J. Am. Chem. Soc.* **2010,** *132*, 14261-14272.

16. Brogden, D. W.; Berry, J. F., Coordination Chemistry of 2,2'-Dipyridylamine: The Gift That Keeps on Giving. *Comments on Inorganic Chemistry* **2016,** *36*, 17-37.

17. Brogden, D. W.; Berry, J. F., Heterometallic Multiple Bonding: Delocalized Three-Center σ and π Bonding in Chains of 4d and 5d Transition Metals. *Inorg. Chem.* **2014,** *53*, 11354-11356.

18. Brogden, D. W.; Berry, J. F., Heterometallic Second-Row Transition Metal Chain Compounds in Two Charge States: Syntheses, Properties, and Electronic Structures of $[Mo–Mo–Ru]^{6+/7+}$ Chains. *Inorg. Chem.* **2015,** *54*, 7660-7665.

19. Brogden, D. W.; Christian, J. H.; Dalal, N. S.; Berry, J. F., Completing the series of Group VI heterotrimetallic $M_2Cr(dpa)_4Cl_2$ (M_2 = Cr_2, Mo_2, MoW and W_2) compounds and investigating their metal–metal interactions using density functional theory. *Inorg. Chim. Acta* **2015,** *424*, 241-247.

20. Christian, J. H.; Brogden, D. W.; Bindra, J. K.; Kinyon, J. S.; van Tol, J.; Wang, J.; Berry, J. F.; Dalal, N. S., Enhancing the Magnetic Anisotropy of Linear Cr(II) Chain Compounds Using Heavy Metal Substitutions. *Inorg. Chem.* **2016,** *55*, 6376-6383.

21. Cheng, M.C.; Mai, C.L.; Yeh, C.Y.; Lee, G.H.; Peng, S.M., Facile synthesis of heterotrimetallic metal-string complex $[NiCoRh(dpa)_4Cl_2]$ through direct metal replacement. *Chem. Commun.* **2013,** *49*, 7938-7940.

22. Huang, G.C.; Bénard, M.; Rohmer, M.-M.; Li, L.A.; Chiu, M.J.; Yeh, C.Y.; Lee, G.H.; Peng, S.M., $Ru_2M(dpa)_4Cl_2$ (M = Cu, Ni): Synthesis, Characterization, and Theoretical Analysis of Asymmetric Heterometal String Complexes of the Dipyridylamide Family. *Eur. J. Inorg. Chem.* **2008**, 1767-1777.

23. Huang, M.J.; Hua, S.A.; Fu, M.D.; Huang, G.C.; Yin, C.; Ko, C.H.; Kuo, C.K.; Hsu, C.H.; Lee, G.H.; Ho, K.Y.; Wang, C.H.; Yang, Y.W.; Chen, I.C.; Peng, S.M.; Chen, C.H., The First Heteropentanuclear

Extended Metal-Atom Chain: [Ni^{+}—Ru_2^{5+}—Ni^{2+}—Ni^{2+}(tripyridyldiamido)$_4$(NCS)$_2$]. *Chem. Eur. J.* **2014,** *20*, 4526-4531.

24. Huang, Y.M.; Lai, S.H.; Lee, S. J.; Chen, I.C.; Huang, C. L.; Peng, S.M.; Wang, W.Z., Metal Metal Bonding and Structures of Metal String Complexes: Tripyridyldiamido Pentanickel and Pentacobalt from IR, Raman, and Surface-Enhanced Raman Scattering Spectra. *J. Phys. Chem. C* **2011,** *115*, 2454-2461.

25. Hung, W.C.; Sigrist, M.; Hua, S.A.; Wu, L.C.; Liu, T.J.; Jin, B.Y.; Lee, G.H.; Peng, S.-M., A heteropentanuclear metal string complex [Mo_2NiMo_2(tpda)$_4$(NCS)$_2$] with two linearly aligned quadruply bonded Mo_2 units connected by a Ni ion and a meso configuration of the complex. *Chem. Commun.* **2016,** *52*, 12380-12382.

26. Liu, I. P.C.; Lee, G.H.; Peng, S.M.; Bénard, M.; Rohmer, M.M., Cu–Pd–Cu and Cu–Pt–Cu Linear Frameworks: Synthesis, Magnetic Properties, and Theoretical Analysis of Two Mixed-Metal Complexes of Dipyridylamide (dpa), Isostructural, and Isoelectronic with [Cu_3(dpa)$_4Cl_2$]$^{+}$. *Inorg. Chem.* **2007,** *46*, 9602-9608.

27. Rohmer, M.M.; Liu, I. P.C.; Lin, J.C.; Chiu, M.J.; Lee, C.-H.; Lee, G.H.; Bénard, M.; López, X.; Peng, S.M., Structural, Magnetic, and Theoretical Characterization of a Heterometallic Polypyridylamide Complex. *Angew. Chemie. Int. Ed.* **2007,** *46*, 3533-3536.

28. Xiang, J.; Jia, L.H.; Wang, B.W.; Yiu, S.M.; Peng, S.M.; Wong, W.Y.; Gao, S.; Lau, T.C., The synthesis, structures and magnetic properties of polynuclear Ru^{III} 3d (3d = $Mn^{II/III}$, Ni^{II}, Cu^{II}) compounds based on [Ru^{III}(Q)$_2$(CN)$_2$]. *Dalton Trans.* **2013,** *42*, 3876-3887.

29. Yu, L. C.; Lee, G. H.; Sigrist, M.; Lin, T. S.; Peng, S. M., Structure and Antiferromagnetism of Trinuclear Heterometallic Strings Containing Mn^{II}—M^{II}—Mn^{II} Frameworks (M = Ni, Pd, Pt. *Eur. J. Inorg. Chem.* **2016,** *2016*, 4250-4256.

30. Aydin-Cantürk, D.; Nuss, H., Synthesis, Structure Determination, and Magnetic Properties of the New Heterometallic Chain Compound CrCrNi(di-2,2-pyridylamido)$_4Cl_2$·Et_2O. *Zeitschrift für anorganische und allgemeine Chemie* **2011,** *637*, 543-546.

31. Arcisauskaite, V.; Spivak, M.; McGrady, J. E., Structure and bonding in trimetallic arrays containing a Cr–Cr quadruple bond: A challenge to density functional theory. *Inorg. Chim. Acta* **2015,** *424*, 293-299.

32. Chang, W.C.; Chang, C.W.; Sigrist, M.; Hua, S.A.; Liu, T.J.; Lee, G.H.; Jin, B.Y.; Chen, C.H.; Peng, S.M., Nonhelical heterometallic [Mo_2M(npo)$_4$(NCS)$_2$] string complexes (M = Fe, Co, Ni) with high single-molecule conductance. *Chem Commun.* **2017,** *53*, 8886-8889.

33. Nippe, M.; Turov, Y.; Berry, J. F., Remote Effects of Axial Ligand Substitution in Heterometallic Cr≡Cr···M Chains. *Inorg. Chem.* **2011,** *50*, 10592-10599.

34. Chilton, N. F.; Anderson, R. P.; Turner, L. D.; Soncini, A.; Murray, K. S., PHI: A powerful new program for the analysis of anisotropic monomeric and exchange-coupled polynuclear d- and f-block complexes. *J. Comp. Chem.* **2013,** *34*, 1164-1175.

35. Nippe, M.; Victor, E.; Berry, J. F., Oxidation Chemistry of Axially Protected Mo_2 and W2 Quadruply Bonded Compounds. *Inorg. Chem.* **2009,** *48*, 11889-11895.

36. Cotton, F. A.; Daniels, L. M.; Hillard, E. A.; Murillo, C. A., Filling a Void: Isolation and Characterization of Tetracarboxylato Dimolybdenum Cations. *Inorg. Chem.* **2002,** *41*, 1639-1644.

37. Chisholm, M. H.; D'Acchioli, J. S.; Pate, B. D.; Patmore, N. J.; Dalal, N. S.; Zipse, D. J., Cations $M_2(O_2CtBu)^{4+}$, Where M = Mo and W, and $MoW(O_2CtBu)^{4+}$. Theoretical, Spectroscopic, and Structural Investigations. *Inorg. Chem.* **2005,** *44*, 1061-1067.

38. Cotton, F. A.; Pedersen, E., Magnetic and electrochemical properties of transition metal complexes with multiple metal-to-metal bonds. IV. Octachlorodimolybdate(n-) with n = 3 and 4 and tetrabutyratodimolybdate(n+) with n = 0 and 1. *Inorg. Chem.* **1975,** *14*, 399-400.

39. Rohmer, M.M.; Strich, A.; Bénard, M.; Malrieu, J.P., Metal–Metal Bond Length Variability in Co_3(dipyridylamide)$_4Cl_2$: Bond-Stretch Isomerism, Crystal Field Effects, or Spin Transition Process? A DFT Study. *J. Am. Chem. Soc.* **2001,** *123*, 9126-9134.

40. Rohmer, M.M.; Bénard, M., Bond Stretch Isomerism Still Elusive in Linear Trimetallic Complexes. DFT Calculations on Co_3(dipyridylamine)$_4Cl_2$. *J. Am. Chem. Soc.* **1998,** *120*, 9372-9373.

41. Benbellat, N.; Rohmer, M.M.; Bénard, M., Electronic origin of the structural versatility in linear trichromium complexes of dipyridylamide. *Chem. Commun.* **2001**, 2368-2369.

42. Rohmer, M.M.; Bénard, M., Structural Versatility in Polyoxometalates and in Some Linear Trimetallic Complexes: An Electronic Interpretation. *J. Cluster Sci.* **2002,** *13*, 333-353.

43. Bailey, B. C.; Basuli, F.; Huffman, J. C.; Mindiola, D. J., Terminal Titanium(IV) (Trimethylsilyl)imides Prepared by Oxidatively Induced Trimethylsilyl Abstraction. *Organometallics* **2006,** *25*, 2725-2728.

44. *Bruker-AXS*, Madison, Wisconsin, USA, 2009.

45. Dolomanov, O. V.; Bourhis, L. J.; Gildea, R. J.; Howard, J. A. K.; Puschmann, H., : a complete structure solution, refinement and analysis program. In *Journal of applied crystallography*, Oxford, England :, 2009; Vol. 42, pp 339-341.

46. Neese, F., The ORCA program system. *Wiley Interdisciplinary Reviews: Computational Molecular Science* **2012,** *2*, 73-78.

47. Becke, A. D., Density-functional exchange-energy approximation with correct asymptotic behavior. *Phys. Rev. A* **1988,** *38*, 3098-3100.

48. Perdew, J. P.; Yue, W., Accurate and simple density functional for the electronic exchange energy: Generalized gradient approximation. *Phys. Rev. B* **1986,** *33*, 8800-8802.

49. Pantazis, D. A.; Chen, X.Y.; Landis, C. R.; Neese, F., All-Electron Scalar Relativistic Basis Sets for Third-Row Transition Metal Atoms. *J. Chem. Theory Comput.* **2008,** *4*, 908-919.

50. Andrae, D.; Haussermann, U.; Doll, G.; P. Stoll, H.; Preuss, H., Energy-Adjusted ab initio Pseudopotentials for the Second and Third Row Transition Elements. *Theor. Chem. Acc.* **1990,** *77*, 123-141.

51. Weigend, F.; Ahlrichs, R., Balanced basis sets of split valence, triple zeta valence and quadruple zeta valence quality for H to Rn: Design and assessment of accuracy. *Phys. Chem. Chem. Phys.* **2005,** *7*, 3297-3305.

52. Weigend, F., Accurate Coulomb-fitting basis sets for H to Rn. *Phys. Chem. Chem. Phys.* **2006,** *8*, 1057-1065.

53. Eichkorn, K.; Treutler, O.; Öhm, H.; Häser, M.; Ahlrichs, R., Auxiliary basis sets to approximate Coulomb potentials. *Chem. Phys. Let.* **1995,** *240*, 283-290.

54. Eichkorn, K.; Weigend, F.; Treutler, O.; Ahlrichs, R., Auxiliary basis sets for main row atoms and transition metals and their use to approximate Coulomb potentials. *Theor. Chem. Acc.* **1997,** *97*, 119-124.

55. Löwdin, P. O., On the Non Orthogonality Problem Connected with the Use of Atomic Wave Functions in the Theory of Molecules and Crystals. *J. Chem. Phys.* **1950,** *18*, 365-375.

56. Löwdin, P.-O., On the Nonorthogonality Problem *Advances in Quantum Chem.* **1970,** *5*, 185-199.

57. Pettersen, E. F.; Goddard, T. D.; Huang, C. C.; Couch, G. S.; Greenblatt, D. M.; Meng, E. C.; Ferrin, T. E., UCSF Chimera—A visualization system for exploratory research and analysis. *J. Comp. Chem.* **2004,** *25*, 1605-1612.

Chapter Four

Facile Axial Ligand Substitution in Linear Mo≡Mo–Ni Complexes

Jill A. Chipman, John F. Berry*

This chapter has been published

Reprinted with permission from Chipman, J.A., Berry, J.F. *Inorg. Chem.* **2018**, *57*, 9354-9363.

4.1 Abstract: Clean axial ligand substitution reactions of heterometallic extended metal atom chains (HEMACs) supported by the dpa ligand (dpa = 2,2'-dipyridylamine) have been synthetically challenging due to side reactions that alter the trimetallic core. Following the hypothesis that a heterometallic core containing second-row transition metals would be more robust toward ligand substitution, we report the synthesis of three new heterotrimetallic compounds, $Mo_2Ni(dpa)_4(OTf)_2$ (**1**), $Mo_2Ni(dpa)_4(NCS)_2$ (**2**), and $Mo_2Ni(dpa)_4(NCSe)_2$ (**3**) that are obtained cleanly and in good yield. Compound **1** may be synthesized either directly by reaction of $Ni(OTf)_2$ with $Mo_2(dpa)_4$ (**4**) or indirectly, by reaction of $Mo_2Ni(dpa)_4Cl_2$ (**5**) with two equivalents of TlOTf. Axial ligand substitution on **1** via solutions containing NaNCS or KNCSe afford **2** or **3**, respectively. X-ray crystal structures of **1**, **2**, and **3** present short Mo–Ni distances of 2.458(8)Å /2.47(1) Å, 2.548(1), and 2.546(1) respectively. Density functional theory (DFT) calculations indicate a 3-center 3-electron σ bonding interaction between the Mo_2 quadruply bonded core and the Ni in both **1** and **2**. These complexes were analyzed by SQUID magnetometry, supporting the presence of a high spin Ni^{2+} center with $S = 1$.

4.2 Introduction

Heterometallic extended metal atom chains (HEMACs) supported by the dpa ligand (dpa = 2,2'-dipyridylamine) were first reported in 2007 independently by us[1] and the group of S.M. Peng.[2] These complexes can be either symmetric of the form $M_A–M_B–M_A$, or unsymmetric with $M_A–M_A–M_B$ structures. Further work in our lab focused on the latter structures has led to the preparation of a large HEMAC family in which M_A is a group VI metal and M_B is either a first or second row transition metal in the +2 oxidation state.[3-10] The overwhelming majority of these compounds feature chloride axial ligands due to the ready availability of MCl_2 starting materials. However, a thorough investigation of the chemical and physical

properties with HEMACs requires the discovery of new complexes with variable axial ligands. Homometallic EMACs have been prepared with axial ligands ranging from other halides, pseudohalides, neutral ligands, and organometallic ligands.[3, 11-17] These modifications have enabled the tuning of electronic, photophysical, and magnetic properties as well as the formation of one-dimensional polymeric chains via molecular linkers.[18-20]

We have examined substitution of axial chloride ligands in $M_A \equiv M_A–M_B$ compounds with M_A= Cr and M_B = Mn, Fe, and Co.[21-22] In these past efforts, the substitution reactions have been hampered by poor yields and/or demetallation of M_B upon introduction of the incoming ligand. It was hypothesized that an excess of the substituting axial ligand, which is needed to achieve useful ligand substitution rate of chloride compounds may be leading to demetallation.

To counter this problem, we have examined adding stoichiometric equivalents of the incoming ligand to complexes featuring labile axial ligands. We experienced some success with these methods, [21-22] particularly when labile axial acetonitrile ligands were used. However, the yields of ligand substitution were inconsistent. Another problem surprised us when we examined the products of ligand substitution of Cr $\equiv$ Cr–Fe compounds. In addition to the expected Cr $\equiv$ Cr–Fe products, there was a small amount of Cr $\equiv$ Cr–Cr impurity, indicating that metal atom substitution also occurs under these conditions.[22]

In this work, we set out to explore whether cleaner axial ligand substitution chemistry can be achieved by switching from Cr $\equiv$ Cr–M_B chains to Mo $\equiv$ Mo–M_B ones. The strength of the Mo $\equiv$ Mo quadruple bond was anticipated to prevent the metal atom scrambling issue that we have previously encountered with Cr $\equiv$ Cr chains. Our recent report of the one-electron oxidized $[Mo_2Ni(dpa)_4Cl_2]^+$ ion[9] provides further support for this hypothesis as moving to a Mo_2 core allowed for the synthesis, isolation, and characterization of this meta stable-complex. In addition, Peng and coworkers have recently reported the preparation of $Mo_2Ni(dpa)_4(NCS)_2$ via a high temperature self-assembly method, which further supports the idea that the Mo_2 complexes are seemingly more robust.[23] However, it is important to note that analogous studies have not yet been completed on $Cr_2Ni(dpa)_4Cl_2$ to fully understand the significance of the Ni atom in the chain in addition to moving to a Mo_2 core. Herein, we report that the use of a Mo $\equiv$ Mo–M_B chain does allow for straightforward axial ligand substitution chemistry to be achieved. Specifically, we report here a systematic series of $Mo_2Ni(dpa)_4X_2$ complexes where X = OTf, NCS, and NCSe. This series

allows us to enumerate trends in electronic structure and heterometallic bonding as a function of the axial ligand, X.

4.3 Results and Discussion

Synthesis

In this work, $Mo_2(dpa)_4$ (**4**) is the key precursor used for the preparation of Mo_2Ni chain complexes. In previous work, **4** was prepared by deprotonation of Hdpa with methyllithium followed by reaction with $Mo_2(OAc)_4$.[1] We report here a modified synthetic procedure for **4** that obviates the need for methyllithium. In this new procedure, the salt Kdpa is prepared and isolated through reaction of $KN(tms)_2$ and Hdpa in ether at room temperature at yields exceeding 80% (tms = trimethylsilyl). This salt was characterized via ^1H and ^{13}C NMR spectroscopy and elemental analysis confirms its identity. When Kdpa is allowed to react with $Mo_2(OAc)_4$ in refluxing THF, the resulting $Mo_2(dpa)_4$ is identical via IR spectroscopy to that prepared via the traditional route but is typically obtained in higher yields, greater than 80%.

From **4**, $Mo_2Ni(dpa)_4(OTf)_2$ (**1**) may be directly synthesized. Reaction of **4** with 1.5 equivalents of $Ni(OTf)_2$ in molten naphthalene at 225°C for two hours affords **1** following workup of the reaction mixture. Complex **1** may also be synthesized via the addition of an acetonitrile solution of 2 equivalents of TlOTf to a solution of $Mo_2Ni(dpa)_4Cl_2$ (**5**) in a slightly lower yield. In order to achieve axial ligand substitution, yielding complexes **2** and **3**, an acetonitrile solution containing 2 equivalents of NaNCS or KNCSe, respectively was added dropwise to a solution of **1** in dry dichloromethane at 0°C. Both reactions are accompanied by a color change by which the forest green solution of **1** changes to a goldenrod solution of **2** or a brown solution of **3**. Complex **2** may be isolated as a brown powder in 72% yield or as brown crystals in a 45% yield. Complex **3** may be obtained as a crystalline product in 44% yield. This overall synthetic methodology is outlined below in Scheme 4.1.

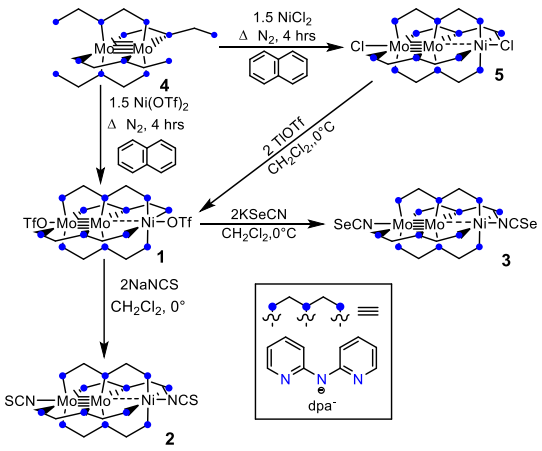

Scheme 4.1. Synthesis of complexes **2** – **5**

In the course of our work, an alternative synthesis of **2** was reported by Peng and coworkers.[23] In this case, $Mo_2(OAc)_4$, Hdpa, $Ni(OAc)\cdot 4H_2O$, and excess NaNCS were heated together in molten naphthalene to afford **2** in 53 % yield. We were surprised that **2** could be prepared under such harsh reaction conditions with an excess of NaNCS. To investigate this further, we therefore attempted to prepare **2** by heating **5** with 36 equivalents of NaNCS in molten naphthalene. In our hands, this reaction did not yield the expected $Mo_2Ni(dpa)_4(NCS)_2$ product. Instead, we obtained what we believe to be a mixture of $Ni(Hdpa)_2(NCS)_2$ and $Mo_2(dpa)_4$ based on MALDI-TOF mass spectrometry data. Although $Ni(Hdpa)_2(NCS)_2$ has not been previously reported, analogous compounds have been characterized by Hurley and Robinson and these show similar solubility properties to the material we obtain.[24]

Geometric Features of Synthesized Complexes

X-ray quality crystals of **1**, **2**, and **3** were obtained by layering separate dichloromethane solutions with hexanes (**1**) or diethyl ether (**2** and **3**). Compound **1** crystallizes in the monoclinic space group $P2_1/c$ while **2** crystalizes in the triclinic space group $P\bar{1}$, and **3** crystallizes in the monoclinic space group $C2/c$ While **1** presents positional metal atom disorder within the Mo ≡ Mo–Ni chain, **2** and **3** do not present this disorder. These three structures are fairly similar all presenting the linear, heterotrimetallic chain encased

by the dpa ligands that wrap the molecular periphery in a helical manner. The molecular structures of compounds **1**, **2**, and **3** are shown in Figure 4.1.

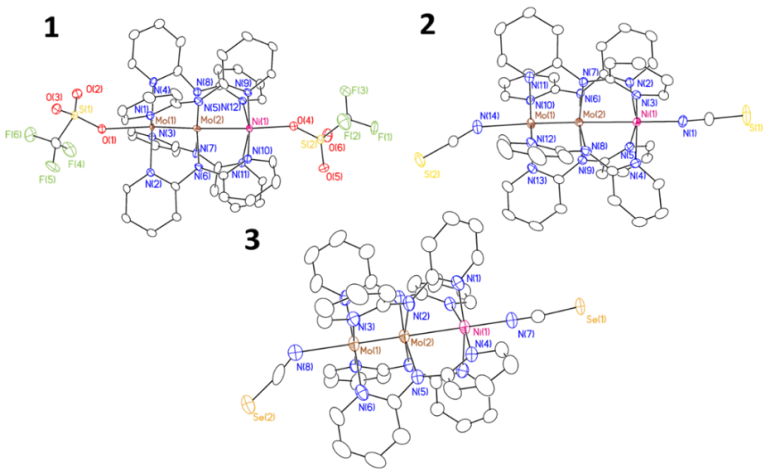

Figure 4.1. Crystal structures of **1**, **2**, and **3**. Ellipsoids are shown at the 50% probability level. All H atoms and molecules of solvation have been omitted for clarity. In addition, the dominant orientation in any instance of disorder is displayed.

In comparison to other Mo≡Mo quadruply bonded species supported by the dpa ligand, the Mo≡Mo bond distances for **1**, **2**, and **3** of 2.110(8) Å, 2.1073(9) Å, and 2.0966(8) Å, respectively (Table 4.1) are similar to those reported for other Mo_2M_B HEMACs that range from 2.096(2) (M=Mn) to 2.104(1) (M=Fe.)[4-6, 8-9] However, the Mo–Ni distances in all three complexes are remarkably short at 2.458(8)/2.47(1) Å, 2.548(1) Å and 2.546(1) Å, for **1**, **2**, and **3**, respectively. To put these distances in perspective, we consider the Mo–M_B distances in $Mo_2M_B(dpa)_4Cl_2$ compounds with M_B = Cr, Mn, Fe, and Co. These distances range from 2.6170(7) Å in $Mo_2Co(dpa)_4Cl_2$ to 2.797(5) Å in the crystal structure of $Mo_2Mn(dpa)_4Cl_2$.[4-6, 8] We may also make a comparison to the Mo–Ni distance in the recently reported [9] $Mo_2Ni(dpa)_4Cl_2$ which was found to be 2.525(4) Å. Indeed, **1**,**2**,**3**, and **5** present consistently short Mo–Ni distances.

Although these Mo–Ni distances are outliers among the $Mo_2M_B(dpa)_4X_2$ series, they agree well with the distance reported for the $[Ru_2Ni(dpa)_4Cl_2]^+$ ion (2.513(9) Å) synthesized by Peng and coworkers, which is described as having a (Ru_2^{5+})–Ni^{2+} electronic structure.[25,26]Additionally, **1**, **2**, **3**, and **5** may be compared to $Cr_2Ni(dpa)_4Cl_2$ reported by Nuss et al.[27] that reported a Cr–Ni bond distance of 2.585(2) Å, which is slightly shorter than the other Cr–M_B distances reported in the $Cr_2M_B(dpa)_4X_2$ series.

Mo_2M_B complexes are advantageous over Cr_2M_B complexes in that, while the electronic structure of the latter complexes are multiconfigurational and mandate a multireference computational approach,[28] the Mo_2M_B complexes may be treated satisfactorily using density functional theory (DFT) methods.[7-8, 10] Crystal structure coordinates were used as starting geometries for DFT geometry optimizations and single point calculations, which allowed for additional comparison as shown in Table 4.2. The metal–metal bond as well as metal axial ligand distances computed for **1**, **2**, and **3** match well with experimental values. However, DFT does not accurately reflect the metal backbone to axial ligand angle ($Ni/Mo–N_{NCS}–C_{NCS}$) in **2**. Experimentally, these angles are observed to have a substantial bend, with metal–nitrogen–carbon angles of 151.6° and 161.1° while computationally, these values were predicted to be 177.3° and 177.4°. We attribute this discrepancy to crystal packing effects. In **3**, the $Ni–N_{NCSe}–C_{NCSe}$ angle of the axial ligand is perfectly linear at 180.0° while the Mo–N–C angle takes a substantial bend and adopts an angle of 133.8°. Computationally, the optimized structure presents angles of 179.9°. The computational and experimental angles of **1** are in good agreement with each other.

Table 4.1. Crystallographic data for $Mo_2Ni(dpa)_4(OTf)_2$, $Mo_2Ni(dpa)_4(NCS)_2{\cdot}CH_2Cl_2$, and $Mo_2Ni(dpa)_4(NCSe)_2{\cdot}CH_2Cl_2$ at 100K.

	1	**2**	**3**
Empirical formula	$Mo_2NiC_{42}H_{32}N_{12}S_2O_6F_6$	$Mo_2NiC_{42}H_{32}N_{14}S_2{\cdot}CH_2Cl_2$	$Mo_2NiC_{42}H_{32}N_{14}Se_2{\cdot}CH_2Cl_2$
Crystal system	monoclinic	triclinic	monoclinic
Space group	$P2_1/c$	$P\bar{1}$	$C2/c$
a/Å	15.67(1)	12.000(2)	18.161(4)
b/Å	17.16(2)	12.840(3)	17.381(4)
c/Å	17.82(2)	16.620(3)	15.556(3)
α/°	90	97.73(3)	90
β/°	107.05(1)	106.17(3)	111.19(3)
γ/°	90	112.06(3)	90
Volume/Å^3	4579(7)	2195.7(9)	4578(2)
Z	4	2	4
ρ_{calc} g/cm^3	1.783	1.713	1.778
R_1[a], wR_2[b] [I>=2σ (I)]	0.0438, 0.1002	0.0343, 0.0805	0.0521, 0.1194
R_1[a], wR_2[b] [all data]	0.0471, 0.1009	0.0444, 0.0859	0.0705, 0.1301

[a] $R1 = \Sigma\big||F_o| - |F_c|\big|/\Sigma|F_o|$

[b] $wR2 = [\Sigma[w(F_o^2 - F_c^2)^2/\Sigma\big[(w(F_o^2)^2\big]]^{\frac{1}{2}}$, $w = 1/\sigma^2(F_o^2) + (aP)^2 + bP$ where $P = [\max(0 \text{ or } F_o^2) + 2(F_c^2)]/3$.

Table 4.2 Crystallographic and computational distances for **1**, **2**, **3**, and **5**. All bond distances are reported in Å

	Mo≣Mo	Mo-Ni	Mo-N_{py} (av)	Mo-N_a (av)	Ni-N_{py} (av)	Mo-X	Ni-X	Mo-L_1-L_2, deg [A]	Ni-L_1-L_2, deg [B]	Ref
1 (major)	2.110(8)	2.485(8)	2.157[5]	2.114[2]	2.157[1]	2.364(4)	2.086(5)	150.5	149.6	*This work*
1 (minor)	2.14(1)	2.475(1)	2.135[5]	2.114[4]	2.1693[9]	2.317(5)	2.117(5)	151.0	149.8	*This work*
1 DFT	2.125	2.516	2.1828	2.1208	2.105	2.273	2.109	156.5	150.8	*This work*
2	2.1073(9)	2.548(1)	2.204[2]	2.131[3]	2.107[4]	2.334(2)	2.025(2)	151.6	161.1	*This work*
2	2.104(5)	2.546(6)	2.199[3]	2.128[3]	2.105[3]	2.333(4)	2.105(3)	150.8	162.0	[23]
2 DFT	2.147	2.549	2.1848	2.1225	2.1208	2.202	2.000	177.3	177.4	*This work*
3	2.0966(8)	2.546(1)	2.211[4]	2.121[4]	2.095[4]	2.403(6)	2.016(6)	180.0	180.0	*This work*
3 DFT	2.146	2.544	2.185	2.122	2.121	2.209	2.000	179.88	170.97	*This work*
5	2.107(2)	2.524(4)	2.115[3]	2.174[3]	2.146[3]	2.627(2)	2.394(3)	N/A	N/A	[9]
5 DFT	2.135	2.550	2.191	2.121	2.120	2.627	2.425	N/A	N/A	[9]

[A] for **1** L_1 = O, L_2 = S

[B] for **2**, **3** L_1 = N, L_2 = C

Solution Properties

The cyclic voltammograms (CVs) for **1** and **2** in dichloromethane are shown in Figure 4.2 (The data for **3** are shown in Figure S4.2). Despite their similarity to existing HEMACs, all three compounds display distinct electrochemical behavior. These compounds all present a reversible feature, attributable to the $[Mo_2Ni]^{6+/7+}$ redox couple, at $E_{1/2}$ = – 0.125 V for **1**, $E_{1/2}$ = – 0.290 V for **2**, and – 0.167 V for **3**. Reversibility of this couple was determined using **2**, the details of which are shown in Figures S4.13 and S4.14. This redox couple has been assigned to the $Mo_2^{4+/5+}$ redox couple of the quadruple bond. We were recently able to isolate the one-electron oxidized $[Mo_2Ni(dpa)_4Cl_2]^+$ cation[9] as a meta-stable complex. In order to access the complex, we resorted to extreme reaction conditions and crystallization at -78 °C. We attempted chemical oxidation of **2** at the same reaction conditions, using FcOTf as an oxidant but allowed for crystallization at room temperature. In this circumstance, instead of yielding a $[Mo_2Ni(dpa)_4(NCS)_2]^+$ cation, the resulting product was $[Mo_2(dpa)_3(NCS)_2]^+$ having Mo–Mo distance of 2.580(1) Å suggestive of loss of the quadruple bond. However, there was also loss of Ni as well as one dpa ligand.[29]

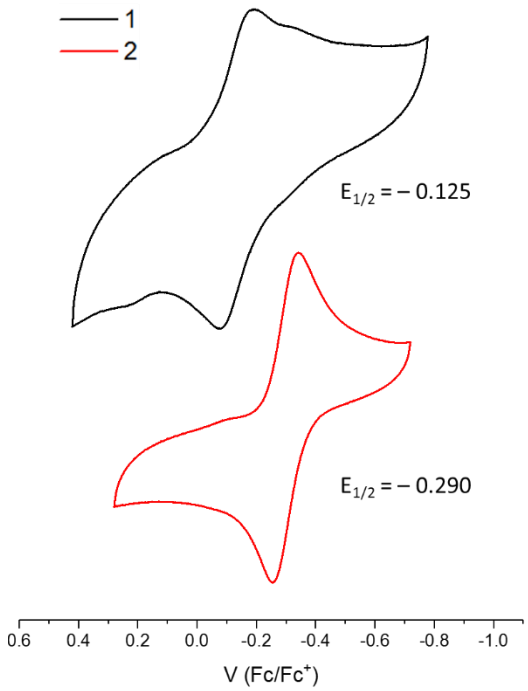

Figure 4.2. Cyclic voltammograms of **1** in **2** in CH_2Cl_2 with 0.1 M NBu_4PF_6 electrolyte and 1 mM substrate, scan rate 100 mv/S.

In the binuclear **4**, this feature is present at $E_{1/2}$ = – 0.83 V. Thus, addition of the heterometal, Ni, leads to complexes with redox potentials one half to three quarters of a volt higher than in the Mo_2 precursor. In comparison to other $Mo_2M_B(dpa)_4Cl_2$ compounds with M_B = Cr, Fe, **1**, **2**, and **3** present more positive redox potentials (Table 4.2). In comparison to $Mo_2Ni(dpa)_4Cl_2$, in which $E_{1/2}$ = – 0.418 V, **1**,**2**, and **3** present more positive potentials. We previously reported Cr ≣ Cr–Fe chain compounds supported by the dpa ligand in which one or both axial chloride ligands were substituted for a triflate ligand. In the monotriflate species, the triflate binds to the terminal Cr atom. Moving from the chloride to monotriflate species, the $E_{1/2}$ attributable to the $Fe^{2+/3+}$ couple was found to shift from – 0.236 V to – 0.050 V consistent with the fact that triflate is a weaker σ donor than chloride.[21] This work illustrates a similar trend comparing the triflate to the thiocyanate and selenocyanate ligand.

Table 4.3 Comparison of electrochemical data.

Compound	$E_{1/2}$ (vs. Fc/Fc^+)	Ref
1	— 0.125	*This work*
2	— 0.290	*This work*
3	— 0.167	*This work*
5	— 0.418	9
$Mo_2Cr(dpa)_4Cl_2$	— 0.860	8
$Mo_2Fe(dpa)_4Cl_2$	— 0.495	6
$MoWCr(dpa)_4Cl_2$	— 0.910*	29

* $[MoW]^{4+/5+}$

Electronic Structure

The differing colors of **1** (forest green), **2** (goldenrod), and **3** (dark brown) in CH_2Cl_2 are due to subtle differences in the three major absorption features in their electronic spectra (Fig. 4.3). We have used our computational models of **1**, **2**, and **3** to predict the electronic transitions by TDDFT (See Figure 4.4).

The remarkably good agreement between experimental and calculated absorption spectra serves as a strong validation for the utilized computational approach and allows us to make definitive assignments of the electronic transitions. The lowest energy transitions (band **A** in Figure 4.3) for all three complexes are experimentally located at 650 nm, 663 nm, and 665 nm for **1**, **2**, and **3**, respectively and are all attributed to Mo_2 $\delta - \delta^*$ transitions with a degree of metal to metal charge transfer character. Compared to their experimental counterparts for transition **A**, the TDDFT calculated values of 697 nm for **1**, 726 nm for **2**, and 726 for **3** are slight energy underestimates of their true experimental values.

In addition a visible energy transition **B** experimentally located at 476 nm for **1**, 477 nm for **2**, and 493 nm for **3** were matched with calculated transitions at 618 nm, 642nm, and 626 nm, respectively that are energy underestimates of their experimental values, as is common in TDDFT predictions of charge transfer transitions. Here the assignments are based more on the agreement between experimental and molar absor6ptivities. This transition is a metal to ligand charge transfer transition from the Mo_2 δ^* orbital to a dpa π^* acceptor orbital. A complete assignment identifying all of the transitions contributing to the highest energy band **C** from the experimental spectra located at 413 nm, 414 nm, and 416 nm for **1**, **2**, and **3** respectively was not possible but this band is expected, based on intensity (ε = 17,900 L mol^{-1} cm^{-1}, 21,000 L mol^{-1} cm^{-1}, 15, 000 L mol^{-1} cm^{-1}) to also be of charge transfer transition character as well. Computationally, a major contributing transition to band **C** is a charger transfer feature located at 521 nm, 536 nm and 545 nm for **1**, **2**, and **3**, respectively. This transition is also a metal to ligand charge transfer transition from the Mo_2 δ^* orbital to a dpa π^* acceptor orbital with inversion to the acceptor orbital localized on the Ni-bound pyridine rings. Representative orbitals associated with these features using **2** as a model are shown in Figure 4.4.

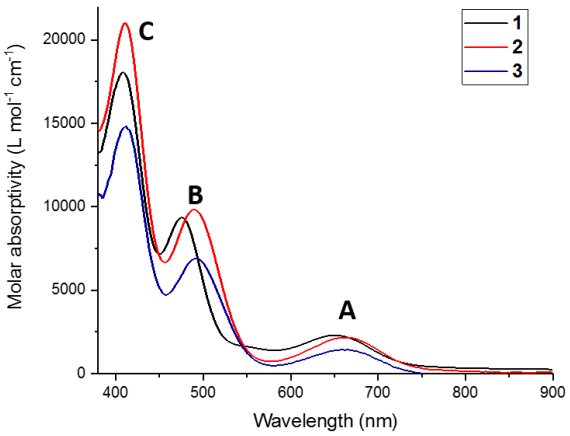

Figure 4.3 Experimental electronic absorbance spectra of CH_2Cl_2 solutions of **1**, **2**, and **3**.

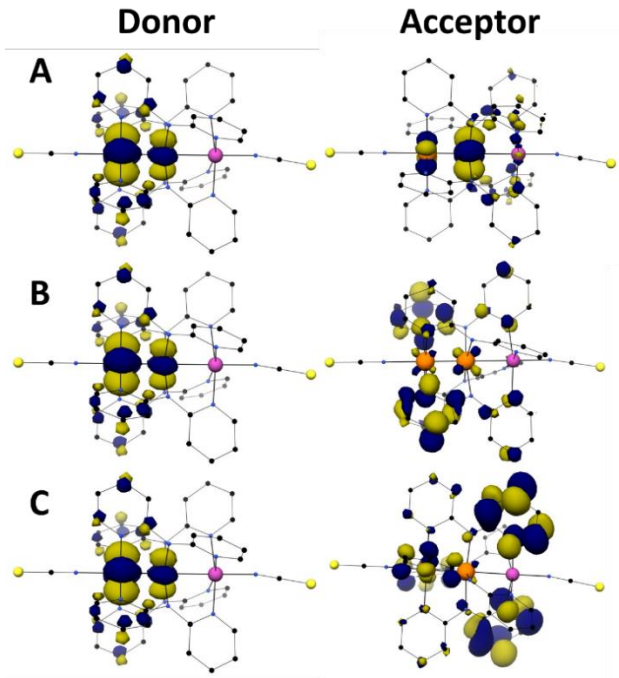

Figure 4.4 Representative TDDFT transitions of δ - δ*(A) and MLCT (B, C) using **2** as a model.

In addition to TDDFT, single-point DFT calculations allow for comparison between the electronic structures of **1** – **3** and other HEMAC and EMAC compounds. The bottom four orbitals of Figure 4.5 derive essentially from the Mo_2 unit, having 2 x π, σ, and δ symmetry (*e*, *a*, and *b* in the C_4 point group, respectively). Being filled, these orbitals contribute to the Mo≣Mo quadruple bond, though the σ symmetry orbital shows significant bonding interaction with the Ni ion as well. The next five orbitals (2*e*,

2*b*, a_{nb} and 3*b*) may be roughly assigned to the square pyramidal $S = 1$ Ni^{2+} center. One major perturbation to this localization of orbitals is that the a_{nb}, of σ symmetry has significant Mo contributions and can be described as Mo–Mo bonding but Mo – Ni antibonding, giving overall Mo_2Ni σ nonbonding character. Its occupation by one electron, together with the corresponding double occupation of *a*, constitute a 3c/3e$^-$ Mo–Mo–Ni bond akin to those originally proposed by Bénard et al. for the homometallic $Co_3(dpa)_4Cl_2$ and $Cr_3(dpa)_4Cl_2$ species.[30-34] For the EMACs (and also for the symmetric M_A–M_B–M_A HEMACs), the D_4 symmetry gives rise to bonding and nonbonding d_{z2} orbital combinations of differing symmetry: a_1 and a_2, respectively. The latter has a nodal plane at the position of the central atom, normal to the trimetallic axis, as seen on the left side of Chart 4.1. In the C_4 symmetric M_A–M_A–M_B HEMACs, all σ-symmetry orbitals, belong to the *a* representation and can mix. For the σ non-bonding combination, the nodal plane lies between M_A and M_B. The compositions of these delocalized orbitals then reflect the differences in effective nuclear charge between M_A and M_B, here 28.13 % : 6.12 % : 64.75 % (α) and 48.80 %: 12.16 %: 39.09 % (β) for Mo_1–Mo_2–Ni for the σ bonding orbital and 33.95 % : 27.16 % : 38.90 % (α) and 13.18 %: 21.06 %: 65.76 % (β) for the σ nonbonding (Chart 4.2).[35] The difference in orbital contributions between the α and β orbitals in the σ bonding contributions can be best attributed to spin polarization. To explain the difference in orbital contribution for the σ_{nb} orbitals, it is important to notice that this orbital is singly occupied and thus a difference in contribution between the α and β components is not unexpected. Similar patterns of metal atom character in the σ and σ_{nb} orbitals is seen for **1** and **3** as shown in Chart S4.1. To summarize the electronic structure of the Mo_2Ni HEMACs, a qualitative MO diagram is shown in Figure 4.5 in which compound **2** is used to illustrate the orbitals participating the 3c-3e$^-$ σ bond. This structure is analogous to that seen in **1**, **3**, and **5**.

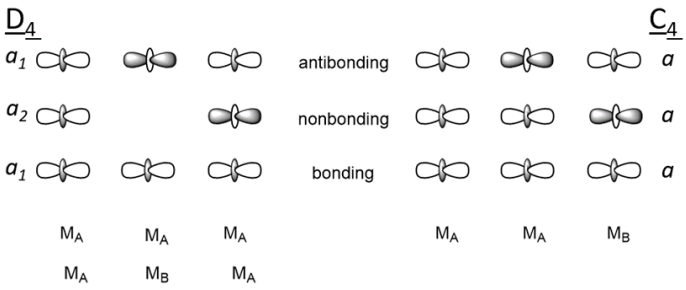

Chart 4.1. A Comparison between the σ type orbitals in symmetric EMACs, HEMACs, and asymmetric HEMACs.

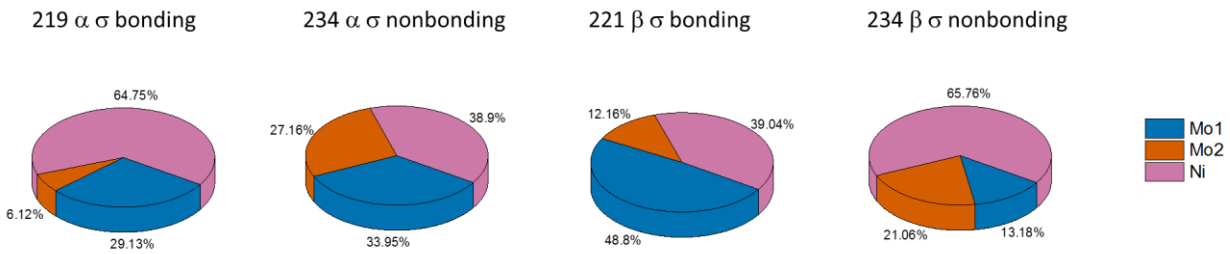

Chart 4.2. Orbital contributions to the σ and σ_{nb} orbitals from the Ni and Mo atoms. Mo1 and Mo2 represents the terminal and central Mo atoms respectively.

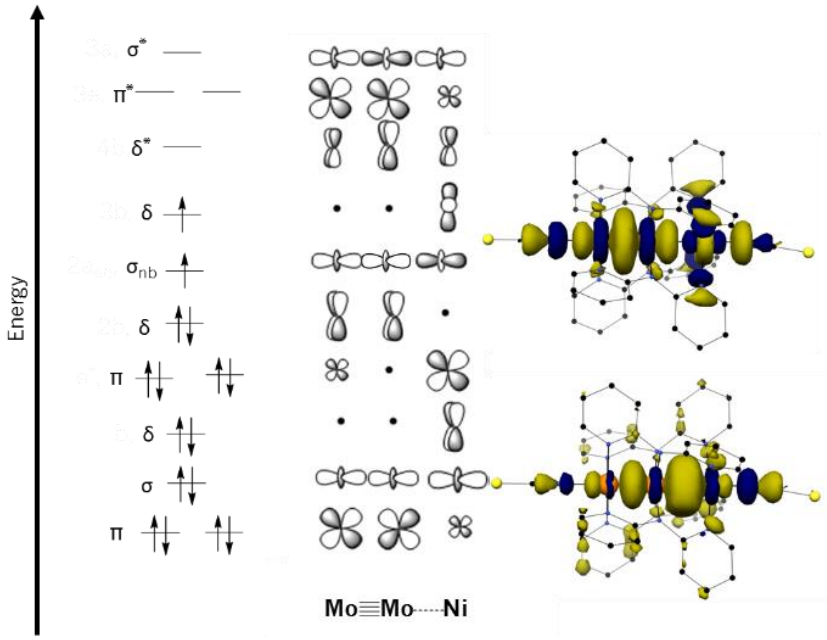

Figure 4.5 A Qualitative MO diagram for $Mo_2Ni(dpa)_4X_2$ HEMACS based on the results of DFT.

Table 4.3. SQUID fitting parameters for 1, 2, 3, compared to existing Mo_2Ni complexes 5 and 5^{ox}.

Compound	χT at 300 K (emu K mol^{-1})	$g_{\parallel}$	$g_{\perp}$	|D| (cm^{-1})	zJ (cm^{-1})	Ref.
1[A]	1.02	1.809(2)	2.297(9)	7.97(3)	0.041(5)	*This work*
2	1.09	1.861(1)	2.157(3)	5.587(5)	0.1834(5)	*This work*
3	1.14	1.800(4)	2.2651(2)	5.394(6)	-0.0691(5)	*This work*
$Mo_2Ni(dpa)_4Cl_2$ **5**	1.09	1.817(4)	2.171(1)	9.19(3)	0.27(3)	9
$[Mo_2Ni(dpa)_4Cl_2]^+$ **5^{ox}**	1.75	1.710(2)	2.299(3)	2.86(4)	n/a	9

[A]These values are derived from fitting of χT and reduced magnetization (variable temperature variable field) data sets.

Magnetic susceptibility data for **1**, **2**, and **3** are shown in Figure 4.6. The χT values for **1**, **2**, and **3** at 300 K, 1.02 emu K mol^{-1}, 1.09 emu K mol^{-1}, and 1.14 emu K mol^{-1}, respectively, agree well with the spin-only value for an S = 1 ground spin state (1.0 emu K mol^{-1}).[9] These values also agree with the previously reported χT value for **5** at 300K, 1.09 emu K mol^{-1}. The data for compounds **1**, **2**, and **3** were all modeled as S = 1 systems including an axial zero-field parameter, D. The data sets for, all three compounds present a sharp downward turn in the χT plots for temperatures below 50 K, suggestive of zero field splitting. Additionally, a variable temperature/variable field (VT/VH) measurement was made for **1** in order to determine the sign of D, which is positive. The VT/VH data for **1** along with the corresponding theoretical fit are shown in Figure 4.7 while the overall fitting parameters data for all compounds are presented in Table 4.4.

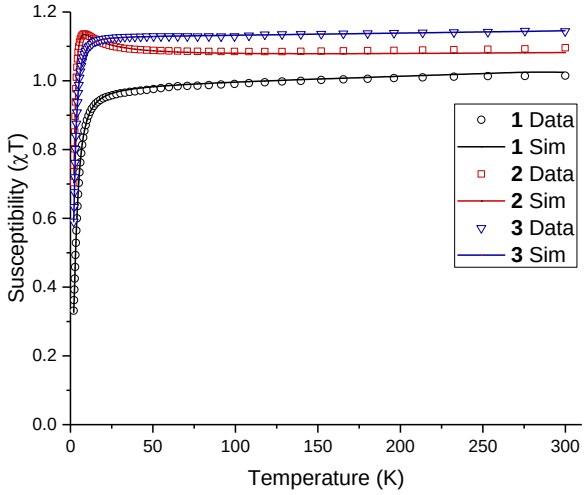

Figure 4.6 Magnetic susceptibility plots for **1**–**3**.

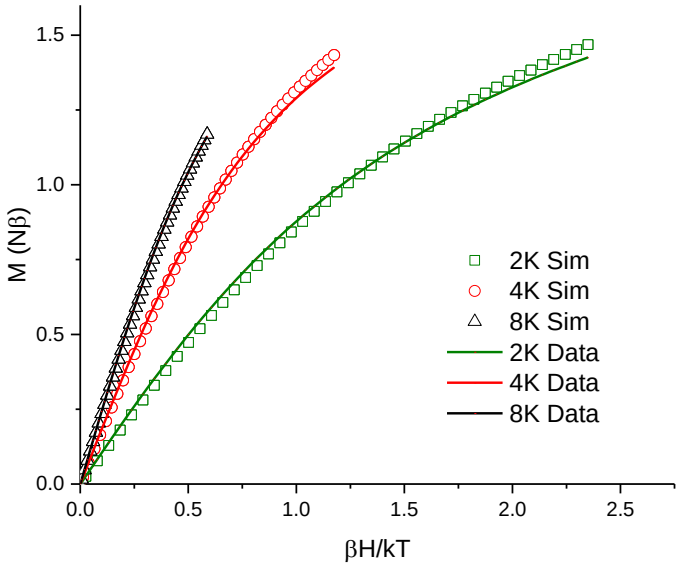

Figure 4.7 Variable temperature/variable field magnetization data for **1**.

The fitted *D* values range from 5 – 10 cm^{-1}, in good agreement with observations for other $S = 1$ Ni^{2+} complexes.[36] For the $Mo_2Ni(dpa)_4X_2$ series, larger *D* values are obtained when X = OTf or Cl as compared to X = NCS or NCSe. This observation is sensible as OTf and Cl are weaker field ligands as compared to NCS and NCSe and in mononuclear Ni^{2+} complexes *D* is inversely proportional to the energies of Ni(II) ligand-field transitions.[36] The *g* and *D* values in Table 4.4 deserve additional commentary. In classic perturbation

theory, g values are given by $g_{\parallel} = g_e - 2\lambda\,\Lambda_{zz}$ and $g_{\perp} = g_e - 2\lambda\,\Lambda_{xx}$, where g_e is the free electron g-value, 2.0023, and λ = - $\xi/2$ where is the spin-orbit coupling constant for the complex. Here, $\Lambda_{ww} = \frac{\sum_{n'}\langle 0|\hat{L}_w|n\rangle\langle n|\hat{L}_w|0\rangle}{E(0)-E(n)}$, which are positive for the case of Ni^{2+}. Since ξ = - 630 cm^{-1} for the free Ni^{2+} ion, values of g_z and g_x are all expected to be greater than 2. Clearly, the g_z values in Table 4.4 do not follow this expectation. Further considering the relationship between D and g anisotropy, $\Delta g = g_{\parallel} - g_{\perp}$, for mononuclear Ni^{2+} complexes, namely, $D = \frac{1}{2}\lambda(\Delta g)$, the D values we observe would predict values of Δg that are too small by an order of magnitude from what we observe. These observations lead to the conclusion that electron delocalization along the Ni^{2+} and the heavier Mo^{2+} ions in these complexes has a major contribution to the g anisotropy. In particular, g_z, mainly affected by $|d_{z^2}\rangle$, is less that g_e as would be much more typical of the g values of a Mo^{2+} ion. Thus, the magnetic data for **1** – **3** and **5** strongly support the result, seen in our DFT calculations, that the Ni^{2+} d_{z^2} unpaired electron is highly delocalized covalently with the Mo^{2+} ions.

4.4 Summary

In previous work, we have made a magnetic comparison between $CrCrCo(dpa)_4Cl_2$ and $MoMoCo(dpa)_4Cl_2$ and found that the $Mo_2(dpa)_4$ "ligand" provides a weaker ligand field to Co^{2+} than does the $Cr_2(dpa)_4$ "ligand."[4] It is therefore surprising that, synthetically, we find demetallation from the $Cr_2(dpa)_4$ ligand to be more facile than from the $Mo_2(dpa)_4$ "ligand." We attribute this effect to the stronger 3c/3e$^-$ interaction involving the more diffuse orbitals of Mo than Cr.

The ability to cleanly and easily substitute the axial ligands of $Mo_2Ni(dpa)_4(OTf)_2$ suggests that other $Mo_2M(dpa)_4(OTf)_2$ HEMACs may behave in a similar way. This, in turn, will allow for additional exploration and tuning of the properties of HEMAC complexes. DFT calculations for all three compounds reported here suggest that the 3c/3e$^-$ σ bond helps support the $Mo_2Ni(dpa)_4X_2$ complexes and greatly enhances the g anisotropy of the compounds. This motif is present along other $Mo_2M(dpa)_4X_2$ complexes providing further impetus to explore their axial ligand substitution chemistry as well.

4.5 Experimental Section

Materials and Methods All reactions were carried out under a dry N_2 atmosphere using Schlenk techniques and glovebox methods. Hexanes, acetonitrile, tetrahydrofuran, and diethyl ether were purified

using a Vacuum Atmospheres solvent purification system and dichloromethane was freshly distilled under an N_2 atmosphere over CaH_2 prior to use. Naphthalene was purchased from Sigma-Aldrich and sublimed prior to use. The ligand Hdpa was purchased from TCI and recrystallized from hot hexanes prior to use. $Ni(OTf)_2$, NaNCS, and KNCSe were purchased from Strem Chemicals. $Ni(OTf)_2$ was used as received while NaNCS and KNCSe were dried under vacuum at 40˚C overnight prior to use. Elemental analysis was carried out by Midwest Microlabs, LLC inc., Indianapolis, IN. IR spectra were taken on a BRUKER TENSOR 27 FTIR spectrometer using an attenuated total reflectance (ATR) adapter. Cyclic voltammograms (CVs) for **1** and **2** were taken on a BASI Epsilon EC potentiostat while **3** was taken on a BioLogic SP200 EC potentiostat. All CVs were obtained using CH_2Cl_2 solutions with 0.1 M NBu_4PF_6 and 1 mM substrate. The electrodes were as follows: glassy carbon (working), Pt wire (auxiliary), and Ag/Ag^+ in CH_3CN (reference). The potentials were referenced against the ferrocene/ferrocenium redox couple by external addition of ferrocene. Variable temperature magnetic susceptibility measurements of crystalline samples of **1**, **2**, and **3** were recorded at the University of Wisconsin-Madison on a SQUID Magnetometer (MPMS 3, Quantum Design) in the temperature range 2 – 300 K with an applied field of 0.1 Tesla. Variable temperature/ variable field measurements of a crystalline sample of **1** were also collected on the same magnetometer at 2, 4, and 8 K at a field ranging from 0.1 to 7 Tesla. Experimental susceptibility and magnetization data were corrected for the underlying diamagnetism using Pascal's constants[37] and for the temperature independent paramagnetism contributions. The data were modeled using the program PHI.[38] ^1H and ^{13}C NMR spectra were obtained on a 500 MHz Bruker Avance III.

Crystallography

Crystallographic data were measured at the Molecular Structure Laboratory of the Chemistry Department of the University of Wisconsin–Madison. Crystals were selected under oil under ambient conditions and attached to the tip of a MiTeGen MicroMount. Each crystal was mounted under a stream of cold nitrogen at 100(1) K and centered in the X-ray beam using a video camera. The crystal evaluation and data collection were performed on a Bruker Quazar SMART APEXII diffractometer with Mo Kα (λ = 0.71073 Å) radiation with a detector to crystal distance of 5.0 cm. The data were collected using a routine to survey the entire sphere of reciprocal space, and were indexed by the SMART program.[39] The structures were solved using direct methods and refined by least-squares refinement on F^2 followed by difference Fourier synthesis.[40]

All hydrogen atoms were included in the final structure factor calculation at idealized positions and were allowed to ride on the neighboring atoms with relative isotropic displacement coefficients.

There was 56% positional metal atom disorder in **1** with the Mo≣Mo–Ni unit ordered in two opposing orientations. The central nitrogen atoms of the dpa ligand were also found to be disordered and were split with occupancies matching the positional metal atom disorder. This nitrogen atom disorder had not been necessary in the refinement of previously synthesized HEMACs. We hypothesize that the two sets of N atom positions reflect the propensity for the Mo≣Mo bond to confer low N–Mo–Mo–N torsion angles, due to the Mo–Mo δ bond. The metal atoms and nitrogen atoms in **2** and **3** are ordered; for **2**, the axial NCS ligand appended to the terminal Mo was also positionally disordered. Complex **3** crystallized as a two-component twin and presented positional disorder of one axial NCSe ligand in addition to positional disorder of the selenium atom of the other ligand.

Computational Methods

The initial coordinates for the calculations were obtained from the crystallographic data for **1**, **2**, and **3** with the solvent molecules of crystallization removed and the dominant orientation for any disorder utilized. All calculations were carried out using the program ORCA version 3.0.3.[41] The BP86 exchange-correlation functional[42-43] including the ZORA approximation was used.[44] The Stuttgart-Dresden effective core potential (ECP), def2-SD,[45] was used along with the valence basis sets def2-TZVP and density fitting basis set def2-TZVP/J for Mo atoms.[46-47] The def2-TZVP basis set and def2-TZVP/J auxiliary basis set was used for Ni.[48-49] The def2-SVP basis set and def2-SVP/J density fitting basis set were used for all other atoms. Tight optimization and tight self-consistent field convergence criteria were employed along with grid4 for all calculations. Frequency calculations were performed following geometry optimizations to ensure the structures were at local minima. Löwdin population analysis was done to determine orbital populations.[50-51] Visualizations were carried out with the UCSF Chimera package.[52] Symmetry labels presented in the molecular orbital diagram were assigned by inspection to conform with the idealized C_4 point group.

Kdpa. The ligand Hdpa (3.30 g, 19.27 mmol) and $KN(TMS)_2$ (3.86g, 19.38 mmol)) were separately dissolved in minimal quantities of diethyl ether. Dropwise, the $KN(TMS)_2$ solution was added to the Hdpa

solution affording a milky off-white precipitate. The reaction mixture was allowed to stir at room temperature for 30 minutes before being filtered and the solid was washed with washed with 2 x 30 mL of additional diethyl ether. The off-white powder was collected and dried under vacuum (3.38 g, 83.8%). ^{1}H NMR (500 MHz, d_8 THF): δ (ppm) 6.24 (ddd, *J* = 6.65, 5.05, 1.07 Hz, 2H), 7.12 (ddd, *J* = 8.70, 6.82, 2.14 Hz, 2H), 7.31 (ddd, *J* = 8.76, 1.04 Hz, 2H), 7.94 (ddd, *J* = 5.01, 2.16, 0.91 Hz, 2H), ^{13}C NMR (500 MHz, d_8 THF): δ (ppm) 109.43, 112.77, 134.73, 147.25, 163.03. Analysis $KC_{10}N_3H_8$ Calc: C 57.38, H 3.85, N 20.07 Found: C 56.62, H 3.82, N 20.07. IR (ATR, cm^{-1}) 1746 w, 1602 m, 1566 s, 1463 s, 1427 s, 1376 s, 1340 w, 1310 m, 1277 w, 1231 m, 1157 m, 1056 m, 1030 m, 861 w, 768 m, 750 m, 740 m, 692 w, 666 w, 636 s.

$Mo_2(dpa)_4$ (4). Canary yellow $Mo_2(OAc)_4$ (2.10 g, 4.91 mmol) and off-white Kdpa (4.20 g, 20.01 mmol) were combined in a Schlenk flask. Upon addition of 100 mL of THF, the contents of the flask turned a brick red color. The reaction was allowed to proceed under refluxing conditions overnight during which time a dark red precipitate formed. This solid was isolated via filtration and washed with 3 x 30 mL MeOH, and 3 x 30 mL diethyl ether. The red powder was then collected and dried under vacuum (3.63g, 84.9%) The IR spectrum was identical to that previously reported.[4]

$Mo_2Ni(dpa)_4(OTf)_2$ (**1**). Solid brick-red $Mo_2(dpa)_4$ (0.446 g, 0.511 mmol) and Ni $(SO_3CF_3)_2$ (0.282 g, 0.790 mmol) were combined with naphthalene (5 g) in a Schlenk flask. The flask was placed in a sandbath that had been pre-heated to 200 °C and stirred for 2 hours during which time the reaction mixture became dark green in color. After cooling to room temperature, the solidified reaction mixture was washed with hot hexanes (4x40 mL). The residual dark solid was dried under vacuum and subsequently extracted with dichloromethane (30 mL). The dark green extract was then layered with hexanes (70 mL). Dark colored X-ray quality blocks of **1** were obtained after 3 days. Yield (212 mg, 33.7%). ^{1}H NMR (500 MHz, CD_2Cl_2): δ (ppm) 0.51 (s), 6.75 (s), 9.64 (s), 12.49 (s), 16.47 (s), 30.15 (s). Analysis $Mo_2Ni(dpa)_4(SO_3CF_3)_2{\cdot}CH_2Cl_2$ Calc: C 39.29, H 2.61, N 12.79 Found C 39.55 H 2.71 N 12.72. IR (ATR, cm^{-1}): 1600 m, 1578 s, 1478 w, 1453 m, 1429 s, 1370 s, 1302 s, 1284 w, 1250 w, 1174 m, 1056 m, 1015 w, 986 w, 878 w, 852 w, 835 w, 768 s, 754 s, 745 w, 728 m, 698 m, 662 m, 642 m, 618 w.

$Mo_2Ni(dpa)_4(NCS)_2$ (**2**). Green **1** (64.8 mg, 0.0600 mmol) was dissolved in 10 mL of CH_2Cl_2 while a 30.3 mM solution of NaNCS in CH_3CN was separately prepared. The solution of **1** was cooled to 0 °C in an ice bath and 3.2 mL of the NaNCS solution was added to it dropwise over the course of several minutes. The resulting solution turned from forest green to goldenrod and was subsequently warmed to room temperature. The solvent was then removed under vacuum and the resulting brown powder was dissolved in 10 mL of CH_2Cl_2 and filtered over a medium porosity filter frit. The brown solution was layered with diethyl ether (40 mL). Dark block X-ray quality crystals of **2** grew after 1 week. Crystalline yield: 24.8 mg, 45%. Following filtration, the filtrate may be concentrated again to afford **2** as a powder in higher yields. ^{1}H NMR (500 MHz, CD_2Cl_2): δ (ppm) 0.35 (s), 6.63 (s), 7.27 (s), 8.63 (s), 12.62 (s), 31.64 (s). Analysis $Mo_2Ni(dpa)_4(NCS)_2 \cdot CH_2Cl_2$ Calc: C 45.61, H 3.03, N 17.32 Found C 45.90 H 3.31 N 16.73. IR (ATR, cm^{-1}): 2063 m, 1602 m, 1592 m, 1550 w, 1456 s, 1420 s, 1359 s, 1308 s, 1279 w, 1150 m, 1051 m, 1017 w, 964 w, 927 w, 894 m, 816 m, 770 s, 761 s, 740 w, 668 m, 640 m.

$Mo_2Ni(dpa)_4(NCSe)_2$ (**2**). Green **1** (28.6 mg, 0.0233 mmol) was dissolved in 25 mL of CH_2Cl_2 while a 22.6 mM solution of KNCSe in CH_3CN was separately prepared. The solution of **1** was cooled to 0 °C in an ice bath to which 2.06 mL of the KNCSe solution was added dropwise over the course of several minutes. The solution turned from forest green to brown and was subsequently warmed to room temperature. The solvent was then removed under vacuum and the resulting brown powder was dissolved in 15 mL of CH_2Cl_2 and filtered over a medium porosity filter frit. The brown solution was layered with diethyl ether (40 mL). Dark needle-block X-ray quality crystals of **3** grew after three days. Crystalline yield: 11.66 mg, 44.0%. Analysis Cald for $Mo_2Ni(dpa)_4(NCSe)_2 \cdot CH_2Cl_2$ Calc: C 42.12, H 2.79, N 15.99 Found C 41.76 H 2.87 N 16.40. IR (ATR, cm^{-1}): 2075 m, 2009 m, 1602 m, 1593 m, 1562 m, 1474 m, 1458 s, 1420 s, 1349 s, 1307 s, 1280 w, 1155 m, 1059 m, 1015 w, 880 m, 857 m, 810 m, 765 s, 750 w, 738 w, 690 m.

4.6 Acknowledgements

We are grateful to the National Science Foundation for support. In addition, Computational Facilities used to support this work were supported by the NSF under Grant CHE-0840494. The NMR spectrometer used is supported under a gift from the Bender Fund. JFB additionally thanks the Alexander

von Humboldt Foundation and Prof. Karsten Meyer for facilitating some preliminary experiments to those reported here. JAC acknowledges Dr. Brian Dolinar for his crystallographic advice, Dr. Tzuhsiung Yang for his computational insight, and Manar Alherech for his NMR assistance.

4.7 Supplementary Information

Figure S4.1. Thermal ellipsoid plot of $[Mo_2(dpa)_3(NCS)_2]OTf$. Ellipsoids are shown at 50% probability. All H atoms, molecules of solvation, and counteranions have been removed for clarity.

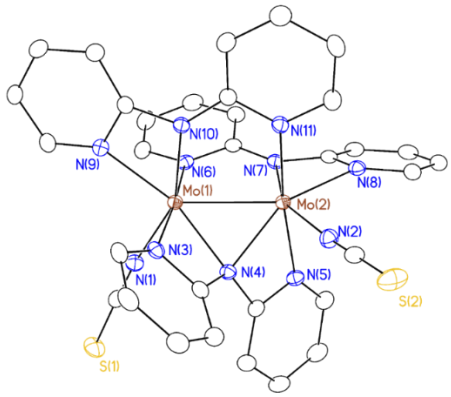

Table S4.1. Crystal Table for $Mo_2(dpa)_3(NCS)_2$

	2
Empirical formula	$Mo_2C_{33}H_{24}N_{11}SO_3F_3$**·$CH_2Cl_2$** ·$CH_2Cl_2$
Crystal system	Triclinic
Space group	$P\bar{1}$
a/Å	11.474(7)
b/Å	13.311(9)
c/Å	13.971(8)
α/°	80.95(1)
β/°	88.202(7)
γ/°	74.25(1)
Volume/Å^3	2028(2)
Z	2
ρ_{calc} g/cm^3	1.724
$R_1{}^a$, $wR_2{}^b$ [I>=2σ (I)]	0.0279, 0.0665
$R_1{}^a$, $wR_2{}^b$ [all data]	0.0312, 0.0681

Fig S4.2. CV of $Mo_2Ni(dpa)_4(NCSe)_2$ in CH_2Cl_2 with NBu_4PF_6 electrolyte. Scan rate 100 mv/s.

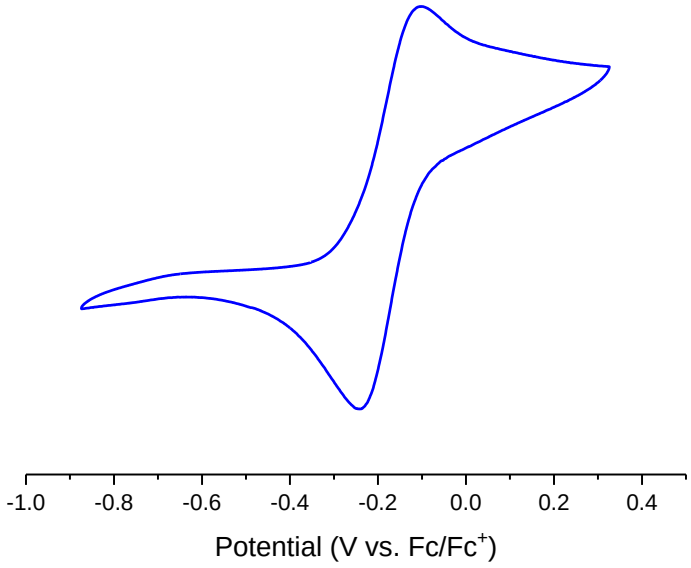

Fig S4.3. ^{1}H NMR Spectrum of Kdpa in D_8THF

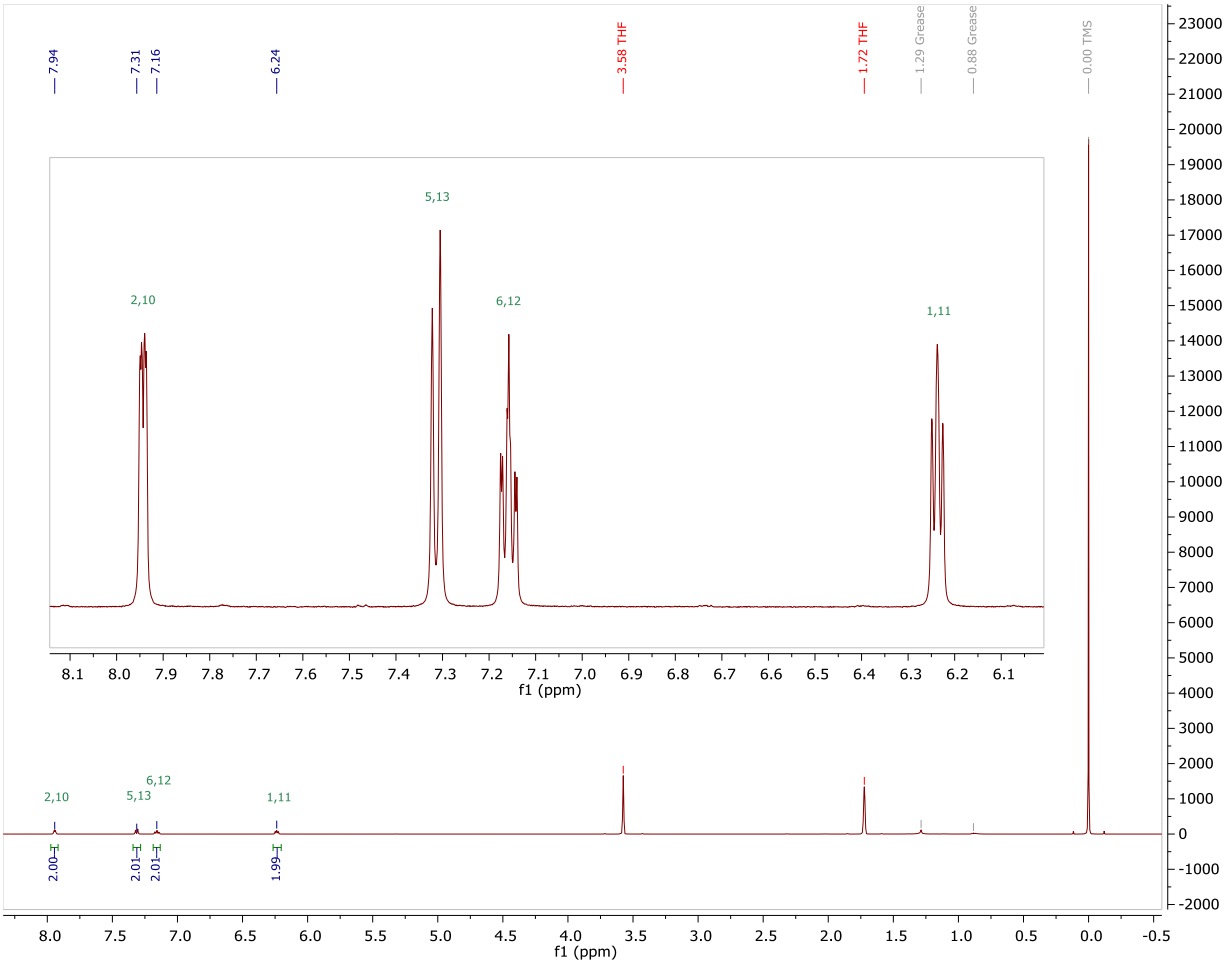

Fig S4.4. ^{1}H NMR Spectrum of Kdpa, with assignments for the four main signals

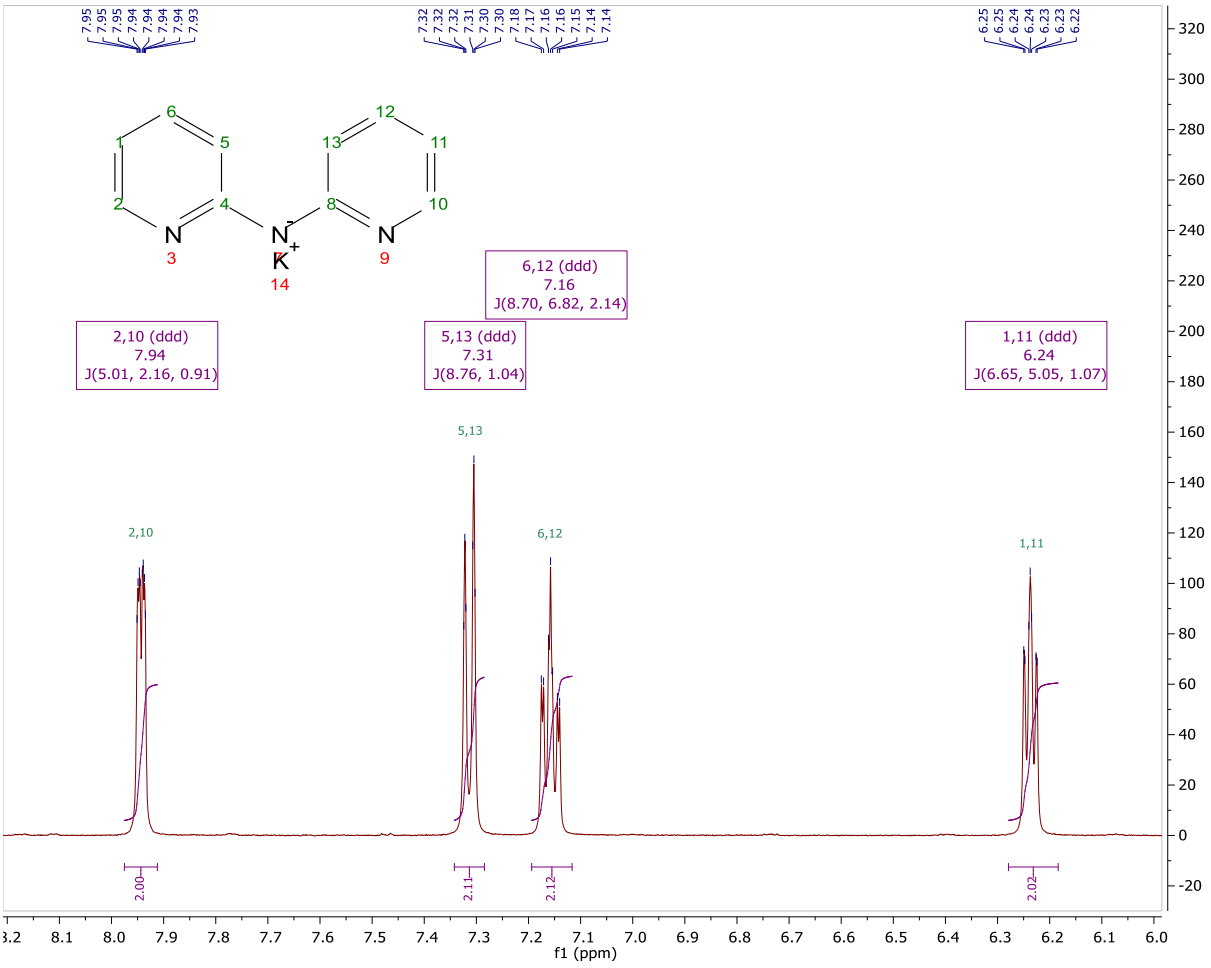

Fig S4.5. ^{1}H NMR Spectrum of Kdpa for signal A with splitting tree

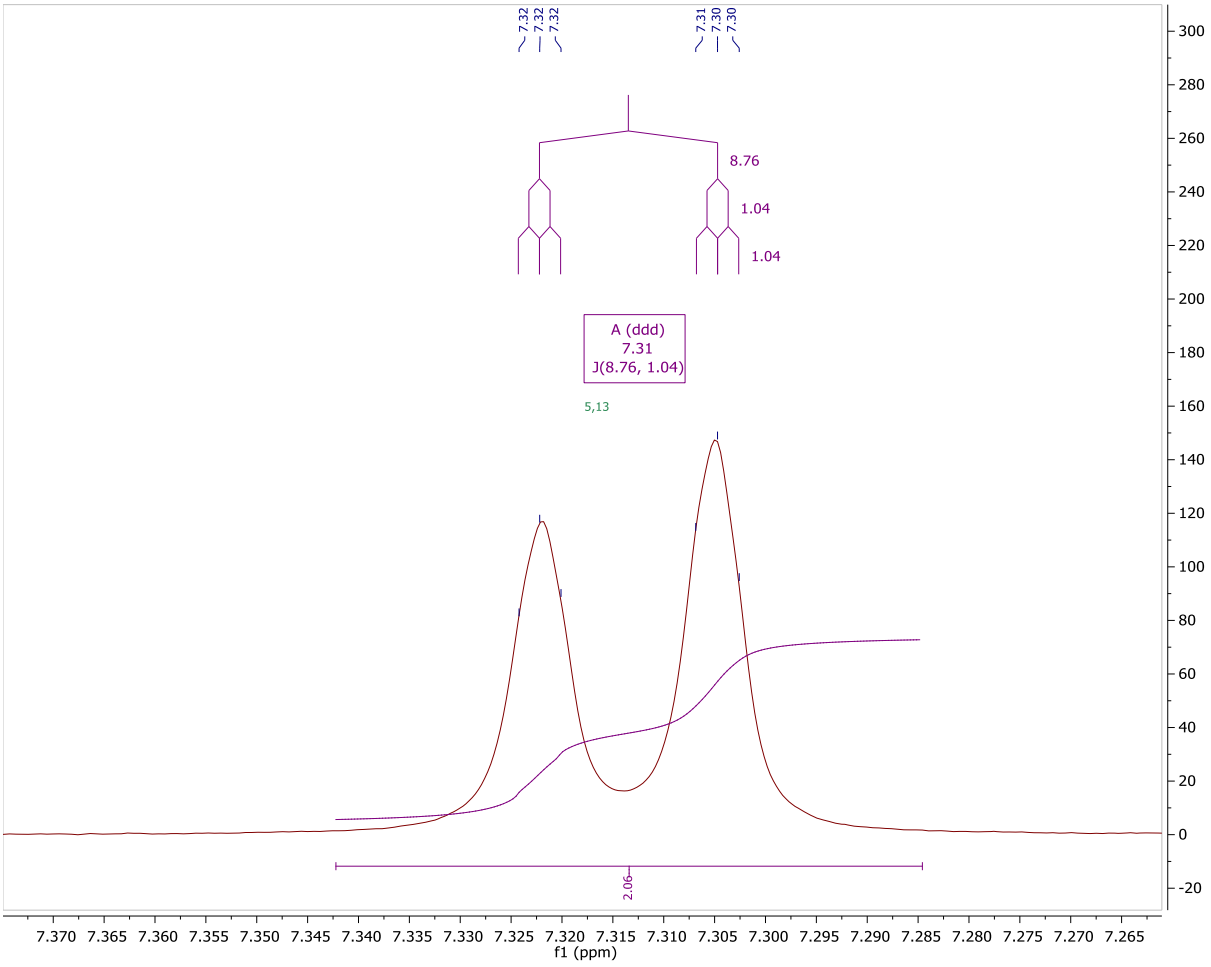

Fig S4.6. ^{1}H NMR Spectrum of Kdpa for signal B with splitting tree

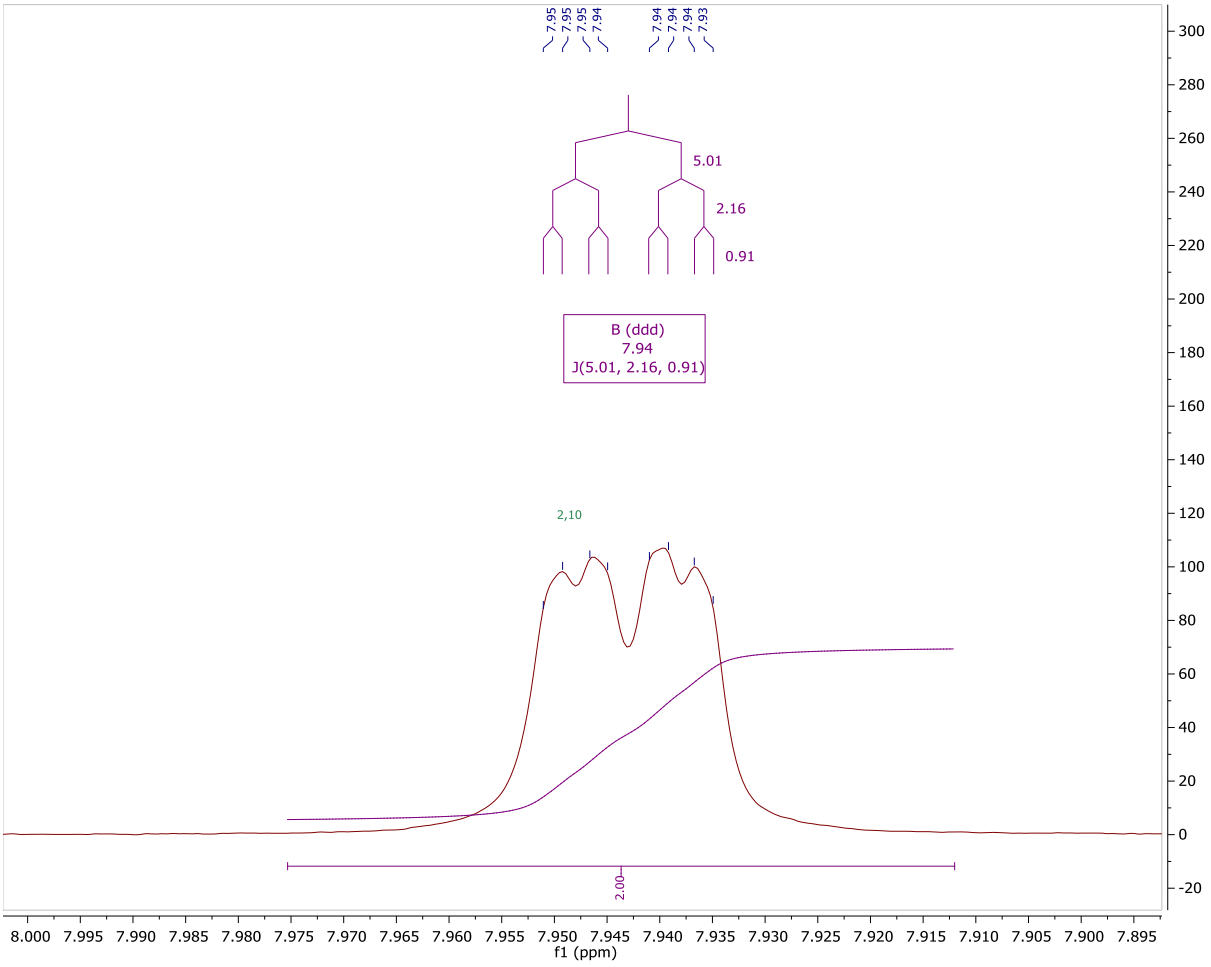

Fig S4.7. ^{1}H NMR Spectrum of Kdpa for signal C with splitting tree

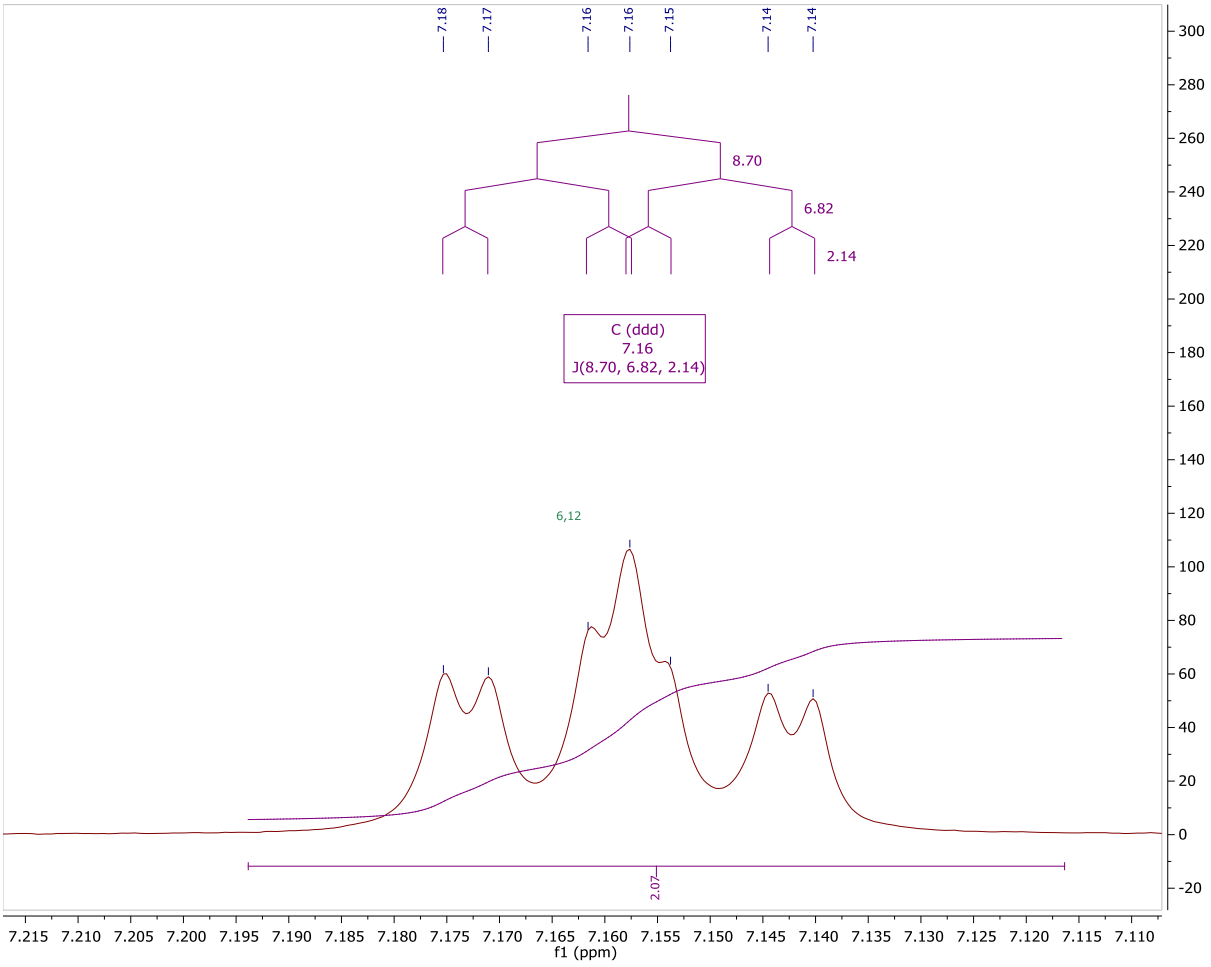

Fig S4.8. ^{1}H NMR Spectrum of Kdpa for signal D with splitting tree

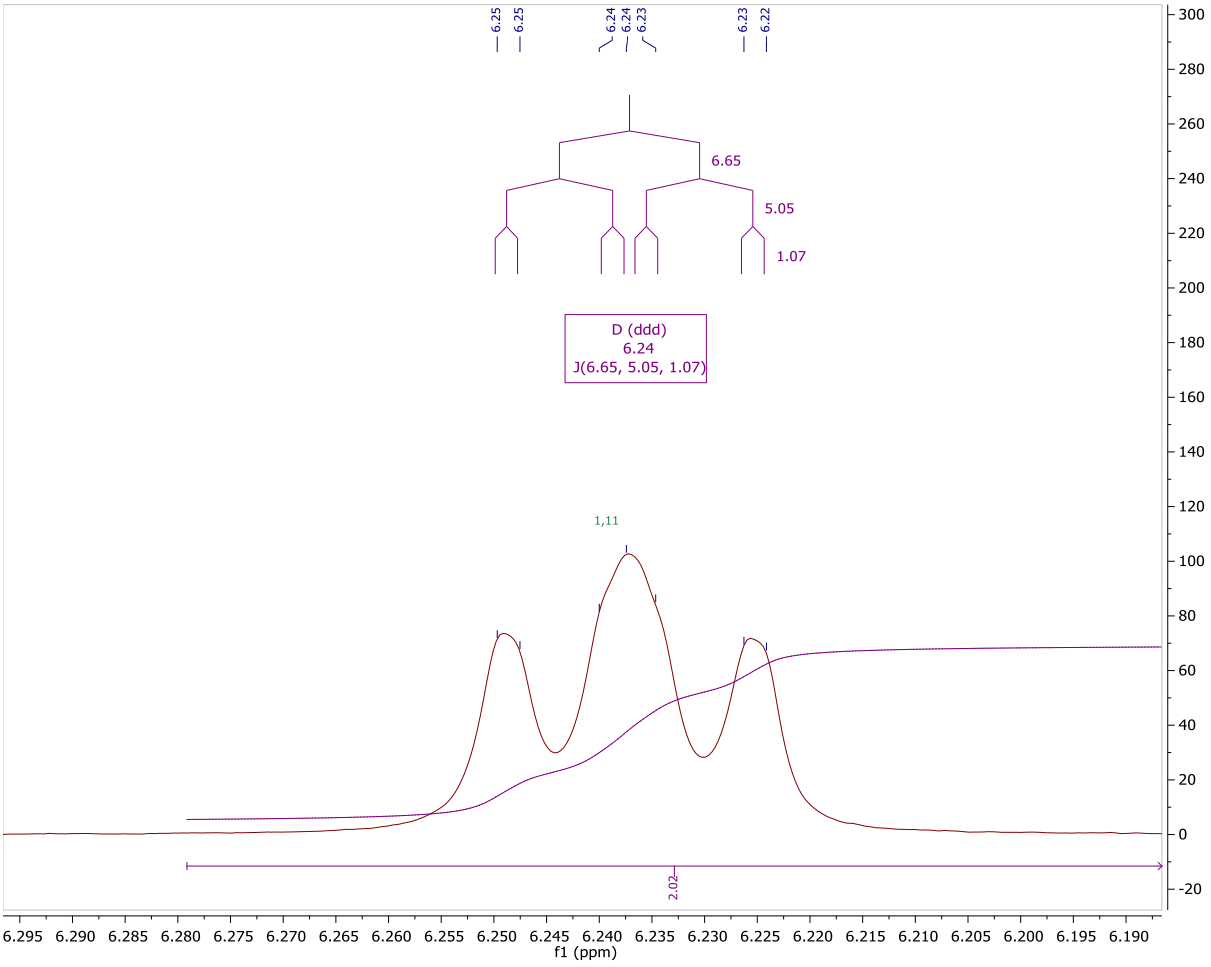

Fig S4.9. ^{13}C NMR Spectrum of Kdpa

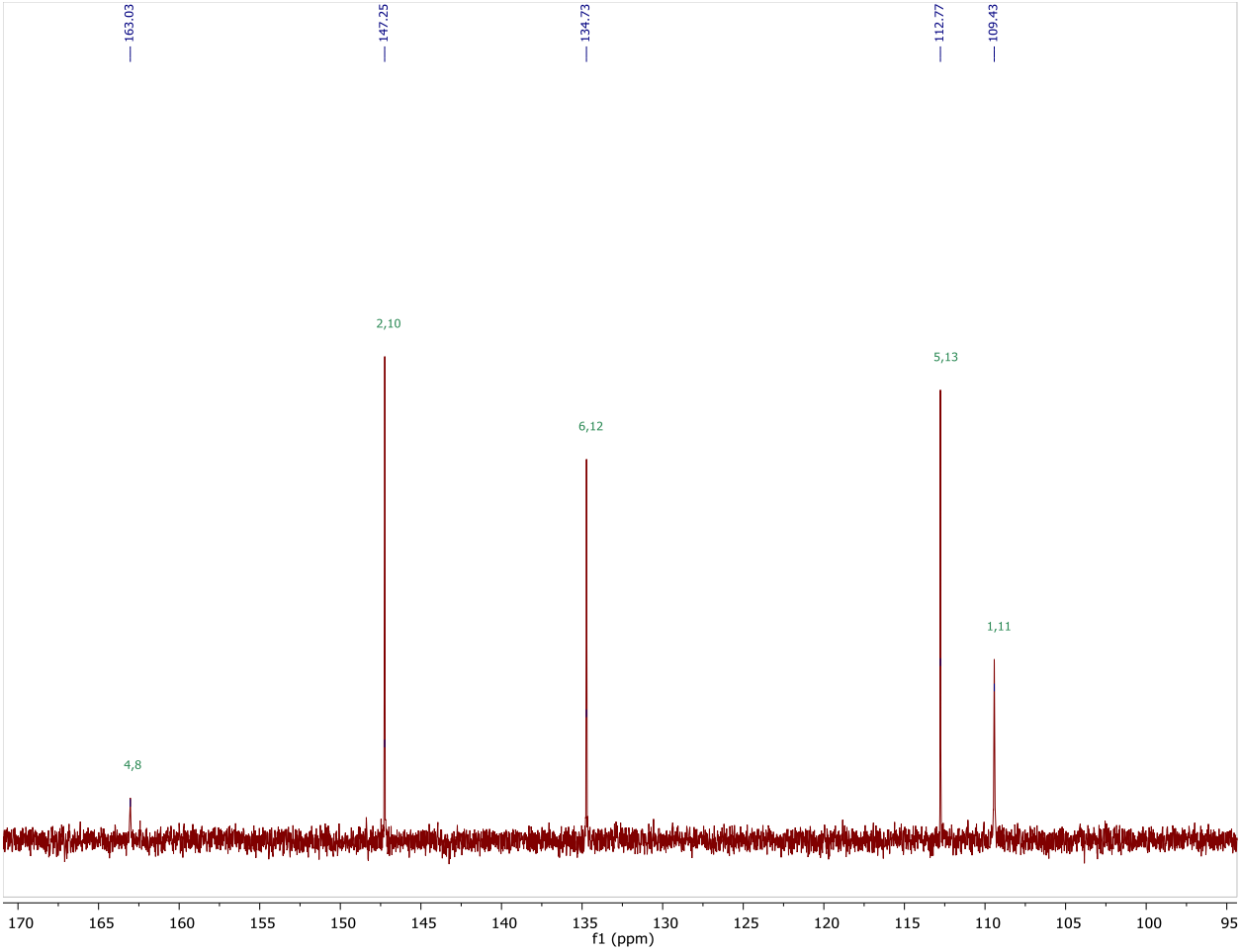

Fig S4.10. Computed (TDDFT) electronic spectra for **1**, **2**, and **3**.

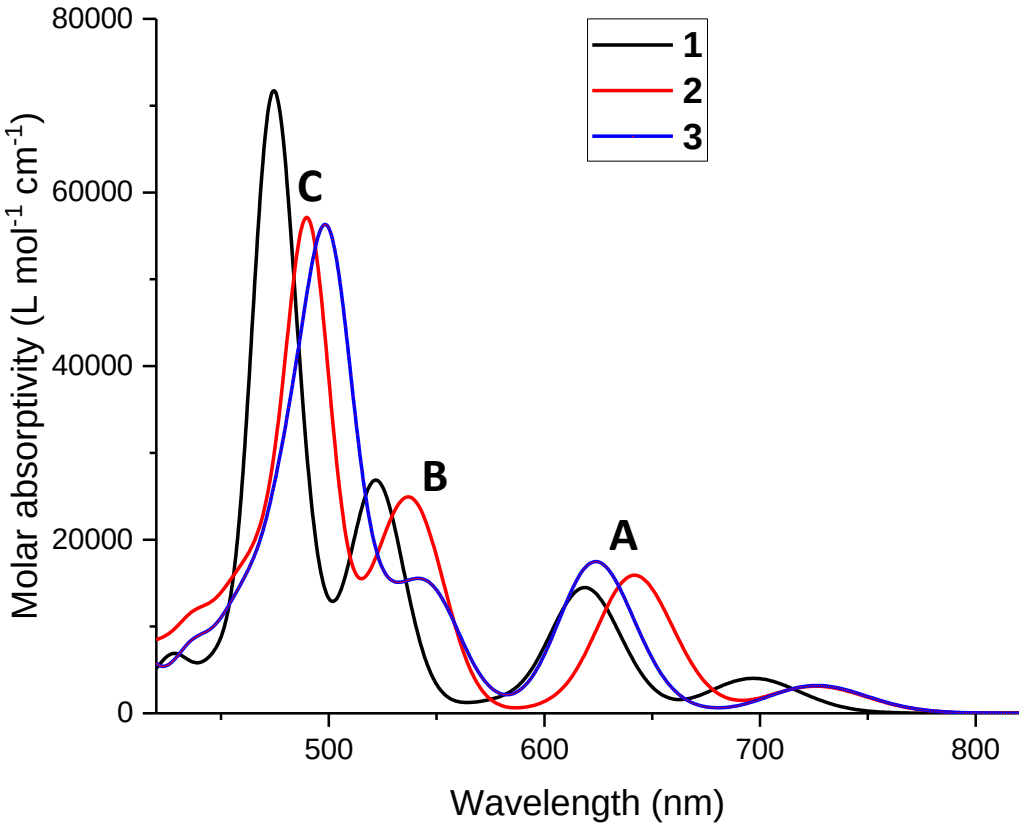

Figure S4.11. ^{1}H NMR for **1** in CD_2Cl_2

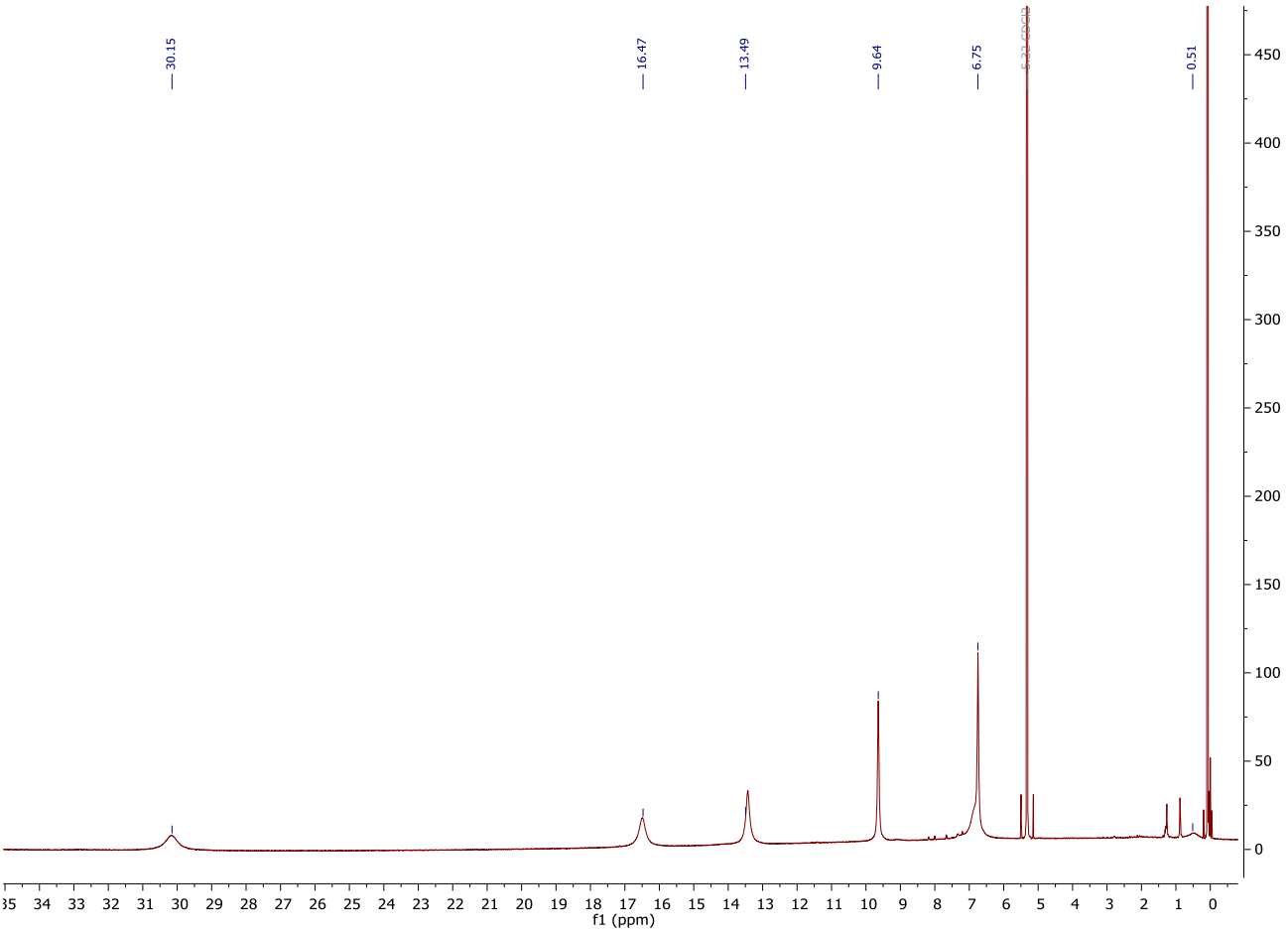

Figure S4.12. ^{1}H NMR for **2** in CD_2Cl_2

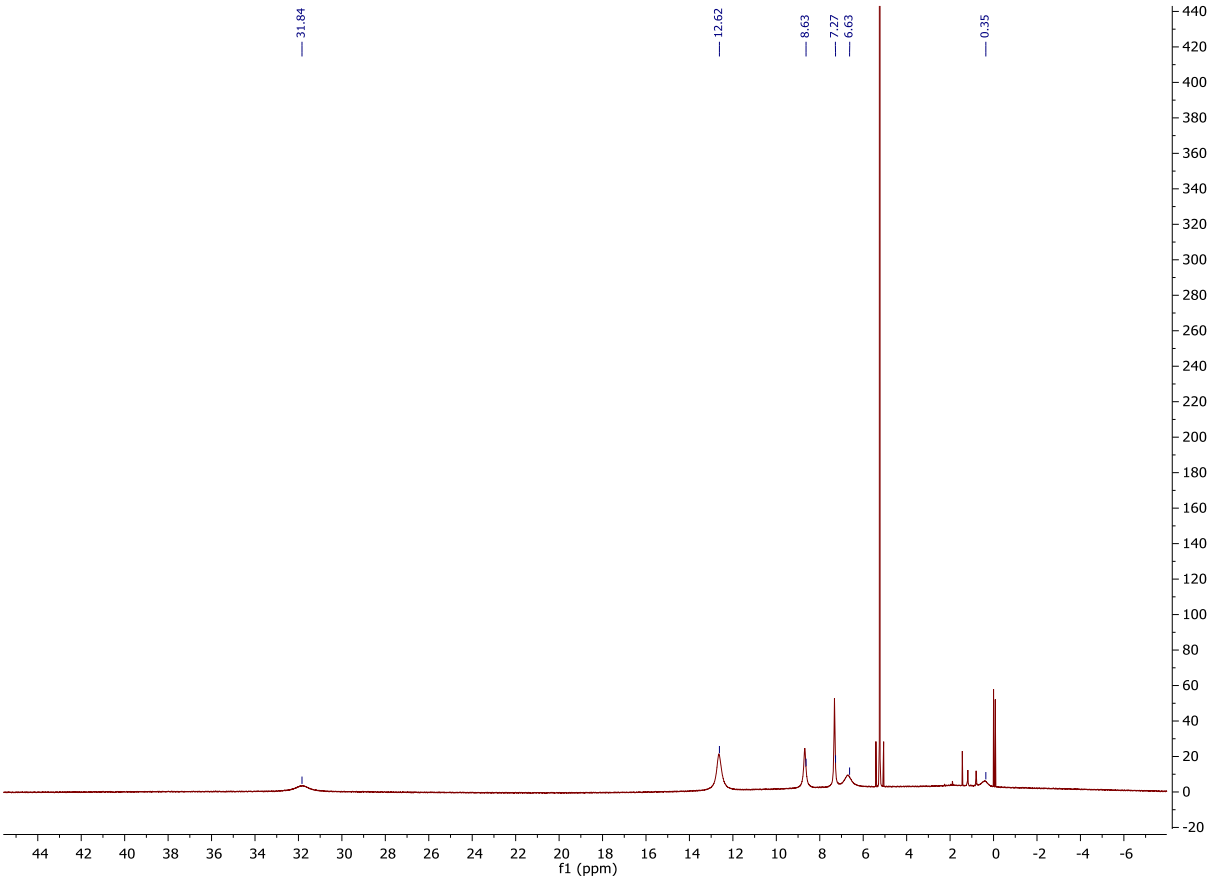

Chart S4.1. Orbital contributions to the σ and σ_{nb} orbitals from the Ni and Mo atoms for **1** and **3**. Mo_1 represent the terminal Mo while Mo_2 represents the central Mo.

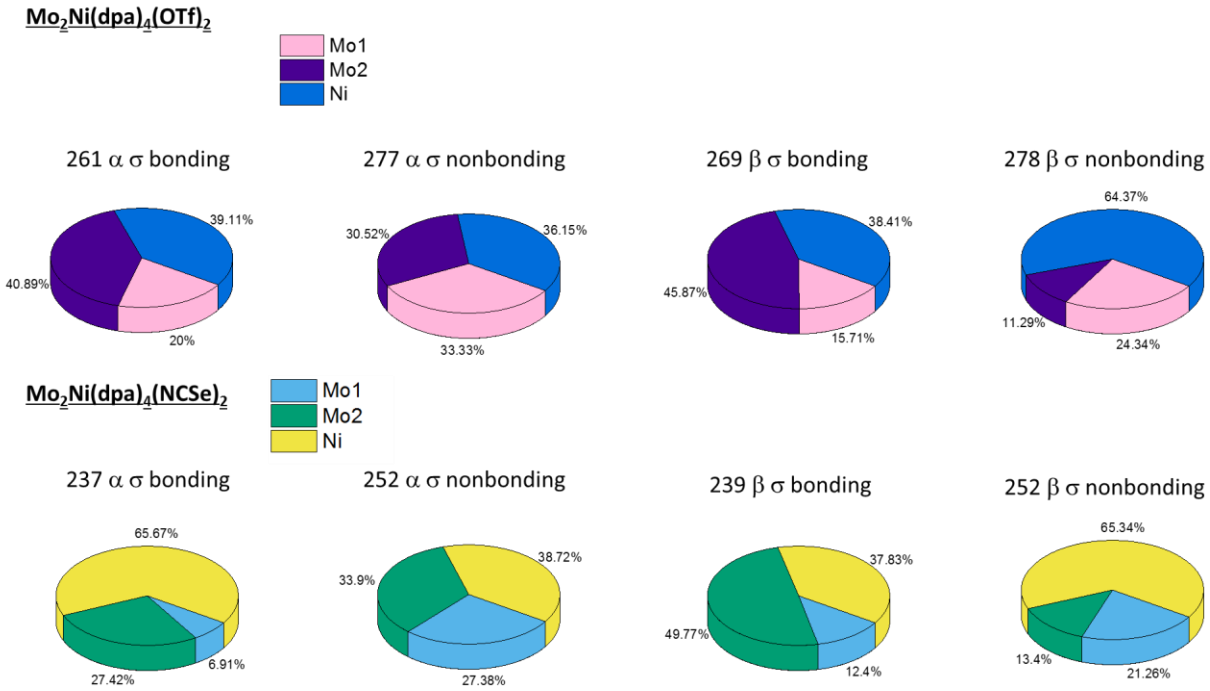

Fig S4.13. Variable scan rate CV of **2** in CH_2Cl_2. Scan rates are in mv/S. The electrolyte is 0.1 M NBu_4PF_6 and the analyte is at 1 mM.

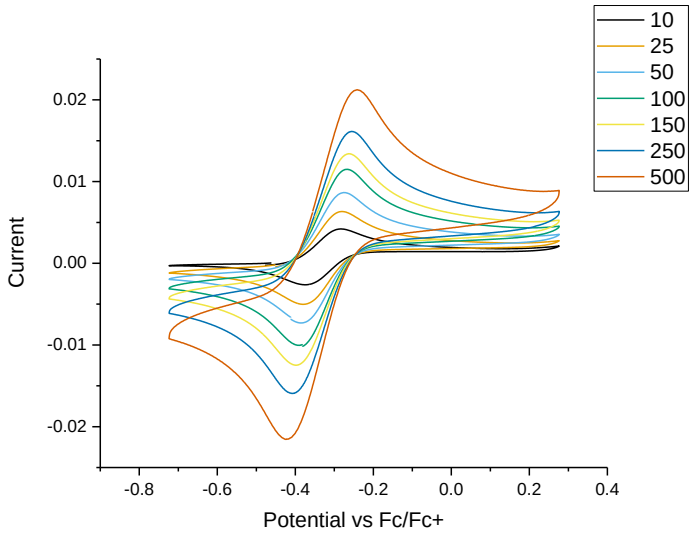

Fig S4.14. Plot of the square root of the scan rate against the current for **2**.

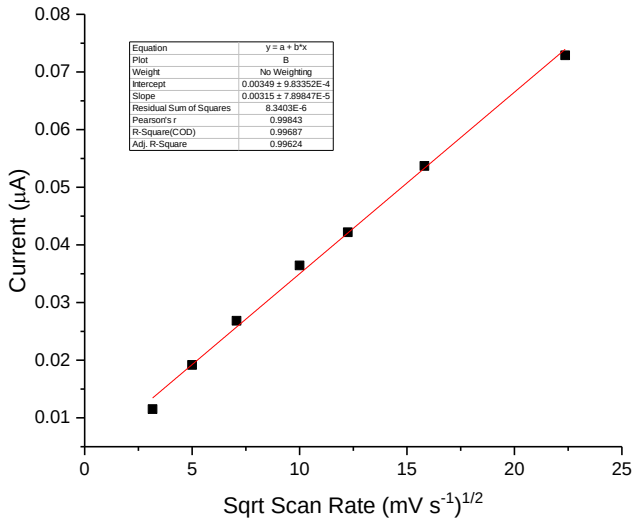

References

1. Nippe, M.; Berry, J. F., Introducing a Metal–Metal Multiply Bonded Group as an "Axial Ligand" to Iron: Synthetic Design of a Linear Cr–Cr···Fe Framework. *J. Am. Chem. Soc.* **2007,** *129*, 12684-12685.

2. Rohmer, M.M.; Liu, I. P.-C.; Lin, J.C.; Chiu, M.J.; Lee, C.H.; Lee, G.H.; Bénard, M.; López, X.; Peng, S.-M., Structural, Magnetic, and Theoretical Characterization of a Heterometallic Polypyridylamide Complex. *Angew. Chemie. Int. Ed.* **2007,** *46*, 3533-3536.

3. Berry, J. F.; Cotton, F. A.; Daniels, L. M.; Murillo, C. A., A Trinickel Dipyridylamido Complex with Metal–Metal Bonding Interaction: Prelude to Polynickel Molecular Wires and Devices? *J. Am. Chem. Soc.* **2002,** *124*, 3212-3213.

4. Nippe, M.; Victor, E.; Berry, J. F., Do Metal–Metal Multiply-Bonded "Ligands" Have a trans Influence? Structural and Magnetic Comparisons of Heterometallic Cr-Cr···Co and Mo-Mo···Co Interactions. *Eur. J. Inorg. Chem.* **2008,** *2008*, 5569-5572.

5. Nippe, M.; Wang, J.; Bill, E.; Hope, H.; Dalal, N. S.; Berry, J. F., Crystals in Which Some Metal Atoms are More Equal Than Others: Inequalities From Crystal Packing and Their Spectroscopic/Magnetic Consequences. *J.Am. Chem. Soc.* **2010,** *132*, 14261-14272.

6. Nippe, M.; Bill, E.; Berry, J. F., Group 6 Complexes with Iron and Zinc Heterometals: Understanding the Structural, Spectroscopic, and Electrochemical Properties of a Complete Series of MM···M′ Compounds. *Inorg. Chem.* **2011,** *50*, 7650-7661.

7. Brogden, D. W.; Berry, J. F., Heterometallic Second-Row Transition Metal Chain Compounds in Two Charge States: Syntheses, Properties, and Electronic Structures of $[Mo–Mo–Ru]^{6+/7+}$ Chains. *Inorg. Chem.* **2015,** *54*, 7660-7665

8. Brogden, D. W.; Christian, J. H.; Dalal, N. S.; Berry, J. F., Completing the series of Group VI heterotrimetallic $M_2Cr(dpa)_4Cl_2$ (M_2 = Cr_2, Mo_2, MoW and W_2) compounds and investigating their metal–metal interactions using density functional theory. *Inorg. Chim. Acta* **2015,** *424*, 241-247.

9. Chipman, J. A.; Berry, J. F., Extraordinarily Large Ferromagnetic Coupling (J≥150 cm−1) by Electron Delocalization in a Heterometallic Mo≡Mo−Ni Chain Complex. *Chem. Eur. J.* **2018,** *24*, 1494-1499.

10. Brogden, D. W.; Berry, J. F., Heterometallic Multiple Bonding: Delocalized Three-Center σ and π Bonding in Chains of 4d and 5d Transition Metals. *Inorg. Chem.* **2014,** *53*, 11354-11356.

11. Clérac, R.; Cotton, F. A.; Dunbar, K. R.; Lu, T.; Murillo, C. A.; Wang, X., New Linear Tricobalt Complex of Di(2-pyridyl)amide (dpa), $[Co_3(dpa)_4(CH_3CN)_2][PF_6]_2$. *Inorg. Chem.* **2000,** *39*, 3065-3070.

12. Clerac, R.; Cotton, F. A.; Daniels, L. M.; Dunbar, K. R.; Murillo, C. A.; Wang, X., Structural and magnetic properties of $Co_3(dpa)_4Br_2$ *Dalton Trans.* **2001**, 386-391.

13. Clérac, R.; Cotton, F. A.; Jeffery, S. P.; Murillo, C. A.; Wang, X., Compounds with Symmetrical Tricobalt Chains Wrapped by Dipyridylamide Ligands and Cyanide or Isothiocyanate Ions as Terminal Ligands. *Inorg. Chem.* **2001,** *40*, 1265-1270.

14. Berry, J. F.; Albert Cotton, F.; Murillo, C. A., Making connections with molecular wires: extending tri-nickel chains with axial cyanide, dicyanamide, and phenylacetylide ligands. *Dalton Trans.* **2003**, 3015-3021.

15. Berry, J. F.; Cotton, F. A.; Lu, T.; Murillo, C. A.; Roberts, B. K.; Wang, X., Molecular and Electronic Structures by Design: Tuning Symmetrical and Unsymmetrical Linear Trichromium Chains. *J. Am. Chem. Soc.* **2004,** *126*, 7082-7096.

16. Berry, J. F.; Cotton, F. A.; Murillo, C. A., A Trinuclear EMAC-Type Molecular Wire with Redox-Active Ferrocenylacetylide "Alligator Clips" Attached. *Organometallics* **2004,** *23*, 2503-2506.

17. Berry, J. F.; Cotton, F. A.; Murillo, C. A.; Roberts, B. K., An Efficient Synthesis of Acetylide/Trimetal/Acetylide Molecular Wires. *Inorg. Chem.* **2004,** *43*, 2277-2283.

18. Cotton, F. A.; Murillo, C. A.; Walton, R. A., Multiple Bonds between Metal Atoms. **2005**.

19. Cotton, F. A.; Murillo, C. A.; Wang, Q., Symmetrical linear Co36+ chains cocooned by two polypyridylamide ligands: How do they compare to open chains? *Inorg. Chim. Acta* **2010,** *363*, 4175-4180.

20. Li, H.; Yan, J.; Xu, Y. Y.; Gao, W. G.; Lee, G.H.; Peng, S.M., Hydrogen-bonded assemblies of trinuclear metal string complexes. *J. Coord. Chem.* **2007,** *60*, 2731-2738.

21. Nippe, M.; Turov, Y.; Berry, J. F., Remote Effects of Axial Ligand Substitution in Heterometallic Cr≡Cr···M Chains. *Inorg. Chem.* **2011,** *50*, 10592-10599.

22. Turov, Y.; Berry, J. F., Synthesis, characterization and thermal properties of trimetallic N3-Cr-Cr···M-N3 azide complexes with M = Cr, Mn, Fe, and Co. *Dalton Trans.* **2012,** *41*, 8153-8161.

23. Chang, W.C.; Chang, C.W.; Sigrist, M.; Hua, S.A.; Liu, T.J.; Lee, G.H.; Jin, B.Y.; Chen, C.H.; Peng, S.M., Nonhelical heterometallic $[Mo_2M(npo)_4(NCS)_2]$ string complexes (M = Fe, Co, Ni) with high single-molecule conductance. *Chem. Commun.* **2017,** *53*, 8886-8889.

24. Hurley, T. J.; Robinson, M. A., Nickel(II)-2,2'-dipyridylamine system. I. Synthesis and stereochemistry of the complexes. *Inorg. Chem.* **1968,** *7*, 33-38.

25. Huang, G.C.; Bénard, M.; Rohmer, M.-M.; Li, L.A.; Chiu, M.J.; Yeh, C.Y.; Lee, G.H.; Peng, S.M., $Ru_2M(dpa)_4Cl_2$ (M = Cu, Ni): Synthesis, Characterization, and Theoretical Analysis of Asymmetric Heterometal String Complexes of the Dipyridylamide Family. *Eur. J. Inorg. Chem.* **2008**, 1767-1777.
26. The neutral $Ru_2Ni(dpa)_4Cl_2$ molecule was studied crystallographically, however, metal atom disorder was so severe that the reported anomalous Ru – Ni distance is fixed to an unreliable value.

27. Aydin-Cantürk, D.; Nuss, H., Synthesis, Structure Determination, and Magnetic Properties of the New Heterometallic Chain Compound CrCrNi(di-2,2′-pyridylamido)$_4Cl_2$·Et_2O. *Zeitschrift für anorganische und allgemeine Chemie* **2011,** *637*, 543-546.

28. Arcisauskaite, V.; Spivak, M.; McGrady, J. E., Structure and bonding in trimetallic arrays containing a Cr–Cr quadruple bond: A challenge to density functional theory. *Inorg. Chim. Acta* **2015,** *424*, 293-299.

29. Unit Cell Parameters: a/Å 11.474(7) b/Å 13.311(9) c/Å 13.971(8) α/° 80.95(1) β/° 88.202(7) γ/° 74.25(1) Volume/Å3 2028(2) Z = 2. Mo2(C10H8N3)3(NCS)2(SO3CF3)*CH2Cl2

30. Rohmer, M.-M.; Bénard, M., Bond Stretch Isomerism Still Elusive in Linear Trimetallic Complexes. DFT Calculations on Co3(dipyridylamine)4Cl2. *J. Am. Chem. Soc.* **1998,** *120*, 9372-9373.

31. Benbellat, N.; Rohmer, M.M.; Bénard, M., Electronic origin of the structural versatility in linear trichromium complexes of dipyridylamide. *Chem. Commun.* **2001**, 2368-2369.

32. Rohmer, M.M.; Strich, A.; Bénard, M.; Malrieu, J.P., Metal–Metal Bond Length Variability in Co_3(dipyridylamide)$_4Cl_2$: Bond-Stretch Isomerism, Crystal Field Effects, or Spin Transition Process? A DFT Study. *J. Am. Chem. Soc.* **2001,** *123*, 9126-9134.

33. Rohmer, M.M.; Benard, M., Bond-stretch isomerism in strained inorganic molecules and in transition metal complexes: a revival? *Chem. Soc. Rev.* **2001,** *30*, 340-354.

34. Rohmer, M.M.; Bénard, M., Structural Versatility in Polyoxometalates and in Some Linear Trimetallic Complexes: An Electronic Interpretation. *J. Cluster. Sci.* **2002,** *13*, 333-353.

35. Values are derived from the Lowdin analysis of the wavefunction

36. Boča, R., Zero-field splitting in metal complexes. *Coord. Chem. Rev.* **2004,** *248*, 757-815.

37. Bain, G. A.; Berry, J. F., Diamagnetic Corrections and Pascal's Constants. *J. Chem.Ed* **2008,** *85* 532.

38. Chilton, N. F.; Anderson, R. P.; Turner, L. D.; Soncini, A.; Murray, K. S., PHI: A powerful new program for the analysis of anisotropic monomeric and exchange-coupled polynuclear d- and f-block complexes. *J. Comput. Chem.* **2013,** *34*, 1164-1175.

39. *Bruker-AXS*, Madison, Wisconsin, USA, 2009.

40. Dolomanov, O. V.; Bourhis, L. J.; Gildea, R. J.; Howard, J. A. K.; Puschmann, H., : a complete structure solution, refinement and analysis program. In *Journal of applied crystallography*, Oxford, England :, 2009; Vol. 42, pp 339-341.

41. Neese, F., The ORCA program system. *Wiley Interdisciplinary Reviews: Computational Molecular Science* **2012,** *2*, 73-78.

42. Becke, A. D., Density-functional exchange-energy approximation with correct asymptotic behavior. *Phys. Rev. A* **1988,** *38*, 3098-3100.

43. Perdew, J. P.; Yue, W., Accurate and simple density functional for the electronic exchange energy: Generalized gradient approximation. *Phys. Rev. B.* **1986,** *33*, 8800-8802.

44. Pantazis, D. A.; Chen, X.Y.; Landis, C. R.; Neese, F., All-Electron Scalar Relativistic Basis Sets for Third-Row Transition Metal Atoms. *J. Chem. Theory Comput,* **2008,** *4*, 908-919.

45. Andrae, D.; Haussermann, U.; Doll, G.; P. Stoll, H.; Preuss, H., Energy-Adjusted ab initio Pseudopotentials for the Second and Third Row Transition Elements. *Theor. Chem Acc.* **1990,** *77*, 123-141.

46. Weigend, F.; Ahlrichs, R., Balanced basis sets of split valence, triple zeta valence and quadruple zeta valence quality for H to Rn: Design and assessment of accuracy. *Phys. Chem. Chem. Phys.* **2005,** *7*, 3297-3305.

47. Weigend, F., Accurate Coulomb-fitting basis sets for H to Rn. *Phys. Chem. Chem. Phys.* **2006,** *8*, 1057-1065.

48. Eichkorn, K.; Treutler, O.; Öhm, H.; Häser, M.; Ahlrichs, R., Auxiliary basis sets to approximate Coulomb potentials. *Chem. Phys. Let.* **1995,** *240*, 283-290.

49. Eichkorn, K.; Weigend, F.; Treutler, O.; Ahlrichs, R., Auxiliary basis sets for main row atoms and transition metals and their use to approximate Coulomb potentials. *Theor. Chem. Acc.* **1997,** *97*, 119-124.

50. Löwdin, P. O., On the Non-Orthogonality Problem Connected with the Use of Atomic Wave Functions in the Theory of Molecules and Crystals. *J. Chem. Phys.* **1950,** *18*, 365-375.

51. Löwdin, P.O., On the Nonorthogonality Problem *Advances in Quantum Chemistry* **1970,** *5*, 185-199.

52. Pettersen, E. F.; Goddard, T. D.; Huang, C. C.; Couch, G. S.; Greenblatt, D. M.; Meng, E. C.; Ferrin, T. E., UCSF Chimera—A visualization system for exploratory research and analysis. *J. Comp. Chem.* **2004,** *25*, 1605-1612.

Chapter Five

Further Investigation of Phase Transitions Driven by Interactions between Halides and Dichloromethane in a Series of Cr_2Fe HEMACs

Chipman, J. A.; SantaLucia, D.J; Brogden, D.W; Berry, J.F.

DWB performed the initial syntheses and characterization, DJS performed the Mössbauer work, JAC performed initial Mössbauer work, SQUID magnetometry, and analysis

5.1 Abstract

The heterometallic chain compounds $Cr_2Fe(dpa)_4X_2$ (X = Cl; **1**, Br; **2**, and I; **3**; dpa = 2,2'-dipyridylamine) were synthesized by reaction of $Cr_2(dpa)_4$ and the corresponding FeX_2. The crystal structures of **1**, **2**, and **3** at 100K show disorder in the metal-atom positions such that the $M_AM_AM_B$ backbone can be orientated in one of two crystallographically identical orientations. At low temperature, 12 K a crystal structure of **1**·CH_2Cl_2 was previously reported [J.Am.Chem.Soc. **2010**, *132*, 14261-14272.] in which these two orientations are no longer crystallographically identical as a result of differences in the interactions between a dichloromethane (DCM) solvent molecule within the unit cell and a terminal Cl bound to the Fe side of the chain. We report here the characterization of **2**·CH_2Cl_2 and **3**·CH_2Cl_2 using SCXRD, Mössbauer spectroscopy, SQUID magnetometry, cyclic voltammetry, and UV-vis spectroscopy. In addition, we report an extensive investigation of **1**·CH_2Cl_2, **2**·CH_2Cl_2, and **3**·CH_2Cl_2 using variable temperature Mössbauer spectroscopy to better understand this phase transition and the nature of the strength of the interaction between the terminal halide and the DCM molecule. Compound **3**·CH_2Cl_2 either does not undergo a phase transition or undergoes the transition at a temperature beyond the range of our instrumentation (< 5K). For **1**·CH_2Cl_2 and **2**·CH_2Cl_2 a phase transition is observed, for **2**·CH_2Cl_2 this transition occurs ~25 K, below that of **1**·CH_2Cl_2. By comparing the $\Delta\Delta E_Q$ values obtained from these data at low temperatures, we determined that **1**·CH_2Cl_2, with a larger $\Delta\Delta E_Q$ possesses a stronger hydrogen-bonding interaction than **2**·CH_2Cl_2.

5.2 Introduction

Heterometallic extended metal atom chain compounds (HEMACs) supported by the 2,2' dipyridylamine (dpa) ligand have been of interest due to their tunable structural,[1-2] magnetic,[1-5] and

spectroscopic properties.[6-7] Our group is specifically interested in HEMACs of the form $M_A \equiv M_A–M_B$ in which M_A is a Group VI metal quadruply bonded to another Group VI metal and M_B is a first–row transition metal or Ru (Scheme 5.1).[1-2, 5, 7-12] Our group has recently focused on altering the two terminal axial ligands of the chain by exploring ligand substitution reactions.[13-15]

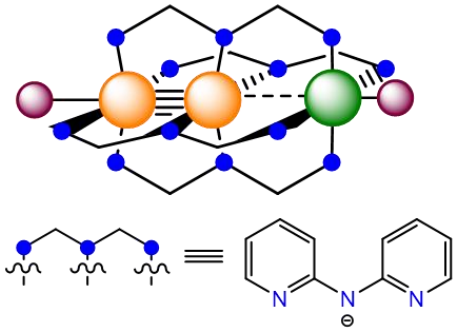

Scheme 5.1 The general structure of an asymmetric $M_A \equiv M_A–M_B$ HEMAC studied in our lab; M_AM_A core (orange), M_B heterometal (green), or axial ligand site (purple).

In our initial report of **1**·CH_2Cl_2, two crystallographic data sets of the crystals **1**·CH_2Cl_2 were collected at 100 K and 11 K.[2, 8] Structurally, the bond metrics for both data sets are similar to one another. At 100 K, **1**·CH_2Cl_2 is in the orthorhombic space group *Pnn*2. The backbone of the trimetallic chain resides on a crystallographic two-fold axis running perpendicular to and bisecting the axis defined by the metal atom chain. As such, the metal atoms are required by crystallographic symmetric to be disordered, and the outer metal atoms are modeled as a half-occupied Cr and half-occupied Fe, respectively. The inner Cr atom displays positional disorder and was modeled as half-occupied; however, this atom dose not reside on the two-fold axis. At 11 K, **1**·CH_2Cl_2 is in the monoclinic space group *Pn*, which does not contain a crystallographic two-fold axis. In this structure, the two Fe sites become chemically distinct from one another as a result of the DCM molecule, which is no longer disordered (Figure 5.1).[2] As a result, one of the crystallographic orientations features an interaction of the C–H bonds in CH_2Cl_2 and one of the terminal Cl ligands axially bound to the Fe forming a weak C–H···Cl interaction at a distance of 4.110 Å.

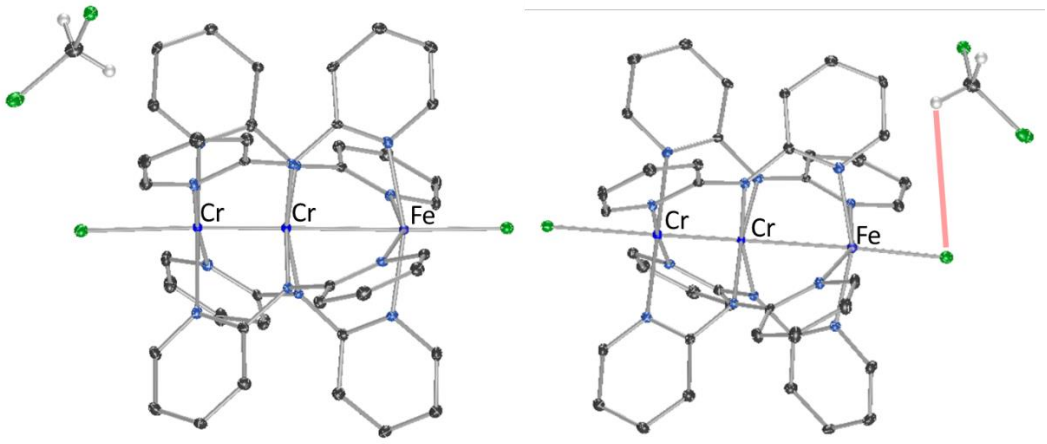

Figure 5.1 X-ray crystal structure for **1**·CH_2Cl_2, with thermal ellipsoids drawn at the 50% probability level. Hydrogen atoms (other than on CH_2Cl_2) have been omitted for clarity.

This phase transition was explored with Mössbauer spectra taken at 240 K and 80 K. At 240 K, where **1**·CH_2Cl_2 is in the *Pnn2* space group, there is one observed quadrupole doublet, consistent with only one chemically distinct Fe site within the crystalline lattice, exhibiting an isomer shift and quadrupole splitting of δ = 0.92 mm s^{-1} and ΔE_Q = 1.20 mm s^{-1}, respectively. When the temperature is lowered to 80 K, *two* distinct quadrupole doublets are observed, supporting the presence of two Fe centers in distinct chemical environments, consistent with the crystallographically-independent Fe centers observed from the diffraction data sets. These two signals were modeled with 42 % and 58 % of the total area; both signals had identical isomer shifts (δ = 1.01 mm s^{-1}) but exhibited different quadrupole splittings (ΔE_Q = 2.39 and 1.63 mm s^{-1}).[2] These Mössbauer populations are in good agreement with the crystallographic occupancies of both orientations of **1**·CH_2Cl_2 (47%, 53 %) as well. In this work, we sought to better define the phase transition in **1**·CH_2Cl_2, and to probe for similar features in the new halide analogs $Cr_2Fe(dpa)_4Br_2$ (**2**) and $Cr_2Fe(dpa)_4I_2$ (**3**). We examine the influence of the identity of the axial halide ligands on the temperature of the crystallographic phase transition in **1**·CH_2Cl_2, **2**·CH_2Cl_2, and **3**·CH_2Cl_2 by variable temperature Mössbauer measurements. The impact of the axial halide ligands upon the strength of the C–H···X interactions is discussed as well.

5.3 Results and Discussion

Synthesis

Direct synthesis of **1** from $Cr_2(dpa)_4$ (**4**) and $FeCl_2$ has been previously reported by our lab.[8] Compounds **2** and **3** can be made using a similar procedure with $FeBr_2$ and FeI_2, respectively. We found FeF_2 to be unreactive under these conditions. In these reactions, **4** and 1.5 equivalents of $FeBr_2$ or FeI_2 are refluxed in tetrahydrofuran (THF) for 12 hours, affording a brown precipitate that is isolated and recrystallized yielding crystals of **2**·CH_2Cl_2 and **3**·CH_2Cl_2 in 42% and 57% yield, respectively (Scheme 5.2).

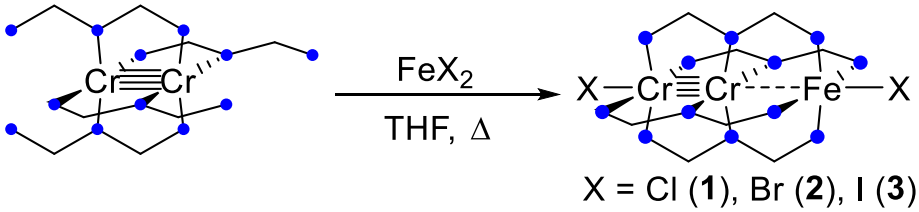

Scheme 5.2 Synthesis of **1**, **2**, and **3** from **4**.[8]

X-ray Crystallography

X-ray quality crystals of **2**·CH_2Cl_2 and **3**·CH_2Cl_2 were obtained from layering pentane on a solution of a given compound in DCM (Figure 5.2). Similar to compound **1**·CH_2Cl_2, **2**·CH_2Cl_2 and **3**·CH_2Cl_2 crystallize in the orthorhombic space group *Pnn*2. As with compound **1**·CH_2Cl_2, the two-fold axis again runs perpendicular to and bisects the axis defined by the metal atom backbone. At 100 K, a disordered CH_2Cl molecule is also present in the crystal structures of **2**·CH_2Cl_2 and **3**·CH_2Cl_2. In **2**·CH_2Cl_2, the closest C–H in CH_2Cl_2 is quite far away, 6.573 Å while in **3**·CH_2Cl_2 the CH_2Cl_2 is much closer, 3.126 Å.

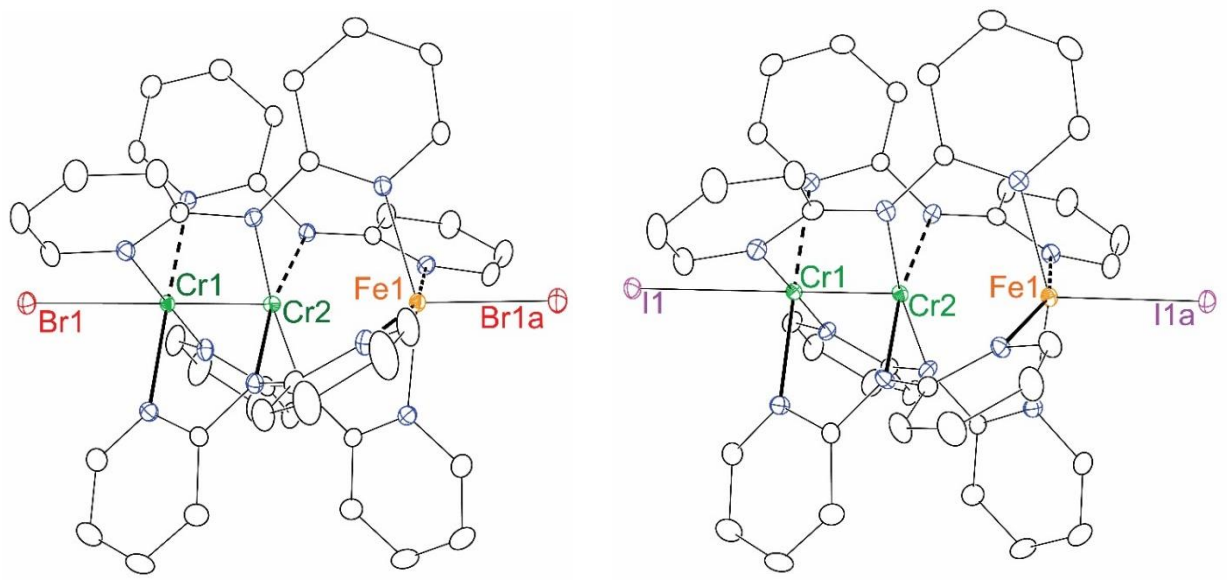

Figure 5.2. X-ray crystal structures of $Cr_2Fe(dpa)_4Br_2$ (**2**·CH_2Cl_2 left) and $Cr_2Fe(dpa)_4I_2$ (**3**·CH_2Cl_2 right), with thermal ellipsoids drawn at the 50% probability level. Hydrogen atoms and interstitial CH_2Cl_2 molecules have been omitted for clarity.

The Cr≣Cr bond distances in **2** and **3** are 2.011(2) Å and 1.990(4) Å, respectively, typical of Cr≣Cr quadruple bonds within HEMACs.[1-2, 7-8] Compound **1** has a Cr≣Cr bond distance of 2.025(1) Å making it longer than both **2**·CH_2Cl_2 and **3**·CH_2Cl_2 while the unappended **4** has a Cr≣Cr bond length of 1.943 Å.[16] This trend of decreasing quadruple bond distance correlates with the weakening of the Cr–X bond from X = Cl to I since larger halides exhibit less trans influence than smaller halide ligands and are weaker-field ligands in general. The Cr–Fe bond distances in **2**·CH_2Cl_2 and **3**·CH_2Cl_2 are the same, within error, of one another at 2.691(1) Å and 2.694(1) Å, respectively. These distances are both shorter than the 2.715(2) Å Cr–Fe distance in **1**·CH_2Cl_2.[8] Crystallographic data for **2**·CH_2Cl_2 and **3**·CH_2Cl_2 are presented Table 5.1 and pertinent bond metrics presented in Table 5.2. The main differences in the crystal structures of **1**·CH_2Cl_2, **2**·CH_2Cl_2, and **3**·CH_2Cl_2 are the Fe–X distances which increase from 2.300(2) in **1**·CH_2Cl_2 to 2.489(1) in **2** to 2.725(1) in **3**·CH_2Cl_2. This trend is expected given the increase in size of the halide ligands from Cl to Br to I (covalent radii: 1.02 Å, 1.20 Å, and 1.39 Å, respectively)[17] In all three cases, the Cr-X distances are longer than the Fe–X distances by roughly 0.4 Å, reflecting the strong *trans* influence of the Cr≣Cr bond.

Table 5.1 Crystallographic data for **2** and **3**.

Compound	**2** (100 K), $Cr_2Fe(dpa)_4Br_2 \bullet (CH_2Cl_2)$	**3** (100 K), $Cr_2Fe(dpa)_4I_2 \bullet (CH_2Cl_2)$
formula	$Cr_2FeBr_2C_{40}H_{32}N_{12} \bullet (CH_2Cl_2)$	$Cr_2FeI_2C_{40}H_{32}N_{12} \bullet (CH_2Cl_2)$
crystal system	orthorhombic	orthorhombic
space group	*Pnn2*	*Pnn2*
a (Å)	12.9869(8)	13.2049(8)
b (Å)	14.1299(9)	14.3004(9)
c (Å)	11.3733(7)	11.4931(7)
α (deg)	90	90
β (deg)	90	90
γ (deg)	90	90
V (Å^3)	2087.0(2)	2170.3(2)
Z	2	2
ρ (Mg m^{-3})	1.727	1.808
R_1[a], wR_2[b] [$I > 2\sigma(I)$]	0.0169, 0.0460	0.0211, 0.0538
R_1[a], wR_2[b] (all data)	0.0176, 0.0462	0.0215, 0.0541

Table 5.2. Bond distances in **1** ,**2**, and **3**. All distances reported in Å.

Compound	Cr–Cr	Cr····Fe	Cr–X	Fe–X	Cr–N_{py}, avg.	Cr–N_a, avg.	Fe–N_{py}, avg.
1[8]	2.025(1)	2.715(2)	2.673(2)	2.300(2)	2.119[5]	2.028[2]	2.157[4]
2	2.011(2)	2.691(1)	2.852(1)	2.489(1)	2.124[4]	2.022[4]	2.158[4]
3	1.990(4)	2.694(1)	3.115(1)	2.725(1)	2.128[4]	2.019[5]	2.165[4]

Electronic Spectroscopy

It was previously reported that **1** shows a low intensity absorption band (ε = 1000 $M^{-1}cm^{-1}$) at 693 nm attributed to the Cr–Cr δ→δ* transition with partial Fe–Cr_2 charge transfer character.[2, 8] Therefore, it is expected that the bromide and iodide analogues display similar absorption spectra. As shown in Figure 5.3, the absorption spectra of **2** and **3** are similar to that of **1**. Compound **2** features a low energy absorption at 687 nm (ε = 1100 $M^{-1}cm^{-1}$) and **3** at 688 nm (ε = 870 $M^{-1}cm^{-1}$), with both compounds displaying more intense charge transfer bands at higher energy.

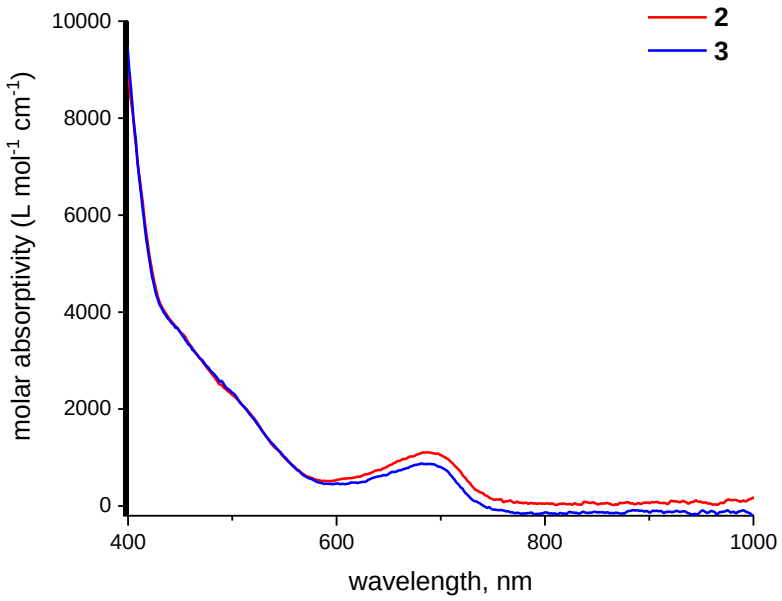

Figure 5.3 Electronic absorption spectra of **2** (black) and **3** (red) in CH_2Cl_2 measured at room temperature.

Electrochemistry

The cyclic voltammogram (CV) of **2** is shown in Figure 5.4. Compound **2** displays a reversible feature at $E_{1/2}$ = −0.190 V and an irreversible oxidation at 0.623 V. These features are similar to those reported for the chloride analogue **1** (Table 5.2). Compound **1** has a reversible wave at $E_{1/2}$ = −0.236 V and an irreversible oxidative wave at $E_{irr.}$ = 0.538 V.[8] These data suggest that by substituting the chloride ligands for bromide ligands, the $Cr_2Fe(dpa)_4$ core is slightly easier to oxidize. This observation corresponds with the trend observed when the chloride axial ligands in the homometallic $Cr_3(dpa)_4Cl_2$ compound were replaced by more strongly donating axial ligands it was shown that in going from Cl to CN to CCPh, the first oxidation

potential decreased by –0.5 V. This was attributed to the ability of the donating ligand to stabilize the oxidized distal Cr^{3+} ion. Interestingly, when the Cl ligands were substituted for Br ligands to form $Cr_3(dpa)_4Br_2$, the observed CV was drastically different. $Cr_3(dpa)_4Br_2$ displayed two irreversible peaks at 0.3 V and 0.6 V.[18]

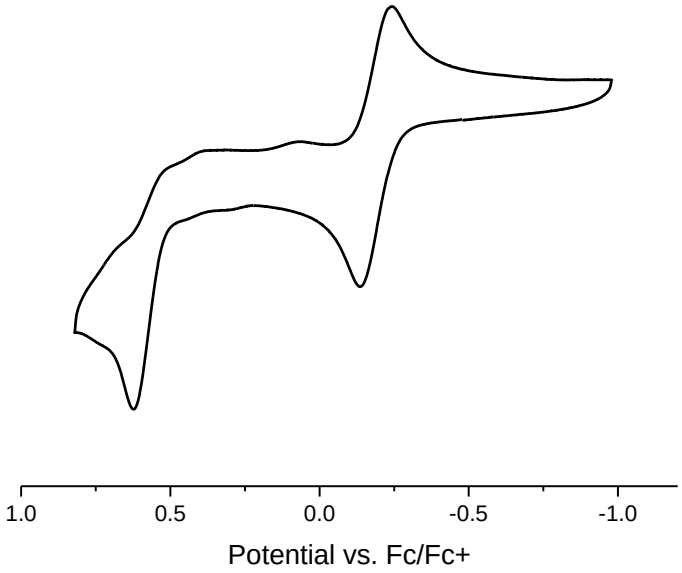

Figure 5.4. Cyclic voltammogram of **2** in CH_2Cl_2 with scan rate = 100 mv/s.

Table 5.3. Electrochemical data for trimetallic compounds. All potentials in V. rev = reversible. irr = irreversible.

Compound	$M_3^{6+/7+}$	$M_3^{7+/8+}$	Ref.
$Cr_2Fe(dpa)_4Cl_2$ (**1**)	-0.236 (rev)	0.538 (irr)	[8]
$Cr_2Fe(dpa)_4Br_2$ (**2**)	-0.190 (rev)	0.623 (irr)	this work
$Cr_3(dpa)_4Cl_2$	0.067 (rev)	0.8534 (rev)	[19]
$Cr_3(dpa)_4Br_2$	0.3 (irr)	0.57 (irr)	[19]

SQUID Magnetometry

Magnetic susceptibility data for **2**, and **3** are shown in Figure 5.5 with corresponding fitting parameters in Table 5.4. Susceptibility data previously collected on compound **1** exhibited a χT value of 3.9 emu K mol^{-1} at 294 K. Compounds **2** and **3** have high temperature χT values of 4.77 emu K mol^{-1} (232 K) 3.41 emu K mol^{-1} (294 K), respectively. The expected spin-only value for χT for these compounds is 3.00 emu K mol^{-1} since each is S = 2. Although compound **1** has a large χT value it is still within the range for a high-spin Fe(II) species, compound **3** is also within this range.[20] Compound **2** is unusually high and this discrepancy has not yet been reconciled, but may be attributed to unusually large spin-orbit coupling contributing to *g*. As temperature is lowered, χT values for **1-3** decrease monatomically with steeper curvature below ~50K. The low temperature behavior is well modeled y zero-field splitting, and there are no discontinuities in the susceptibility data nor are there changes in spin state that might be associated with a structural phase transition. Comparison of the zero-field splitting (ZFS, denoted by D) values for the **1-3** reveal a trend of increasing |D| from 8.3 cm^{-1} for **1** to 20.6 cm^{-1} for **2** to 22.0 cm^{-1} for **3**. This trend is consistent with the increase in axial halide size increasing the spin orbit coupling influence on the system. Thus, **3**, with the largest iodide axial ligand has the largest ZFS parameter and **1**, the smallest. We suspect that D is negative, as attempts to fit the magnetometry data using a positive D parameter led to physically unreasonable *g* values.

Table 5.4 SQUID fitting parameters for compounds **1**–**3**. *The g-value for this compound was fit isotropically instead of axially.

Compound	χT @ 294 K (emu K mol^{-1})	$g_\perp$	$g_\parallel$	|D| (cm^{-1})	zJ (cm^{-1})	Ref
1	3.9	2.28*	N/A	8.3	N/A	[8]
2	4.77 (232 K)	2.425(3)	2.516(2)	20.6(2)	-0.0778(8)	This work
3	3.41	1.973(3)	2.229(1)	22.0(3)	-0.0296(7)	This work

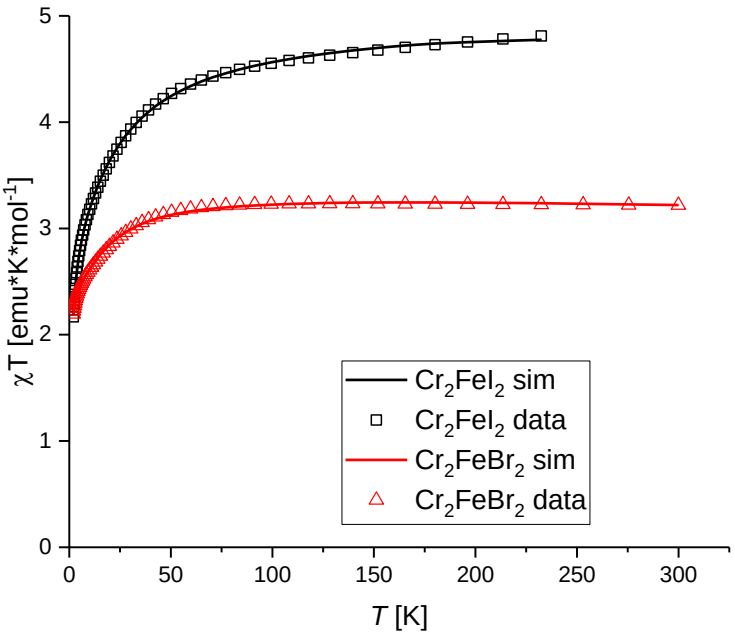

Figure 5.5 χT plots for **2** (black) and **3** (red). (Note: due to an instrument malfunction, data collection for **2** halted at 232 K).

Mössbauer Spectroscopy

As reported previously in our lab, **1**·CH_2Cl_2 a phase transition occurs somewhere between 100 K and 80 K as evidenced by the *Pnn*2 space groups observable by SCXRD measurements at 100K and a pair of Mössbauer doublets observable at 80 K. We probed for similar phase transitions for **2**·CH_2Cl_2 and **3**·CH_2Cl_2 using variable temperature Mössbauer spectroscopy. Compound **2**·CH_2Cl_2 was found to undergo a phase transition, albeit at a lower temperature than for **1**·CH_2Cl_2. If **3**·CH_2Cl_2 undergoes a phase transition, it is at a temperature too low to be observed on our instrumentation (< 5K).

Variable temperature Mössbauer spectroscopy was used as a probe to extract accurate temperatures that the crystallographic phase transitions occurred for **1**·CH_2Cl_2 and **2**·CH_2Cl_2. Spectra for **1**·CH_2Cl_2 were obtained in the temperatures range of 77 K to 240 K. Spectra obtained at 77 K and 240 K are displayed in **Figure 5.6** as representative data sets both crystallographically distinct phases. The models of the data with quadrupole doublets and their fit parameters are also displayed. The spectrum obtained at 77 K clearly displays two quadrupole doublets that have the same isomer shifts and partially overlap one another.

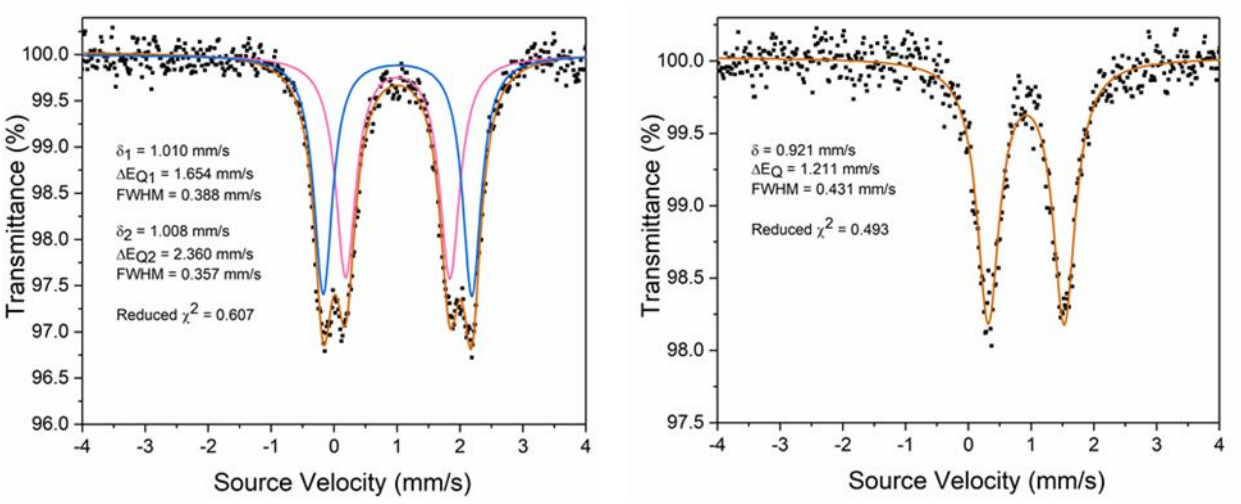

Figure 5.6 Left: Mössbauer spectrum of **1**·CH_2Cl_2 at 77 K along with fit parameters. Right: Mössbauer spectrum of 1 at 240 K with fit parameters. The 77 K data set was fit with two quadrupole doublets (pink and blue) each with the same area; the overall fit is displayed in orange. The 240 K data set was fit with one quadrupole doublet, displayed in orange.

The data were fitted with two quadrupole doublets, one for each Fe center, each having the same isomer shift but different quadrupole splittings, indicative of their different chemical environments. These fits are nearly identical to the ones previously reported for this compound.[2, 8]The relative areas of each quadrupole doublet spectrum were fixed at exactly 0.50, consistent with the crystallographic data, while the other parameters were allowed to freely refine. The isomer shifts and quadrupole splittings for each quadrupole doublet are consistent with high-spin Fe(II) centers[21] in good agreement with the DC magnetic susceptibility data. It is estimated that the phase transition temperature occurs at approximately 110 K; spectra collected below this temperature were best fit with two quadrupole doublets, as visually apparent by the data. At and above this temperature, the data was fit with one quadrupole doublet since it was not apparent by looking at the data that they should be fit with two quadrupole doublets. This is consistent with the previously collected crystallographic data.[2, 8]

Similar variable temperature Mössbauer experiments were conducted on **2**·CH_2Cl_2**.** The phase transition temperature for this compound is estimated to occur at approximately 25 K; data at and above this temperature is best fit with a single quadrupole doublet, while data below this temperature is best fit

with two, as depicted in Figure 5.7. The lower phase-transition temperature for this compound is rationalized with the expectation that the weak non-classical hydrogen bonding interaction between

The terminal halide and one of the C–H bonds of the DCM solvent molecule is expected to be weaker for the bromide than the chloride. Chlorine is smaller and more electronegative than bromine, meaning that there is a greater charge density on chloride than bromide in **1**·CH_2Cl_2 and **2**·CH_2Cl_2, respectively, which allows for the terminal chloride to be a better hydrogen bond acceptor than the bromide.

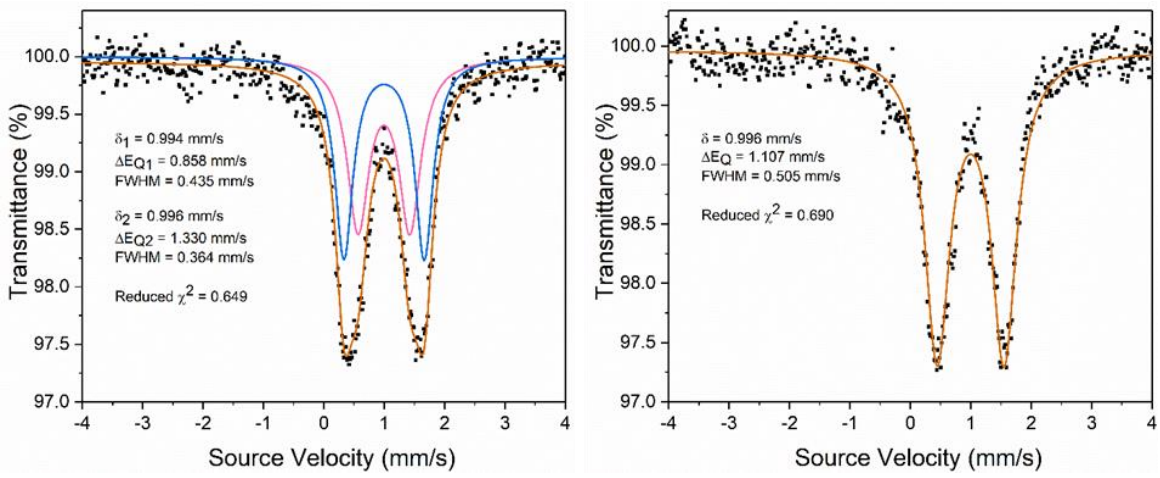

Figure 5.7 Left: Mössbauer spectrum of **2** at 20 K along with fit parameters. Right: Mössbauer spectrum of **2** at 35 K with fit parameters. The 20 K data set was fit with two quadrupole doublets (pink and blue) each with the same area; the overall fit is displayed in orange. The 35 K data set was fit with one quadrupole doublet, displayed in orange.

These Mössbauer experiments allow for qualitative descriptions of the hydrogen bond strengths. It is expected, however, that ΔS for both compounds are similar, and therefore that the difference in phase-transition temperatures is enthalpically-driven, consistent with the expected differences in hydrogen-bond strengths between both compounds. Variable temperature Mössbauer experiments were also conducted on **3** (Figure 5.8); however, even collecting data as low as 8 K yielded spectra best fit with one quadrupole doublet, implying that the phase-transition temperature for this complex, if there is one, is too low to be measured by our instrumentation (< 5K).

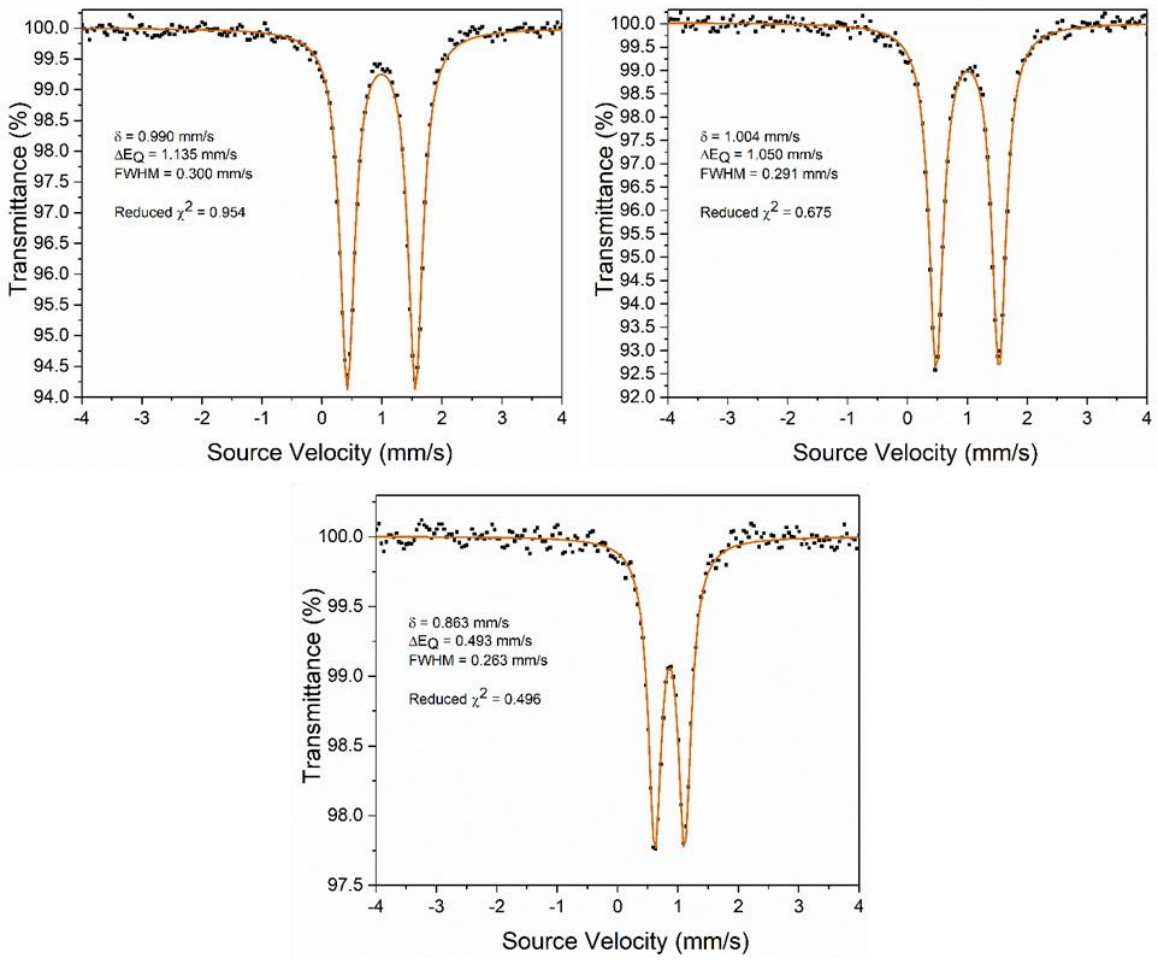

Figure 5.8. Top left: Mössbauer spectrum of **3** at 8 K along with fit parameters. Top right: Mössbauer spectrum of **3** at 77 K with fit parameters. Bottom: Mössbauer spectrum of **3** at 8 K with fit parameters. Each data set was fit with one quadrupole doublet; the overall fits for each spectrum are displayed in orange. No phase transition was observed for this compound, apparent by the single Fe site for each spectrum.

As highlighted in our previous analysis of **1**·CH_2Cl_2,[2] the value of $\Delta\Delta E_Q$ (i.e. the difference in quadrupole splittings for the two unique iron sites) for **1**·CH_2Cl_2 is unusually large, 0.71 mm/s at 80 K. We had suggested that $\Delta\Delta E_Q$ was magnified at the Fe center in **1**·CH_2Cl_2 by the presence of the highly anisotropic Cr$\equiv$Cr quadruple bond. To investigate this proposal further, we were curious to find the $\Delta\Delta E_Q$ for **2**·CH_2Cl_2 in its low-temperature phase to be 0.472 mm/s at 20 K. The different chemical environments of both Fe sites are again dictated by the presence of a weak hydrogen-bonding interaction between a solvent CH_2Cl_2 and a terminal halide for one of the Fe sites in this low-temperature phase. However, the

smaller $\Delta\Delta E_Q$ value for **2** in its low-temperature phase further suggests that the hydrogen bonding interaction in this compound is even weaker than the hydrogen bonding interaction present in **1**.

5.4 Conclusions

The variable temperature Mössbauer data for compounds **1**·CH_2Cl_2 and **2**·CH_2Cl_2 provide evidence for the previously observed crystallographic phase transitions for each compound. Based on the whether the data was best fit with one or two quadrupole doublets, the phase transition temperatures are estimated at 110 K and 25 K for **1**·CH_2Cl_2 and **2**·CH_2Cl_2, respectively. Compound **3**·CH_2Cl_2 either has no phase transition, or a phase transition temperature that is too low to be observable by our instrumentation. The difference in phase transition temperatures between compounds **1**·CH_2Cl_2 and **2**·CH_2Cl_2 is explained by the expected difference in hydrogen bond interactions between the terminal halides and the solvent CH_2Cl_2 molecules in the crystalline lattice for these two complexes. This is confirmed by comparing the $\Delta\Delta E_Q$ values for both Fe centers in the low-temperature phase for each complex, whereby the larger $\Delta\Delta E_Q$ value for **1**·CH_2Cl_2 indicates a stronger hydrogen-bonding interaction than **2**·CH_2Cl_2

5.5 Experimental Information

All reactions were carried out under a dry N_2 atmosphere using Schlenk techniques and glovebox methods. Pentane, hexanes, and acetonitrile were purified using a Vacuum Atmospheres solvent purification system. Dichloromethane was freshly distilled under N_2 over CaH_2 prior to use. $Cr_2(dpa)_4$[16] and $Cr_2Fe(dpa)_4Cl_2$[8] were prepared according to literature procedures. $FeBr_2$ and $FeCl_2$ were purchased from Alfa Aesar and used as received. FeI_2 was purchased from Strem Chemicals and used as received. The ligand Hdpa was purchased from TCI and recrystallized from hot hexanes prior to use. Elemental analyses were carried out by Midwest Microlab, LLC Indianapolis, IN. IR spectra were taken on a BRUKER TENSOR 27 FTIR spectrometer using an attenuated total reflectance (ATR) adapter. Cyclic voltammograms (CVs) were taken on a BASI Epsilon EC instrument using CH_2Cl_2 solutions with 0.1 M NBu_4PF_6 electrolyte and 1 mM substrate. The electrodes were as follows: glassy carbon (working), Pt wire (auxiliary), and Ag/Ag^+ in CH_3CN (reference). The potentials were referenced against the ferrocene/ferrocenium redox couple by external addition of ferrocene. Variable temperature magnetic susceptibility measurements of crystalline samples of **2**, and **3** were recorded at the University of Wisconsin-Madison on a MPMS 3 Quantum Design

SQUID Magnetometer in the temperature range 2–300 K with an applied field of 0.1 Tesla. Experimental susceptibility and magnetization data were corrected for the underlying diamagnetism using Pascal's constants[22] and for the temperature independent paramagnetism contributions. The data were fit using the program PHI.[23] All Mössbauer data were collected at the University of Wisconsin-Madison with a 1024 channel See Co model W304 resonant gamma-ray spectrometer. The source in the Mössbauer drive was ^{57}Co on Rh foil obtained from Ritverc Isotope Products. The velocity range used was ±4 mm/s for each sample. Each spectrum was collected with the sample under vacuum. Sample temperatures were set with a Lakeshore model 336 temperature controller in conjunction with a Janis model SHI-850 cryostat. Mössbauer data were fit using the WMOSS4F software package. The fitting method used for each fit was an adaptive nonlinear least-squares algorithm developed by Dennis et al. in 1981 available within the WMOSS4F software.[24] Each distinct Fe signal was fit with a quadrupole doublet. The parameters fit for each quadrupole doublet were their isomer shifts (δ), quadrupole splittings (ΔE_Q), linewidths (FWHM), while their relative areas were fixed when appropriate. The reduced χ^2 values for each fit were also obtained to assess the quality of the fits.

Crystallography

Crystallographic data were measured at the Molecular Structure Laboratory of the Chemistry Department of the University of Wisconsin-Madison. Crystals were selected under oil under ambient conditions and attached to the tip of a MiTeGen MicroMount©. Each crystal was mounted under a stream of cold nitrogen at 100(1) K and centered in the X-ray beam using a video camera. The crystal evaluation and data collection were performed on a Bruker Quazar SMART APEXIII diffractometer with Mo K-α (λ = 0.71073 A) radiation with a detector to crystal distance of 5.0 cm. The data were collected using a routine to survey the entire sphere of reciprocal space and were indexed by the SMART program.[25] The structures were solved using direct methods and refined by least-squares refinement on F^2 followed by difference Fourier synthesis.[26] All hydrogen atoms were included in the final structure factor calculation at idealized positions and were allowed to ride on the neighboring atoms with relative isotropic displacement coefficients.

$Cr_2Fe(dpa)_4Br_2$ (**2**). THF (25 mL) was added to a mixture of solid orange $Cr_2(dpa)_4$ (165 mg, 0.210 mmol) and anhydrous $FeBr_2$ (53 mg, 0.25 mmol). The mixture was stirred for 30 min at room temperature, during which time the reaction mixture color turned from orange to brown. The mixture was heated to reflux for 12 h. After cooling the mixture to room temperature, the volume was reduced to half under reduced pressure. The solid was then separated by filtration, extracted with CH_2Cl_2 (20 mL), and the resulting brown solution was layered with hexanes (30 mL). Black block crystals of **2** grew overnight. Yield: 88 mg, 42 %. Anal. Calcd. for $Cr_2FeC_{42}H_{34}N_{12}Br_2Cl_2$ (**2** • CH_2Cl_2): C, 45.37 %; H, 3.16 %; N, 15.49 %. Found: C, 45.51 %; H, 3.07 %; N, 15.40 %. IR (ATR, cm^{-1}): 1606 m, 1594 m, 1548 w, 1467 s, 1424 s, 1360 m, 1318 m, 1284 w, 1166 m, 1151 m, 1110 w, 1016 m, 918 m, 877 m, 860 m, 764 s, 748 m, 733 s, 643 w.

$Cr_2Fe(dpa)_4I_2$ (**3**). THF (25 mL) was added to a mixture of solid orange $Cr_2(dpa)_4$ (200. mg, 0.255 mmol) and anhydrous FeI_2 (95 mg, 0.31 mmol). The mixture was stirred for 30 min at room temperature, during which time the reaction mixture color turned from orange to brown. The mixture was heated to reflux for 12 h. After cooling the mixture to room temperature, the volume was reduced to half under reduced pressure. The solid was then separated by filtration, extracted with CH_2Cl_2 (20 mL), and the resulting brown solution was layered with hexanes (30 mL). Black block crystals of **3** grew overnight. Yield: 159 mg, 57 %. Anal. Calcd. for $Cr_2FeC_{42}H_{34}N_{12}I_2Cl_2$ (**3** • CH_2Cl_2): C, 41.76 %; H, 2.91 %; N, 14.25 %. Found: C, 41.94 %; H, 2.76 %; N, 13.99 %. IR (ATR, cm^{-1}): 1605 m, 1594 m, 1548 w, 1466 s, 1459 s, 1424 s, 1360 m, 1316 m, 1283 w, 1164 m, 1151 m, 1110 w, 1015 m, 878 m, 763 m, 748 w, 733 m, 661 w, 628 w.

References

1. Nippe, M.; Victor, E.; Berry, J. F., Do Metal–Metal Multiply-Bonded "Ligands" Have a trans Influence? Structural and Magnetic Comparisons of Heterometallic Cr≡Cr···Co and Mo≡Mo···Co Interactions. *Eur. J. Inorg. Chem.* **2008**, 5569-5572.

2. Nippe, M.; Wang, J.; Bill, E.; Hope, H.; Dalal, N. S.; Berry, J. F., Crystals in Which Some Metal Atoms are More Equal Than Others: Inequalities From Crystal Packing and Their Spectroscopic/Magnetic Consequences. *J. Am. Chem. Soc.* **2010,** *132*, 14261-14272.

3. Rohmer, M. M.; Liu, I. P. C.; Lin, J. C.; Chiu, M. J.; Lee, C. H.; Lee, G. H.; Bénard, M.; López, X.; Peng, S. M., Structural, Magnetic, and Theoretical Characterization of a Heterometallic Polypyridylamide Complex. *Angew. Chemie. Int. Ed.* **2007,** *46*, 3533-3536.

4. Christian, J. H.; Brogden, D. W.; Bindra, J. K.; Kinyon, J. S.; van Tol, J.; Wang, J.; Berry, J. F.; Dalal, N. S., Enhancing the Magnetic Anisotropy of Linear Cr(II) Chain Compounds Using Heavy Metal Substitutions. *Inorg. Chem.* **2016,** *55*, 6376-6383.

5. Chipman, J. A.; Berry, J. F., Extraordinarily Large Ferromagnetic Coupling (J≥150 cm^{-1}) by Electron Delocalization in a Heterometallic Mo≣Mo–Ni Chain Complex. *Chem. Eur. J.* **2018,** *24*, 1494-1499.

6. Liu, I. P.C.; Lee, G.H.; Peng, S.M.; Bénard, M.; Rohmer, M.M., Cu–Pd–Cu and Cu–Pt–Cu Linear Frameworks: Synthesis, Magnetic Properties, and Theoretical Analysis of Two Mixed-Metal Complexes of Dipyridylamide (dpa), Isostructural, and Isoelectronic with $[Cu_3(dpa)_4Cl_2]^+$. *Inorg. Chem.* **2007,** *46*, 9602-9608.

7. Nippe, M.; Bill, E.; Berry, J. F., Group 6 Complexes with Iron and Zinc Heterometals: Understanding the Structural, Spectroscopic, and Electrochemical Properties of a Complete Series of MM···M′ Compounds. *Inorg. Chem.* **2011,** *50*, 7650-7661.

8. Nippe, M.; Berry, J. F., Introducing a Metal–Metal Multiply Bonded Group as an "Axial Ligand" to Iron: Synthetic Design of a Linear Cr–Cr···Fe Framework. *J. Am. Chem. Soc.* **2007,** *129*, 12684-12685.

9. Nippe, M.; Timmer, G. H.; Berry, J. F., Remarkable regioselectivity in the preparation of the first heterotrimetallic Mo≡W-Cr chain. *Chem Commun.* **2009**, 4357-4359.

10. Brogden, D. W.; Berry, J. F., Heterometallic Multiple Bonding: Delocalized Three-Center σ and π Bonding in Chains of 4d and 5d Transition Metals. *Inorg. Chem.* **2014,** *53*, 11354-11356.

11. Brogden, D. W.; Berry, J. F., Heterometallic Second-Row Transition Metal Chain Compounds in Two Charge States: Syntheses, Properties, and Electronic Structures of $[Mo–Mo–Ru]^{6+/7+}$ Chains. *Inorg. Chem.* **2015,** *54*, 7660 - 7665.

12. Brogden, D. W.; Christian, J. H.; Dalal, N. S.; Berry, J. F., Completing the series of Group VI heterotrimetallic $M_2Cr(dpa)_4Cl_2$ (M_2 = Cr_2, Mo_2, MoW and W_2) compounds and investigating their metal–metal interactions using density functional theory. *Inorg. Chim. Acta* **2015,** *424*, 241-247.

13. Chipman, J. A.; Berry, J. F., Facile Axial Ligand Substitution in Linear Mo≣Mo–Ni Complexes. *Inorg. Chem.* **2018,** *57*, 9354-9363.

14. Nippe, M.; Turov, Y.; Berry, J. F., Remote Effects of Axial Ligand Substitution in Heterometallic Cr≡Cr···M Chains. *Inorg. Chem.* **2011,** *50*, 10592-10599.

15. Turov, Y.; Berry, J. F., Synthesis, characterization and thermal properties of trimetallic N_3-Cr-Cr-M-N_3 azide complexes with M = Cr, Mn, Fe, and Co. *Dalton Trans.* **2012,** *41*, 8153-8161.

16. Clérac, R.; Albert Cotton, F.; Jeffery, S. P.; Murillo, C. A.; Wang, X., Isomerization by ligand shuffling along a Cr_2^{4+} unit: further reactions leading to cleavage of a quadruple bond. *Dalton Trans.* **2003**, 3022-3027.

17. Cordero, B.; Gómez, V.; Platero-Prats, A. E.; Revés, M.; Echeverría, J.; Cremades, E.; Barragán, F.; Alvarez, S., Covalent radii revisited. *Dalton Trans.* **2008,** *21*, 2832-2838.

18. Berry, J. F.; Cotton, F. A.; Lu, T.; Murillo, C. A.; Roberts, B. K.; Wang, X., Molecular and Electronic Structures by Design: Tuning Symmetrical and Unsymmetrical Linear Trichromium Chains. *J. Am. Chem. Soc.* **2004,** *126*, 7082-7096.

19. Cotton, F. A.; Daniels, L. M.; Murillo, C. A.; Pascual, I.; Zhou, H. C., Remarkable Effects of Axial π* Coordination on the Cr–Cr Quadruple Bond in Dichromium Paddlewheel Complexes. *J. Am. Chem. Soc.* **1999,** *121*, 6856-6861.

20. Solomon, E. I.; Zhou, J.; Neese, F.; Pavel, E. G., New insights from spectroscopy into the structure/function relationships of lipoxygenases. *Chemistry & Biology* **1997,** *4*, 795-808.

21. Gütlich, P.; Bill, E.; Trautwein, A. X., *Mössbauer Spectroscopy and Transition Metal Chemistry: Fundamentals and Applications*. Springer Berlin Heidelberg: 2010.

22. Bain, G. A.; Berry, J. F., Diamagnetic Corrections and Pascal's Constants. *J. Chem. Ed.* **2008,** *85*, 532.

23. Chilton, N. F.; Anderson, R. P.; Turner, L. D.; Soncini, A.; Murray, K. S., PHI: A powerful new program for the analysis of anisotropic monomeric and exchange-coupled polynuclear d- and f-block complexes. *J. Comp. Chem.* **2013,** *34*, 1164-1175.

24. Dennis, J. E.; Gay, D. M.; Welsch, R. E., An Adaptive Nonlinear Least Square Algorithm. *National Bureau of Economic Research Working Paper Series* **1977,** *No. 196*.

25. *Bruker-AXS*, Madison, Wisconsin, USA, 2009.

26. Dolomanov, O. V.; Bourhis, L. J.; Gildea, R. J.; Howard, J. A. K.; Puschmann, H., Olex: a complete structure solution, refinement and analysis program. In *Journal of applied crystallography*, Oxford, England :, 2009; Vol. 42, pp 339-341.

Chapter Six

Guilt by Dissociation: Unusual Spin States of Mo_2Co Heterometallic Chain Compounds

Chipman, J.A; Greenhalgh, E; Brunold, T.C.; Berry, J.F.

EG collected the magnetic circular dichroism (MCD) spectra for both compounds. All other work was performed by JAC.

6.1 Abstract

The heterometallic chains $Mo_2Co(dpa)_4Cl_2$ (**1**) and $Mo_2Co(dpa)_4Br_2$ (**2**) were synthesized via reaction of $Mo_2(dpa)_4$ (**3**) with either $CoCl_2$ or $CoBr_2$. Compound **1** was communicated previously and contains a high spin Co^{2+} center bound to a diamagnetic Mo_2^{4+} group. Structurally, compound **2** presents Co–N distances that are ~ 0.121 Å shorter than in **1** and with an extremely long Co–Br distance, at 100 K suggests a low-spin Co^{2+} center, the first example of a low-spin Mo_2M complex with a first-row transition metal. This anomaly in compound **2** was investigated using SQUID magnetometry, which suggested that **2** displays incomplete spin-crossover behavior with ~40% permanent high-spin. This spin crossover behavior is a first for Mo_2 supported HEMACs while the corresponding $Cr_2Co(dpa)_4Cl_2$ complex also presents spin crossover behavior. Both **1** and **2** were further characterized via EPR spectroscopy. Surprisingly, compounds **1** and **2** present rhombic signals in addition and contain high and low spin components, respectively. Magnetic circular dichroism (MCD) spectra for **1** and **2** are dominated by $S = 3/2$ signals for both species, the latter likely stemming from the permanent high-spin component.

6.2 Introduction

Linear trimetallic chain compounds supported by the dpa (2,2' dipyridylamine) ligand possess unique structural,[1-6] magnetic,[7-12] spectroscopic, [9, 13-15] and electron transport[16-18] properties that have drawn considerable interest over the past decades. Notably, $Co_3(dpa)_4X_2$ compounds present many different structural polymorphs with widely varying Co–Co distances leading to the consideration of Co_3 based extended metal atom (EMAC) chains as "bond-stretch isomers".[4, 19-29] This unusual structural behavior is intimately linked to spin equilibria within the compounds between geometrically distinct $S = 1/2$ and $S = 3/2$ states.

Until 2007, EMACs were limited to homometallic species until our lab[30] and the lab of Peng[11] independently reported heterometallic extended metal atom chain (HEMAC) compounds supported by the dpa ligand. Our group has focused on HEMACs of the form $M_A \equiv M_A–M_B$ in which M_A represents a Group VI metal quadruply bonded to another Group VI metal and M_B is either a first-row transition metal or Ru. (Scheme 6.1).

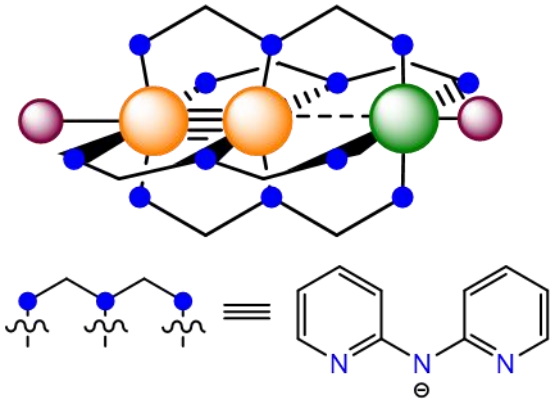

Scheme 6.1 The general structure of an asymmetric $M_A \equiv M_A–M_B$ HEMAC studied in our lab; M_AM_A core (orange), M_B heterometal (green), or axial ligand site (purple).

In 2008, our group communicated our first investigation of Co-containing HEMACs, $Cr_2Co(dpa)_4Cl_2$ and $Mo_2Co(dpa)_4Cl_2$ (**1**).[8] We found that the $Cr_2Co(dpa)_4Cl_2$ compound behaved as a spin crossover compound moving from low to high temperatures. Between 4 and 50 K, $Cr_2Co(dpa)_4Cl_2$ displays a plateau in χT at 0.5 emu K mol^{-1}, indicative of an S = 1/2 center. Moving to room temperature, the χT value rises to 2.5 emu K mol^{-1}, indicative of an S = 3/2 center. Crystal structures were obtained at 100 K and room temperature detailing the structural features of the S = 1/2 and S = 3/2 forms of the compound. At 100 K the Co–N distance of 2.054[2] is ~0.74 Å shorter than in the room temperature structure (2.128[9] Å). Similarly, the Mo–Co distance shortens by 0.132 Å from 2.618(7) Å at room temperature to 2.491(1) Å at 100 K while the Co–Cl elongates by 0.197 Å from 2.370(1) Å at room temperature to 2.567(5) Å at 100 K. These data further suggest a spin equilibrium. At 100 K, $Cr_2Co(dpa)_4Cl_2$ exists in a low-spin form while at room temperature, the complex exists in a high-spin state. In contrast to the Cr_2 supported compound, the Mo_2 supported compound (**1**) presented no such behavior. The room temperature value of χT at 3.00 emu

K mol^{-1} remained constant with only a slight downturn at low temperatures, attributable to zero field splitting. These data suggested that **1** contained an $S = 3/2$ Co^{2+} center. In our further investigation of **1**, we sought to model the magnetic data to determine the nature of the zero-field splitting (ZFS) tensor. We also sought to tune the ZFS by examining the analogous bromide compound $Mo_2Co(dpa)_4Br_2$ (**2**), and we were quite surprised to find that **2** displays completely different magnetic behavior to **1** and undergoes temperature-driven spin crossover with a permanent high-spin component.

6.3 Results and Discussion

Synthesis

The preparation of **1** was previously reported and a similar method was used to synthesize **2**. The brick-red quadruply bonded $Mo_2(dpa)_4$ (**3**) and the corresponding CoX_2 dihalide are refluxed together in molten naphthalene to afford the desired HEMAC (Scheme 6.2). Successful synthesis of **2** requires careful attention to detail. An initial color change from red to green black occurs after 20 – 40 minutes at 180 °C, signaling reaction completion. Continued heating (or heating above ~205 °C) yields another color change to brown. Attempts to workup the overheated brown reaction mixtures have not yielded crystalline material. It is interesting to note that this overcooking does not occur with the $CoCl_2$ complex suggesting that even in molten naphthalene at high temperatures, these reactions must be monitored carefully

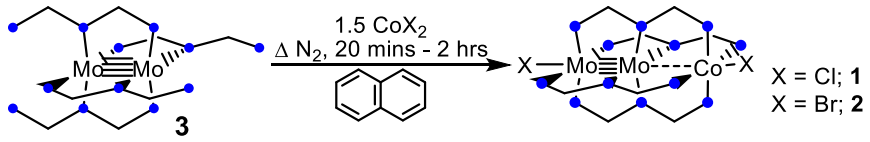

Scheme 6.2 Synthesis of compounds **1** and **2** from **3**.[8]

X – Ray Crystallography

X–ray quality crystals of **2** were obtained from dichloromethane solutions layered with pentane. The structures of **1** and **2** are compared in Figure 6.1. Compound **2** crystallizes in the monoclinic space group *C*2/*c*, identical to **1**. The asymmetric unit in both **1** and **2** contain a disordered DCM solvent molecule. There are two primary distances that best illustrate the difference in Co spin state between these two structures; the Mo–Co distance and Co–N_{pyr} distance (crystallographic data for **2** are presented in Table

6.1; notable bond distances for **1** and **2** are compared in Table 6.2) Bond distance differences in **1** and **2** are reminiscent of differences between high and low spin $Cr_2Co(dpa)_4Cl_2$. Comparing the Mo–Co distances between **1** and **2** we see a 0.136 Å decrease. We also notice that the Co–N_{pyr} distance in **2** is remarkably short in comparison to the other M–N_{pyr} distances in the other $Mo_2M(dpa)_4Cl_2$ species which range from 2.127[2] (M=Cr)[31] to 2.249[5] (M=Mn)[9]. The Co–N_{pyr} distance in **2** is more similar to the Co–N_{pyr} distance in the homometallic $Co_3(dpa)_4Cl_2$ crystal structure (1.984[1] and 1.978[1]).[4, 20] It is also important to note that the Co–Br distance of 3.034 Å in **2** is extraordinarily long, outside the bonding range. Thus, **2** is better represented with an ionic formula $[Mo_2Co(dpa)_4Br]Br$. If Br were a ligand to Co in this complex, we would anticipate from the spectrochemical series that it would be a weaker-field ligand than Cl^- and support a high-spin state. Instead, dissociation of the Br^- appears to induce a low spin state for Co^{2+}.

Table 6.1 Crystallographic data for compound **2**

	2
Formula	$Mo_2(dpa)_4Br_2$
Crystal System	Monoclinic
Space Group	*C2/c*
a/Å	18.6230(4)
b/Å	16.3131(3)
c/Å	15.7276(3)
α/°	90
β/°	111.950(1)
γ/°	90
Volume/Å^3	4431.6(7)
Z	4
ρ_{calc}g/cm^3	1.889
R_1[a] [I>=2σ (I)]	R_1 = 0.0400 wR_2 = 0.1093
R_1[b] [all data]	R_1 = 0.0405 wR_2 = 0.1098

[a] $R1 = \Sigma\big||F_o| - |F_c|\big|/\Sigma|F_o|$

[b] $wR2 = [\Sigma[w(F_o^2 - F_c^2)^2/\Sigma\big[(w(F_o^2)^2\big]]^{\frac{1}{2}}$, $w = 1/\sigma^2(F_o^2) + (aP)^2 + bP$ where $P = [\max(0 \text{ or } F_o^2) + 2(F_c^2)]/3$.

Table 6.2 Selected bond distances for **1** and **2**

	Mo	Mo – Co	Mo – N_o (avg)	Mo – N_i (avg)	Co – N_o (avg)	Mo – X	Co – X
1[8]	2.1027(5)	2.6170(7)	2.216(2)	2.121(2)	2.103	2.720(1)	2.430(1)
2	2.1002(5)	2.4812(8)	2.229(3)	2.111(3)	1.982[2]	2.8517(6)	3.034*

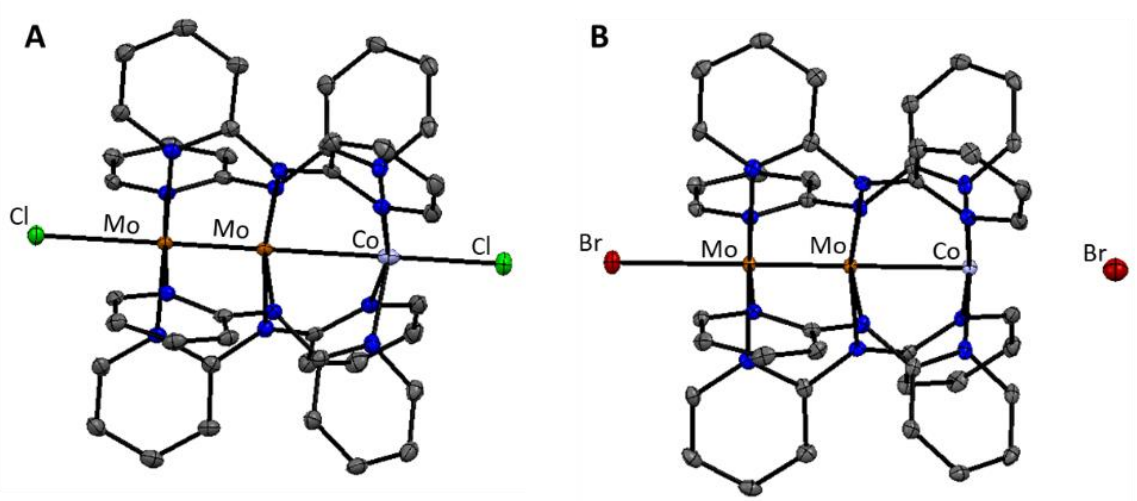

Figure 6.1. X - ray crystal structures of **1**(A) and **2**(B). Ellipsoids are shown at 50 %. H atoms and molecules of solvation have been omitted for clarity.

Electronic Structure

The primary structural differences between **1** and **2** led us to further investigate the electronic structures of these two compounds. We employed magnetic circular dichroism (MCD), UV-vis spectroscopy, magnetic susceptibility measurements, EPR spectroscopy and density functional theory (DFT) computations to understand these differences.

Magnetic susceptibility measurements were collected on microcrystalline samples of **1** and **2** (Figure 6.2). Magnetic susceptibility data for **1** are in good agreement with those reported previously with a room temperature χT value of 3.00 emu K mol^{-1}, consistent with an isolated $S = 3/2$ species.[8] The data were fitted to determine the spin Hamiltonian parameters with the results given in Table 6.3. The magnetic susceptibility data for **2** are strikingly different, and indicative of a spin equilibrium. For Co^{2+} a crossover

from $S = 1/2$ at low temperatures to $S = 3/2$ is possible. However, at low temperatures, the χT value of ~1.5 emu K mol^{-1} is substantially larger than the spin-only value expected for an isolated $S = ½$ species (0.3875 emu K mol^{-1}). These data are consisted with an incomplete spin crossover in which a certain amount of the sample, P_{HS} remains high spin at all temperatures. The χT plot for **2** was thus fitted using Equation 6.1, which accounts for both a low and high spin component. In equation 6.1, F_{HS} is a function that simulates the high–spin component of the species while F_{LS} is a function that simulates the low–spin, ΔH is the enthalpy difference between the two spin states, R is the gas constant and T_C is the critical temperature. The functions F_{HS} and F_{LS} contain the spin Hamiltonian parameters. The data for **1** and **2** are summarized in Table 6.3. We also compare aspects of **2** to the known spin crossover compound $Cr_2Co(dpa)_4Cl_2$ and note that the parameters for $Cr_2Co(dpa)_4Cl_2$ are nearly identical to those for **2** except that $Cr_2Co(dpa)_4Cl_2$ does not have a permanent high-spin component.

Table 6.3. SQUID fitting parameters for compounds **1**, **2**, and $Cr_2Co(dpa)_4Cl_2$

Compound	$g_\perp$	$g_\parallel$	|D| (cm-1)	TC (K)	ΔH (kJ/mol)	% HS
1	2.751(8)	2.615(2)	81.27	N/A	N/A	N/A
2	$g_{LS} = 2.30$ $g_{HS\perp} = 2.55$	$g_{HS\parallel} = 2.22$	27.0	208	13.95	40%
$Cr_2Co(dpa)_4Cl_2$	$g_{LS} = 2.31$ $g_{HS} = 2.575$	N/A	N/A	210	5.7	0 %

$$\chi T = (1 - P_{HS})\,\frac{F_{HS} - F_{LS}}{1 + \exp\frac{\Delta H}{R} * \left(\frac{1}{T} - \frac{1}{T_C}\right)} + F_{LS} + P_{HS}F_{HS}$$

Equation 6.1 Incomplete spin crossover equation used to fit the magnetic susceptibility data for **2**.

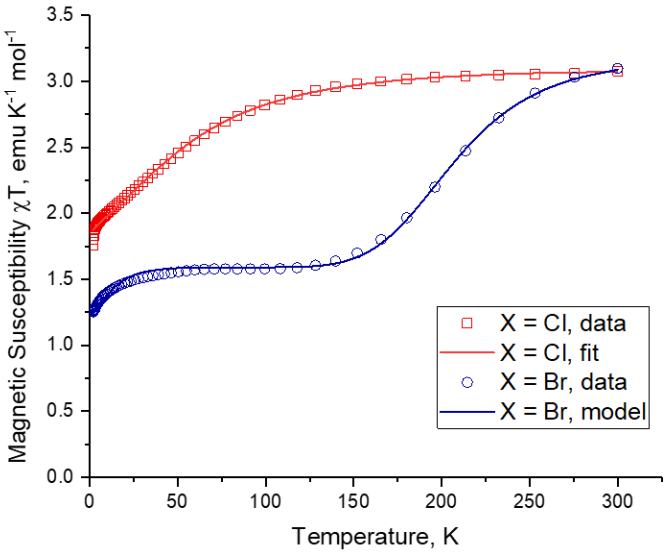

Figure 6.2. χT vs. T plots for **1** (red) and **2** (blue).

In addition to these magnetic susceptibility measurements, frozen solution X–band EPR spectra were collected for both **1** and **2** (Figure 6.3). The major features in each spectra are in agreement with an $S = 1/2$ species for **2** and an $S = 3/2$ species for **1**. Each spectrum also contains additional features that appears to be a radical and a minor component corresponding to the other spin state. These data are summarized in Table 6.4. These data suggest that **1** and **2** contain low and high spin polymorphs to different intensities. To date, we have only been able to structurally characterize the high-spin form of **1** and the low-spin form of **2**. To fully understand these structural polymorphs, we need to crystallize the low-spin form of **1** and the high-spin form of **2**.

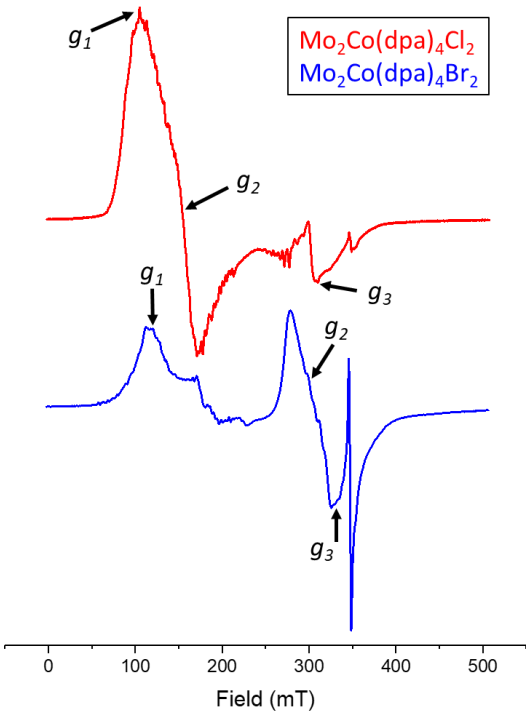

Figure 6.3 X–band EPR spectra for **1** (red) and **2** (blue).

Table 6.4 *g* values obtained by inspection from X–band EPR for compounds **1** and **2**.

Compound	g_1	g_2	g_3
1	6.36	4.39	2.19
2	5.49	2.26	2.07

The electronic absorption spectra and magnetic circular dichroism spectra were recorded for **1** and **2** (Figure 6.4). The spectra for **1** and **2** are incredibly similar suggesting a similar electronic structure and the presence of a permanent high-spin component in **2**, which dwarfs any low-spin signal in the MCD spectra.

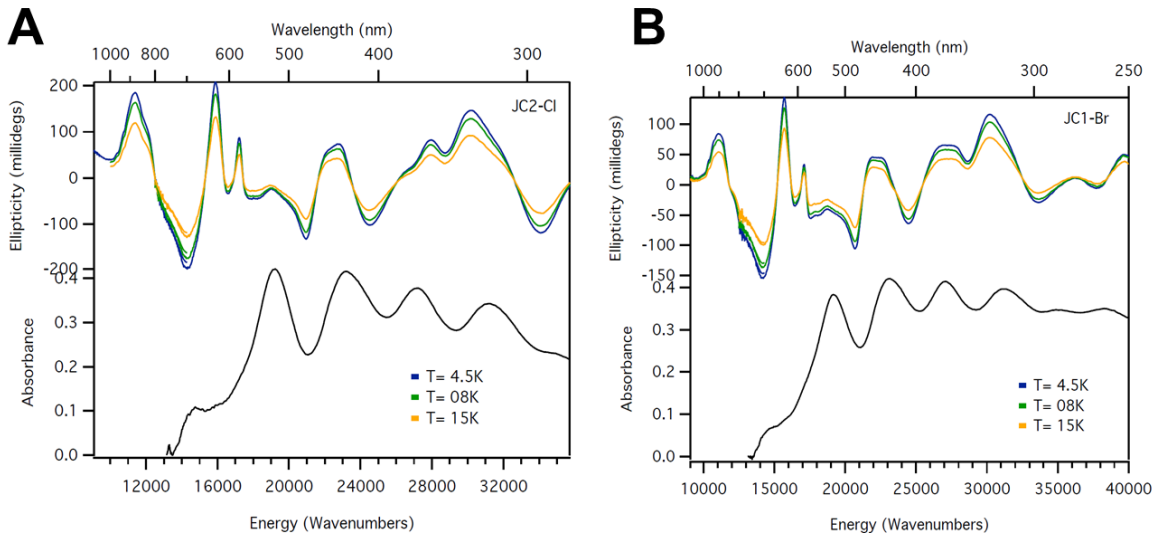

Figure 6.4 MCD spectra of **1** (A) and **2** (B), electronic absorption spectra are below the MCD data.

These experimental findings were further supported via single-point DFT calculations. The electronic structure of both **1** and **2** is based on one of idealized C_4 symmetry and qualitative MO diagrams for both are presented in Figure 6.5 with the singly occupied molecular orbitals (SOMOs) for **1** and **2** shown in Figure 6.6. The primary difference in structure between **1** and **2** is that the ground state of **1** is $S = 3/2$ while for **2** the ground state is $S = 1/2$. The $S = 1/2$ state is favored by 48.83 kJ/mol over the $S = 3/2$. For **1**, two unpaired electrons lie in Co centered *d* orbitals with the third residing in a σ_{nb} orbital delocalized over the Co and Mo atoms. For **2**, there is only one unpaired electron and it resides in the σ_{nb} orbital as well. As seen in previously reported HEMACs and EMACs, the σ_{nb} orbital (a_{nb}) is significantly delocalized across the entire chain. In both **1** and **2**, this orbital is singly occupied and in conjunction with the doubly occupied σ orbital constitutes a 3c/3e- bond along the Mo–Mo–Co chains as originally reported in the $Co_3(dpa)_4Cl_2$ and $Cr_3(dpa)_4Cl_2$ EMACs by Bénard et al.[32-33]

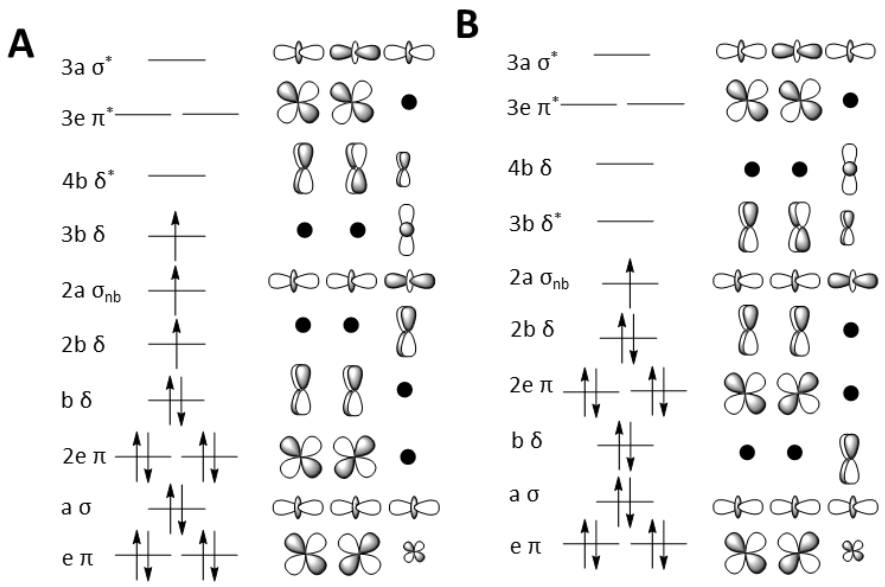

Figure 6.5 Qualitative MO diagrams for **1**(A) and **2**(B).

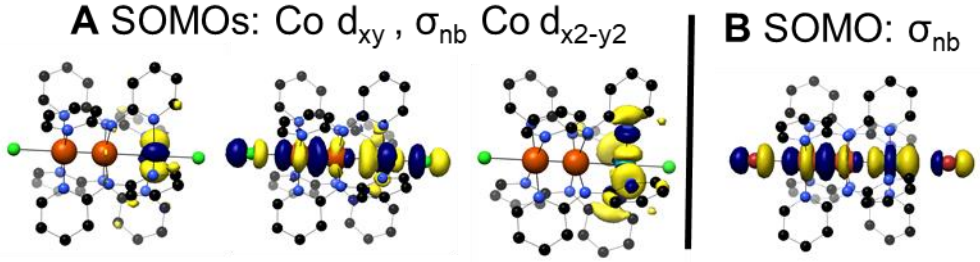

Figure 6.6 SOMOs for **1**(A) and **2**(B). Both **1** and **2** contain an unpaired electron in the σ_{nb} orbital.

6.4 Conclusions

In contrast to $Mo_2Co(dpa)_4Cl_2$ (**1**), which contains an isolated $S = 3/2$ spin center, we have now observed the presence of incomplete spin crossover in **2** through SQUID magnetometry, EPR, and MCD spectroscopy. Structurally, we believe that **2** must exist as a set of polymorphs although we have only been able to characterize one of them, which contains the low-spin Co^{2+} ion. The currently unknown polymorph must have a spin ground state of $S = 3/2$ analogous to **1**. Despite the fact that Br^- is a weaker field ligand than Cl^-, **2** can achieve a low-spin state where **1** does not. The low-spin state in **2** is attributed to dissociation of the Br^- ligand to a non-bonded distance in the structure, leaving the Co^{2+} ion in a pseudo square planar ligand field with a σ_{nb}^1 electron configuration.

6.5 Experimental Information

All reactions were carried out under a dry N_2 atmosphere using Schlenk techniques and glovebox methods. Pentane, hexanes, and acetonitrile was purified using a Vacuum Atmospheres solvent purification system. Dichloromethane was freshly distilled under N_2 over CaH_2 prior to use. $Mo_2(dpa)_4$ and $Mo_2Co(dpa)_4Cl_2$[8] were prepared according to literature procedures. $CoCl_2$ and $CoBr_2$ were purchased from Strem Chemicals and used as received. The ligand Hdpa was purchased from TCI and recrystallized from hot hexanes prior to use. IR spectra were taken on a BRUKER TENSOR 27 FTIR spectrometer using an attenuated total reflectance (ATR) adapter. SQUID. Variable temperature magnetic susceptibility measurements of crystalline samples of **1** and **2** were recorded at the University of Wisconsin-Madison on a SQUID Magnetometer (MPMS 3, Quantum Design) in the temperature range 2–300 K with an applied field of 0.1 Tesla. Experimental susceptibility and magnetization data were corrected for the underlying diamagnetism using Pascal's constants and for the temperature independent paramagnetism contributions. The data were modeled using the program PHI. The EPR measurements was carried out at 10K using a Bruker EleXeys EPR Spectrometer (E-500A console with ER 0495X SuperX bridge and SuperX cavity). The parameters were as follows: for **1** frequency = 9.3820 GHz, microwave power = 0.5024 mW; field center 2500 G; time constant 10.24; for **2** frequency = 9.3828 GHz, microwave power = 1.002 mW; field center 2500 G; time constant 10.24. Magnetic Circular Dichroism measurements and electronic absorption spectra were performed on mulls of compounds **1** and **2**. They were prepared by grinding crystalline samples with poly(dimethylsiloxane). Mulls were sandwiched between quartz windows and mounted in MCD cells. MCD data were collected at 4.5 K, 8 K, and 15 K with +7 T with a Jasco J-715 spectropolarimeter in conjunction with an Oxford Instruments SM4000-8T superconducting magnetocryostat. Al MCD spectra reported in this paper were obtained by subtracting the – 7 T spectrum from the + 7 spectrum.

$Mo_2Co(dpa)_4Br_2$ (**2**) Solid red $Mo_2(dpa)_4$ (225 mg, 0.258 mmol) and solid green $CoBr_2$ (96 mg, 0.44 mmol) were loaded into a 50 mL Schlenk Flask containing 5 g of naphthalene. The flask was then placed in a preheated sand bath at 195 C for 40 mins. After 40 minutes the reaction mixture changed in color from red to green black. The reaction mixture was cooled to room temperature and washed with 5 x 30 mL hot hexanes to remove the naphthalene. The resultant black solid was extracted using 15 mL DCM and layered

with pentane. Black block X–ray quality crystals were obtained after 3 days. (121 mg, yield; 43.2%) Calc: C 41.86%, H 2.91%, N 14.29 % Found C 14.77%, H 2.93 %, N 14.43 %. IR (ATR, cm^{-1}) 1638 w, 1602 m, 1593 m, 1561 m, 1527 w, 1462 s, 1419 s, 1352 s, 1312 s, 1283 w, 1262 w, 1237 w, 1154 m, 1057 m, 1014 w, 909 m, 858 m, 763 m, 655 m, 636 m, 623 m.

Crystallography

Crystallographic data were measured at the Molecular Structure Laboratory of the Chemistry Department of the University of Wisconsin—Madison. Crystals were selected under oil under ambient conditions and attached to the tip of a MiTeGen MicroMount©. Each crystal was mounted under a stream of cold nitrogen at 100(1) K and centered in the X-ray beam using a video camera. The crystal evaluation and data collection were performed on a Bruker Quazar SMART APEXIII diffractometer with Mo K-α (λ = 0.71073 A) radiation with a detector to crystal distance of 5.0 cm. The data were collected using a routine to survey the entire sphere of reciprocal space, and were indexed by the SMART program.[34] The structures were solved using direct methods and refined by least-squares refinement on F^2 followed by difference Fourier synthesis.[35] All hydrogen atoms were included in the final structure factor calculation at idealized positions and were allowed to ride on the neighboring atoms with relative isotropic displacement coefficients.

Computational Methods

The initial coordinates for **1** and **2** were obtained from the crystallographic data for the compounds with the solvent molecules of crystallization removed and the dominant orientation for any disorder utilized. All calculations were carried out using the program package ORCA version 4.1.1.[36] The BP86 exchange-correlation functional[37-38] was used. The Stuttgart-Dresden effective core potential (ECP), def2-SD,[39] was used along with valence basis sets def2-TZVP and density fitting basis set def2-TZVP/J for Mo atoms.[40] The def2-TZVP basis set and def2-TZVP/J auxiliary basis set was used for Co.[41-42] The def2-SVP basis set and def2-SVP/J density fitting basis set were used for all other atoms.[43-44] Tight optimization and tight self-consistent field convergence criteria were employed along with grid4 for all calculations. Frequency calculations were formed following geometry optimizations to ensure the structures were at local minimum. Löwdin population analysis was done to determine orbital populations.[45-46] Visualizations were

performed with the UCSF Chimera package.[47] Symmetry labels presented in the molecular orbital diagrams were assigned by inspection to conform to the idealized C_4 point group.

References

1. Rohmer, M.M.; Bénard, M., Bond Stretch Isomerism Still Elusive in Linear Trimetallic Complexes. DFT Calculations on Co_3(dipyridylamine)$_4Cl_2$. *J. Am. Chem. Soc.* **1998,** *120*, 9372-9373.

2. Rohmer, M.M.; Strich, A.; Bénard, M.; Malrieu, J.P., Metal–Metal Bond Length Variability in Co_3(dipyridylamide)$_4Cl_2$: Bond-Stretch Isomerism, Crystal Field Effects, or Spin Transition Process? A DFT Study. *J. Am. Chem. Soc.* **2001,** *123*, 9126-9134.

3. Rohmer, M.M.; Bénard, M., Bond-stretch isomerism in strained inorganic molecules and in transition metal complexes: a revival? *Chem. Soc. Rev.* **2001,** *30*, 340-354.

4. Clérac, R.; Cotton, F. A.; Daniels, L. M.; Dunbar, K. R.; Murillo, C. A.; Wang, X., Tuning the Metal–Metal Bonds in the Linear Tricobalt Compound $Co_3(dpa)_4Cl_2$: Bond-Stretch and Spin-State Isomers. *Inorg. Chem.* **2001,** *40*, 1256-1264.

5. Rohmer, M.M.; Bénard, M., Structural Versatility in Polyoxometalates and in Some Linear Trimetallic Complexes: An Electronic Interpretation. *J. Cluster Sci.* **2002,** *13*, 333-353.

6. Lai, S. H.; Hsiao, C. J.; Ling, J. W.; Wang, W. Z.; Peng, S. M.; Chen, I. C., Metal-metal bonding in metal?string complexes $M_3(dpa)_4X_2$ (M = Ni, Co, dpa = di(2-pyridyl)amido, and X = Cl, NCS) from resonance Raman and infrared spectroscopy. *Chem. Phys. Let.* **2008,** *456*, 181-185.

7. Chipman, J. A.; Berry, J. F., Extraordinarily Large Ferromagnetic Coupling ($J \geq 150$ cm^{-1}) by Electron Delocalization in a Heterometallic Mo≣Mo–Ni Chain Complex. *Chem. Eur. J.* **2018,** *24*, 1494-1499.

8. Nippe, M.; Victor, E.; Berry, J. F., Do Metal–Metal Multiply-Bonded "Ligands" Have a trans Influence? Structural and Magnetic Comparisons of Heterometallic Cr≡Cr···Co and Mo≡Mo···Co Interactions. *Eur. J. Inorg. Chem.* **2008**, 5569-5572.

9. Nippe, M.; Wang, J.; Bill, E.; Hope, H.; Dalal, N. S.; Berry, J. F., Crystals in Which Some Metal Atoms are More Equal Than Others: Inequalities From Crystal Packing and Their Spectroscopic/Magnetic Consequences. *J. Am. Chem. Soc.* **2010,** *132*, 14261-14272.

10. Christian, J. H.; Brogden, D. W.; Bindra, J. K.; Kinyon, J. S.; van Tol, J.; Wang, J.; Berry, J. F.; Dalal, N. S., Enhancing the Magnetic Anisotropy of Linear Cr(II) Chain Compounds Using Heavy Metal Substitutions. *Inorg. Chem.* **2016,** *55*, 6376-6383.

11. Rohmer, M. M.; Liu, I. P. C.; Lin, J. C.; Chiu, M. J.; Lee, C. H.; Lee, G. H.; Bénard, M.; López, X.; Peng, S. M., Structural, Magnetic, and Theoretical Characterization of a Heterometallic Polypyridylamide Complex. *Angew. Chemie. Int. Ed.* **2007,** *46*, 3533-3536.

12. Liu, I. P.C.; Lee, G.H.; Peng, S.M.; Bénard, M.; Rohmer, M.-M., Cu–Pd–Cu and Cu–Pt–Cu Linear Frameworks: Synthesis, Magnetic Properties, and Theoretical Analysis of Two Mixed-Metal Complexes of Dipyridylamide (dpa), Isostructural, and Isoelectronic with $[Cu_3(dpa)_4Cl_2]^+$. *Inorg. Chem.* **2007,** *46*, 9602-9608.

13. Nippe, M.; Bill, E.; Berry, J. F., Group 6 Complexes with Iron and Zinc Heterometals: Understanding the Structural, Spectroscopic, and Electrochemical Properties of a Complete Series of MM···M′ Compounds. *Inorg. Chem.* **2011,** *50*, 7650-7661.

14. Chipman, J. A.; Berry, J. F., Facile Axial Ligand Substitution in Linear Mo≣Mo–Ni Complexes. *Inorg. Chem.* **2018,** *57*, 9354-9363.

15. Huang, G. C.; Bénard, M.; Rohmer, M. M.; Li, L. A.; Chiu, M. J.; Yeh, C. Y.; Lee, G. H.; Peng, S. M., $Ru_2M(dpa)_4Cl_2$ (M = Cu, Ni): Synthesis, Characterization, and Theoretical Analysis of Asymmetric Heterometal String Complexes of the Dipyridylamide Family. *Eur. J. Inorg. Chem.* **2008**, 1767-1777.

16. Chang, W. C.; Chang, C. W.; Sigrist, M.; Hua, S. A.; Liu, T. J.; Lee, G. H.; Jin, B. Y.; Chen, C. H.; Peng, S. M., Nonhelical heterometallic $[Mo_2M(npo)_4(NCS)_2]$ string complexes (M = Fe, Co, Ni) with high single-molecule conductance. *Chem Commun.* **2017,** *53*, 8886-8889.

17. DeBrincat, D.; Keers, O.; McGrady, J. E., Can heterometallic 1-dimensional chains support current rectification? *Chem Commun.* **2013,** *49*, 9116-9118.

18. Weng, T.; DeBrincat, D.; Arcisauskaite, V.; McGrady, J. E., In search of structure-function relationships in transition-metal based rectifiers. *Inorg. Chem. Front.* **2014,** *1*, 468-477.

19. Clérac, R.; Cotton, F. A.; Dunbar, K. R.; Murillo, C. A.; Pascual, I.; Wang, X., Further Study of the Linear Trinickel(II) Complex of Dipyridylamide. *Inorg. Chem.* **1999,** *38*, 2655-2657.

20. Clérac, R.; Cotton, F. A.; Daniels, L. M.; Dunbar, K. R.; Kirschbaum, K.; Murillo, C. A.; Pinkerton, A. A.; Schultz, A. J.; Wang, X., Linear Tricobalt Compounds with Di(2-pyridyl)amide (dpa) Ligands: Temperature Dependence of the Structural and Magnetic Properties of Symmetrical and Unsymmetrical Forms of $Co_3(dpa)_4Cl_2$ in the Solid State. *J. Am. Chem. Soc.* **2000,** *122*, 6226-6236.

21. Clérac, R.; Cotton, F. A.; Daniels, L. M.; Dunbar, K. R.; Murillo, C. A.; Wang, X., Structural and magnetic properties of $Co_3(dpa)_4Br_2$ *Dalton Trans.* **2001**, 386-391.

22. Pantazis, D. A.; Murillo, C. A.; McGrady, J. E., A re-evaluation of the two-step spin crossover in the trinuclear cation $[Co_3(dipyridylamido)_4Cl_2]^+$. *Dalton Trans.* **2008**, 608-614.

23. Yang, E. C.; Cheng, M. C.; Tsai, M. S.; Peng, S. M., Structure of a linear unsymmetrical trinuclear cobalt(II) complex with a localized CO–CO bond: dichlorotetrakis[μ3-bis(2-pyridyl)amido]tricobalt(II). *J. Chem. Soc. Chem. Commun* **1994**, 2377-2378.

24. Albert Cotton, F.; M. Daniels, L.; T. Jordan Iv, G., Efficient preparation of a linear, symmetrical, metal–metal bonded tricobalt compound; should we believe there is a bond stretch isomer? *Chem Commun.* **1997**, 421-422.

25. Clérac, R.; Cotton, F. A.; Jeffery, S. P.; Murillo, C. A.; Wang, X., Compounds with Symmetrical Tricobalt Chains Wrapped by Dipyridylamide Ligands and Cyanide or Isothiocyanate Ions as Terminal Ligands. *Inorg. Chem.* **2001,** *40*, 1265-1270.

26. Pantazis, D. A.; McGrady, J. E., A Three-State Model for the Polymorphism in Linear Tricobalt Compounds. *J. Am. Chem. Soc.* **2006,** *128*, 4128-4135.

27. Cotton, F. A.; Murillo, C. A.; Wang, Q., Symmetrical linear Co_3^{6+} chains cocooned by two polypyridylamide ligands: How do they compare to open chains? *Inorg. Chim. Acta* **2010,** *363*, 4175-4180.

28. Berry, J. F.; Cotton, F. A.; Murillo, C. A.; Chan, Z.-K.; Yeh, C.W.; Chen, J.-D., Linear Trichromium, Tricobalt, Trinickel, and Tricopper Complexes of 2,2′-Dipyridylamide. In *Inorganic Syntheses: Volume 36*, John Wiley & Sons, Inc.: 2014; pp 102-110.

29. Lin, S.-Y.; Chen, I. W. P.; Chen, C.-h.; Hsieh, M.-H.; Yeh, C.-Y.; Lin, T.-W.; Chen, Y.-H.; Peng, S.-M., Effect of Metal–Metal Interactions on Electron Transfer: an STM Study of One-Dimensional Metal String Complexes. *J. Chem. Phys. B* **2004,** *108*, 959-964.

30. Nippe, M.; Berry, J. F., Introducing a Metal–Metal Multiply Bonded Group as an "Axial Ligand" to Iron: Synthetic Design of a Linear Cr–Cr···Fe Framework. *J. Am. Chem. Soc.* **2007,** *129*, 12684-12685.

31. Brogden, D. W.; Christian, J. H.; Dalal, N. S.; Berry, J. F., Completing the series of Group VI heterotrimetallic $M_2Cr(dpa)_4Cl_2$ (M_2 = Cr_2, Mo_2, MoW and W_2) compounds and investigating their metal–metal interactions using density functional theory. *Inorg. Chim. Acta* **2015,** *424*, 241-247.

32. Rohmer, M.-M.; Bénard, M., Structural Versatility in Polyoxometalates and in Some Linear Trimetallic Complexes: An Electronic Interpretation. *J. Cluster Sci.* **2002,** *13*, 333-353.

33. Benbellat, N.; Rohmer, M.-M.; Benard, M., Electronic origin of the structural versatility in linear trichromium complexes of dipyridylamide. *Chem. Commun.* **2001**, 2368-2369.

34. *Bruker-AXS*, Madison, Wisconsin, USA, 2009.

35. Dolomanov, O. V.; Bourhis, L. J.; Gildea, R. J.; Howard, J. A. K.; Puschmann, H., Olex: a complete structure solution, refinement and analysis program. In *Journal of applied crystallography*, Oxford, England :, 2009; Vol. 42, pp 339-341.

36. Neese, F., Software update: the ORCA program system, version 4.0. *Wiley Interdisciplinary Reviews: Computational Molecular Science* **2018,** *8*, e1327.

37. Becke, A. D., Density-functional exchange-energy approximation with correct asymptotic behavior. *Phys. Rev. A* **1988,** *38*, 3098-3100.

38. Perdew, J. P.; Yue, W., Accurate and simple density functional for the electronic exchange energy: Generalized gradient approximation. *Phys. Rev. B* **1986,** *33*, 8800-8802.

39. Pantazis, D. A.; Chen, X.-Y.; Landis, C. R.; Neese, F., All-Electron Scalar Relativistic Basis Sets for Third-Row Transition Metal Atoms. *J. Chem. Theory Comput.* **2008,** *4*, 908-919.

40. Andrae, D.; Haussermann, U.; Doll, G.; P. Stoll, H.; Preuss, H., Energy-Adjusted ab initio Pseudopotentials for the Second and Third Row Transition Elements. *Thoer. Chem. Acc.* **1990,** *77*, 123-141.

41. Weigend, F.; Ahlrichs, R., Balanced basis sets of split valence, triple zeta valence and quadruple zeta valence quality for H to Rn: Design and assessment of accuracy. *Phys. Chem. Chem. Phys.* **2005,** *7*, 3297-3305.

42. Weigend, F., Accurate Coulomb-fitting basis sets for H to Rn. *Phys. Chem. Chem. Phys.* **2006,** *8*, 1057-1065.

43. Eichkorn, K.; Treutler, O.; Öhm, H.; Häser, M.; Ahlrichs, R., Auxiliary basis sets to approximate Coulomb potentials. *Chem. Phys. Let.* **1995,** *240*, 283-290.

44. Eichkorn, K.; Weigend, F.; Treutler, O.; Ahlrichs, R., Auxiliary basis sets for main row atoms and transition metals and their use to approximate Coulomb potentials. *Theor. Chem. Acc.* **1997,** *97*, 119-124.

45. Löwdin, P. O., On the Non-Orthogonality Problem Connected with the Use of Atomic Wave Functions in the Theory of Molecules and Crystals. *J. Chem. Phys.* **1950,** *18*, 365-375.

46. Löwdin, P.O., On the Nonorthogonality Problem. *Advances in Quantum Chemistry* **1970,** *5*, 185-199.

47. Pettersen, E. F.; Goddard, T. D.; Huang, C. C.; Couch, G. S.; Greenblatt, D. M.; Meng, E. C.; Ferrin, T. E., UCSF Chimera—A visualization system for exploratory research and analysis. *J. Comp. Chem.* **2004,** *25*, 1605-1612.

Chapter Seven

Synthesis and Characterization of Metal Atom Chain Compounds as Molecular Wires

Chipman, J.A; Fu, T*; Venkataraman, L*; Berry, J.F

TF conducted the STM–bj measurements. All other work was performed by JAC.

7.1 Abstract

The ability to tune electron transport properties in molecular electronics is a desirable feature. Furthermore, the configuration of the linking group that binds a molecule to an electrode have been shown to have a significant impact on electron transport in organic compounds. The homometallic $Ni_3(dpa)_4I_2$ (**1**), $Ni_3(dpa)_4(NCS)_2$ (**2**), $Ni_3(dpa)_4(NCSe)_2$ (**3**) and the heterometallic $Mo_2Ni(dpa)_4(CN)_2$ (**4**), $Mo_2Ni(dpa)_4(NCS)_2$ (**5**), and $Mo_2Ni(dpa)_4(NCSe)_2$ (**6**) have been prepared in order to understand their electron transport properties in the context of molecular conductivity. Initial conductivity measurements suggest that compounds **2** and **5** are capable of electron transport, in agreement with prior reports. However, in contrast to earlier conductivity measurements in which **2** and **5** present distinct conductivity behavior, with our measurements both **2** and **5** illustrate nearly identical conductivity profiles. Compound **1** presents no conductivity behavior. Further work is needed to understand the electron transport capabilities of **3**, **4**, **5**, and **6**.

7.2 Introduction

Metal–atom chain compounds have recently attracted interest due to their potential to act as components in molecular electronics.[1-7] Of particular interest to our group are extended metal atom chains (EMACs) and heterometallic extended metal atom chains (HEMACs) supported by the dpa (2,2' dipyridylamine) ligand (Figure 7.1). On a superficial level, these chains bear a striking resemblance to macroscopic wires. Each chain is composed of a metal–atom core, analogous to the metal core of a macroscopic wire. The metal–atom chain is then encapsulated by a sheath of organic ligand, which is analogous to the insulation on a macroscopic wire (Figure 7.2).

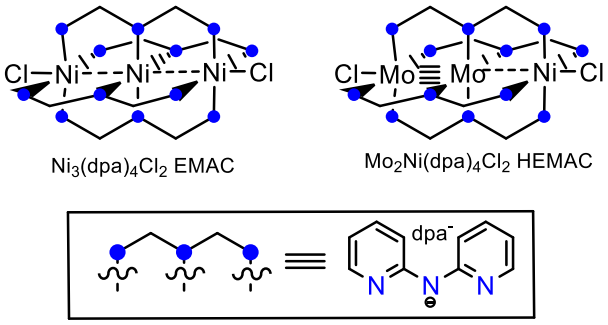

Figure 7.1 Homometallic $Ni_3(dpa)_4Cl_2$ EMAC (left) and heterometallic $Mo_2Ni(dpa)_4Cl_2$ HEMAC (right).

EMACs that range from three to eleven metal atoms long with axial thiocyanate (NCS) have been synthesized and evaluated with respect to electron transport.[5, 7, 11-20] These investigations rely on a modified scanning tunneling microscopy break junction (STM–bj) technique, which will be described later. It was determined that compounds with higher bond orders and greater electron delocalization had higher conductance values. For example, in comparing the trio of $M_3(dpa)_4(NCS)_2$ (M = Cr, Co, and Ni), Cr_3 demonstrated the highest conductance followed by Co_3 then Ni_3 compounds.[11] This trend is in accordance with the decreasing metal–metal bond order moving from $Cr_3 > Co_3 > Ni_3$. The pentametallic analogues of these compounds were also explored and presented the same trend in conductance values. These experimental conductance trends were also critically examined computationally using a non-equilibrium Green's function to calculate transmission spectra for each chain. These transmission spectra allow for the determination of the dominant electron transport channel and its symmetry.[21-22] The supporting dpa ligand was predicted to not contribute significantly to conductance. However, for Cr_3 and Co_3 chains, the conductance was found to depend on how close the singly occupied σ_{nb} orbital is to the Fermi level of the Au contacts. Moreover, the delocalization of the σ_{nb} orbitals onto the two terminal ligands suggests that the identity of these ligands can play an important role in modulating the conductance.

Experimental single – molecule conductance work has not yet been completed for HEMACs, however asymmetric HEMACs of the form $M_A–M_A–M_B$ have been explored computationally. Given their asymmetry it is not unreasonable to hypothesize that current will flow asymmetrically in these chains and that asymmetric HEMACs will behave as molecular diodes (rectifiers). Using a non-equilibrium Green's

function, the McGrady group examined $Mo_2M(dpa)_4(NCS)_2$ (M = Cr, Mn, Co) as well as $Ru_2M(dpa)_4(NCS)_2$ (M = Ni, Cu) HEMACs in the context of current rectification by calculating transmission plots of each compound.[23-24] From these plots they predicted that the Mo_2Co compound followed by Mo_2Cr provided the greatest potential as rectifiers. In contrast, they also calculated that the Mo_2Mn core would show only negligible current rectification. Given these computational data, there is a strong impetus to validate these results experimentally.

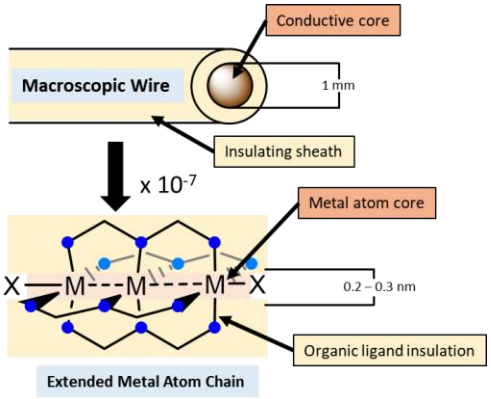

Figure 7.2. Macroscopic wires and the analogous molecular wires made with extended metal chains.

Recently, the lab of Peng and coworkers reported a trio of HEMACs supported by the npo (1,8–napthyridin–2(1H)–one ligand; $Mo_2M(npo)_4(NCS)_2$ (M = Fe, Co, and Ni).[25] The conductance values for these compounds are similar to one another, which suggests that the HEMACs' electron transport capabilities do not strongly depend on the metal atom identity. The $Mo_2Ni(dpa)_4(NCS)_2$ compound was also synthesized and examined with respect to electron transport. While it was found to support electron transport, the measured conductance values were lower than that of the npo supported compounds.[25] It is worth noting however, that the two Mo_2Ni conductance values are within the same as one another when the measurement errors are included in the comparison.

While the length of the metal–atom core,[5, 11, 20] the identity of the metals,[11] and the organic sheath ligand[25] have all been varied, the axial ligand identities have remained constant in all measurements. This is perhaps surprising given that in the realm of organic molecular electronics the identity of the linking moiety is found to be a critical component in determining the molecule's electron transport capabilities.[26-29] Through choice of linking group, the binding geometry of the molecule to the electrode is altered, which

further influences the orbital pathway available for electron transport. With a means of facile axial ligand substitution for both Ni_3 EMACs[4] and Mo_2Ni HEMACs,[30] we sought to provide a better understanding of the relationship between axial ligand identity and electron transport capabilities in the context of EMACs and HEMACs. Furthermore, we are interested in understanding the differences in the electron transport properties of EMACs and HEMACs.

7.3 Results and Discussion

Previously, our lab has reported a series of differently ligated Mo_2Ni compounds; $Mo_2Ni(dpa)_4(OTf)_2$, **5**, and **6**. $Mo_2Ni(dpa)_4(OTf)_2$ can be made directly via reaction of $Mo_2(dpa)_4$ and 1.5 equivalents of $Mo(OTf)_2$. Alternatively, it can be made through addition of 2 equivalents of TlOTf to $Mo_2Ni(dpa)_4Cl_2$. Compounds **5** and **6** can be subsequently made via addition of 2 equivalents of either NaNCS (**5**) or KNCSe (**6**) to a solution of $Mo_2Ni(dpa)_4(OTf)_2$ (Scheme 7.1).[30]

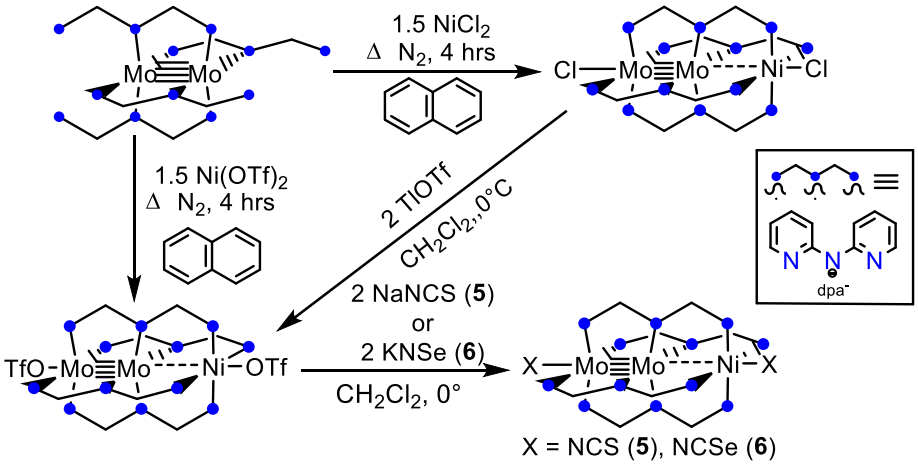

Scheme 7.1 Axial ligand substitution method to form **5** and **6**.[30]

Attempts to synthesize **4** directly via reaction of $Mo_2Ni(dpa)_4(OTf)_2$ with two equivalents of NaCN in the same method used to form **5** and **6** were unsuccessful. We attribute this to demetallation of Ni^{2+} from the chain, since NaCN is utilized as a reagent to extract a Cr atom from $Cr_3(dpa)_4Cl_2$ to form $Cr_2(dpa)_4$ presumably yielding the $[Cr(CN)_6]^{4-}$ ion as a byproduct. This hypothesis was further supported by the observation of a MALDI–TOF signal at 872 m/z, a mass consistent with the $Mo_2(dpa)_4$ moiety. Given the need for an alternative synthetic pathway, we took advantage of an existing synthetic protocol used to form

$SePPh_3$ via reaction of KSeCN with PPh_3.[31] Compound **6** was treated with 2.2 equivalents of PPh_3 in order to extract the terminal Se on either end of the Mo_2Ni chain (Scheme 7.2). After several hours of stirring at room temperature, the DCM is removed under vacuum and the product is washed with Et_2O. Both $SePPh_3$ and PPh_3 are soluble in Et_2O, while **6** is not. ^{31}P NMR spectra were taken of the Et_2O wash in order to confirm Se atom transfer from **6** to PPh_3. Two features are present in the spectrum at -34.19 ppm and -6.86 ppm attributable to $SePPh_3$ and PPh_3, respectively. Furthermore, the ^{31}P peak at -34.09 displays ^{77}Se satellites at -36.37 ppm and 31.82 ppm (Figure 7.3). The desired **6** is soluble in toluene while $SePPh_3$ and PPh_3 are not. Compound **6** can be extracted with toluene however, X–ray quality crystals of **6** were obtained using DCM. $SePPh_3$ is soluble in DCM hence the initial extraction was done in toluene. X–ray quality crystals could not be achieved using toluene and thus moving forward, we utilized DCM. ^{31}P NMR spectra of the DCM extract were blank and confirmed that no phosphine compounds were present. An IR spectrum of **4** presents a strong stretch at 2018 cm^{-1}, indicating C–bound cyano ligands.

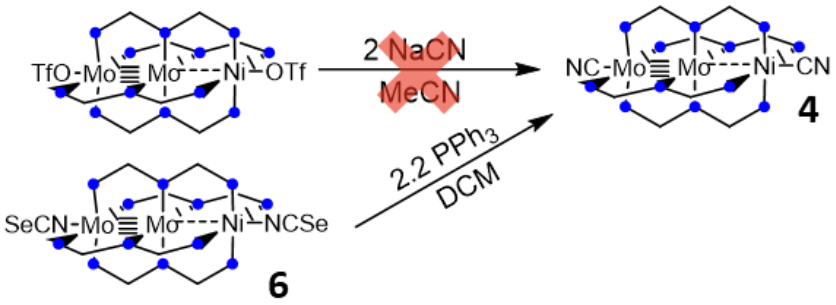

Scheme 7.2. Synthesis of **4** from **6**.

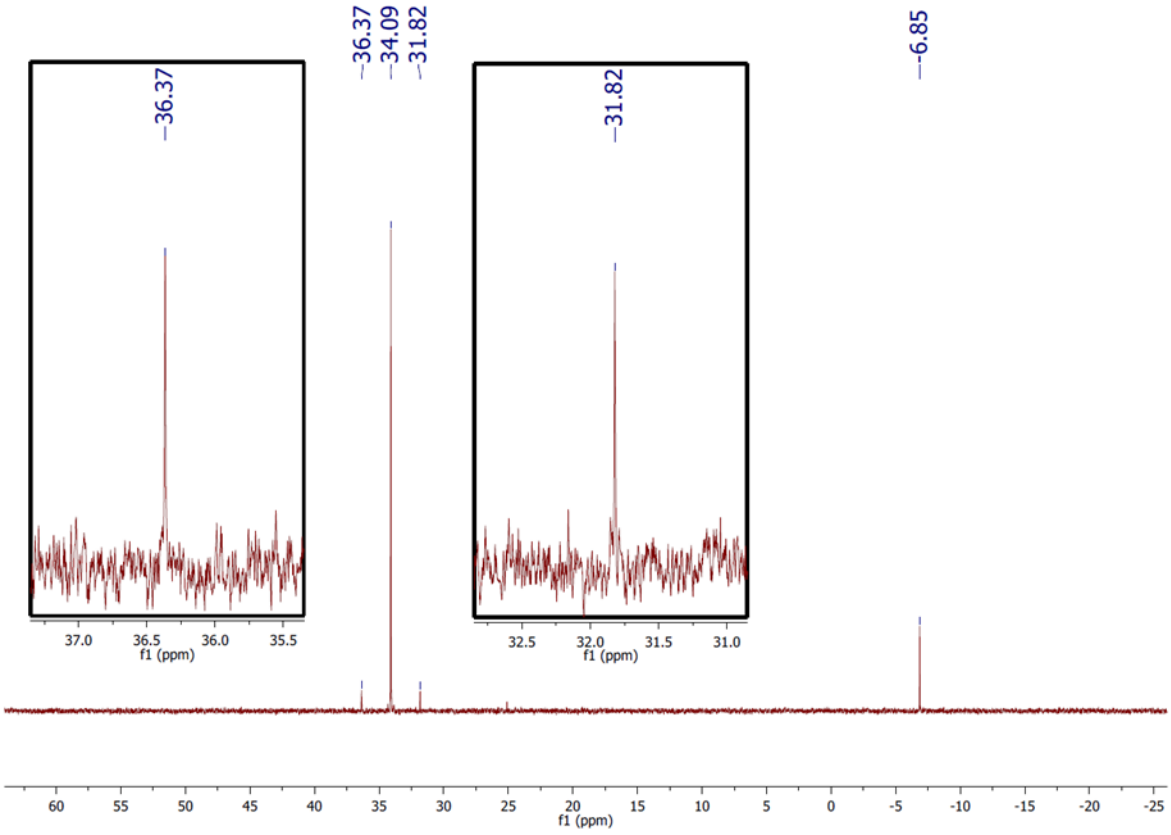

Figure 7.3 ^{31}P NMR of the reaction mixture of compound **6** with 2.2 equivalents of PPh_3.

Compound **4** contains similar core metrics to the other Mo_2Ni HEMACs that have been reported. The Mo≣Mo bond distance of 2.1249 Å (Table 7.2) slightly longer than previously reported which range from 2.0966(8) Å (**6**) to 2.110(8) Å ($Mo_2Ni(dpa)_4(OTf)_2$). As with the other reported $Mo_2Ni(dpa)_4X_2$ species, **4** contains a notably short Mo–Ni distance of 2.5481(8) Å. In comparison, the Mo–Ni distances reported thus far range from 2.458(8) ($Mo_2Ni(dpa)_4(OTf)_2$) to 2.5461(1) Å for **6**. To further put these distances in context, we may consider the Mo–M_B distances in $Mo_2M_B(dpa)_4Cl_2$ compounds with M_B = Cr, Mn, Fe, and Co. These distances range from 2.6170(7) Å in $Mo_2Co(dpa)_4Cl_2$ to 2.797(5) Å in $Mo_2Mn(dpa)_4Cl_2$.[32-35] We also considered the fact that the orientation of the cyanide ligand could be either C bound or N bound to the metal centers. We explored possibility of both arrangements in the crystal structure of **4**however, only the C–bound orientation yields a satisfactory model that is computationally sound and chemically reasonable. It is also important to note the incomplete occupancy of the cyanide moiety to our chain on the Mo side. An 11% occupancy of axial Cl was found in the crystal structure. The source of this chlorine is

currently unknown although we believe it may come from the DCM used in the synthesis of **4**. Given that the N–bound –NCSe must detach from the metal–atom chain and rearrange before reattaching, it is not unreasonable to hypothesize that DCM becomes activated during this process. Subsequent syntheses will be focused on using non–halogenated solvents. The other possible source for this Cl atom is in the initial starting material $Mo_2Ni(dpa)_4Cl_2$, which is subsequently transformed into the $Mo_2Ni(dpa)_4(OTf)_2$ followed by **6** before it is reacted with PPh_3 to form **4**. We have seen no evidence for Cl ligation in any other precursor however and thus we believe the first option for Cl integration into the crystal structure of **4** to be more likely.

The trimetallic $Ni_3(dpa)_4X_2$ (X = I, NCS, and NCSe) species were all synthesized using a method similar to that used previously to form Ni_3 chains ligated by CN, NCNCN, and C≡CPh.[2] The synthesis of $Ni_3(dpa)_4(NCS)_2$ has been previously reported via a self–assembly method by Peng and coworkers. We utilized an axial ligand substitution method for its gentler reaction conditions (Scheme 7.3). This method proceeds readily at room temperature in good yield. Crystal structures of the new compounds **1**, **3**, and **4** are shown in Figure 7.4 and crystallographic data are shown in Table 7.1 with selected bond distances in Table 7.3 (Compound **1** and **3**). Structurally, compounds **1** and **3** present similar bond metrics to those synthesized previously which range from 2.398 Å to 2.481 Å. The $Ni–N_{Outer}$ distances are elongated relative to the $Ni–N_{Inner}$ as well by 0.234 Å and 0.210 Å for **1** and **3**, respectively.

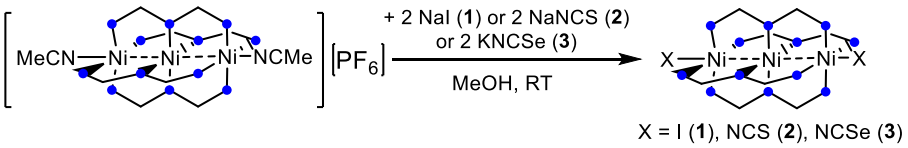

Scheme 7.3 Axial ligand substitution on a trinickel chain.

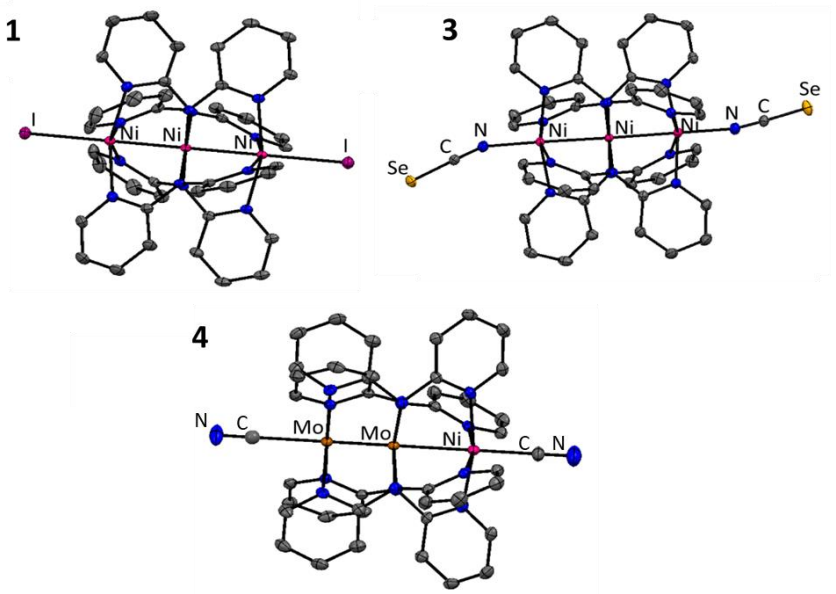

Figure 7.4 Crystal structures of the new compounds (from top to bottom) **1**, **3**, and **4**.

Table 7.1 Crystallographic data for compounds **1**, **3**, and **4**

Compound	**1**	**3**	**4**
Formula	$Ni_3(dpa)_4I_2$	$Ni_3(dpa)_4(NCSe)_2{\cdot}CH_2Cl_2$	$Mo_2Ni(dpa)_4(CN)_2{\cdot}CH_2Cl_2$
Crystal System	Tetragonal	Orthorhombic	Monoclinic
Space Group	*P*4/*n*	*Fddd*	*C*2/*c*
a/Å	11.6967(4)	21.1873(6)	18.913(4)
b/Å	11.6967(4)	22.9750(6)	16.182(3)
c/Å	15.8650(6)	35.9716(9)	15.864(3)
α/°	90	90	90
β/°	90	90	112.45(3)
γ/°	90	90	90
Volume/Å^3	2170.5(2)	17510.2(8)	4487.4(2)
Z	2	16	4
ρ_{calc}g/cm^3	1.699	1.7474	1.706
R_1[a] [I>=2σ (I)]	R_1 = 0.0201 wR_2 = 0.0542	R1 = 0.0280 wR2 = 0.0622	R_1 = 0.0276 wR_2 = 0.0700
R_1[b] [all data]	R_1 = 0.0201 wR_2 = 0.0542	R1 = 0.0364 wR2 = 0.0654	R_1 = 0.0367 wR_2 = 0.0746

[a] $R1 = \Sigma\big||F_o| - |F_c|\big|/\Sigma|F_o|$

[b] $wR2 = [\Sigma[w(F_o^2 - F_c^2)^2/\Sigma\big[(w(F_o^2)^2\big]]^{\frac{1}{2}}$, $w = 1/\sigma^2(F_o^2) + (aP)^2 + bP$ where $P = [\max(0 \text{ or } F_o^2) + 2(F_c^2)]/3$.

Table 7.2 Selected bond distances for heterometallic **4**

	4
Mo	2.1249(6
Mo···Ni	2.5481(8)
Mo–N_{Outer} (avg.)	2.204[2]
Mo–N_{Inner} (avg.)	2.119[2]
Ni–N_{Outer} (avg.)	2.113[2]
Mo–X_{Axial}	C: 2.373(9) Cl: 2.69(2)
Ni–X_{Axial}	C: 2.054(4)

Table 7.3 Selected bond distances for homometallic **1** and **3**

	1	**3·CH_2Cl_2**
Ni···Ni	2.4239(5) 2.4090(5)	2.4231(2)
Ni – N_{Outer} (avg.)	2.111[1]	2.084[2]
Ni – N_{Inner}	1.877(1)	1.884[2] (avg.)
Ni – X_{Axial}	2.6960(4) 2.7236(4)	2.004(2)

Conductivity measurements were obtained using a modified scanning tunneling microscopy break junction (STM–bj) methodology.[29, 36-39] In this methodology, a gold electrode is first bathed in a solution of the analyte. A gold STM tip is smashed into a gold substrate until a conductance value greater than 10 G_o (where G_o is the single quantum of conductance) is obtained. The tip is then removed slowly until the physical contact between the gold electrode and gold tip is broken, which allows for a single molecule of analyte to enter the gap. Eventually, the contact between the molecule and electrode is elongated and ruptured. This measurement is then repeated at a different location on the electrode. The overall process is repeated thousands of times in order to form a histogram of conductance values. In addition to a standard histogram of counts vs. conductance values, we also have obtained 2D histograms incorporating displacement distance and conductance in a "heat map" type plot. The area of interest in each histogram heat map is the oval in the center of each plot. The large block of yellow/red at the bottom of each plot results from background behavior in which no molecule is present between the tip and electrode.

The homometallic **1** presented no conductivity, suggesting that an iodine bridge is incapable at forming a contact with the gold electrode. Compounds **3** also failed to illustrate conductivity. However, given the past precedent for gold–selenium contacts in organic molecular electronics,[40-41] we are interested in repeating these measurements for **3** as well as taking initial measurements for **6**. Compound **4** has not yet been tested.

Compound **2** has been previously explored in terms of electron transport and was found to have a conductance of 3.8 (± 0.6) x 10^{-3} G_0 with a resistance of 3.4(± 0.5) MΩ. [25] In our measurements, we obtained a value of 10.0 x 10^{-3} G this translates to a resistance of 14.2 MΩ. This discrepancy may be the result of a difference in the number of measurements taken or a difference in testing methodology. Previous work in this area relied on manual measurements. A similar case is seen in compound **5**, which was recently reported. A conductance of 6.2 (± 5.4) x 10^{-3} G_0 corresponding to a resistance of 2.1 (± 1.9) MΩ. For our sample, we obtained values of 7.75 x 10^{-3} G_0 and 15.2 MΩ for conductance and resistance, respectively. In contrast to the previous report of **2** and **5**, we observe that these two species behave effectively the same in terms of electron transport. We are currently exploring the potential of **5** in the context of preferential current flow. The histograms for **2** and **5** are shown in Figure 7.5.

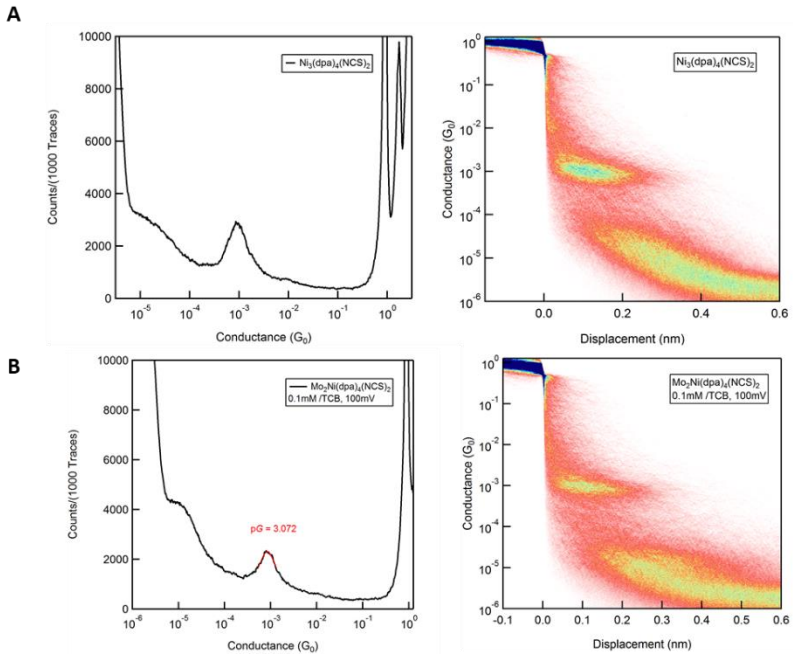

Figure 7.5 Histograms of conductance (left) and distance conductance (right) for **2** (A) and **5** (B) All measurements were collected at 0.1 mM concentration in 1,3,5 trichlorobenzene.

7.4 Conclusions

Preliminary work toward the testing the single molecule conductivity in heterometallic chain compounds has been presented. In comparison to the homometallic **2**, the heterometallic **5** illustrates similar conductivity values. Future work in this area will continue to explore the ability of asymmetric HEMACs to preferentially allow current flow. We also are planning future work toward better understanding axial ligation effects on electron transport. We have determined that the iodine axial ligands are not conducive to electron transport. However, we remain optimistic that the selenocyanate and cyano compounds will allow electron transport.

7.5 Experimental Section

Materials and Methods

All reactions were carried out under a dry N_2 atmosphere using Schlenk techniques and glovebox methods. Pentane was purified using a Vacuum Atmospheres solvent purification system. Dichloromethane was freshly distilled under N_2 over CaH_2 prior to use. Methanol was freshly distilled under N_2 over Mg prior to use. $Ni_3(dpa)_4Cl_2$, $[Ni_3(dpa)_4(MeCN)_2][PF_6]_2$, $Mo_2Ni(dpa)_4$, $Mo_2Ni(dpa)_4(NCS)_2$, $Mo_2Ni(dpa)_4(NCSe)_2$ were prepared according to previous literature procedures. Naphthalene was purchased from Sigma-Aldrich and sublimed prior to use. Anhydrous hexanes, ether, acetonitrile, and toluene were purchased from Sigma–Aldrich and degassed prior to use. KNCSe, and NaNCS were purchased from Sigma–Aldrich and dried under vacuum at 40 C for 8 hours prior to use. The ligand Hdpa was purchased from TCI and recrystallized from hot hexanes prior to use. Elemental analysis was carried out by Midwest Microlabs, LLC, Indianapolis, IN. IR spectra were taken on a BRUKER TENSOR 27 FTIR spectrometer using an attenuated total reflectance (ATR) adapter. MALDI mass spectra were obtained on Bruker Impact™ II MALDI mass spectrometer. ^{1}H and ^{31}P NMR spectra were obtained on a 500 MHz Bruker Avance III. ^{31}P NMR was absolute referenced to a ^{1}H NMR spectrum. STM-bj measurements were performed at Columbia University by TF.

Crystallography

Crystallographic data were measured at the Molecular Structure Laboratory of the Chemistry Department of the University of Wisconsin—Madison. Crystals were selected under oil under ambient conditions and attached to the tip of a MiTeGen MicroMount©. Each crystal was mounted under a stream of cold nitrogen at 100(1) K and centered in the X-ray beam using a video camera. The crystal evaluation and data collection were performed on a Bruker Quazar SMART APEXIII diffractometer with Mo K-α (λ = 0.71073 A) radiation with a detector to crystal distance of 5.0 cm. The data were collected using a routine to survey the entire sphere of reciprocal space, and were indexed by the SMART program.[1] The structures were solved using direct methods and refined by least-squares refinement on F^2 followed by difference Fourier synthesis.[2] All hydrogen atoms were included in the final structure factor calculation at idealized positions and were allowed to ride on the neighboring atoms with relative isotropic displacement coefficients. Due to crystallographic disorder, C22 and Cl3 were unable to be refined anistoropically and were thus left refined isotropically.

$Mo_2Ni(dpa)_4(CN)_2$ Solid brown microcrystalline $Mo_2Ni(dpa)_4(NCSe)_2$ (71.2 mg, 0.0623 mmol) and PPh_3 (54.1 mg, 0.138 mmol) were dissolved in 20 mL DCM. The reaction mixture was allowed to stir at room temperature for 3 hours with no apparent color change. The solvent was removed under reduced pressure. The residual brown solid was washed with 3 x 30 mL Et_2O to remove and $SePPh_3$. The brown solid was extracted in 10 mL toluene, which was subsequently removed under reduced pressure. The brown solid was redissolved in 10 mL DCM and layered with pentane. X–ray quality crystals were obtained after 3 days. Yield: IR (ATR, cm^{-1}): 2018 s, 1603 m, 1594 m, 1561, 1543 w,1474 w, 1459 s, 1422 s, 1353 s, 1309 s, 1282 w, 1261 w, 1158 m, 1097 m, 1017 w, 878 m, 856 m, 802 m, 763 s, 739 w, 692 m, 639 m.

$Ni_3(dpa)_4I_2$ Solid purple $[Ni_3(dpa)_4(MeCN)_2][PF_6]_2$ (224 mg, 0.180 mmol) and solid NaI (55 mg, 0.31 mmol) were loaded into a 100 mL Schlenk Flask with 40 mL dry MeOH. The reaction mixture was allowed to stir for 3 hours after which time a brown-purple microcrystalline precipitate had formed. The precipitate was collected on a frit and washed with 2 x 40 mL Et_2O. The brown solid was dried overnight under vacuum. Yield (144 mg, 67 %) Alternatively, the solid may be extracted with DCM and layered with hexanes to afford X – ray quality crystals after several days at a lower yield. Anal. Calcd. for $Ni_3C_{40}H_{32}N_{12}I_2$•0.33 CH_2Cl_2: C,

42.53%; H, 2.87 %; N, 14.76 %. Found: C, 42.35 %, H, 2.83 %; N, 14.72 %. IR (ATR, cm^{-1}): 1603 m, 1592 m, 1550, 1460 s, 1424 s, 1361 s, 1314 s, 1197 m, 1152 m, 1012 w, 895 m, 759 s, 737 w, 659 m.

$Ni_3(dpa)_4(NCS)_2$ Solid purple $[Ni_3(dpa)_4(MeCN)_2][PF_6]_2$ (137 mg, 0.111 mmol) and white solid NaNCS (39 mg, 0.48 mmol) were loaded into a 100 mL Schlenk flask with 25 mL dry MeOH. The reaction mixture was allowed to stir for 3 hours after which time a purple precipitate had formed. The precipitate was collected on a frit and washed with 2 x 40 mL Et_2O and extracted with 20 mL DCM. The purple solution was layered with hexanes. After several days, dark purple needles suitable for diffraction were collected Yield: 77.8 mg, 72%. Product identity confirmed via unit cell.

$Ni_3(dpa)_4(NCSe)_2$ Solid purple $[Ni_3(dpa)_4(MeCN)_2][PF_6]_2$ (152 mg, 0.124 mmol) and white solid KSeCN (47 mg, 0.33 mmol) were loaded into a 100 mL Schlenk flask with 25 mL dry MeOH. The reaction mixture was allowed to stir for 3 hours after which time a purple precipitate had formed. The precipitate was collected on a frit and washed with 2 x 40 mL Et_2O and extracted with 20 mL DCM. The purple solution was layered with hexanes. After several days, dark purple needles suitable for diffraction were collected Yield: 96.4 mg 73.1 %. Anal. Calcd. for $Ni_3C_{42}H_{34}N_{14}Se_2 \cdot CH_2Cl_2$: C, 44.84 %; H, 2.98 %; N, 17.03 %. Found: C, 44.92 %, H, 2.95 %; N, 16.90 %. IR (ATR, cm^{-1}): 2067 m, 1603 m, 2594 m, 1550 m, 1466 s, 1458 m, 1420 s, 1394 m, 1357 s, 1311 s, 1242 s, 1154 m, 1066 m, 1018 m, 897 m, 879 m, 761 s, 737 w, 675 m, 665 m, 646 w.

References

1. Berry, J. F.; Cotton, F. A.; Daniels, L. M.; Murillo, C. A., A Trinickel Dipyridylamido Complex with Metal–Metal Bonding Interaction: Prelude to Polynickel Molecular Wires and Devices? *J. Am. Chem. Soc.* **2002,** *124*, 3212-3213.

2. Berry, J. F.; Albert Cotton, F.; Murillo, C. A., Making connections with molecular wires: extending tri-nickel chains with axial cyanide, dicyanamide, and phenylacetylide ligands. *Dalton Trans.* **2003**, 3015-3021.

3. Berry, J. F.; Cotton, F. A.; Murillo, C. A., A Trinuclear EMAC-Type Molecular Wire with Redox-Active Ferrocenylacetylide "Alligator Clips" Attached. *Organometallics* **2004,** *23*, 2503-2506.

4. Berry, J. F.; Cotton, F. A.; Murillo, C. A.; Roberts, B. K., An Efficient Synthesis of Acetylide/Trimetal/Acetylide Molecular Wires. *Inorg. Chem.* **2004,** *43*, 2277-2283.

5. Yeh, C. Y.; Wang, C. C.; Chen, C. H.; Peng, S. M., Molecular Metal Wires Built from a Linear Metal Atom Chain Supported by Oligopyridylamido Ligands. In *Redox Systems Under Nano-Space Control*, Hirao, T., Ed. Springer Berlin Heidelberg: Berlin, Heidelberg, 2006; pp 85-117.

6. Berry, J. F., Metal–Metal Bonds in Chains of Three or More Metal Atoms: From Homometallic to Heterometallic Chains. In *Metal-Metal Bonding*, Parkin, G., Ed. Springer Berlin Heidelberg: Berlin, Heidelberg, 2010; pp 1-28.

7. Hua, S.A.; Cheng, M.C.; Chen, C.H.; Peng, S.M., From Homonuclear Metal String Complexes to Heteronuclear Metal String Complexes. *Eur. J. Inorg. Chem.* **2015,** *2015*, 2510-2523.

8. Hurley, T. J.; Robinson, M. A., Nickel(II)-2,2'-dipyridylamine system. I. Synthesis and stereochemistry of the complexes. *Inorg. Chem.* **1968,** *7*, 33-38.

9. Aduldecha, S.; Hathaway, B., Crystal structure and electronic properties of tetrakis[μ3-bis(2-pyridyl)amido]dichlorotrinickel(II)–water–acetone (1/0.23/0.5). *Dalton Trans.* **1991**, 993-998.

10. Chipman, J. A.; Berry, J. F., Extraordinarily Large Ferromagnetic Coupling ($J \geq 150$ cm^{-1}) by Electron Delocalization in a Heterometallic Mo≡Mo–Ni Chain Complex. *Chem. Eur. J.* **2018,** *24*, 1494-1499.

11. Chen, I. W. P.; Fu, M.D.; Tseng, W.H.; Yu, J.Y.; Wu, S.H.; Ku, C.J.; Chen, C.H.; Peng, S.M., Conductance and stochastic switching of ligand-supported linear chains of metal atoms. *Angew. Chem. Int. Ed.* **2006** *45* , 5814-8.

12. Huang, M. J.; Hua, S. A.; Fu, M.D.; Huang, G. C.; Yin, C.; Ko, C. H.; Kuo, C. K.; Hsu, C.H.; Lee, G. H.; Ho, K. Y.; Wang, C. H.; Yang, Y. W.; Chen, I. C.; Peng, S. M.; Chen, C. H., The First Heteropentanuclear Extended Metal-Atom Chain: $[Ni^{+}\text{-}Ru_2^{5+}\text{-}Ni^{2+}\text{-}Ni^{2+}(tripyridyldiamido)_4(NCS)_2]$. *Chem. Eur. J.* **2014,** *20*, 4526-4531.

13. Berry, J. F.; Cotton, F. A.; Lei, P.; Lu, T.; Murillo, C. A., Additional Steps toward Molecular Scale Wires: Further Study of $Ni_5^{10/11+}$ Chains Embraced by Polypyridylamide Ligands. *Inorg. Chem.* **2003,** *42*, 3534-3539.

14. Lin, S.Y.; Chen, I. W. P.; Chen, C.H.; Hsieh, M.H.; Yeh, C.Y.; Lin, T.-W.; Chen, Y.H.; Peng, S.M., Effect of Metal–Metal Interactions on Electron Transfer: an STM Study of One-Dimensional Metal String Complexes. *J. Phys. Chem. B* **2004,** *108*, 959-964.

15. Shih, K.N.; Huang, M.J.; Lu, H.C.; Fu, M.D.; Kuo, C.K.; Huang, G.C.; Lee, G.H.; Chen, C.H.; Peng, S.m., On the tuning of electric conductance of extended metal atom chains via axial ligands for $[Ru_3(dpa)_4(X)_2]^{0/+}$ (X = NCS, CN). *Chem Commun.* **2010,** *46*, 1338-1340.

16. Tsai, T. W.; Huang, Q. R.; Peng, S. M.; Jin, B. Y., Smallest Electrical Wire Based on Extended Metal-Atom Chains. *J. Phys. Chem. C* **2010,** *114*, 3641-3644.

17. Ismayilov, R. H.; Wang, W. Z.; Lee, G. H.; Yeh, C. Y.; Hua, S. A.; Song, Y.; Rohmer, M. M.; Bénard, M.; Peng, S. M., Two Linear Undecanickel Mixed-Valence Complexes: Increasing the Size and the Scope of the Electronic Properties of Nickel Metal Strings. *Angew. Chemie. Int. Ed.* **2011,** *50*, 2045-2048.

18. Yang, C. C.; Liu, I. P. C.; Hsu, Y. J.; Lee, G. H.; Chen, C. H.; Peng, S. M., Synthesis, Structure, Magnetism, and Single Molecular Conductance of Linear Trinickel String Complexes with Sulfur Containing Ligands. *Eur. J. Inorg. Chem.* **2013,** *2013*, 263-268.

19. Ting, T. C.; Hsu, L. Y.; Huang, M. J.; Horng, E. C.; Lu, H. C.; Hsu, C. H.; Jiang, C. H.; Jin, B. Y.; Peng, S. M.; Chen, C. H., Energy-Level Alignment for Single-Molecule Conductance of Extended Metal-Atom Chains. *Angew. Chem. Int. Ed.* **2015**.

20. Chen, P. J.; Sigrist, M.; Horng, E. C.; Lin, G. M.; Lee, G. H.; Chen, C. H.; Peng, S. M., A ligand design with a modified naphthyridylamide for achieving the longest EMACs: the 1st single-molecule conductance of an undeca-nickel metal string. *Chem Commun.* **2017,** *53* (34), 4673-4676.

21. Georgiev, V. P.; McGrady, J. E., Influence of Low-Symmetry Distortions on Electron Transport through Metal Atom Chains: When Is a Molecular Wire Really "Broken"? *J. Am. Chem. Soc.* **2011,** *133*, 12590-12599.

22. Mohan, P. J.; Georgiev, V. P.; McGrady, J. E., Periodic trends in electron transport through extended metal atom chains: comparison of $Ru_3(dpa)_4(NCS)_2$ with its first-row analogues. *Chem. Sci.* **2012,** *3* , 1319-1329.

23. DeBrincat, D.; Keers, O.; McGrady, J. E., Can heterometallic 1-dimensional chains support current rectification? *Chem Commun.* **2013,** *49*, 9116-9118.

24. Weng, T.; DeBrincat, D.; Arcisauskaite, V.; McGrady, J. E., In search of structure-function relationships in transition-metal based rectifiers. *Inorg. Chem. Front.* **2014,** *1*, 468-477.

25. Chang, W. C.; Chang, C. W.; Sigrist, M.; Hua, S. A.; Liu, T. J.; Lee, G. H.; Jin, B. Y.; Chen, C. H.; Peng, S. M., Nonhelical heterometallic $[Mo_2M(npo)_4(NCS)_2]$ string complexes (M = Fe, Co, Ni) with high single-molecule conductance. *Chem Commun.* **2017,** *53*, 8886-8889.

26. Quek, S. Y.; Venkataraman, L.; Choi, H. J.; Louie, S. G.; Hybertsen, M. S.; Neaton, J. B., Amine–Gold Linked Single-Molecule Circuits: Experiment and Theory. *Nano Lett* **2007,** *7*, 3477-3482.

27. Park, Y. S.; Whalley, A. C.; Kamenetska, M.; Steigerwald, M. L.; Hybertsen, M. S.; Nuckolls, C.; Venkataraman, L., Contact Chemistry and Single-Molecule Conductance: A Comparison of Phosphines, Methyl Sulfides, and Amines. *JACS* **2007,** *129* (51), 15768-15769.

28. Kamenetska, M.; Koentopp, M.; Whalley, A. C.; Park, Y. S.; Steigerwald, M. L.; Nuckolls, C.; Hybertsen, M. S.; Venkataraman, L., Formation and Evolution of Single-Molecule Junctions. *Physical Review Lett* **2009,** *102*, 126803.

29. Su, T. A.; Neupane, M.; Steigerwald, M. L.; Venkataraman, L.; Nuckolls, C., Chemical principles of single-molecule electronics. *Nat. Rev. Mat.* **2016,** *1*, 16002.

30. Chipman, J. A.; Berry, J. F., Facile Axial Ligand Substitution in Linear Mo≣Mo–Ni Complexes. *Inorg. Chem.* **2018,** *57*, 9354-9363.

31. Spirk, S.; Pietschnig, R., *NMR Properties of $SePPh_3$ in the Solid State*. 2006; p 1430.

32. Nippe, M.; Victor, E.; Berry, J. F., Do Metal–Metal Multiply-Bonded "Ligands" Have a trans Influence? Structural and Magnetic Comparisons of Heterometallic Cr≡Cr···Co and Mo≡Mo···Co Interactions. *Eur. J. Inorg. Chem.* **2008**, 5569-5572.

33. Nippe, M.; Wang, J.; Bill, E.; Hope, H.; Dalal, N. S.; Berry, J. F., Crystals in Which Some Metal Atoms are More Equal Than Others: Inequalities From Crystal Packing and Their Spectroscopic/Magnetic Consequences. *J. Am. Chem. Soc.* **2010,** *132*, 14261-14272.

34. Nippe, M.; Bill, E.; Berry, J. F., Group 6 Complexes with Iron and Zinc Heterometals: Understanding the Structural, Spectroscopic, and Electrochemical Properties of a Complete Series of MM···M′ Compounds. *Inorg. Chem.* **2011,** *50*, 7650-7661.

35. Brogden, D. W.; Christian, J. H.; Dalal, N. S.; Berry, J. F., Completing the series of Group VI heterotrimetallic $M_2Cr(dpa)_4Cl_2$ (M_2 = Cr_2, Mo_2, MoW and W_2) compounds and investigating their metal–metal interactions using density functional theory. *Inorg. Chim. Acta* **2015,** *424*, 241-247.

36. Xu, B.; Tao, N. J., Measurement of Single-Molecule Resistance by Repeated Formation of Molecular Junctions. *Science* **2003,** *301*, 1221-1223.

37. Quek, S. Y.; Kamenetska, M.; Steigerwald, M. L.; Choi, H. J.; Louie, S. G.; Hybertsen, M. S.; Neaton, J. B.; Venkataraman, L., Mechanically controlled binary conductance switching of a single-molecule junction. *Nature Nano.* **2009,** *4*, 230.

38. Li, H.; Su, T. A.; Camarasa-Gómez, M.; Hernangómez-Pérez, D.; Henn, S. E.; Pokorný, V.; Caniglia, C. D.; Inkpen, M. S.; Korytár, R.; Steigerwald, M. L.; Nuckolls, C.; Evers, F.; Venkataraman, L., Silver Makes Better Electrical Contacts to Thiol-Terminated Silanes than Gold. *Angew. Chem. Int. Ed.* **2017,** *129*, 14333-14336.

39. Hybertsen, M. S.; Venkataraman, L., Structure–Property Relationships in Atomic-Scale Junctions: Histograms and Beyond. *Acc. Chem. Res.* **2016,** *49*, 452-460.

40. Patrone, L.; Palacin, S.; Bourgoin, J. P.; Lagoute, J.; Zambelli, T.; Gauthier, S., Direct comparison of the electronic coupling efficiency of sulfur and selenium anchoring groups for molecules adsorbed onto gold electrodes. *Chem. Phys.* **2002,** *281*, 325-332.

41. Patrone, L.; Palacin, S.; Bourgoin, J. P., Direct comparison of the electronic coupling efficiency of sulfur and selenium alligator clips for molecules adsorbed onto gold electrodes. *Applied Surface Science* **2003,** *212-213*, 446-451.